博士論文

Study on Brittle Crack Propagation and Arrest Behavior in Steels from the Perspective of Local Fracture Stress

(局所破壊応力に着目した鋼材における
脆性亀裂伝播・停止挙動の研究)

柳本 史教

Acknowledgement

This dissertation is a collection of a series of studies conducted while I am a student of the Graduate School of Engineering, the University of Tokyo. I would like to express my sincere gratitude to kind and beneficial supervision of Associate Professor Dr. Kazuki Shibanuma. This study has not been able to be conducted without his supervision. And, I would like to express my thanks to Professor Dr. Katsuyuki Suzuki for his instructions to this dissertation. Especially, I would like to be grateful that he has undertaken the chief examiner of this dissertation.

I would also like to express my gratitude to Professor Dr. Mitsuru Ohata, Division of Materials and Manufacturing Science, Osaka University, Professor Dr. Satoshi Izumi in Dept. Mechanical Engineering, the University of Tokyo, Associate Professor Dr. Taira Okita, Research into Artifacts, Center for Engineering, the University of Tokyo, for their valuable comments on this study in the dissertation committee.

It should be noted that this dissertation has been supported by many people. This dissertation has been conducted as the collaborative researchers with Nippon Kaiji Kyokai (classNK) and Nippon Steel & Sumitomo Metal Cooperation. And, this dissertation has been supported in financial manner by KAKENHI and Fundamental Research Developing Association for Shipbuilding and Offshore. In particular, the author has been granted as Research Fellowship DC2 for Young Scientists of Japan Society for the Promotion of Science (JSPS). Professor Dr. Shuji Aihara and Associate Professor Dr. Tomoya Kawabata, the University of Tokyo, provided many advices to complete this dissertation. The steel N was provided by ATE committee in Japan Welding Engineering Society and the three steels employed in Chapter 8 were provided by Dr. Shirahata in Nippon Steel & Sumitomo Metal Cooperation. Some of crack propagation experiments were supported by Mr. Takashimizu and Mr. Hosoda in Kashima Unit, Nippon Steel & Sumikin Technology. Wide plate experiments in Chapter 5 were carried out under cooperation with Dr. Okawa in Nippon Steel & Sumitomo Metal Cooperation. Mr. Akiyasu Morita supported my experiments for 5 years although I made a lot of inconvenience to him. Mr. Takumi Ozawa in National Maritime Research Institute, provided some technical advices to my experiments using high speed camera. Mrs. Ohmori carried out a lot of paperwork related to this study. I would be grateful to them.

To complete this dissertation, I would like to express many thanks to my colleague students. Especially, this dissertation includes some collaboration works with Mr. Yo Nishioka, Mr.

Takuhiro Hemmi and Mr. Yuya Shirai. Mr. Toshiaki Maegawa, Mr. Kuriya Miyamoto, Mr. Masaki Sano, Mr. Daichi Yanagisawa, Mr. Daishi Sagawa were my first colleagues in Dept. Systems Innovation. Mr. Yoshiki Nemoto, Mr. Yuki Yamamoto Mr. Shohei Asako, Mr. Yuki Nishizono, Mr. Kazuya Kiriyama, Mr. Takahiro Hosoe, Mr. Koya Ueda, Mr. Hiroaki Ito, Mr. Kota Kishi, and Mr. Yuta Suzuki were also good colleagues to study together. In particular, Dr. Kawata was always instructive to me, and thus I would like to heavy thanks to him. Furthermore, my attitude to scientific research was partly influenced by Professor Emeritus Takahisa Kato and Dr. Shu Sawai when I carried out a bachelor thesis in Dept. Mechanical Engineering, School of Engineering, the University of Tokyo.

At last, I would like to express thanks to my parents to support my PhD life.

November, 30th , 2018

Fuminori Yanagimoto

Table of Contents

Chapter 1 Introduction 1

1.1. Background 1

1.1.1. Social background 1

1.1.2. Demands of brittle crack arrest concept 4

1.1.3. Fundamental concept of brittle crack arrest 7

1.1.4. Local fracture stress criterion 9

1.2. Review of recent related researches 11

1.2.1. Conventional approach: Stress intensity factor 11

1.2.2. Alternative method to evaluate brittle crack arrestability 16

1.2.3. Numerical methods and modelling 18

1.2.4. Experimental techniques 24

1.2.5. Critical condition of brittle crack propagation and arrest behaviors 27

1.2.6. 3D effect 30

1.2.7. Crack arrest design 32

1.2.7.1. Material design 32

1.2.7.2. Structural design 35

1.3. Objective and contents 39

Chapter 2 Local stress evaluation in finite element analyses 55

2.1. Introduction 55

2.2. Nodal force release technique and finite element mesh 56

2.3. Evaluation of local stress by generation phase 61

2.3.1. Numerical conditions and employed error indicators 61

2.3.2. Evaluation of conventional methods 63

2.3.2.1. Conventional nodal force release methods for two minimum mesh sizes 64

2.3.2.2. Time increment dependency 66
2.3.3. Optimization of nodal release path control 67
2.3.4. Application of artificial damping 71
2.3.4.1. Viscous term in time integration (HHT method) 71
2.3.4.2. Rayleigh damping 72
2.4. Application phase analyses 76
2.5. Discussion 80
2.5.1. Generation phase analyses 80
2.5.2. Application phase analyses 81
2.6. Conclusion 82
Chapter 3 Local tensile stress in the vicinity of the propagating crack tip ... 89
3.1. Introduction 89
3.2. Materials 91
3.3. Experiments 96
3.3.1. Concept of experiments 96
3.3.2. Specimen 96
3.3.3. Procedure 101
3.3.4. Results 103
3.4. Local fracture stress evaluation by finite element analysis 110
3.4.1. Procedure 110
3.4.2. Result 113
3.5. Discussion 119
3.5.1. Characteristics of local fracture stress 119
3.5.2. Microstructure and local fracture stress 120
3.5.3. Scatter of the local fracture stresses 121
3.5.4. Temperature dependency of the local fracture stresses 122

3.6. Conclusion 124

Chapter 4 Governing factors of local stresses in the vicinity of the running crack tip in elastic- viscoplastic solids 129

4.1. Introduction 129

4.2. Method 131

4.3. Steady state crack propagation 134

4.3.1. Stress intensity factor 135

4.3.2. Crack velocity 140

4.3.3. Temperature and temperature gradient 142

4.4. Unsteady state crack propagation 145

4.4.1. Linear elastic problem 147

4.4.2. Elastic-viscoplastic problem 151

4.5. Discussion 156

4.5.1. Factors governing the local tensile stresses 156

4.5.2. Maximum stress velocity 158

4.6. Conclusion 159

Chapter 5 Brittle crack propagation/arrest behaviors under high stress intensity factor and isothermal conditions 163

5.1. Introduction 163

5.2. Preparation of experiments 166

5.2.1. Material 166

5.2.2. Specimen and experimental environment 167

5.2.3. Preliminary model calculation 169

5.2.4. Determination of experimental conditions 171

5.3. Experiments under high SIF conditions 172

5.3.1. Experimental procedure 172

5.3.2. Experimental results 173
5.3.3. Finite element analysis 178
5.4. Model modification 181
5.5. Discussion 183
5.5.1. Crack arrest SIF of Wide2016 183
5.5.2. Required K_{ca} 184
5.6. Conclusion 184
Chapter 6 Shear lip closure stress and its formation 189
6.1. Introduction 189
6.2. Closure stress 190
6.2.1. Calculation of closure effect 190
6.2.2. Finite element analyses to evaluate the closure stress 192
6.2.2.1. Finite element model and analysis conditions 192
6.2.2.2. Analysis results 194
6.2.3. Closure stress approximation 198
6.3. Shear lip thickness 200
6.3.1. Conventional formulation 200
6.3.2. Shear lip formation experiments 202
6.3.2.1. Specimen and experimental procedure 202
6.3.2.2. Experimental results 205
6.3.3. Shear lip thickness measurement 207
6.3.4. Formulation of shear lip thickness 209
6.3.4.1. Calculation of effective SIFs 210
6.3.4.2. Crack velocity coefficient 212
6.4. Discussion 215
6.5. Conclusion 216

Chapter 7 Development of a numerical model to simulate brittle crack propagation and arrest behaviors in steel 221

7.1. Introduction 221

7.2. Model development concept 222

7.3. Element models 224

7.3.1. Local tensile stress 224

7.3.2. Closure effect 227

7.3.3. Shear lip thickness 230

7.4. Model formulation 231

7.4.1. Model integration 231

7.4.2. Simulation procedure 232

7.5. Validation 234

7.5.1. Temperature gradient crack arrest test 234

7.5.2. Impact effect 238

7.5.3. Model simulation 240

7.6. Discussion 242

7.6.1. Local fracture stress criterion 242

7.6.2. $K_{\mathrm{ca}} - T$ relationship 244

7.6.3. Fracture surface simulation 246

7.7. Conclusion 248

Chapter 8 Experimental investigation of grain size effect to cleavage crack propagation resistance in ferrite-pearlite steel 253

8.1. Introduction 253

8.2. Materials 254

8.3. Local fracture stress estimation 257

8.3.1. Estimation procedure 257

8.3.2. Specimen and experimental procedure 258
8.3.3. Experimental results 260
8.3.4. Estimation of the local fracture stress 261
8.4. Discussion 264
8.5. Conclusion 267
Chapter 9 High speed observation of rapidly propagating cracks in 3D structures 271
9.1. Introduction 271
9.2. Experiments 273
9.2.1. Materials and specimens 273
9.2.2. Experimental procedure 276
9.2.3. Experimental result 277
9.3. Discussion 285
9.3.1. Crack front shape effect 285
9.3.2. Fillet welding effect 291
9.3.3. Transferability to steel 292
9.4. Conclusion 293
Chapter 10 Conclusion 297
10.1. Conclusions and implications 297
10.2. Limitations of this study 300
Associated achievements 301

Chapter 1 Introduction

1.1. Background

1.1.1. Social background

Steels have played important roles to support human lives for a long time. Even in modern civilizations, steels have also been applied to various fields including automobiles, buildings, and so on. Especially, large scale structures such as ships and pressure vessels of power plants are usually composed of steels in spite of expansion of usage of other materials such as aluminum and CFRP because of the lower costs and usability of steels. In order to support the large steel structures which become larger and larger, thicker steels with higher strength have been developed. For example, the size of container ships (Fig. 1-1) has rapidly become larger and larger [1,2] as shown in Fig. 1-2 because of rapid expansion of world trade using marine transportation as shown in Fig. 1-3. Therefore, the steels employed have become thicker and stronger to follow the trend of the container ship sizes shown in Fig. 1-4 [3]. Because container ships have a characteristic cross section whose roof is open shown in Fig. 1-5 [4], thicker steels with higher strength and thicker thickness are likely to be used for large size container ships [5]. Because recently, container ships become larger than 20,000TEU at most, extremely thick steel plates are frequently used for such large size container ships. Considering that the container transportation is expected to increase in the future [6], the upsizing of the container ships is also expected to continue from now on.

In general, thicker and stronger steel plates tend to cause brittle fracture due to high yield stress and thicker thickness effect although it is usually paid attention to toughness to develop advanced steels. Considering that brittle fracture initiation is governed by so called weakest link theory, which means that brittle fracture initiation is probabilistic phenomenon, it is needed to prevent the structures from collapsing even when brittle fracture is initiated. Such concept is called as double integrity. The amount of damage due to the collapse of a large size container ship is

recently enormous [7], to prevent the collapse of the whole structure is meaningful. In addition, the recent global warming enables the ships to navigate in the arctic route [8,9], which is severer environment in the context of the lower temperature and existence of iceberg, which can be causes of brittle fracture. Therefore, the integrity against brittle fracture will be required more in the future.

Fig. 1-1 Container ship [10]

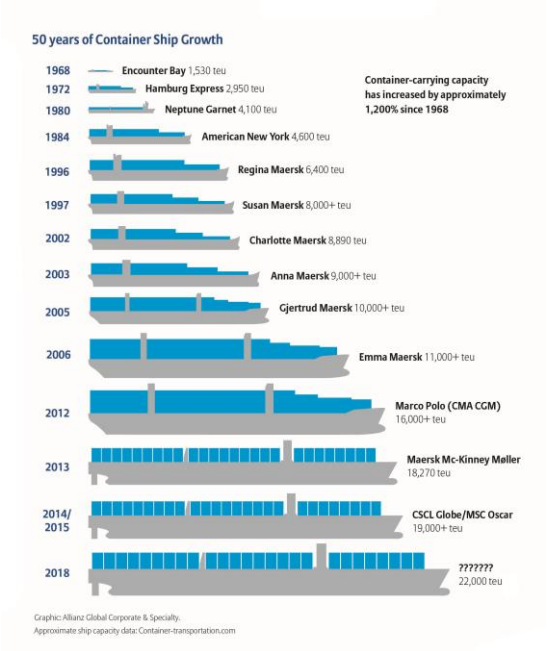

Fig. 1-2 History of container ship size [1]

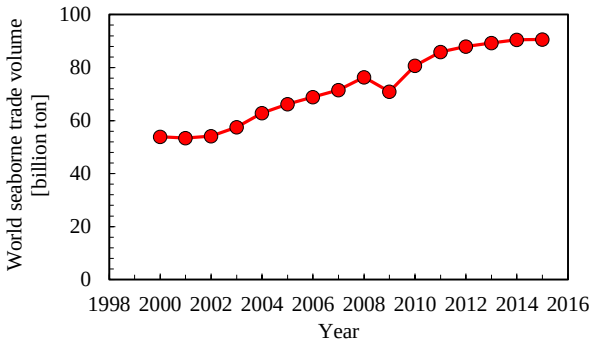

Fig. 1-3 World seaborne trade volume [11]

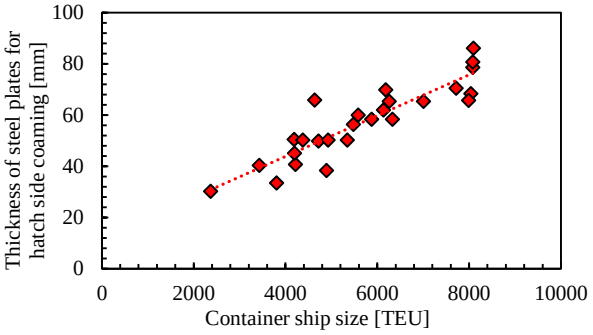

Fig. 1-4 Steel thickness and container ship size [3]

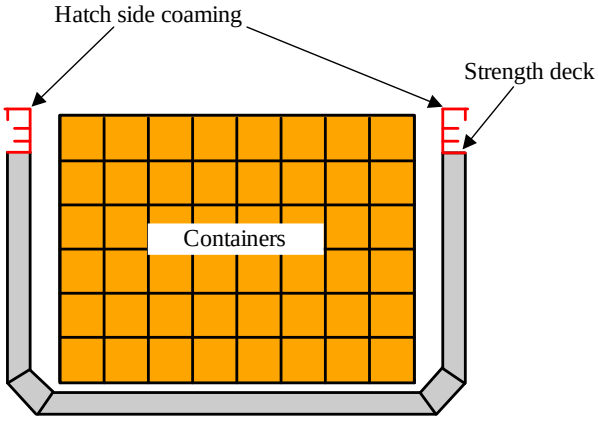

Fig. 1-5 Cross section of container ship

1.1.2. Demands of brittle crack arrest concept

In order to achieve double integrity of the structures, the capability of brittle crack arrest is required. Brittle crack arrest capability has already been introduced to design of large container ships as Guideline on Brittle Crack Arrest Design of Nippon Kaiji Kyokai [12] and an international standard in International Association of Classification Societies (IACS) [13]. Experimental methods to evaluate brittle crack arrest toughness is also proposed and standardized for steels used for container ships [14].

In addition to container ships, this double integrity based on brittle crack arrest concept is also applied in other types of large steel structures. Liquefied Natural Gas (LNG) tanks are one of typical structures to employ double integrity concept. Following a catastrophic accident of LNG tank in United States in 1944 and Liquid Propane Gas tank in Qatar in 1977, double integrity becomes an important property of steels used for storages [15]. Especially, because LNG is kept under cryogenic condition, brittle fracture risk is higher and specialized steel plates including nickel are employed for them [16,17]. Because brittle fracture is also concerned in the case of neutron embrittlement and Pressurized Thermal Shock (PTS) events in nuclear power plants [18], brittle crack arrest has been studied to assure the safety of pressure vessels of nuclear power plants [19–21]. As above discussion noted, demand of double integrity has increased in many fields [5,22,23] and some requirement standards have been already established.

In fact, based on scientific interest and above social demands to consider brittle crack arrest concept, a lot of studies have been carried out to contribute to more efficient brittle crack arrest concept for a long time. The origin of the studies was located on the famous case of a series of accidents of Liberty ships which modern fracture mechanics started from [24]. Afterward, brittle crack propagation and arrest behaviors have been one of the most important issues in structural integrity of naval architects and other structures and a lot of studies focused on it. Especially, these researches were actively carried out for 1950~1990. During the period, although surface energy and applied stress were sometimes employed to evaluate crack behaviors in the early stage of the period [25–27], stress intensity factor (SIF) was mainly applied to describe brittle crack propagation and arrest behaviors in brittle crack arrest experiments of steels [28–31]. During this period, a lot of studies were carried out to characterize brittle crack propagation and arrest behaviors from the perspective of fracture mechanics. Although they were noted in the past review articles such as Ref. [23,32], it is worth noting that those studies showed that there is a unique relationship between temperature and brittle crack arrestability as shown in Fig. 1-6 [33]. For

example, brittle crack arrest toughness K_{ca}, which is measured by temperature gradient crack arrest test, is a function of reciprocal number of temperature [14]. This relationship between K_{ca} and reciprocal number of temperature is called as Arrhenius plot because the relationship is approximated by exponential function. The results obtained from these studies are utilized even now.

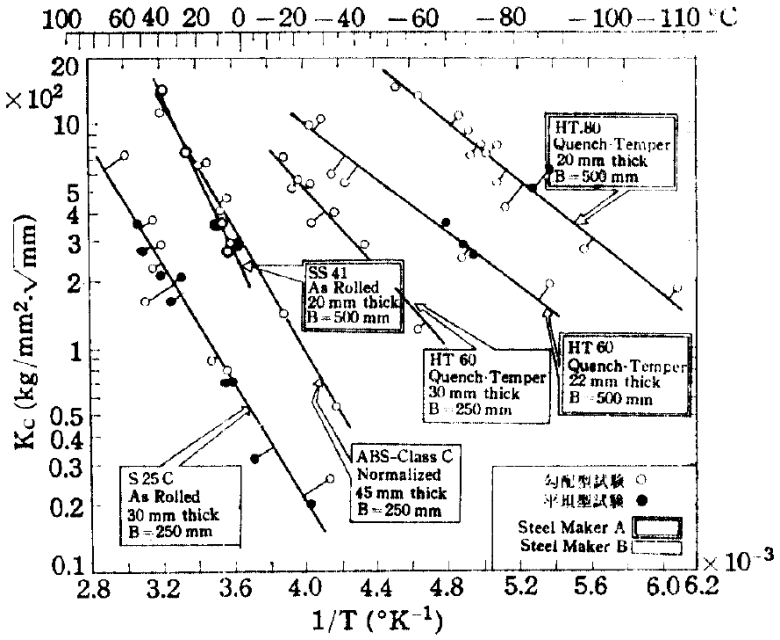

Fig. 1-6 Brittle crack arrest toughness against temperature [33]

Because of the developments of measurement and computational tools, dynamic effects was able to be considered to analyze brittle crack propagation and arrest behaviors during the period [20,34]. These dynamic approaches mentioned that a unique relationship between crack velocity and dynamic stress intensity was observed in brittle crack propagation and arrest behaviors in steels [34–36]. This relationship shown in Fig. 1-7 was originally found in the crack propagation experiments using brittle elastic media like PMMA [34]. Numerical methods such as finite element methods and finite difference methods were essential to analyze these dynamic crack behaviors. [20].

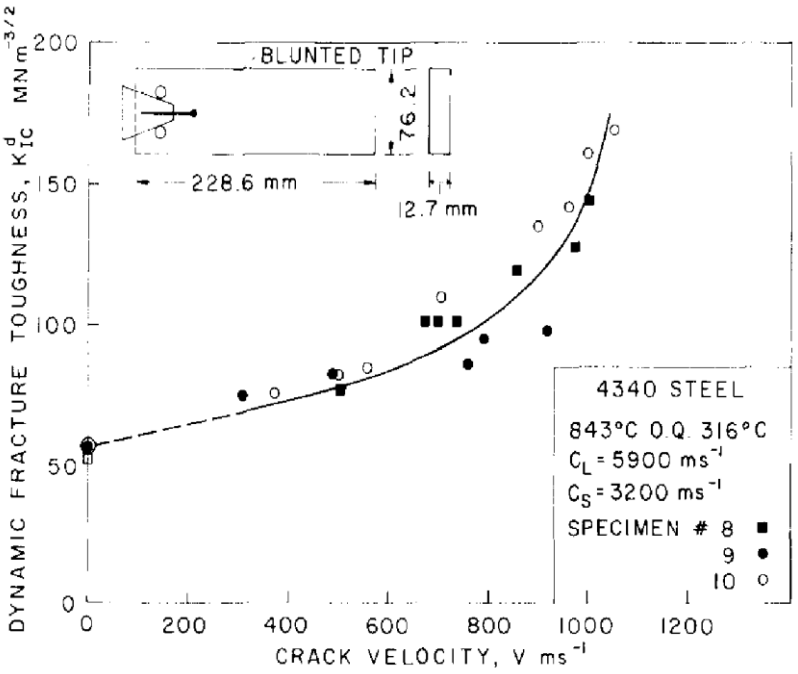

Fig. 1-7 Dynamic stress intensity factor against crack velocity [36]

A series of studies introduced above could not explain brittle crack propagation and arrest behaviors in steels, especially so called Long Brittle Crack Problem. This problem mentioned that the SIF at crack arrest in larger specimen was much higher than K_{ca} evaluated in normal specimen [37]. This finding has been interpreted as saturation of SIF along crack propagation [38], but the cause of it has not been clarified. A series of studies indicated that SIF was useful to describe brittle crack propagation and arrest behaviors, but it was not a concept to explain it.

Although, on the other hand, after the late of 1990s, the number of papers on brittle crack arrest were relatively small, efforts for structural integrity based on crack arrest concept have been carried out. For a recent example, Nippon Kaiji Kyokai presented the required brittle crack arrestability of steels employed for large container ships based on the systematic research of brittle crack arrest [12]. To achieve such requirement, steel makers have made a lot of efforts to develop steel plates with higher crack arrestability. From a series of studies on evaluation of brittle crack arrestability, addition of nickel highly improves not only toughness against brittle crack initiation, but also brittle crack arrestability of steels [37,39].

However, they depended heavily on empirical knowledge and lacked theoretical backgrounds. Because theoretical mechanism of brittle crack propagation and arrest behaviors are not clear

despite of the long history of studies. In particular, in spite of above efforts based on fracture mechanics parameters, it has been pointed out that these approaches based on the fracture mechanics parameters such as K cannot explain brittle crack propagation and arrest behaviors in steel although they are convenient parameters to discuss the brittle crack propagation and arrest behaviors [40,41]. Because above relationship of K_{d} and V shown in Fig. 1-7 is pointed out to depend on loading type and specimen geometries, it is not the universal fracture criterion of brittle crack propagation and arrest behaviors [42]. Therefore, it is needed to establish the theory to universally explain brittle crack propagation and arrest behaviors to achieve rational design of materials and structures in the context of double integrity.

1.1.3. Fundamental concept of brittle crack arrest

Based on linear elastic fracture mechanics [43], the fundamental concept of brittle crack propagation and arrest behavior is expressed as

$$\begin{gathered} K \geq K_{\mathrm{res}}\text{: crack propagation} \\ K < K_{\mathrm{res}}\text{: arrest} \end{gathered} \tag{1-1}$$

where K is static stress intensity factor and K_{res} is static resistance against crack propagation, i.e., brittle crack arrest toughness. Although steel is an elastic-viscoplastic solid, it has been considered that linear elastic fracture mechanics can be applied because a strain rate near the crack tip is much high and the plastic zone is small enough in brittle crack propagation. This concept based on stress intensity factor corresponds to concept based on energy release rate.

On the other hand, dynamic stress intensity factor to represent crack driving force during crack propagates is also defined. In linear elastic fracture mechanics, dynamic stress intensity factor $K_{\mathrm{d}}(V)$ is expressed by multiplication of static stress intensity factor and dynamic coefficient as

$$K_{\mathrm{d}}(V) = B(V)K \tag{1-2}$$

where V is crack velocity and $B(V)$ is the coefficient proposed by Broberg [44]. $B(V)$ is a monotonically decreasing function against crack velocity as shown in Fig. 1-8. $B(V)$ is zero when crack velocity is the Rayleigh wave velocity.

As noted Section 1.1.3, dynamic stress intensity factor is a monotonically increasing function against crack velocity as shown in Fig. 1-7 [36]. Although this concept to represent dynamic toughness by using crack velocity was supported by subsequent experiments [45], it was pointed out that the relationship depended on specimen configuration shown in Fig. 1-9 [46], temperature Fig. 1-10 [34,47,48], and so on. Accordingly, dynamic fracture toughness against crack velocity cannot uniformly explain brittle crack propagation and arrest behaviors in steels and it is needed to employ other fracture criterion of brittle crack propagation and arrest behaviors in steel.

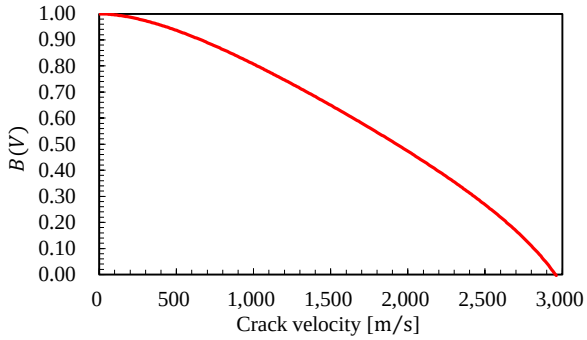

Fig. 1-8 $B(V)$ against crack velocity (material constants are same as those of steels)

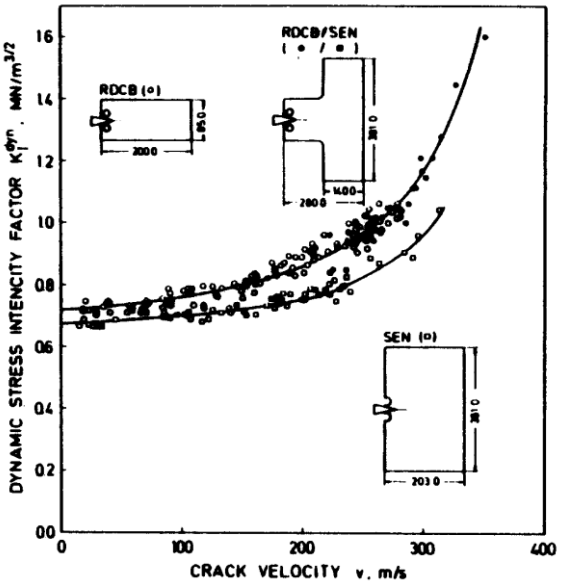

Fig. 1-9 Dependency of $K_{\mathrm{d}} - V$ relationship on specimen geometry [46]

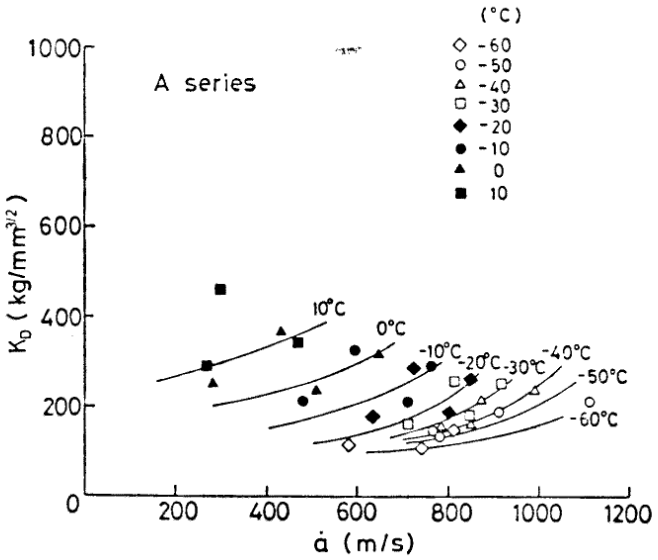

Fig. 1-10 Dependency of $K_{\mathrm{d}} - V$ relationship on experimental temperature [47]

1.1.4. Local fracture stress criterion

SIF, J, and other parameters express the energy available for the crack propagation from macroscopic view. These energy approach have been employed as an indicator of critical conditions of fracture mechanics. These approach focuses global fracture mechanics parameters and thus is called as global approach. On the other hand, the local stress, strain, or damage in the vicinity of the crack tip are also used to judge whether fracture occurs or not [49]. This approach is called as local approach and employed to explain fracture phenomena. In particular, brittle fracture initiation in steels has been regarded to be governed by the local stress near the crack tip based on local approach [50]. This local approach is desirable in the context of the transferability from laboratory scale test to the actual engineering structures although the global approach parameters frequently depend on the specimen conditions.

Considering that SIF could not express the critical condition of brittle crack propagation in steels as noted in previous sections, local approach was introduced to brittle crack propagation based on an analogy of brittle crack propagation to brittle fracture initiation for the first time by Machida et al. [40,51] and Aihara et al [52,53]. This approach, which was called as the local fracture stress criterion, indicated that the satisfaction of energy balance was just a necessary condition and the crack behaviors depended on the crack length. Their simulations based on the local fracture stress

criterion showed Arrhenius plot of brittle crack arrest toughness.

According to the local fracture stress criterion, the fracture criterion is expressed as

$$\sigma_{\mathrm{F}} = \sigma_{yy}(r_{\mathrm{c}}) \text{: continue to propagate}$$
$$\sigma_{\mathrm{F}} > \sigma_{yy}(r_{\mathrm{c}}) \text{: arrest} \tag{1-3}$$

where σ_{F} is the local fracture stress and $\sigma_{yy}(r_{\mathrm{c}})$ is the maximum principal stress at the characteristic distance r_{c} from the crack tip. The local fracture stress was assumed to be the material constant. After above work, the local fracture stress criterion has been employed by some researches, and especially, the numerical simulation (Fig. 1-11) based on the local fracture stress criterion by Shibanuma et al. showed that the Long Brittle Crack Problem can be explained by the growth of unbroken shear lip [54,55]. Namely, the long crack can be arrested because SIF decreases due to the closure effect of unbroken shear lips.

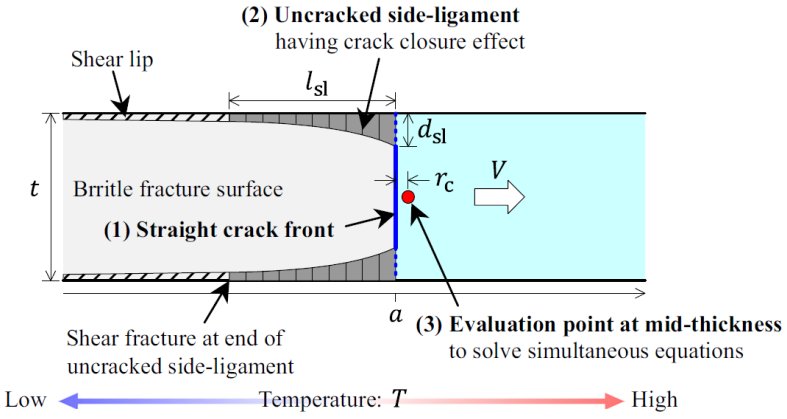

Fig. 1-11 Concept of the simulation model [54]

Although above simulation model indicated that the local fracture stress criterion is the promising concept to explain brittle crack propagation and arrest behaviors by considering 3D effect appropriately, this simulation model has placed a lot of assumptions which were not based on any analyses of actual phenomena and thus it is difficult to say that they were based on the physically meaning basis the each phenomenon in the model was appropriately considered. In particular, the above model incorporated the local fracture stress criterion and unbroken shear lip growth (3D

effect) to explain brittle crack propagation and arrest behaviors. However, these modellings were not supported by experiments or numerical analyses and thus it is regarded the above simulation did not appropriately reproduce actual phenomena although the model is useful to determine what factors should be focused to study brittle crack propagation and arrest behaviors. Especially, the local fracture stress identified in the model simulation was thousands MPa, which was much higher than values expected from the local fracture stress of cleavage crack initiation in steel.

Accordingly, it is needed to investigate brittle crack propagation and arrest behaviors in detail from the perspective of the local fracture stress criterion. In particular, referring to the above conventional simulation model, the local fracture stress and unbroken shear lip are key factors which should be examined in this study. Thus, this study carried out comprehensive investigations of them. However, as the beginning of this study, recent studies related to brittle crack propagation and arrest behaviors will be reviewed thoroughly to clarify the latest findings of brittle crack propagation and arrest behaviors in steels because there are no review articles citing recent achievements on brittle crack arrest. Although some old studies were cited, the next section mainly focused on the studies published in this 20 years.

1.2. Review of recent related researches

1.2.1. Conventional approach: Stress intensity factor

Although the local approach is hopeful as a critical criterion of brittle crack propagation and arrest behaviors in steel as noted in Section 1.1, stress intensity factor is still employed to characterize brittle crack propagation and arrest behaviors due to its convenience to use. In particular, SIF has been employed to express the material resistance against brittle crack propagation in steels. Recent requirements on brittle crack arrest and standardized methods to evaluate brittle crack arrestability were based on stress intensity factor [13,14,56]. As a parameter to represent brittle crack arrestability, K_{Ia} and K_{ca} are proposed and widely used in engineering applications.

K_{ca} measured by standard width specimen under temperature gradient condition depends on a reciprocal number of absolute temperature [14]. This relationship between the temperature and K_{ca} is known to be approximated by exponential function [30]. This relationship has been widely known and employed as an indicator to express brittle crack arrestability of steels [26,32,57,58]. Nowadays, a series of researches to standardize the evaluation procedure of K_{ca} was carried out [59]. Those studies included investigation of the influences of specimen size, applied stress, the

distance between pins, tab plate configurations, and temperature gradient on measured K_{ca} [60], limitation of impact energy for brittle fracture initiation [61–63]. The procedure was standardized as WES2815 [14]. One example following the standardized procedure is shown in Fig. 1-12. Instead of impact to initiate brittle fracture, double tension system has been sometimes employed [64,65]. Although the double tension system, whose specimen is shown in Fig. 1-13, has an advantage to exclude impact effect to the crack behaviors, it is not widely used because it is likely to cause invalid experiments due to crack deviation or non-occurrence of brittle fracture.

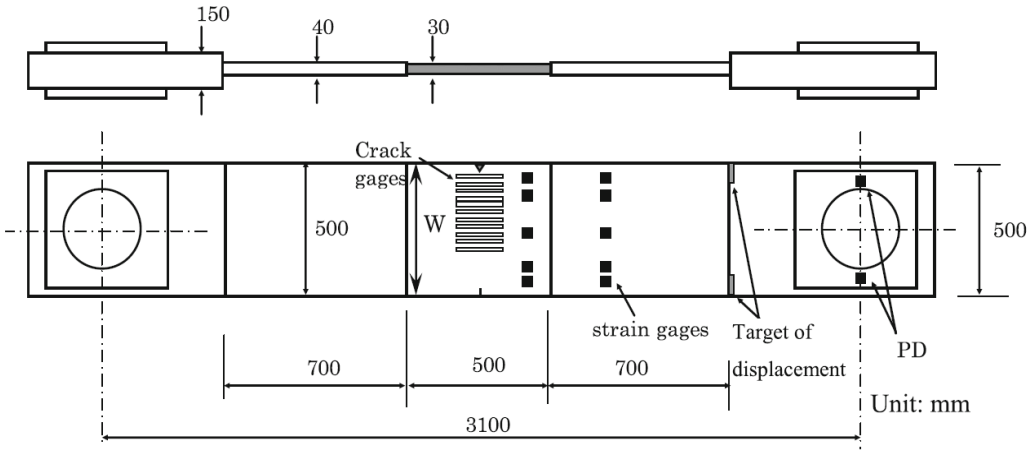

Fig. 1-12 Specimen configuration following WES2815 [66]

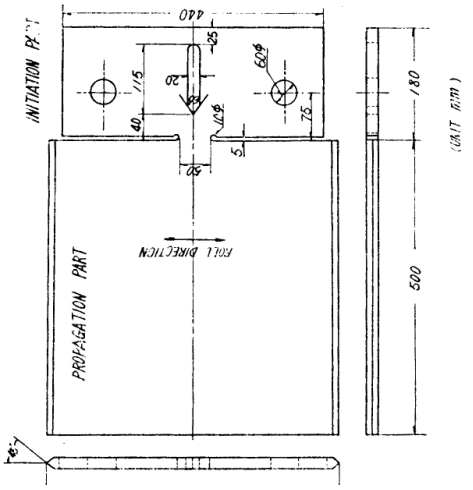

Fig. 1-13 Double tension test specimen [65]

The required brittle crack arrest toughness for large size container ships was also investigated experimentally [67,68]. The required toughness was determined by large size model experiments simulating actual structures of hatch side coamings and upper deck including welding joint [67] as shown in Fig. 1-14. The design stress is applied to the specimen simulating the actual structure and the brittle crack runs along the welded bead to enter the joint in the above model experiment. The required brittle crack arrest toughness is determined so as not to allow the crack to run through the joint. K_{ca} is also being worked to be associated with the concept of Crack Arrest Temperature (CAT) [69]. CAT which was first proposed by Wiesner et al. [70] expresses the temperature that the brittle crack with a certain SIF is arrested. Because K_{ca} is determined against temperature, CAT can be associated with K_{ca} to control the SIF to judge whether the crack is arrested or not. The test method of CAT is also studied [71]. In the CAT test, it is needed for the crack to enter the test plate when it has a certain value of SIF although the specimen is basically kept isothermal. Thus, embrittled zone is made by using embrittle welding or local temperature gradient as shown in Fig. 1-15 [71,72]. To use the local temperature gradient is recently developed by An et al. for application to shipbuilding steels [73].

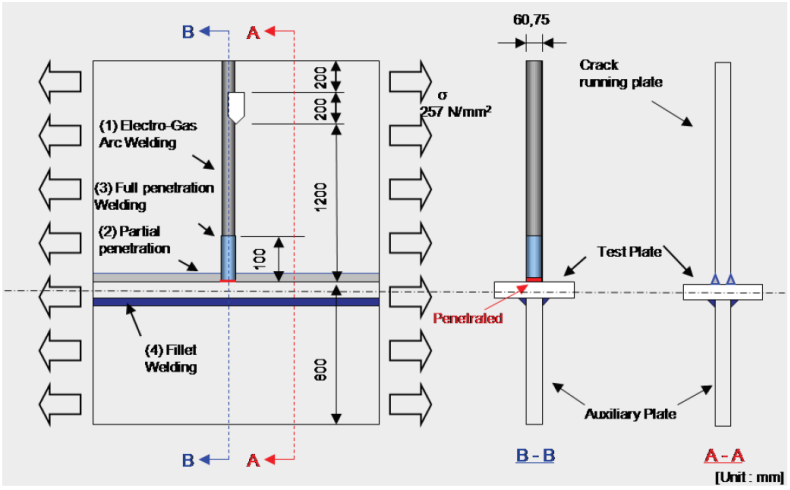

Fig. 1-14 Crack arrest test specimen simulating actual ship structure [74]

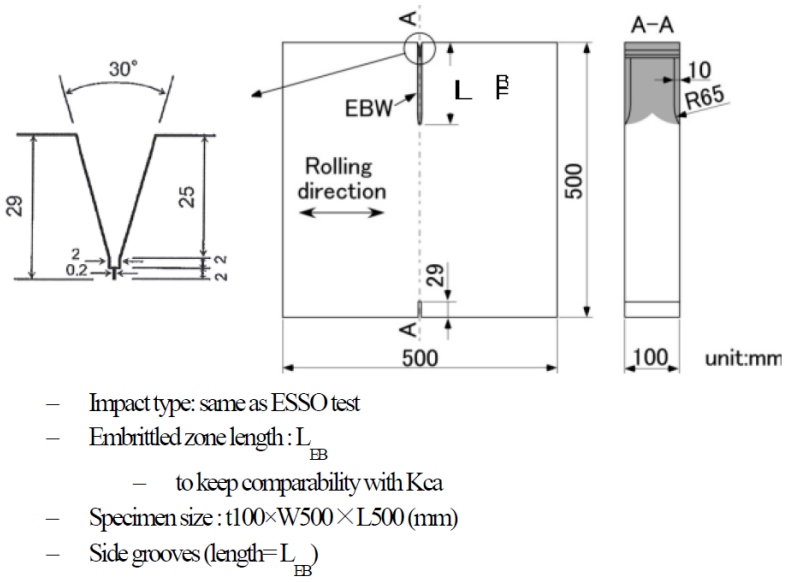

Fig. 1-15 Crack arrest temperature specimen (embrittle welding) [72]

On the other hand, K_{IA} is measured assuming plain strain (infinite thickness) condition because K_{Ia} assumes brittle crack propagates in thickness direction. Compact crack arrest test (CCA) is usually used to measure K_{Ia} [75]. Side groove is processed on CCA specimen shown in Fig. 1-16 to make it plain strain condition. K_{Ia} is also expressed as a function of temperature. In some cases, K_{Ia} is represented by a function of $T_{\mathrm{arrest}} - T_{\mathrm{ref}}$ [76]. T_{ref} is reference temperature, which corresponding to temperature that satisfy a certain material property. For example, reference temperature of nil-ductility transition (RT_{NDT}) is used as the reference temperature [20,77]. K_{Ia} is also evaluated based on so called Master curve method [78]. When Master curve method is employed, T_{ref} can be set to the temperature that mean value of K_{Ia} is $100\mathrm{MPa}\sqrt{\mathrm{m}}$ according to ASTM E1221 [56,79]. One example to describe master curve approach of brittle crack arrest is shown in Fig. 1-17 [79]. Even though the data shown in Fig. 1-17 includes various types of steels and some outliers can be found, the master curve can uniformly describe temperature dependency of brittle crack arrest toughness data of all steels using $T_{K1\mathrm{a}} = 100\ \mathrm{MPa}\sqrt{\mathrm{m}}$. This reference temperature concept has been employed to characterize brittle crack arrest capability [76,80].

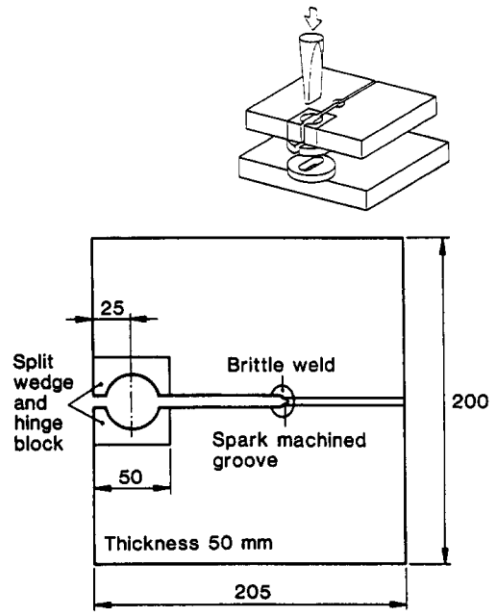

Fig. 1-16 Compact crack arrest test specimen [81]

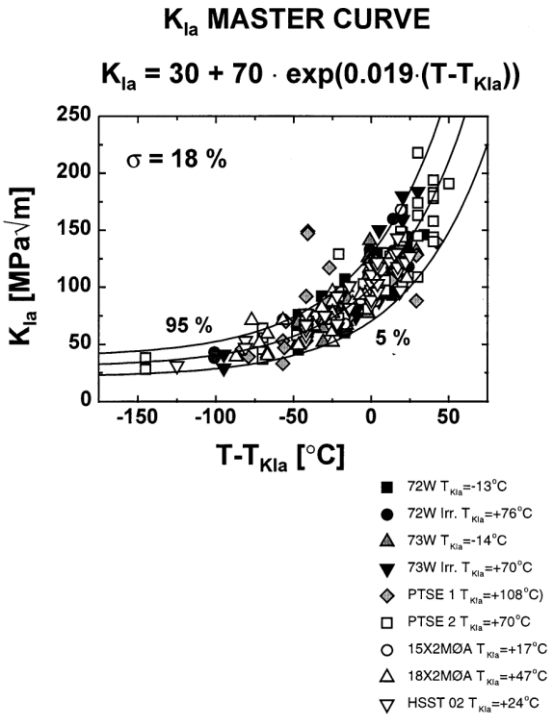

Fig. 1-17 Master curve description of brittle crack arrest toughness [79]

Above indicators are used for research of brittle crack arrest phenomena because of its convenience to express crack driving force and crack arrest performance. Bouyne et al. used CCA tests and thermal shock ring tests to evaluate K_{Ia} of 2.5% Cr-1% Mo steel [82]. An et al. investigated input heat effect to brittle crack arrest toughness of welded section by using temperature gradient crack arrest experiments [57,58].

1.2.2. Alternative method to evaluate brittle crack arrestability

Because brittle crack arrest tests such as so temperature gradient crack arrest test need a lot of time and cost, alternative methods to evaluate brittle crack arrestability were also tried to propose. Some of them tried to evaluate brittle crack arrestability directly in small scale tests and investigated transferability of small tests to actual scale crack arrestability [83,84]. One of difficulties of the small scale tests is connectivity of the evaluated brittle crack arrest toughness with full scale crack arrest test such as temperature gradient crack arrest test. For example, three point bending test has been a hopeful alternative of temperature gradient test [85], it was pointed out that $K_{\mathrm{ca-3PB}}$, which is brittle crack arrest toughness evaluated in the bending test, did not consist with K_{ca} measured by temperature gradient crack arrest test as shown in Fig. 1-18 [83]. CCA test is one of the hopeful method to evaluate K_{ca} in laboratory scale, but the inconsistency was already reported [86]. These inconsistency corresponds to loss of uniqueness of the $K_{\mathrm{d}} - V$ relationship explained in Section 1.1.3. In other words, because SIF cannot express critical criterion of brittle crack propagation and arrest behaviors in steel, the evaluated arrest toughness expressed by SIF depends on the specimen configurations. Nonetheless, because macroscopic approach is convenient, it is used to express apparent crack arrest toughness.

Although above alternative methods are based on fracture mechanics, other ways to propose the alternative method which is not based on fracture mechanics, have been investigated. Conversion formula from results obtained from industrial tests such as Charpy impact tests, NRL test and Drop Weight Tear Test (DWTT) to brittle crack arrestability were attractive due to the easiness and lower cost of the test [87–91]. As the recent study, it was reported that chevron notched Charpy test expresses brittle crack arrest toughness better than other Charpy test because the energy for brittle fracture initiation is relatively small in chevron notched Charpy test as shown in Fig. 1-19 [92]. Okawa et al. analyzed NRL (Naval Research Laboratory) drop weight experiments to relate the test results to brittle crack arrest capability because the NRL test results

were empirically known to be correlated to brittle crack arrest toughness [93]. Although these tests are easy to conduct, because these tests cannot evaluate brittle crack propagation and arrest behaviors directly, these tests provide only correlation between the obtained values and brittle crack arrest toughness. Therefore, the applicability of the correlation cannot be guaranteed.

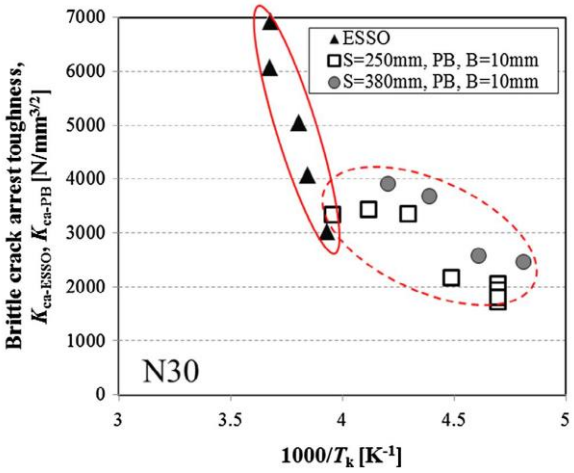

Fig. 1-18 Brittle crack arrest toughness evaluated by temperature gradient crack arrest test and three point bending test [83]

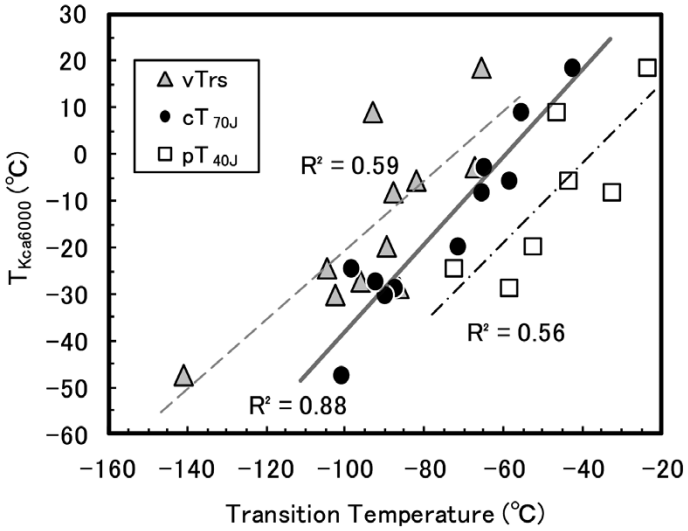

Fig. 1-19 Correlation between brittle crack arrest toughness and some types of Charpy impact test result [92]

1.2.3. Numerical methods and modelling

Along with rapid developments of computers, numerical methods have become important tools to study fracture mechanics. Because brittle crack runs too fast to observe precisely, numerical methods are essential to study it in particular. Numerical analyses of crack propagation can be broadly classified to two types: generation phase analysis and application phase analysis [94]. In the former type, crack path and crack velocity are input information and in the latter type, fracture critical criterion is input information to predict crack velocity, crack path, and crack arrest event. Therefore, the generation phase analysis is used to analyze experimentally obtained crack behaviors and the application phase analysis is used to predict crack path and where the crack is arrested.

Although for computational continuous mechanics, finite element method is the most common and widely used method, other methods have been proposed to solve fracture mechanics problems because finite element method is essentially not good at dealing with discontinuity due to the existence of cracks. Peridynamics is a recent example proposed for fracture mechanical analyses based on formulation similar to molecular dynamics [95]. This method expresses the continuous mechanics by the interaction between particles. Imachi et al. applied peridynamics to dynamic crack propagation problems to evaluate dynamic stress intensity factor of a propagating crack in brittle media [96]. Discrete element method employs similar expression of solid and it is also applied to dynamic fracture mechanics problem [97]..

Although the above methods were proposed because finite element method (FEM) is not necessarily good at dealing with discontinuity due to crack, FEM is widely used in fracture mechanics and modified to fracture mechanics analyses. The most basic way to express crack propagation in FEM is nodal force release technique [98] and frequently applied to brittle crack arrest in steels [20,99]. This nodal force release technique needs a priori crack path. In many cases, the crack path consists with symmetry line of the finite element model although double node technique is sometimes employed. In generation phase analysis, nodal force release technique is convenience because it can easily model the crack behaviors. On the other hand, because the nodal force release technique is not suitable for crack path prediction, other method is needed to express crack in finite element models in application phase analysis.

Remeshing technique shown in Fig. 1-20 is one of practical and famous methods to express crack path in finite element analyses especially when the crack path is unknown. Although remeshing

technique has been mainly applied to fatigue crack propagation, which is static phenomena, this technique has been applied to rapid crack propagation in PMMA [100,101]. Nishioka et al. has developed moving finite element method, which is a technique similar to remeshing [94,101,102]. In this method, the fine mesh zone moves so as to locate the crack tip at the center of the fine mesh zone by using delaunay automatic mesh division as shown in Fig. 1-21.

On the other hand, because how to remesh the finite element model is a troublesome problem, other methods without remeshing have been proposed. Extended finite element method (XFEM) is a representative method to analyze crack propagation in finite element analysis without remeshing [103,104]. This method expresses the crack existence and crack tip singularity in elastic solid by the additional degree of freedom called as enrichment as shown in Fig. 1-22. XFEM was originally proposed for static crack problems, but it has been applied to rapid crack propagation in elastic solids [105,106], and recently employed to analyze brittle crack propagation and arrest behaviors in steel [107–109]. These researchers employed XFEM for generation phase analysis to evaluate local stresses near the crack tip as well as they carried out application phase analysis based on the local fracture stress criterion [107–109]. Fig. 1-23 shows the predicted crack path by 2D XFEM using the local fracture stress criterion with the experimental crack path [107].

However, because the singularity near the crack tip has to be known to provide crack tip enrichment in XFEM, the crack tip enrichment cannot be added in the problem in elasto-plastic solids. Thus, the study to use only the Heaviside enrichment to express the existence of the crack has been also carried out to apply XFEM to elasto-plastic problems [110] although other study introduced crack tip enrichment of singularity to the nodes just near the crack tip [111,112] or singularity obtained from Ramberg-Osgood exponent to approximate plastic constitutive law was employed in elasto-plastic solids [113,114]. The XFEM used for the brittle crack arrest problem also employed the elastic singularity enrichment [107].

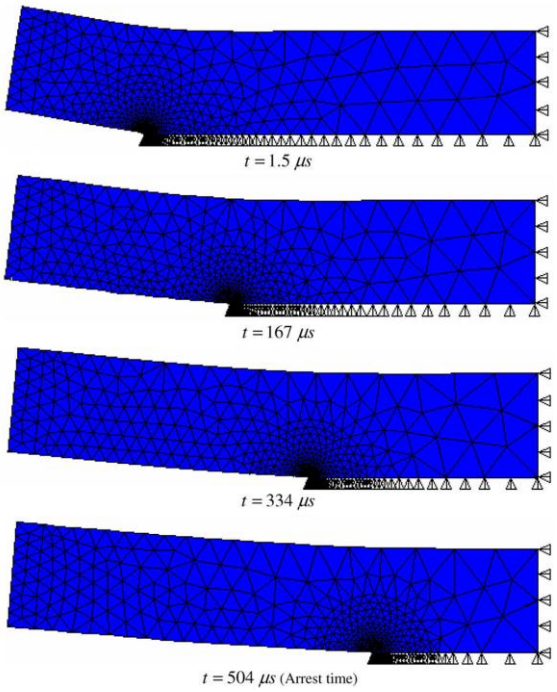

Fig. 1-20 Remeshing procedure near the crack tip [100]

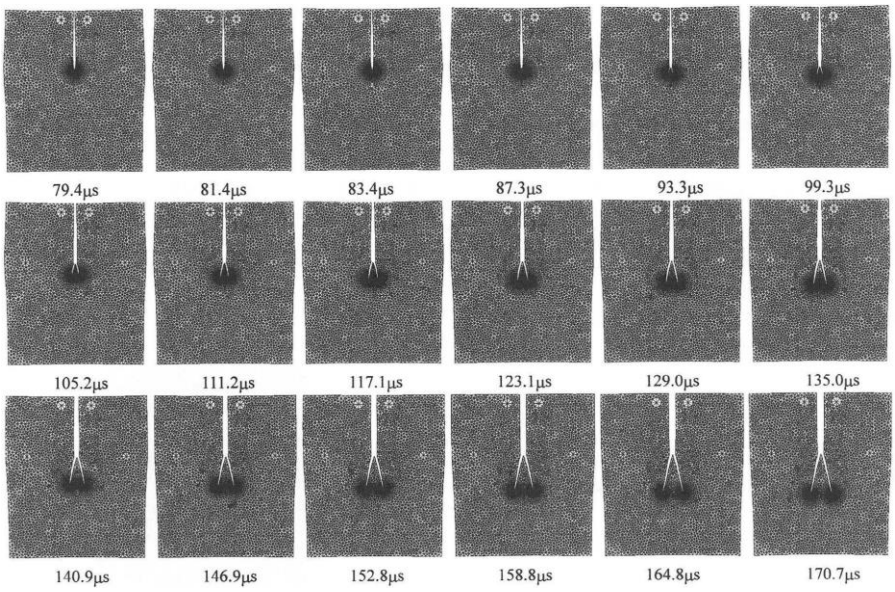

Fig. 1-21 Moving finite element mesh near the crack tip [102]

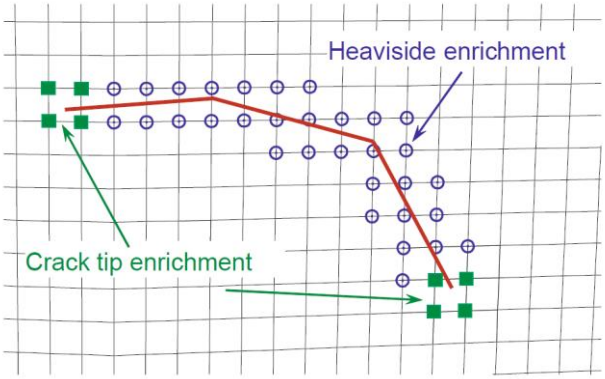

Fig. 1-22 Enrichment in XFEM [115]

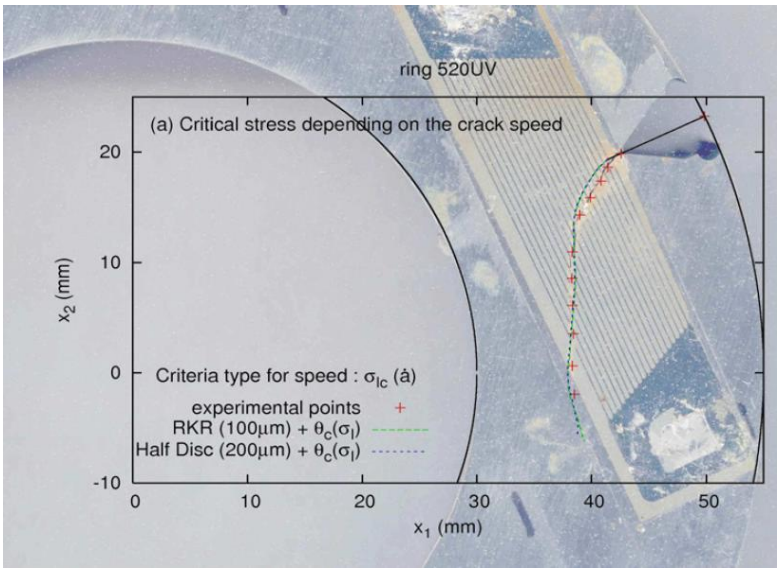

Fig. 1-23 Crack path prediction by Prabel et al. [107]

The other method to avoid remeshing to analyze cracks in finite element analyses is mesh superposion method [116,117], which is sometimes called as s-version FEM. The advantage of this method is to model the crack and the whole body separately as shown in Fig. 1-24. Namely, complicated geometry can be reproduced easily in superposition method. This advantage is also useful to consider crack growth because the zone near the crack tip can be always fine by moving the fine local mesh along the crack growth [118,119]. Therefore, this method is expected to be suitable for the local stress evaluation of the rapid crack propagation by moving the fine local

mesh along crack growth although it still focused on 2D elastic problem [120].

As one of the application phase analysis methods, fracture critical condition is modelled by dissipation energy in cohesive method, which is a recently developed numerical methods in fracture mechanics [121,122]. Although cohesive method is frequently employed to incorporate cohesive tractions due to Dugdale effect or crack tip damages in finite element analysis [123,124], it has been also employed in some studies of brittle crack propagation arrest behaviors in steel to model energy dissipation [100,125–127]. Although the mesh size is not fine, Pandolfi et al. carried out first 3D cohesive analyses considering both brittle fracture and formation of shear lip as shown in Fig. 1-25. Valorosso et al. introduced rate dependency of cohesive energy to consider dynamic effects to reproduce brittle crack propagation and arrest behavior in steel observed in CT specimen [126]. Additionally, Kawabata et al. considered both of the local fracture stress and dissipated energy for surface creation in their numerical model by using cohesive FEM [128,129].

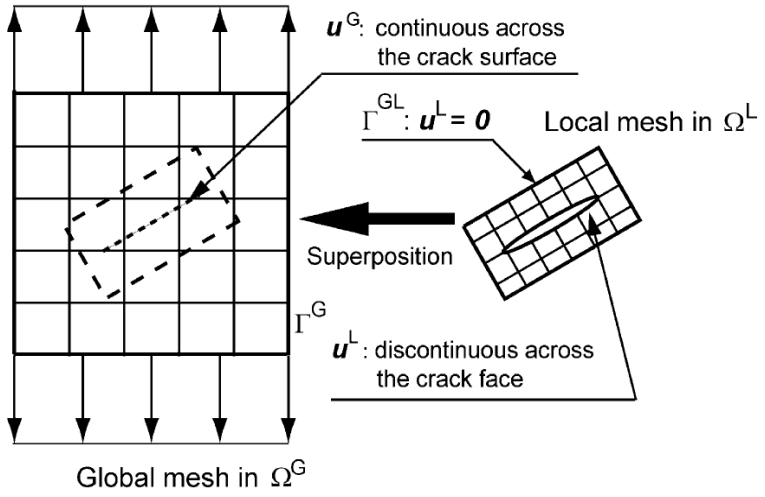

Fig. 1-24 Mesh superposition method for crack analysis [116]

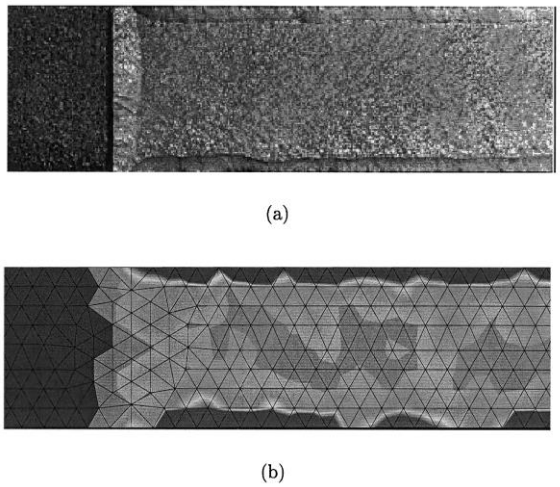

Fig. 1-25 Experimental fracture surface (a) and cohesive method results (b) [125]

Besides above numerical methods to analyze rapid crack propagation problems, modelling cleavage crack propagation has been developed. The local fracture stress criterion model proposed by Shibanuma et al. is the representative example [54]. Yoshinari et al. proposed macroscopic simulation using linear elastic fracture mechanics to examine residual stress and toughness distribution effect to brittle crack propagation path [130]. This simulation was applied to investigate how the welding condition influenced the crack path and showed the smaller but shift caused the transit of the brittle crack between the shifted weld line as shown in Fig. 1-26 [131]. This simulation implied that the residual stress is needed to control the crack path in welded part. This simulation model was extended to 3D to analyze the influence of 3D distribution of residual stress and 3D welding groove [132]. These simulations showed the deviation of brittle crack running in welded bead to base metal was caused by toughness distribution of welded metal and base metal in addition to the residual stress.

Although a lot of numerical methods have been developed for fracture mechanics studies, the local stress evaluation near the propagating crack tip has been almost ignored. This is because the conventional studies mainly considered the fracture mechanics parameters. Thus, it is expected to investigate fundamental features of the local stress evaluation in finite element method.

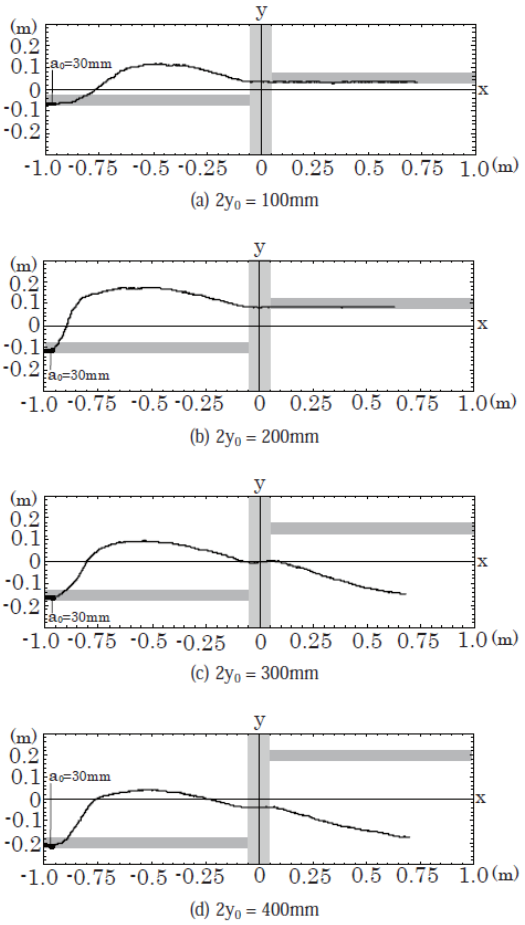

Fig. 1-26 Crack path variation due to the length of butt shift [131]

1.2.4. Experimental techniques

Although numerical methods have been rapidly developed, experimental studies are essential to elucidate actual crack behaviors. In particular, high speed measurement tools are recently available to observe rapid crack propagation. These tools are mainly used to evaluate crack velocity. Strain gauges and crack gauges connected to high speed oscilloscopes are still important tools. Time resolution of recent oscilloscopes used for dynamic fracture mechanics studies is about 10 MHz [61,133]. This time resolution is generally better than high speed camera, whose frame rate is usually smaller than 1M per second [108]. In addition, in steels, because the crack front shape is usually tunneling, the high speed camera cannot measure the actual crack propagation because it can only observe the specimen surface. Thus, the strain gauge, which measure strain transition, is more appropriate to measure the brittle crack propagation behaviors

because of the time resolution and accuracy. However, the strain gauges are not useful to determine crack path history and high speed camera can be powerful tool to observe the crack path history when the crack path is expected to deviate from straight as shown in Fig. 1-27 [42,109]. In addition, Nakanishi et al. employed high speed camera to observe brittle crack propagation in coarse ferrite grains steel specimens and indicated that crack delay when it entered grain boundaries [134]. The comparison between strain gauge data and high speed camera images indicated the delay of the crack at the grain boundary to work as a resistance against cleavage crack propagation.

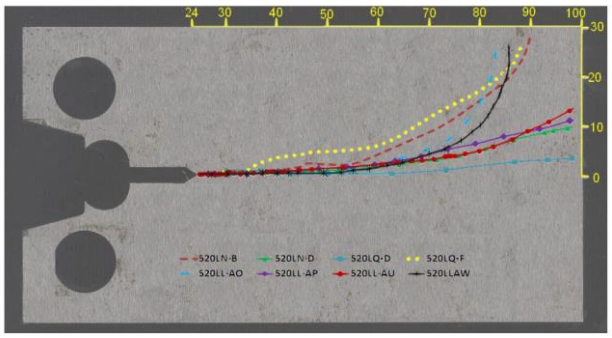

Fig. 1-27 Experimentally obtained brittle crack propagation path [42]

The gauges record voltage history used to determine when the crack propagates just side of the gauges. Although because of technical problems caused by noises during recording, it is practically difficult to obtain detailed information other than crack velocity from the gauges' data, it was attempted that strain gauges were employed to evaluate accurate strain history or stress intensity factor during crack propagation [61,135].

It is worth noting that because of complexity of steel fracture phenomena, relatively simple material, which is basically elastic, brittle, and transparent, has been employed to study fast crack propagation and arrest behaviors [136,137]. Although of course, the results obtained from them cannot be directly applied to fracture phenomena of steels, they have provided findings useful for study of brittle crack propagation and arrest behaviors in steel and contributed to development of dynamic fracture mechanics. For the experiments using transparent model materials, high speed camera is a powerful tool to understand fast crack propagation and arrest behaviors. An advantage of high speed camera is to observe change of a crack path including branch and bent as noted

above [94,138]. The gauges are not suitable to clarify crack paths because they can only record voltage histories. In addition, stress intensity factors during rapid crack propagation can be evaluated experimentally by using high speed camera combined with mirrors and lenses. Shadow pattern method and Schlieren technique are famous examples of such techniques [139,140].

Because of difficulties to observe brittle crack propagation and arrest behaviors during its propagation, fractography is an important method to understand the phenomena. Nakano et al. carried out X-ray fractography of brittle fracture surfaces obtained by some types of brittle crack arrest experiments [45,141]. Their study showed that dynamic stress intensity factor at the crack arrest event is almost equal to crack arrest toughness obtained by static calculation. Takashima et al. counted the number of micro cracks which formed near the main cleavage fracture surface as shown in Fig. 1-28 [142] and pointes that the number of micro cracks was smaller in higher temperature. Such micro cracks have been reported to be arrested at twist-type grain boundary or in the upper bainite carbide colony in baintic microstructures [143]. The retained austenite near brittle fracture surface in 9% Ni steel was evaluated as shown in Fig. 1-29 by Nakanishi et al. to evaluate influence of transformation of retained austenite due to brittle crack propagation [144]. The study investigated the amount of retained austenite near the fracture surface by using X-ray diffraction and pointed that martensite transformation had positive effect for brittle crack arrest toughness.

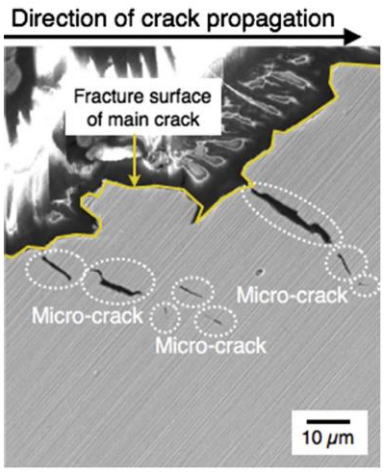

Fig. 1-28 Micro cracks beneath the cleavage fracture surface [142]

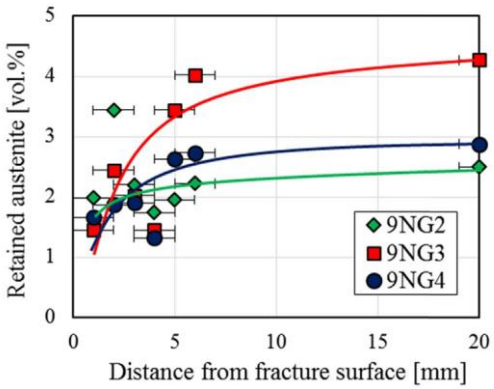

Fig. 1-29 Retained austenite evaluated evaluated by X-ray diffraction [144]

1.2.5. Critical condition of brittle crack propagation and arrest behaviors

The critical condition of brittle crack propagation and arrest behavior still remains controversial issue. As noted in Section 1.1.2, Section 1.1.3 and 1.1.4, energy approach, which corresponds to stress intensity factor concept, has been employed to represent critical conditions of brittle crack propagation and arrest behaviors. Priest calculated energy balance during brittle crack propagation including shear lip formation [145]. He also indicated that linear elastic fracture mechanics could not predict crack arrest temperature and it was needed to consider plastic work due to unbroken shear lips. Cohesive method in finite element analysis is also one of energy approach and applied to brittle crack propagation and arrest behaviors by Pandolfi [125] and Valorosso [126]. Cohesive finite element analysis was combined with the local fracture stress criterion by Kawabata and his coworkers [93,128,129]. This cohesive simulation has been also applied to cleavage crack propagation in micro scale, which is the early stage of cleavage fracture initiation [146–148].

As noted before, after the first proposal of so called local approach based on the local fracture stress criterion [40], it was employed as the critical condition by researchers other than Japanese researchers. Berdin and her coworkers carried out measurement of the local fracture stress and application phase analyses using 3D finite element analyses based on the local fracture stress criterion [133,149]. The feature of their studies was to consider temperature dependency of the local fracture stress based on nil ductility temperature and Weibull distribution of the local fracture stress. Such probability of the local fracture stress made unbroken section in the predicted fracture

surface as shown in Fig. 1-30. Jang et al. also made a finite element model based on the local fracture stress criterion although the mesh size employed by their model was much larger than the characteristic length employed by other studies [150]. The local fracture stress in Jang et al. was also assumed to have temperature dependency [150].

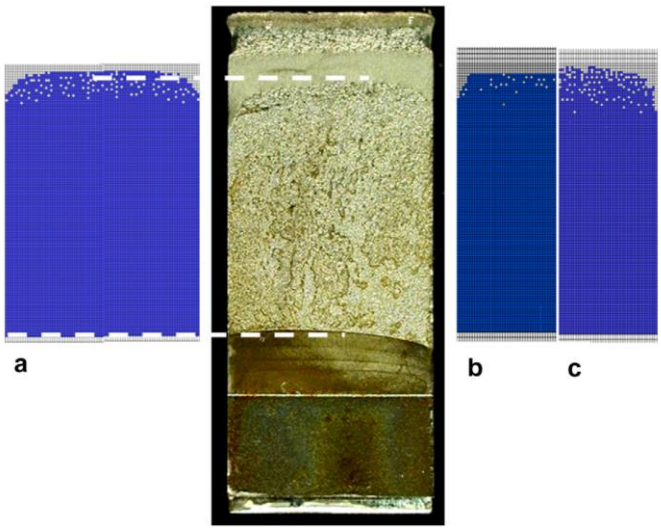

Fig. 1-30 Comparison of fracture surfaces obtained by the experiment and predicted by Berdin [149]

This assumption of temperature dependency was different from the results obtained by Prabel et al.[107], Bousquet et al. [108], and Yang et al. [109]. They introduced the local fracture stress criterion to XFEM and tried to predict not only crack arrest position but also crack path [109]. They pointed that the local fracture stress depended on strain rate as shown in Fig. 1-31 and did not depend on temperature based on their experimental studies using ferritic steels. According to them, the difference with Berdin's result was caused by the difference of employed steels. However, if the dependency on strain rate was attributed to formation of tear ridge as noted by Yang et al. [109], the local fracture stress should depend on temperature because the dependency of yield stresses of tear ridge on temperature and strain rate are generally equivalent [151]. It should be pointed out that the local fracture stress at too low strain rate in brittle crack propagation in steel was measured in their studies as shown in Fig. 1-31. Furthermore, their results that the local fracture stress depended on temperature or strain rate do not correspond to assumption

employed in Aihara et al. [51–53] and Shibanuma et al. [54,55]. It is worth noting that the previous finite element models based on the local fracture stress have been applied to only the crack arrest cases where the arrested crack length is too short (about 10~40 mm). Namely. they these have not yet reached to predict the brittle crack arrest toughness of steels although the local fracture stress criterion mode developed by Shibanuma et al. can be applied to analyze temperature gradient crack arrest tests.

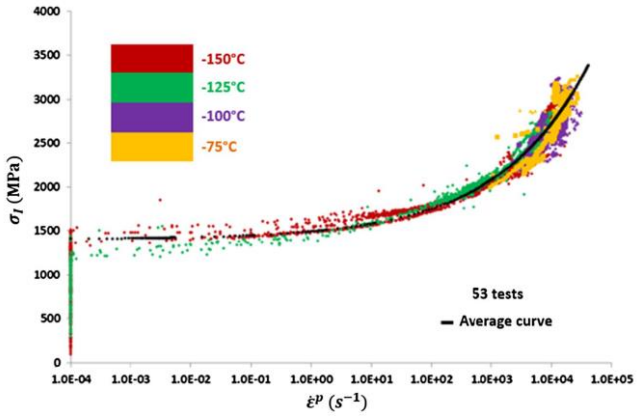

Fig. 1-31 the local fracture stress obtained by Yang et al. [109]

In addition to the characteristics of the local fracture stress, the local stress field in the vicinity of the propagating crack tip is also important. Because contrary to linear elastic solids, steels have complicated elastic-viscoplastic constitutive laws, the crack tip stress fields are expected to be complicated especially for rapid crack propagation. The local stress fields in linear elastic solids and relatively simple elastic-plastic solids have been investigated and their characteristics have been elucidated. Nishioka and his coworkers analytically solved the higher order terms of asymptotic solutions in the elastic local tensile fields [152–155]. In addition, relatively simple elastic plastic solids such as linear hardening materials were studied by previous literatures [156,157]. The simulation model based on the local fracture stress criterion proposed by Aihara et al. and Shibanuma et al. evaluated the local stress using the combination of some asymptotic solutions such as the crack tip singularity in linear hardening materials by Achenbach et al. [52–54,158,159]. Therefore, the identified local fracture stresses were unrealistically high as noted Section 1.1.4. In addition, although the simulation models regarded that SIFs, crack velocities, temperatures were the factors governing the local tensile stress fields, these governing factors

have not been examined yet. Although the brittle crack usually experiences crack velocity transitions, the model did not consider such unsteady effects without detail investigations.

Accordingly, to appropriately model the local tensile stresses, it is required to characterize the local tensile stress field. Although it has been attempted to analytically calculate the local tensile stress field of the propagating crack tip [156,157,160], the complicated constitutive laws of steels are not suitable to analytically calculate the local tensile stress. In addition, the dynamic effect including unsteady effect is hard to consider in such analytical methods.

1.2.6. 3D effect

Although the 3D effect due to shear lip (shown in Fig. 1-32) formations plays an important role in brittle crack propagation and arrest behaviors in steels, it has been often ignored in previous literatures [76,107–109]. Its importance was pointed out early in Japan. For example, Machida et al. mentioned the shear lip formation changed the $K_{\mathrm{d}} - V$ relationship of brittle crack propagation and arrest behaviors shown in Fig. 1-33 [161,162]. Although a mechanisms of the shear lip formation had not been explained, it was explained by the non-uniform distribution of the degree of plastic constraint in the thickness direction. In other words, the local fracture stress cannot be satisfied in the region where the plastic constraint is weak near the surface. Although this was modelled using the distribution of the plastic strain in the thickness direction calculated from the 3D finite element analyses in the conventional model [54,55], it was not supported by experimentally. The conventional model formulated the shear lip thickness by relating this distribution to the plastic zone size assuming small scale yielding according to the previous experiments. This formulation led the thicker shear lips when the SIF is higher, which consisted with the qualitative knowledge mentioned in the previous study [163]. This tendency is also supported by the 3D application phase analysis using cohesive method and the local fracture stress criterion which showed the crack front tunneling became remarkable along the crack propagation [129].

However, although it is therefore needed to qualitatively characterize the shear lip thickness, the accurate measurements have not been carried out. Although some literatures measured the shear lip thickness, their measurement were carried out only for limited cases [161,162,164]. And, these data were unreliable because the methods to measure were not noted.

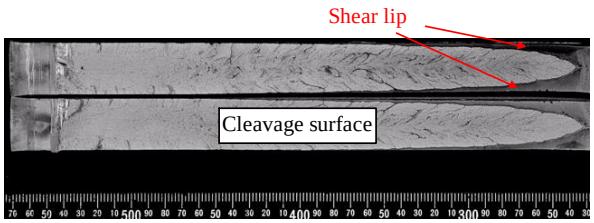

Fig. 1-32 Shear lip with cleavage surfaces

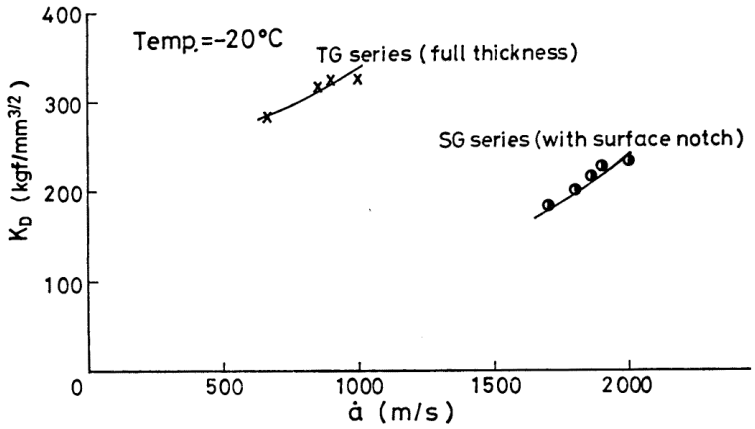

Fig. 1-33 Comparison of $K_{\mathrm{d}} - V$ relationships with and without shear lips [161]

In addition to the shear lip formation mechanism, the closure stress of the unbroken shear lips is also unclear. The closure stress works to reduce the crack driving force until the unbroken shear lips is broken in ductile manner. Although the previous literatures considered the closure stress equivalent to the yield stress at high strain rate ($10^3 \sim 10^4$ s^{-1}) [54,163,165], such high strain rate is hardly expected to actually cause in the unbroken shear lip because such rate is almost equal to that near the crack tip. And, although the crack arrest experiments using with and without shear lips were carried out to evaluate shear lip effects [166], such comparison is not appropriate to quantitatively characterize the closure stress because the crack arrest experiment easily includes a lot of scatters. Therefore, the conventional modellings of the closure stress are unrealistic and should be modified based on the detail investigations.

1.2.7. Crack arrest design

1.2.7.1. Material design

In order to develop steels with high crack arrestability, it is needed to relate steel microstructures with brittle crack propagation and arrest behavior. To consider cleavage cracking in microscopic view, some studies have been conducted by Qiao [167–171], Aihara [172], Snartland [173], and Stec [146,174]. However, the works of Qiao and Stec mainly focused on orientation of grains to measure the influence of misorientation between the bicrystal relationships (Fig. 1-34). Because the cleavage crack propagation related to the brittle crack arrest is generally composed of cleavage crack propagation across various grains, their studies just dealt with the latter stage of cleavage crack initiation rather than cleavage crack propagation. The work of Snartland et al. was also related to cleavage fracture initiation program, and did not focused on the characteristics of brittle crack arrest event [173]. Crack propagation in a grain and across neighboring grains was experimentally studied to use miniature strain gauges and high speed camera [134,175].

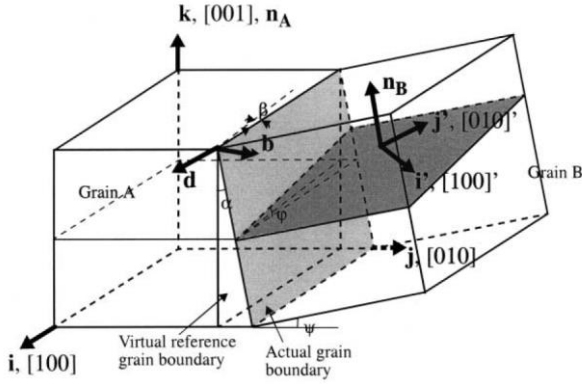

Fig. 1-34 Bicrystal relationship considered in Qiao and Argon [169]

On the other hand, Aihara and Tanaka considered ductile ligaments between cleavage fracture plane of each grains to calculate cleavage plane extension for simulation of cleavage fracture surface composed of aggregate of cleavage planes as shown in Fig. 1-35 [172]. Each cleavage plane is modelled by each square and the crack propagation is judged by the comparison of SIF and critical SIF at each edge of the square. This ligament which is called as tear ridge forms between the cleavage planes [176]. This model was applied to Charpy impact test specimen with anisotropic microstructures to simulate fracture surface morphology [177].

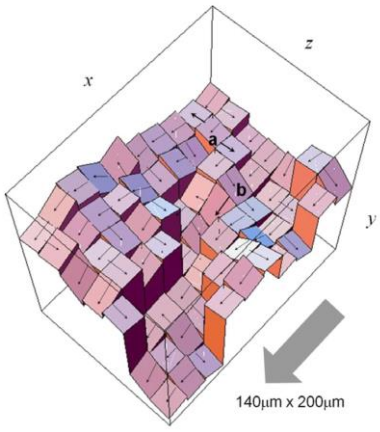

Fig. 1-35 Simulated fracture surface by Aihara and Tanaka [172]

Although cleavage crack initiation process is usually explained by so called multi barrier model, where the grain boundary is a main resistance [178], in steels, the energy absorption in cleavage crack propagation across various grains is mainly attributed to tear ridge formation [109,176,179,180]. Nilson et al. pointed out the energy dissipation due to such ductile ligament depended on the crack velocity [180]. Namely, the resistance mechanism of cleavage crack propagation is much different from that of cleavage crack initiation.

The model proposed by Aihara and Tanaka was extended to analyses of macroscopic fracture morphology and toughness distributions along thickness direction. The former one was carried out to simulate macroscopic chevron pattern found in fracture surface of bending crack arrest tests [181]. The latter one was proposed to reproduce a characteristic fracture surface morphology called as split nail in steel with inhomogeneous microstructure [182,183]. This model is composed of both microscopic model and macroscopic model. In microscopic model, each unit cell corresponds to grain. The calculation area is 1×1 mm. On the other hand, the unit cell of the macroscopic model consists with the calculation area of the microscopic model. Texture and grain size are used in the microscopic model and effective surface energy and normal vector of each calculation area of the microscopic model are determined by the microscopic model. The macroscopic model uses these characteristics of the calculation area to determine macroscopic fracture surface morphology and crack arrest positions. This model successfully reproduced the characteristic fracture surface called as split nail as shown in Fig. 1-36. The fracture surface morphology is considered to be related to energy dissipation and pointed out to be controlled by

stress triaxiality [184]. Therefore, to utilize artificial roughness of the surface may be contribute to improve brittle crack arrestability.

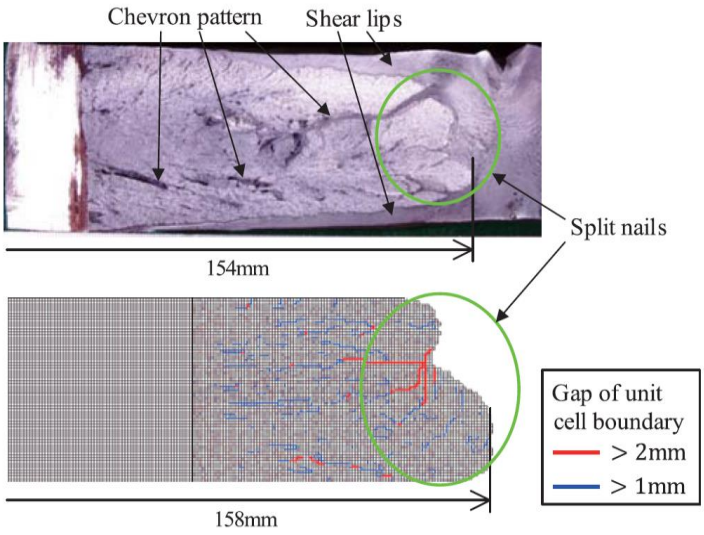

Fig. 1-36 Macroscopic fracture surface of the experiment and simulation [183]

Split nail fracture surface is usually observed in the brittle fracture of steels with non-uniform texture along thickness direction [185]. SIF at the crack tip in the split nail type crack becomes smaller than that in the thumb nail type crack and thus the crack is easier to be arrested in the split nail type fracture surface as compared by Tsuyama et al. (in Fig. 1-37).

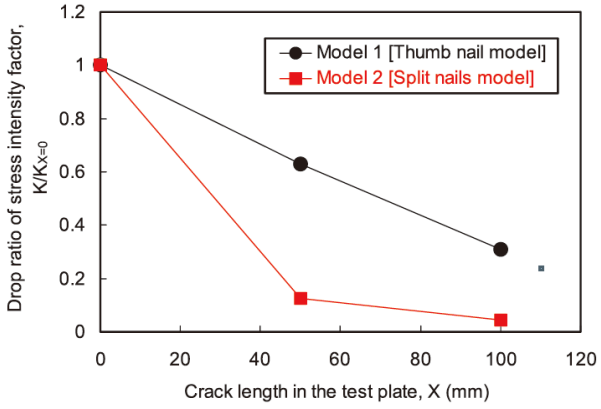

Fig. 1-37 SIF comparison between thumb- and split- nail fracture surface [185]

As mentioned above, addition of nickel highly increases brittle crack arrestability of steels and thus addition of nickel has been frequently employed to improve brittle crack arrest toughness of the steels [186]. However, because such addition makes the rise of steel costs, it has been attempted to decrease the rate of addition of nickel [187]. However, to use nickel is undesirable from the perspective of the cost and weldability. Thus, other approach of material design to improve brittle crack arrest toughness of steels. By controlling texture in Thermo Mechanical Control Process (TMCP), improvement of brittle crack arrest toughness has been reported [188]. This mechanism was explained by micro sub cracks generated to shield the main crack tip to decrease the crack tip stress intensity factor [189]. Such TMCP was also combined with micro-alloy design to cope with both weldability and higher crack arrest toughness [64]. On the other hand, however, it cannot be concluded that the relationship between microstructural feature and brittle crack arrest toughness is clear. In particular, the role of grain size, which is the most fundamental feature of microstructures, is not clear. In addition, the efforts to reduce the usage of nickel was also carried out so as not to decrease the crack arrestability [190].

1.2.7.2. Structural design

Because it is practically difficult to use steels with much nickel for naval architects from the perspective of economic costs, structural design like T-joint and cross-joint is employed to increase brittle crack arrestability in naval architects. Such approach is called as “Structural crack arrest”. This structural crack arrest design is used to determine the required brittle crack arrest toughness for steel plates used for large container ships [74,191]. Thus, this design is essential to provide enough capability of brittle crack arrest to the ships.

In fact, the crack arrester is usually designed so as to deploy higher steel plates appropriately [192,193]. In particular, brittle crack initiating and running on the welded bead was designed to be arrested by guiding it to base metal. It was pointed out the distance between the welded bead play an important role to appropriately arrest the crack in base metal [131]. This is because the welded metal has usually has low toughness than the base metal. Fig. 1-38 is the comparison of brittle crack arrest toughness obtained by An et al. [57], which showed that the crack arrest toughness in the weld is clearly low. This shift of the welded bead is called as butt shift explained in Fig. 1-39. The required distance between the two welded bead was estimated as 300 mm according to numerical simulation considering residual stress distribution [131]. And, it is also

reported that the appropriate choice of welding metal enables the brittle crack deviate from the welded bead and enter the base metal [194]. The factors related to the brittle crack path in welding such as the residual stress, mismatch, and toughness distribution depend on not only weld metal and welding procedure, but also geometry of welded section [195,196].

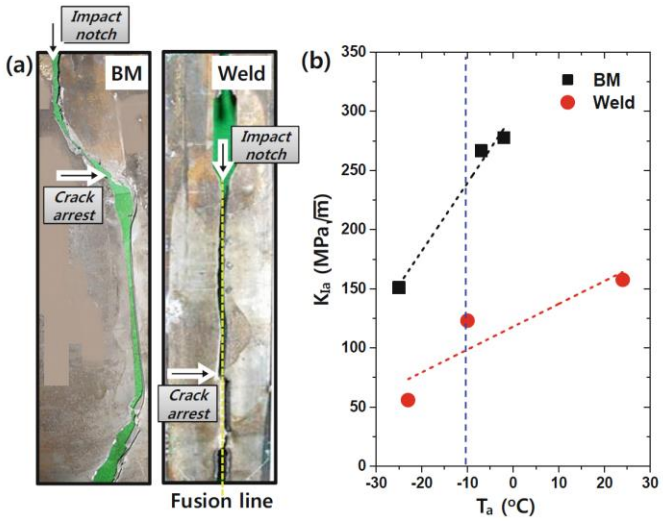

Fig. 1-38 Comparison of brittle crack arrest toughness between base metal and weld [57]

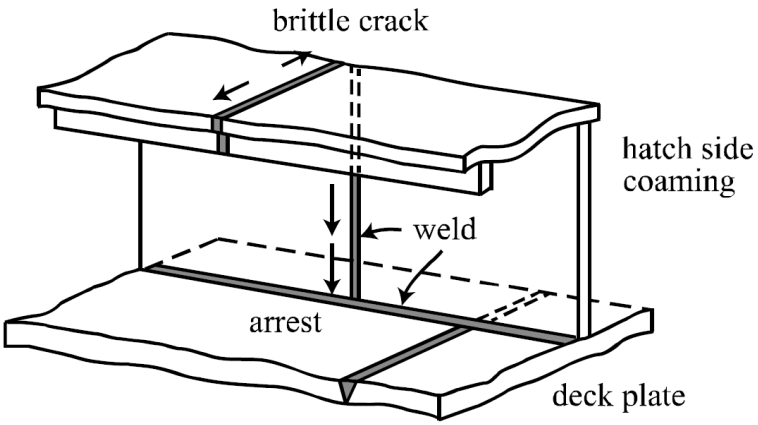

Fig. 1-39 Butt shift in weld [193]

On the other hand, structural factors have been studied to improve double integrity without high performance steels, which usually cost greater money. Crack arrest hole is one of famous examples of structural design as a crack arrestor [197,198]. A series of studies by Kanazawa and

his coworkers were carried out to investigate various types of crack arrester, including utilization of the cross-joint, which was almost same as the structural crack arrest design [38,197,199–203]. These studies pointed out that the crack arrester using the cross-joint (called as stiffener type crack arrester in Fig. 1-40, which is almost same as the structural crack arrest design) had enough crack arrest capability without higher grade steels when the structural configuration was appropriately designed [203].

Recent crack arrest design employs the combined approach. Namely, using butt shift guides the crack propagating welded bead to enter the base metal plate, and the structural crack arrest makes the required brittle crack arrest toughness of the plate smaller [204]. The structural crack arrest design assumes two crack propagation scenarios explained in Fig. 1-41. One is called scenario 1, where the brittle crack is initiated in hutch side coaming. The crack is supposed to be arrested in the base metal of upper deck in this scenario. One the other hand, in scenario 2, the crack is assumed to be initiated in the upper deck, and expected to be arrested in the base metal of the hutch side coaming. Generally, the required brittle crack arrest toughness is higher in scenario 2 than in scenario 1[67]. Although this trend corresponds to the fact that K_{ca} against the crack propagating along thickness direction was higher than K_{ca} against the crack propagating along other direction [205], a lot factors such as residual stress and microstructure distribution are related to the difference, and thus what makes the two scenarios different is not clear.

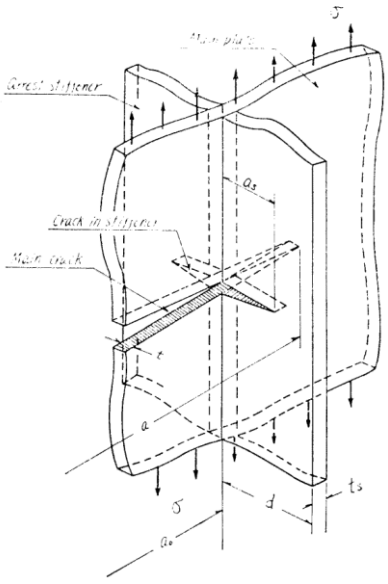

Fig. 1-40 stiffener type crack arrester [200]

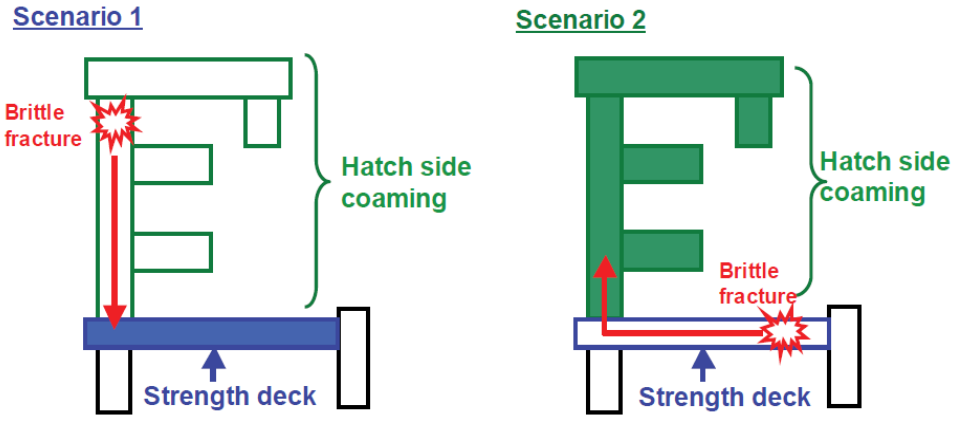

Fig. 1-41 Crack arrest scenario of structural crack arrest design [59]

A series of experimental studies have been carried out to determine the required crack arrest toughness for the heavy-section steel plates. These requirements were determined using the structural crack arrest design [67]. The experiments used the specimens simulating the actual ship structure as shown in Fig. 1-42.

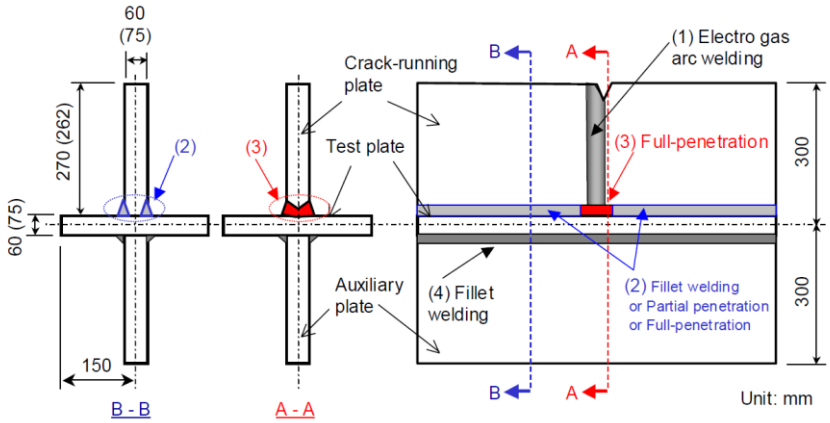

Fig. 1-42 Brittle crack arrest test specimen simulating actual ship structures [206]

Although these studies provided some useful findings, a lot of assumptions were employed for simplification. In particular, the study assumed the crack propagation behaviors in the structure to calculate SIF transitions without detail observation. In addition, the study mainly considered the crack open constraint by the stiffener and simply assumed the through crack, but Handa et al. pointed out the crack front shape played a crucial role to arrest the crack in the structural crack arrest design [207,208]. Handa et al. also indicated from their finite element analyses that to consider crack front shape made it possible to explain improvement of brittle crack arrestability in fillet welding compared to the full penetration welding [209]. However, the study of Handa et al. also assumed dynamic crack propagation behaviors and was not based on the actual crack propagation behaviors. Therefore, it is essentially needed to grasp actual crack propagation behaviors in the 3D structure for appropriate design of structural crack arrest.

1.3. Objective and contents

According to above review of previous studies, the theory to explain brittle crack propagation and arrest behaviors in steel has not been established although the local fracture criterion is a promising concept. Especially, the characteristics of the local fracture stress is still controversial and thus the validity of the local fracture stress criterion is not clear. Because the numerical method suitable for the local stress evaluation has not been discussed, it is needed to pay attention to the numerical method.

In addition, although the 3D effect represented by shear lips plays an important role in brittle crack propagation and arrest behaviors in steel, the conventional study was based on only assumptions and detail investigation to support the modelling has not been carried out.

In addition to the necessity to study brittle crack propagation and arrest behaviors theoretically, it is needed to examine the arrest design for engineering application. Systematic investigation on influence of steel microstructures to crack arrest performance and fundamental investigation of crack arrest mechanism in structural crack arrest design have to be clarified considering their importance in actual design.

According to these necessities to clarify brittle crack propagation and arrest behaviors, the overview of this dissertation is schematically illustrated in Fig. 1-43. The perspectives for this study are roughly divided to two types. One is the fracture mechanical perspective to aim to propose a theory to explain brittle crack propagation and arrest behaviors in steels by focusing on

the local fracture stress criterion. According to the review of previous studies, the dominant factors of brittle crack propagation and arrest behaviors can be roughly divided to the fracture criterion and the 3D effects. Although the fracture criterion and 3D effect are significantly important, they also remain unclear problems. The key factors in the fracture criterion are the local fracture stress and the local stress field in the vicinity of the crack tip. And the key factors governing 3D effect are the thickness of shear lips and the closure stress. Therefore, these factors have to be investigated in detail and formulated in each element model. These element models representing each fracture phenomena are integrated to develop a simulation model to explain brittle crack propagation and arrest behaviors in steels. In addition to this perspective, this dissertation considers crack arrest design perspective for both materials and structures based on the findings obtained through the studies on the brittle crack propagation and arrest behavior theory. These studies on crack arrest design is important for engineering application of brittle crack arrest concept.

Based on the schematically illustrated overview shown in Fig. 1-43, this dissertation shows the contents as below;

Chapter 2: Local stress evaluation in finite element analyses

Chapter 3: Local tensile stress in the vicinity of the propagating crack tip

Chapter 4: Governing factors of local stresses in the vicinity of the running crack tip in elastic-viscoplastic solids

Chapter 5: Brittle crack propagation/arrest behaviors under high stress intensity factor and isothermal conditions

Chapter 6: Shear lip closure stress and its formation

Chapter 7: Development of a numerical model to simulate brittle crack propagation and arrest behaviors in steel

Chapter 8: Experimental investigation of grain size effect to cleavage crack propagation resistance in ferrite-pearlite steel

Chapter 9: High speed observation of rapidly propagating cracks in 3D structures

And Chapter 10 is a conclusion and mentions the limitation of this study.

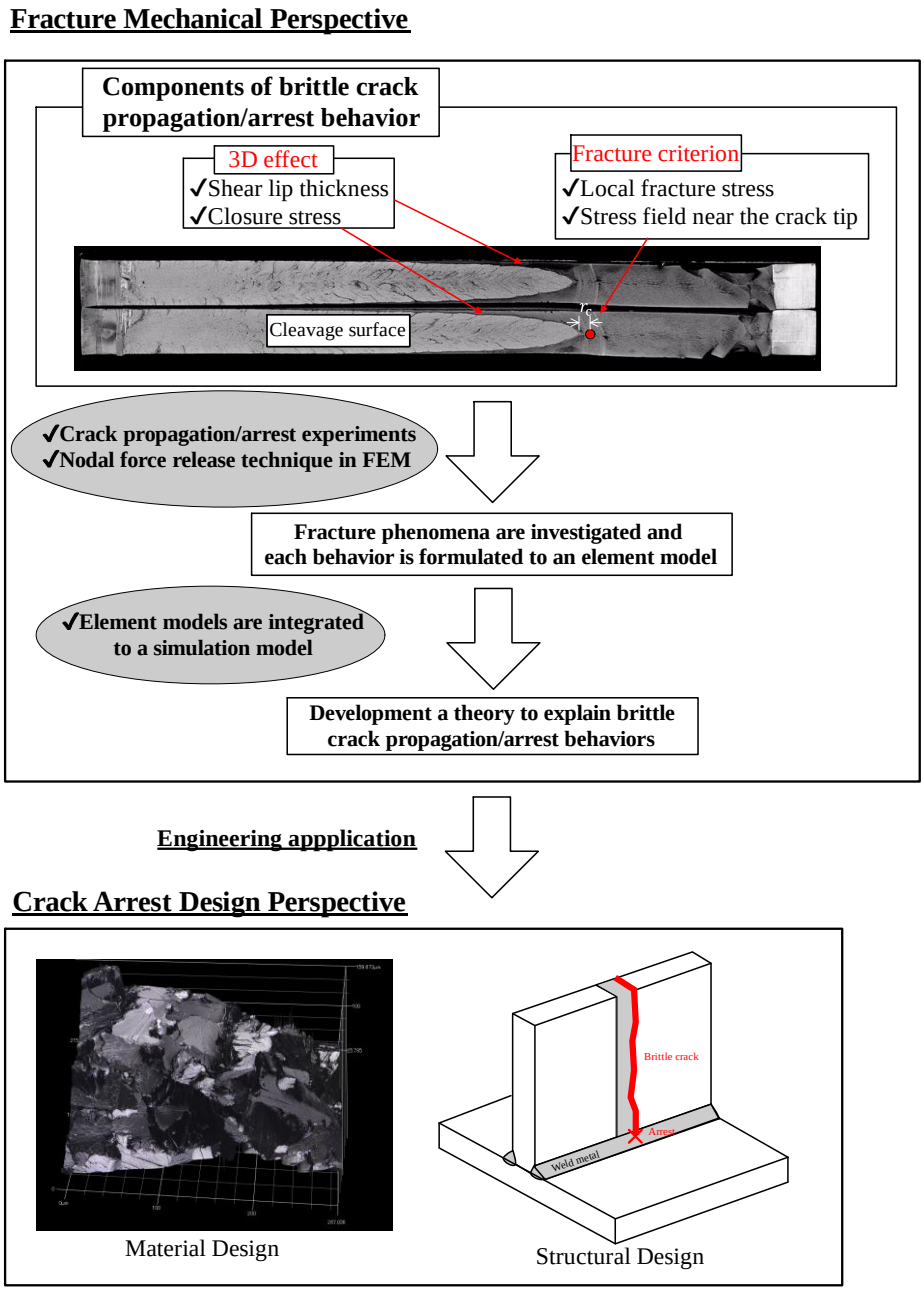

Fig. 1-43 Overview of studies in this dissertation

The relationship among these contests is illustrated in Fig. 1-44. The contents are roughly categorized to two parts, (A) and (B), which correspond to fracture mechanical perspective and crack arrest design perspective in Fig. 1-43, respectively. In Category (A), the fracture criterion

is studied in Chapter 2, 3, and 4 ((a) in Fig. 1-44) and the 3D effect is described in Chapter 5 and 6 ((b) in Fig. 1-43). These findings are integrated to develop a simulation model to explain brittle crack propagation and arrest behaviors in steels in Chapter 7. Category (B) is explain in Chapter 8 and 9. These are about the material design and structural design, respectively.

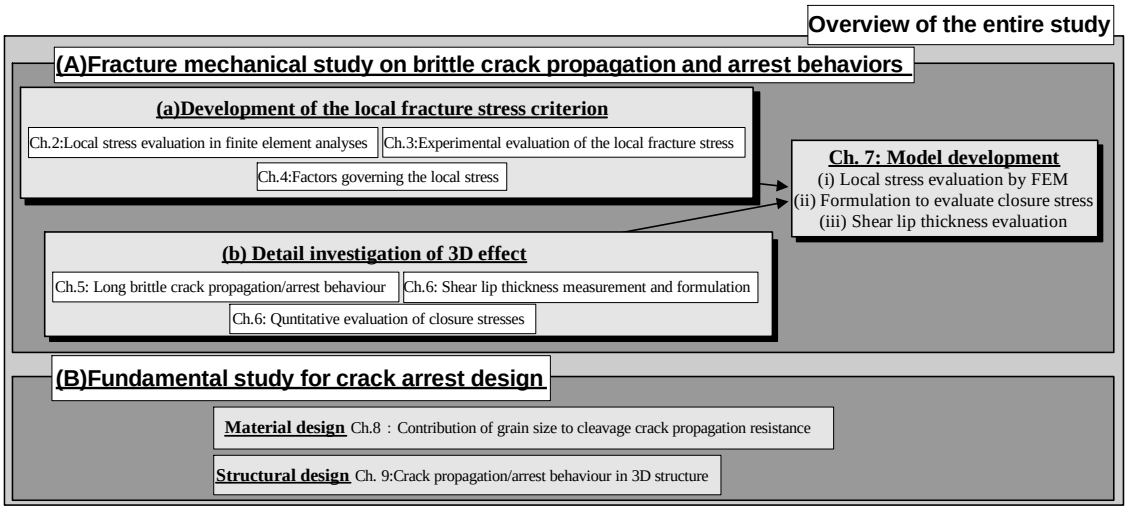

Fig. 1-44 Contents of this dissertation

Reference

[1] World Shipping Council, Container Ship Design, (2018). http://www.worldshipping.org/about-the-industry/liner-ships/container-ship-design (accessed May 15, 2018).

[2] M. Furuichi, R. Shibasaki, Cascade strategy of container terminals to maximize their quantitative and qualitative capacity, in: IAME 2015 Conf., 2015.

[3] K. Yamaguchi, H. Kitada, H. Yajima, K. Hirota, H. Shirakihara, Development of Extremely Large Container Ships, KANRIN. 3 (2005) 70–76.

[4] C. Wang, J. Wu, D. Wang, Numerical investigation of three-dimensional hull girder ultimate strength envelope for an ultra large container ship, Ocean Eng. 149 (2018) 23–37. doi:10.1016/j.oceaneng.2017.12.001.

[5] Y. Sumi, H. Yajima, M. Toyosada, T. Yoshikawa, S. Aihara, K. Gotoh, Y. Ogawa, T. Matsumoto, K. Hirota, H. Hirasawa, M. Toyoda, Y. Morikage, Fracture control of extremely thick welded steel plates applied to the deck structure of large container ships, J. Mar. Sci. Technol. 18 (2013) 497–514. doi:10.1007/s00773-013-0222-5.

[6] Y. Akakura, D. Araki, K. Tamai, Medium and long term future estimation of origin destination volume of world maritime container flow, J. Japan Soc. Civ. Eng. Ser. B3 (Ocean Eng. 73 (2017) I_989-I_994.

[7] J.G. MILLMAN, The Wall Street Journal, (2015). https://jp.wsj.com/articles/SB11815783148186973545804580453212289350120

(accessed November 7, 2018).
[8] A. Buixadé Farré, S.R. Stephenson, L. Chen, M. Czub, Y. Dai, D. Demchev, Y. Efimov, P. Graczyk, H. Grythe, K. Keil, N. Kivekäs, N. Kumar, N. Liu, I. Matelenok, M. Myksvoll, D. O'Leary, J. Olsen, S. Pavithran.A.P, E. Petersen, A. Raspotnik, I. Ryzhov, J. Solski, L. Suo, C. Troein, V. Valeeva, J. van Rijckevorsel, J. Wighting, Commercial Arctic shipping through the Northeast Passage: routes, resources, governance, technology, and infrastructure, Polar Geogr. 37 (2014) 298–324. doi:10.1080/1088937X.2014.965769.
[9] F. Lasserre, S. Pelletier, Polar super seaways? Maritime transport in the Arctic: An analysis of shipowners' intentions, J. Transp. Geogr. 19 (2011) 1465–1473. doi:10.1016/j.jtrangeo.2011.08.006.
[10] Fortune, Maersk's Terrible Earnings Report Shows Ocean Shippers Are Sinking Themselves, (2015). http://fortune.com/2015/11/06/maersks-terrible-earnings-report-shows-ocean-shippers-are-sinking-themselves/ (accessed February 14, 2019).
[11] Japan Maritime Center, (2016). http://jpmac.or.jp/relation/transport.html?id=1 (accessed September 28, 2018).
[12] Nippon Kaiji Kyokai, Guideline on Brittle Crack Arrest Design, 2009.
[13] International Association of Classification Societies, UR S33 Requirements for Use of Extremely Thick Steel Plates, (2014).
[14] The Japan Wedling Engineering Society, WES2815 Test method for brittle crack arrest toughness, (2014). http://www-it.jwes.or.jp/wes_ki/wesippan.jsp?arg=2815e-1.
[15] T. Kawabata, Review of Research on Fast Crack Propagation (Theory, Measurements and Numerical Simulations), Q. J. Japan Weld. Soc. 84 (2015) 75–82. doi:10.2207/jjws.84.75.
[16] J. Jang, B. Lee, J. Ju, D. Kwon, W. Kim, Crack-initiation toughness and crack-arrest toughness in advanced 9 pct Ni steel welds containing local brittle zones, Metall. Mater. Trans. A. 33 (2002) 2615–2622. doi:10.1007/s11661-002-0383-z.
[17] T. Nishi, Study on the Welding of 9%Ni Steel, Tetsu-to-Hagane. 66 (1980) 565–572.
[18] K. Osakabe, K. Onizawa, K. Shibata, M. Suzuki, Development of Probabilistic Fracture Mechanics Analysis Code PASCAL ver. 2 for Reactor Pressure Vessel, Japan, Trans. At. Energy Soc. 6 (2007) 161–171.
[19] M. Chen, W. Yu, G. Qian, J. Shi, Y. Cao, Y. Yu, Crack initiation, arrest and tearing assessments of a RPV subjected to PTS events, Ann. Nucl. Energy. 116 (2018) 143–151. doi:10.1016/j.anucene.2018.01.032.
[20] B.R. Bass, C.E. Pugh, J.K. Walker, Elastodynamic fracture analysis of large crack-arrest experiments, Nucl. Eng. Des. 98 (1987) 157–169. doi:10.1016/0029-5493(87)90164-6.
[21] E. Smith, T.J. Griesbach, Predicting crack arrest in reactor pressure vessels, Nucl. Eng. Des. 137 (1992) 305–314. doi:10.1016/0029-5493(92)90253-R.
[22] F.M. Burdekin, J.F. Knott, J.D.G. Sumpter, A.H. Sherry, TAGSI views on aspects of crack arrest philosophies for pressure vessels with thicknesses up to 100 mm, Int. J. Press. Vessel. Pip. 76 (1999) 879–883. doi:10.1016/S0308-0161(99)00066-6.
[23] R.A. Ibrahim, Overview of Structural Life Assessment and Reliability, Part VI: Crack Arresters, J. Sh. Prod. Des. 32 (2016) 71–98.
[24] The Transportation Safety Board of Canada, Marine Investigation Report Hull Fracture Bulk Carrier Lake Carling Gulf of St . Lawrence , Quebec 19 March 2002, 2003.
[25] F. Koshiga, On the Critical Temperature for Propagation of Brittle Crack in Steel Plate, J. Zosen Kiokai. 108 (1960) 355–363.
[26] Y. Akita, K. Ikeda, On the Brittle Crack Propagation and Arrest with Special Reference to ESSO Test with Temperature Gradient, J. Zosen Kiokai. 112 (1962) 153–162.
[27] M. Yoshiki, T. Kanazawa, H. Itagaki, A Study on the Propagation of a Brittle Fracture 3rd Report, J. Zosen Kiokai. 114 (1963) 191–199.

[28] R.G. Hoagland, A.R. Rosenfield, G.T. Hahn, Mechanisms of fast fracture and arrest in steels, Metall. Trans. 3 (1972) 123–136. doi:10.1007/BF02680591.
[29] G.R. Irwin, A.A. Wells, A continuum-mechanics view of crack propagation, Metall. Rev. 10 (1965) 223–270. doi:10.1179/mtlr.1965.10.1.223.
[30] F. Koshiga, O. Imazawa, S. Takehana, Arrest-Transition of Brittle Crack in Steel Plate, J. Zosen Kiokai. 114 (1963) 200–209.
[31] D.J. Naus, J. Keeney-Walker, B.R. Bass, R.J. Fields, R. deWit, S.R. Low, High-temperature crack-arrest behavior of prototypical and degraded (simulated) reactor pressure vessel steels, Int. J. Press. Vessel. Pip. 39 (1989) 189–208. doi:10.1016/0308-0161(89)90024-0.
[32] T. Kanazawa, Recent Studies on Brittle Crack Propagation in Japan, J. Japan Weilding Soc. 42 (1973) 68–84.
[33] M. Yoshiki, T. Kanazawa, F. Koshiga, Recent Studies on Bittle Fracture Propagation-Arrest in Japan, J. Japan Weilding Soc. 34 (1965) 21–28.
[34] S. Machida, T. Teramoto, H. Yoshinari, Study on Fast Fracture and Crack Arrest, Exp. Mech. 21 (1981) 78–88. doi:10.2534/jjasnaoe1968.1977.290.
[35] A.T. Zehnder, A.J. Rosakis, Dynamic fracture initiation and propagation in 4340 steel under impact loading, Int. J. Fract. 43 (1990) 271–285. doi:10.1007/BF00035087.
[36] A.J. Rosakis, J. Duffy, L.B. Freund, The determination of dynamic fracture toughness of AISI 4340 steel by the shadow spot method, J. Mech. Phys. Solids. 32 (1984) 443–460. doi:10.1016/0022-5096(84)90030-9.
[37] S. Machida, Y. Kawaguchi, M. Tsukamoto, An Evaluation of the Crack Arrestability of 9% Ni Steel Plate to a Extremely Long Brittle Crack, J. Japan Soc. Nav. Archit. 150 (1981) 511–517.
[38] S. Machida, M. Aoki, Some Basic Considerations on Crack Arresters for Welded Steel Structures (The 7 th Report) with special reference to arrest of a extremely long crack and the design of crack arresters, J. Soc. Nav. Archit. Japan. 131 (1972) 367–378.
[39] T. Kanazawa, S. Machida, S. Yano, K. Tanaka, S. Yamamoto, H. Matsumura, K. Itoga, Experim,ental Investigation on the Relationshio between Brittle Fracture Initiation and Arrest Toughness of 9% Ni Steel, J. Japan Soc. Nav. Archit. Ocean Eng. 153 (1983) 306–315.
[40] S. Machida, M. Matoba, H. Yoshinari, C. Tone, A Model for Brittle Crack Propagation and Arrest in Structural Steel, J. Soc. Nav. Archit. Japan. 172 (1992) 637–647.
[41] M.F. Kanninen, S.J. Hudak, H.R. Couque, R.J. Dexter, P.E. O'Donoghue, Viscoplastic-dynamic crack propagation: Experimental and analysis research for crack arrest applications in engineering structures, Int. J. Fract. 42 (1990) 239–260. doi:10.1007/BF00013216.
[42] X. Yang, S. Marie, C. Jacquemoud, Cleavage crack path prediction in a PWR vessel steel, in: Proc. ASME 2014 Press. Vessel. Pip. Conf. PVP2014, 2014: pp. 1–10.
[43] T.L. Anderson, Fracture Mechanics Fundamentals and Applircations 3rd ed., CRC Press, 2005.
[44] K.B. Broberg, Cracks and Fracture, Academic Press, 1999.
[45] Y. Nakano, Dynamic Fracture Toughness and Its Measurement, Tetsu-to-Hagane. 16 (1986) 37–43.
[46] J.W. Dally, W.L. Fourney, G.R. Irwin, On the uniqueness of the stress intensity factor - crack velocity relationship, Int. J. Fract. 27 (1985) 159–168. doi:10.1007/BF00017965.
[47] T. Kanazawa, S. Machida, T. Teramoto, H. Yoshinari, T. Miyahara, Study on Fast Fracture and Crack Arrest (The 5th Report), J. Soc. Nav. Archit. Japan. 150 (1981) 504–510.
[48] T. Kanazawa, S. Machida, H. Yajima, H. Kawano, Study on Brittle Crack Propagation and Arrest Behaviour in Plates and Beams Structures (1st. report), J. Soc. Nav. Archit.

149 (1981) 211–218.
[49] J. Lemaitre, Local approach of fracture, Eng. Fract. Mech. 25 (1986) 523–537.
[50] A. Pineau, Development of the Local Approach to Fracture over the Past 25 years: Theory and Applications, Int. J. Fract. 138 (2006) 139–166. doi:10.1007/s10704-006-0035-1.
[51] S. Machida, H. Yoshinari, M. Yasuda, S. Aihara, H. Mabuchi, Fracture mechanicsl modeling of brittle fracture propagation and arrest of steel (1) A fundamental model, J. Soc. Nav. Archit. Japan. 177 (1995) 243–258.
[52] S. Aihara, S. Machida, H. Yoshinari, H. Mabuchi, Fracture mechanical model of brittle fracture propagation and arrest of steel (2) Application to Temperature-gradient Type Test, J. Soc. Nav. Archit. Japan. 178 (1995) 545–554.
[53] S. Aihara, S. Machida, H. Yoshinari, Y. Tsuchida, Fracture mechanical modeling of brittle fracture propagation and arrest of steel (3) Application to Duplex Type Test, J. Soc. Nav. Archit. Japan. 179 (1996).
[54] K. Shibanuma, F. Yanagimoto, T. Namegawa, K. Suzuki, S. Aihara, Brittle crack propagation/arrest behavior in steel plate - Part I: Model formulation, Eng. Fract. Mech. 162 (2016) 324–340. doi:10.1016/j.engfracmech.2016.02.054.
[55] K. Shibanuma, F. Yanagimoto, T. Namegawa, K. Suzuki, S. Aihara, Brittle crack propagation/arrest behavior in steel plate - Part II: Experiments and model validation, Eng. Fract. Mech. (2016). doi:10.1016/j.engfracmech.2016.02.053.
[56] ASTM E1221-12, Standard Test Method for Determining Plane-Strain Crack-Arrest Fracture Toughness, KIa, of Ferritic Steels, ASTM B. Stand. 96 (2007) 1–19. doi:10.1520/E1221-12A.2.
[57] G.B. An, W. Woo, J.U. Park, Brittle crack-arrest fracture toughness in a high heat-input thick steel weld, Int. J. Fract. 185 (2014) 179–185. doi:10.1007/s10704-013-9900-x.
[58] G.B. An, W. Woo, J.U. Park, V. Em, Comparison of crack-arrest fracture toughness between low and high heat-input thick weld specimens, Int. J. Fract. 194 (2015) 197–203. doi:10.1007/s10704-015-0041-2.
[59] Y. Yamaguchi, H. Yajima, S. Aihara, H. Yoshinari, K. Hirota, T. Kiyosue, T. Tani, Development of G uidelines on Brittle Crack Arrest Design - Brittle Crack Arrest Design for Large Container Ships -1 -, in: Proc. Twent. Int. Offshore Polar Eng. Conf., 2010.
[60] Y. Shimada, T. Inoue, T. Kawabata, S. Aihara, Effect of specimen size, applied stress and temperature gradient on brittle crack arrest toughness test, Int. J. Fract. 204 (2017) 245–260. doi:10.1007/s10704-016-0179-6.
[61] T. Kawabata, M. Kaneko, S. Aihara, Effect of Impact Energy in the Esso Test (Part 1 : Basic Experiments and Validation of FEM Analysis), J. Test. Eval. 46 (2018). doi:10.1520/JTE20170045.
[62] M. Kaneko, T. Kawabata, S. Aihara, Effect of Impact Energy in ESSO Test (Part 3: Experimental Validation for New Validity Criteria of Impact Condition Giving Constant Evaluation in ESSO Test), J. Test. Eval. 47 (2019) 20170150. doi:10.1520/JTE20170150.
[63] M. Kaneko, T. Kawabata, S. Aihara, Effect of Impact Energy in ESSO Test ((Part 2: Proposal of Validity Criteria of Impact Condition in ESSO Test by FEM Crack Propagation Analysis), J. Test. Eval. 47 (2019) 20170151. doi:10.1520/JTE20170150.
[64] S. Gao, X. Lu, C. Zhang, Research and Development of Crack Arrest Steel for Ultra Large Container Ships, in: Twenty-Seventh Int. Ocean Polar Eng. Conf., 2017: pp. 7–13.
[65] M. Yoshiki, T. Kanazawa, S. Machida, A Consideration on Brittle Fracture Test of Steel Plates -with special reference to flat-temperature & gradient-temperature type Double Tension Test-, J. Zosen Kiokai. 113 (1963) 125–135.
[66] Y. Shimada, T. Inoue, T. Kawabata, S. Aihara, Effect of specimen size, applied stress and temperature gradient on brittle crack arrest toughness test, Int. J. Fract. 204 (2017).

doi:10.1007/s10704-016-0179-6.
[67] K. Matsumoto, T. Fukui, S. Nanno, S. Aihar, T. Kawabata, K. Shibanuma, T. Inoue, T. Okawa, T. Tagawa, H. Tajika, H. Imamura, Brittle Crack Arrest Toughness for Extremely Thick Steel Plates -Required Kca Value of Steel Plates with Thickness of 100 mm Used in Ultra-Large Container Ships-, in: Proc. 28th Int. Ocean Polar Eng. Conf., 2018: pp. 91–97.
[68] T. Kawabata, K. Matsumoto, T. Ando, H. Yajima, S. Aihara, H. Yoshinari, K. Hirota, T. Kiyosue, T. Inoue, T. Tani, Development of Brittle Crack Arrest Toughness Kca Test Method - Brittle Crack Arrest Design for Large Container Ships -2 - Review of Wide Plate Test Method for Arrest Toughness, in: Proc. Twent. Int. Offshore Polar Eng. Conf., 2010: pp. 80–87.
[69] T. Tagawa, T. Inoue, H. Tajika, T. Okawa, H. Imamura, T. Kawabata, K. Shibanuma, S. Aihara, Investigation of Isothermal Crack Arrest Test Procedure Consistent with K ca - Development of Isothermal Crack Arrest Test Procedure - 2, in: Proc. 28th Int. Ocean Polar Eng. Conf., 2018: pp. 86–90.
[70] C.S. Wiesner, B. Hayes, S.D. Smith, A.A. Willoughby, INVESTIGATIONS INTO THE MECHANICS OF CRACK ARREST IN LARGE PLATES OF 1.5%Ni TMCP STEEL, Fatigue Fract. Eng. Mater. Struct. 17 (1994) 221–233. http://doi.wiley.com/10.1111/j.1460-2695.1994.tb00802.x%0Apapers3://publication/doi/10.1111/j.1460-2695.1994.tb00802.x.
[71] G. An, H. Bae, B. Jeong, Y. An, H. Jeong, CAT (Crack Arrest Temperature) Test Method Using Local Temperature Gradient System for Estimate of Fracture Toughness with Shipbuilding Steel, in: Proc. 28th Int. Ocean Polar Eng. Conf., 2018: pp. 107–108.
[72] T. Inoue, T. Tagawa, T. Okawa, H. Tajika, H. Imamura, K. Matsumoto, T. Fukui, S. Nanno, T. Kawabata, K. Shibanuma, S. Aihara, Effects of Test Parameters on Crack Arrest Temperature in Isothermal Brittle Crack Arrest Test - Development of Isothermal Crack Arrest Test Procedure -1, in: Proc. 28th Int. Ocean Polar Eng. Conf., 2018: pp. 98–101.
[73] G. An, H.-Y. Bae, J.-U. Park, Development of Crack Arrest Temperature Test Method by Using a Local Temperature Gradient, J. Test. Eval. 48 (2020) 20180341. doi:10.1520/JTE20180341.
[74] T. Inoue, Y. Yamaguchi, H. Yajima, S. Aihara, H. Yoshinari, K. Hirota, T. Kiyosue, T. Tani, Required Brittle Crack Arrest Toughness Kca Value with Actual-scale Model Tests -Brittle Crack Arrest Design for Large Container Ships -4-, in: Proc. Tweintieth Int. Offshore Polar Eng. Conf., 2010: pp. 95–101.
[75] E.J. Ripling, P.B. Crosley, S.J. Wiersma, A REVIEW OF STATIC CRACK ARREST CONCEPTS, Eng. Fract. Mech. 23 (1986) 21–33.
[76] J.A. Joyce, R.E. Link, C. Roe, J.C. Sobotka, Dynamic and static characterization of compact crack arrest tests of navy and nuclear steels, Eng. Fract. Mech. 77 (2010) 337–347. doi:10.1016/j.engfracmech.2009.04.006.
[77] D.J. Naus, B.R. Bass, J. Keeney-Walker, R.J. Fields, R. deWit, S.R. Low III, HSST Wide-plate Test Results and Analysis, Nucl. Eng. Des. 118 (1990) 283–295.
[78] B.T. Timofeev, G.P. Karzov, A.A. Blumin, V.I. Smirnov, Determination of crack arrest toughness for Russian light water reactor pressure vessel materials, Int. J. Press. Vessel. Pip. 77 (2000) 519–529. doi:10.1016/S0308-0161(00)00049-1.
[79] K. Wallin, Statistical re-evaluation of the ASME KICand KIRfracture toughness reference curves, Nucl. Eng. Des. 193 (1999) 317–326. doi:10.1016/S0029-5493(99)00187-9.
[80] R.E. Link, J.A. Joyce, C. Roe, Crack arrest testing of high strength structural steels for naval applications, Eng. Fract. Mech. 76 (2009) 402–418.

doi:10.1016/j.engfracmech.2008.11.006.
[81] K. Rahka, Instrumented Compact Crack Arrest Testing, Eng. Fract. Mech. 32 (1989) 493–497.
[82] E. Bouyne, P. Joly, B. Houssin, C.S. Wiesner, A. Pineau, Mechanical and microstructural investigations into the crack arrest behaviour of a modern 2 1/4 Cr-1 Mo pressure vessel steel, Fatigue Fract. Eng. Mater. Struct. 24 (2001) 105–116. doi:10.1046/j.1460-2695.2001.00363.x.
[83] T. Kawabata, Y. Nishizono, S. Aihara, Brittle crack propagation behavior in a member subjected to bending load, Theor. Appl. Fract. Mech. 92 (2017) 266–275. doi:10.1016/j.tafmec.2017.09.005.
[84] C.S. Wiesner, Predicting crack arrest behaviour of structural steels using small-scale material characterisation tests, Int. J. Press. Vessel. Pip. 69 (1996) 185. doi:10.1016/S1566-1369(02)80030-9.
[85] The Japan Wedling Engineering Society, WES TS2816 Simplified test method for brittle crack arrest toughness using press-notched bend specimen, 2015.
[86] Y. Nakano, M. Tanaka, Crack Arrest Toughness of Structural Steels Evaluated by Compact Test, Trans. ISIJ. 22 (1982) 147–153.
[87] S. Sathyanarayanan, A. Moitra, G. Sasikala, A.K. Bhaduri, Evaluation of Crack Arrest Toughness (KIA) of P91 Steel in Various Cold Worked and Thermally Aged Conditions, J. Mater. Eng. Perform. 24 (2014) 909–919. doi:10.1007/s11665-014-1322-z.
[88] Y. Liu, Y. Feng, Q. Ma, X. Song, Dynamic fracture toughness of X70 pipeline steel and its relationship with arrest toughness and CVN, Mater. Des. 23 (2002) 693–699. doi:10.1016/S0261-3069(02)00077-8.
[89] The Japan Wedling Engineering Society, WES3003: 1995 Evaluation Criterion of Rolled Steels for Low Temperature Application, (1995).
[90] T. Okawa, H. Shirahata, K. Nakashima, K. Yanagita, T. Inoue, Simplified Evaluation of Brittle Crack Arrest Toughness in Heavy-Thick Plate by Combined Small-scale Tests, in: Proc. 25th Int. Offshore Polar Eng. Conf., 2015: pp. 1153–1157.
[91] S. Sathyanarayanan, A. Moitra, G. Sasikala, A. Dasgupta, S. Saroja, A.K. Bhaduri, B. Raj, V. Singh, Characterization of Crack Arrest Phenomena in a Modified 9Cr-1Mo Steel, J. Test. Eval. 39 (2011) 448–455. doi:10.1520/JTE103048.
[92] H. Shirahata, T. Okawa, T. Inoue, K. Ushida, Simplified Evaluation Method for Brittle Crack Arrest Toughness of Steel Plates Exploiting Charpy Impact Test, Tetsu-to-Hagane. 104 (2018) 155–165.
[93] T. Okawa, T. Kawabata, Numerical Simulation of Brittle Crack Propagation in NRL Drop-Weight Test by Finite Element Analysis, in: Proc. 28th Int. Ocean Polar Eng. Conf., 2018: pp. 102–106.
[94] T. Nishioka, H. Tokudome, M. Kinoshita, Dynamic fracture-path prediction in impact fracture phenomena using moving finite element method based on delaunay automatic mesh generation, Int. J. Solids Struct. 38 (2001) 5273–5301. doi:10.1016/S0020-7683(00)00345-0.
[95] Y.D. Ha, F. Bobaru, Characteristics of dynamic brittle fracture captured with peridynamics, Eng. Fract. Mech. 78 (2011) 1156–1168. doi:10.1016/j.engfracmech.2010.11.020.
[96] M. Imachi, S. Tanaka, Dynamic stress intensity factors evaluation employing ordinary state-based peridynamics, Trans. JSCES. (2016) 20160017.
[97] A. Coré, J.-B. Kopp, J. Girardot, P. Viot, Dynamic energy release rate evaluation of rapid crack propagation in discrete element analysis, Int. J. Fract. (2018). doi:10.1007/s10704-018-0314-7.
[98] M. Kuna, Finite Elements in Fracture Mechanics Theory-Numerics-Applications, Springer, 2010.

[99] T. Handa, S. Igi, S. Endo, S. Tsuyama, H. Shiomi, Effect of Distance of Loading Points on Long Brittle Crack Propagation / Arrest Behavior, Q. J. Japan Weld. Soc. 30 (2012) 213–219.
[100] A.R. Shahani, M.R. Amini Fasakhodi, Finite element analysis of dynamic crack propagation using remeshing technique, Mater. Des. 30 (2009) 1032–1041.
[101] T. Nishioka, T. Otsuka, T. Fujimoto, The Developments of Three-Dimensional Moving Finite Element Method Based on Delaunay Automatic Tetrahedronization and Evaluation Method of Fracture Mechanics Parameters for Three-Dimensionally Propagating Complicated Crack Fronts, Trans. JSME (in Japanese). 75 (2009) 1374–1380.
[102] T. Nishioka, S. Tchouikov, T. Fujimoto, Study of Dynamic Branching Fracture by Numerical Simulation, J. Soc. Mater. Sci. Japan. 51 (2002) 1359–1366.
[103] N. Moes, J. Dolbow, T. Belytschko, A finite element method for crack growth without remeshing, Int. J. Numer. Meth. Engng. 46 (1999) 131–150. doi:10.1002/(SICI)1097-0207(19990910)46:1<131::AID-NME726>3.0.CO;2-J.
[104] J. Song, H. Wang, T. Belytschko, A comparative study on finite element methods for dynamic fracture, Comput. Mech. Springer-Verlag. 42 (2008) 239–250. doi:10.1007/s00466-007-0210-x.
[105] T. Belytschko, H. Chen, J. Xu, G. Zi, Dynamic crack propagation based on loss of hyperbolicity and a new discontinuous enrichment, Int. J. Numer. Methods Eng. 58 (2003) 1873–1905. doi:10.1002/nme.941.
[106] D. Grégoire, H. Maigre, A. Combescure, New experimental and numerical techniques to study the arrest and the restart of a crack under impact in transparent materials, Int. J. Solids Struct. 46 (2009) 3480–3491. doi:10.1016/j.ijsolstr.2009.06.003.
[107] B. Prabel, S. Marie, A. Combescure, Using the X-FEM method to model the dynamic propagation and arrest of cleavage cracks in ferritic steel, Eng. Fract. Mech. 75 (2008) 2984–3009. doi:10.1016/j.engfracmech.2008.01.008.
[108] A. Bousquet, S. Marie, P. Bompard, Propagation and arrest of cleavage cracks in a nuclear pressure vessel steel, Comput. Mater. Sci. 64 (2012) 17–21. doi:10.1016/j.commatsci.2012.04.026.
[109] X. Yang, S. Marie, C. Jacquemoud, P. Bompard, Prediction of cleavage crack propagation path in a nuclear pressure vessel steel, Eng. Fract. Mech. 191 (2018) 486–503. doi:10.1016/j.engfracmech.2018.01.015.
[110] L. Bingqi, C. Yatomi, X-FEM Analysis of stress fields near a crack tip under compressive loads using the implicit return mapping algorithm in an elastic-plastic material, J. Appl. Mech. 8 (2005). http://ac.els-cdn.com/S001379440800297X/1-s2.0-S001379440800297X-main.pdf?_tid=44f70b12-6175-11e7-bc26-00000aab0f27&acdnat=1499254376_b8c912e13364c235b949be5e20a2d7c0.
[111] B. Prabel, A. Combescure, A. Gravouil, S. Marie, Level set X-FEM non-matching meshes : Application to dynamic crack propagation in elastic – plastic media, Int. J. Numer. Methods Eng. (2007) 1553–1569. doi:10.1002/nme.
[112] H. Nguyen-Xuan, L. V. Tran, C.H. Thai, C. V. Le, Plastic collapse analysis of cracked structures using extended isogeometric elements and second-order cone programming, Theor. Appl. Fract. Mech. 72 (2014) 13–27. doi:10.1016/j.tafmec.2014.07.008.
[113] S. Kumar, I. V. Singh, B.K. Mishra, XFEM simulation of stable crack growth using J-R curve under finite strain plasticity, Int. J. Mech. Mater. Des. 10 (2014) 165–177. doi:10.1007/s10999-014-9238-1.
[114] S. Kumar, A.S. Shedbale, I. V. Singh, B.K. Mishra, Elasto-plastic fatigue crack growth analysis of plane problems in the presence of flaws using XFEM, Front. Struct. Civ. Eng. 9 (2015) 420–440. doi:10.1007/s11709-015-0305-y.
[115] E. Giner, N. Sukumar, J.E. Tarancón, F.J. Fuenmayor, An Abaqus implementation of the

extended finite element method, Eng. Fract. Mech. 76 (2008) 347–368. doi:10.1016/j.engfracmech.2008.10.015.
[116] H. Okada, S. Endoh, M. Kikuchi, On fracture analysis using an element overlay technique, Eng. Fract. Mech. 72 (2005) 773–789. doi:10.1016/j.engfracmech.2004.05.003.
[117] A. Yazid, N. Abdelkader, H. Abdelmadjid, A state-of-the-art review of the X-FEM for computational fracture mechanics, Appl. Math. Model. 33 (2009) 4269–4282. doi:10.1016/j.apm.2009.02.010.
[118] S. Nakasumi, K. Suzuki, H. Ohtsubo, Crack growth analysis using mesh superposition technique and X-FEM, Int. J. Numer. Methods Eng. 75 (2008) 291–304. doi:10.1002/nme.
[119] M. Kikuchi, Y. Wada, Y. Shintaku, K. Suga, Y. Li, Fatigue crack growth simulation in heterogeneous material using s-version FEM, Int. J. Fatigue. 58 (2014) 47–55. doi:10.1016/j.ijfatigue.2013.04.022.
[120] K. Kishi, K. Shibanuma, F. Yanagimoto, K. Suzuki, Development of dynamic mesh superposition method for local tensile stress evaluation, in: 22nd Eur. Conf. Fract., 2018.
[121] M. Elices, G.V. Guinea, J. Gómez, J. Planas, The cohesive zone model: advantages, limitations and challenges, Eng. Fract. Mech. 69 (2002) 137–163. doi:10.1016/S0013-7944(01)00083-2.
[122] G. Debruyne, J. Laverne, P.E. Dumouchel, Dynamic crack growth: Analytical and numerical cohesive zone models approaches from basic tests to industrial structures, Eng. Fract. Mech. 90 (2012) 1–29. doi:10.1016/j.engfracmech.2012.04.002.
[123] Y. SHINTAKU, M. MURAMATSU, S. TSUTSUMI, K. TERADA, T. KYOYA, J. KATO, S. MORIGUCH, An analysis of fatigue crack propagation in pollycrystalline metals using cohesive zone model with damage variable, Trans. Japan Soc. Comput. Eng. Sci. (2014). doi:http://doi.org/10.11421/jsces.2014.20140014.
[124] K. Harada, K. Gotoh, Improvement of the Strip Yield Model Considering the Work Hardening Effect of Materials, J. Japan Soc. Nav. Archit. Ocean Eng. 14 (2011) 39–46.
[125] A. Pandolfi, P.R. Guduru, M. Ortiz, A.J. Rosakis, Three dimensional cohesive-element analysis and experiments of dynamic fracture in C300 steel, Int. J. Solids Struct. 37 (2000) 3733–3760. doi:10.1016/S0020-7683(99)00155-9.
[126] N. Valoroso, G. Debruyne, J. Laverne, A cohesive zone model with rate-sensitivity for fast crack propagation, Mech. Res. Commun. 58 (2014) 82–87. doi:10.1016/j.mechrescom.2013.12.008.
[127] B. Brickstad, A Viscoplastic Analysis of Rapid Crack Propagation Experiments in Steel, J. Mech. Phys. Solids. 31 (1983) 307–327.
[128] T. Kawabata, A. Inami, S. Aihara, Numerical model of brittle crack propagation considering surface energy on high tensile strength steel - Proposal of a numerical model of brittle crack propagation (report I), J. Japan Soc. Nav. Archit. Ocean Eng. 16 (2012) 77–87.
[129] T. Kawabata, S. Aihara, Effects of stress field around the crack tip on fracture surface energy during brittle crack propagation -Proposal of a numerical model of brittle crack propagation (report2)-, J. Japan Soc. Nav. Archit. Ocean Eng. 21 (2016) 63–73.
[130] H. Yoshinari, S. Aihara, T. Iwata, Influence of Residual Stress and Fracture Toughness on Brittle Crack Propagation Behaviour along Welded Joint, J. Japan Soc. Nav. Archit. Ocean Eng. 6 (2007) 371–377.
[131] H. Yoshinari, S. Aihara, Brittle Crack Propagation Behavior at Butt Shifted Welded Joint -Numerical Simulation of Brittle Crack Propagation along Welded Joint (3rd Report)-, J. Japan Soc. Nav. Archit. Ocean Eng. 9 (2009) 177–182.
[132] H. Nakai, H. Yoshinari, T. Inoue, S. Aihar, Development of Three-Dimensional Crack Path Prediction Model for Brittle Fracture in Welded Joint with Residual Stress,

Toughness Distribution and Various Types of Welding Groove, J. Japan Soc. Nav. Archit. Ocean Eng. 19 (2014) 123–137.
[133] C. Berdin, M. Hajjaj, P. Bompard, S. Bugat, Local approach to fracture for cleavage crack arrest prediction, Eng. Fract. Mech. 75 (2008) 3264–3275. doi:10.1016/j.engfracmech.2007.08.013.
[134] D. Nakanishi, T. Kawabata, S. Aihara, Brittle crack propagation resistance inside grain and at high angle grain boundary in 3% Si-Fe alloy, Acta Mater. 144 (2018) 768–776. doi:10.1016/j.actamat.2017.11.020.
[135] Z. Yue, Y. Song, R. Yang, Q. Yu, Comparison of caustics and the strain gage method for measuring mode I stress intensity factor of PMMA material, Polym. Test. 59 (2017) 10–19. doi:10.1016/j.polymertesting.2017.01.012.
[136] J. Fineberg, E. Bouchbinder, Recent developments in dynamic fracture: some perspectives, Int. J. Fract. 196 (2015) 33–57. doi:10.1007/s10704-015-0038-x.
[137] K. Arakawa, T. Mada, Unsteady dynamic crack propagation in a brittle polymer, Exp. Mech. 47 (2007) 609–615. doi:10.1007/s11340-006-9020-x.
[138] T. Nishioka, Y. Negishi, H. Sumii, T. Fujimoto, Ultra High-Speed Photography and Moving Finite Element Analysis for Dynamic Crack Branching under Impact Loading, J. Soc. Mater. Sci. Japan. 61 (2012) 894–899.
[139] X.F. Yao, W. Xu, M.Q. Xu, K. Arakawa, T. Mada, K. Takahashi, Experimental study of dynamic fracture behavior of PMMA with overlapping offset-parallel cracks, Polym. Test. 22 (2003) 663–670. doi:10.1016/S0142-9418(02)00173-3.
[140] G. Gao, Z. Li, M. Negahban, Dynamic Fracture Analysis of Polycarbonate by the Optical Method of Caustics, Procedia Mater. Sci. 3 (2014) 165–176. doi:10.1016/j.mspro.2014.06.031.
[141] Y. Nakano, M. Katayama, Stress Intensity Factors during Brittle Crack Propagation and at Crack Arrest, J. Soc. Mater. Sci. Japan. 30 (1981) 21–26.
[142] Y. Takashima, T. Kawabata, S. Yamada, F. Minami, Observation of micro-cracks beneath fracture surface during dynamic crack propagation, Theor. Appl. Fract. Mech. 92 (2017) 178–184. doi:10.1016/j.tafmec.2017.07.013.
[143] J. Nohava, P. Haušild, M. Karlík, P. Bompard, Electron backscattering diffraction analysis of secondary cleavage cracks in a reactor pressure vessel steel, Mater. Charact. 49 (2002) 211–217. doi:10.1016/S1044-5803(02)00360-1.
[144] D. Nakanishi, T. Kawabata, S. Aihara, Effect of dispersed retained γ-Fe on brittle crack arrest toughness in 9% Ni steel in cryogenic temperatures, Mater. Sci. Eng. A. 723 (2018) 238–246. doi:10.1016/j.msea.2018.03.056.
[145] A.H. Priest, An energy balance in crack propagation and arrest, Eng. Fract. Mech. 61 (1998) 231–251. doi:10.1016/S0013-7944(98)00075-7.
[146] M. Stec, J. Faleskog, Influence of grain size on arrest of a dynamically propagating cleavage crack in ferritic steels - Micromechanics, Int. J. Fract. 158 (2009) 51–71. doi:10.1007/s10704-009-9374-z.
[147] G. Hütter, T. Linse, S. Roth, U. Mühlich, M. Kuna, A modeling approach for the complete ductile-brittle transition region: Cohesive zone in combination with a non-local Gurson-model, Int. J. Fract. 185 (2014) 129–153. doi:10.1007/s10704-013-9914-4.
[148] Y. Shintaku, K. Terada, S. Tsutsumi, Anisotropic Damage Constitutive Law for Cleavage Failure in Crystalline Grain by Cohesive Zone Model, Q. J. Japan Weld. Soc. 35 (2017) 165–168.
[149] C. Berdin, 3D modeling of cleavage crack arrest with a stress criterion, Eng. Fract. Mech. 90 (2012) 161–171. doi:10.1016/j.engfracmech.2012.05.002.
[150] Y.C. Jang, Y. Lee, G.B. An, J.S. Park, J.B. Lee, S. Il Kim, Temperature Dependent Fracture Model and Its Application To Ultra Heavy Thick Steel Plate Used for Shipbuilding, Int. J. Mod. Phys. B. 22 (2008) 5483–5488.

doi:10.1142/S0217979208050693.
[151] P.E. Bennett, G.M. Sinclair, Parameter Representation of Low-Temperature Yield Behavior of Body-Centered Cubic Transition Metals, J. Basic Eng. 88 (1966) 518–524.
[152] T. Nishioka, K. Kondo, Derivation of In-plane Mixed-Mode Asymptotic Solutions ofr an Unsteadily Fast-Propagating Crack Tip Using a Sympolic Manipulation System, Trans. Japan Soc. Mech. Eng. Ser. A. 62 (1996) 945–952. doi:10.1248/cpb.37.3229.
[153] T. Nishioka, Mathematical and computational studies in fracture mechanics, Bull. Japan Soc. Ind. Appl. Math. 5 (1995) 293–313.
[154] T. Nishioka, S.N. Atluri, Path-independent integrals, energy release rates, and general solutions of near-tip fields in mixed-mode dynamic fracture mechanics, Eng. Fract. Mech. 18 (1983) 1–22. doi:10.1016/0013-7944(83)90091-7.
[155] T. Nishioka, K. Kondo, Deviation of Mode-III Asymptotic Solutions for an Unsteadily Fast-Propagating Crack Tip Using a Symbolic Manipulation System, Trans. Japan Soc. Mech. Eng. Ser. A. 62 (1996) 666–670. doi:10.1061/ASCE1090-0241(2003)129:1(12).
[156] X.K. Zhu, K.C. Hwang, Dynamic crack-tip field for tensile cracks propagating in power-law hardening materials, Int. J. Fract. 115 (2002) 323–342.
[157] B. Jia, Z.Q. Wang, Y.D. Li, W.Y. Liang, Viscoplastic solution to field at steadily propagating crack tip in linear-hardening materials, Appl. Math. Mech. 27 (2006) 527–533. doi:10.1007/s10483-006-0413-1.
[158] S. Machida, H. Yoshinari, M. Yasuda, S. Aihara, H. Mabuchi, Fracture mechanical modeling of brittle crack propagation and arrest of steel, in: Proceedins 1995 Jt. ASME/JSME Press. Vessel. Pip. Conf., 1995: pp. 183–195.
[159] J.D. Achenbach, M.F. Kanninen, C.H. Popelar, Crack-tip fields for fast fracture of an elastic-plastic material, J. Mech. Phys. Solids. 29 (1981) 211–225. doi:10.1016/0022-5096(81)90027-2.
[160] M. Lu, Q.-H. Qin, First- and second-order asymptotic solutions of fast fracture in an elastic-visco-plastic solids, Int. J. Non. Linear. Mech. 36 (2001) 861–877.
[161] S. Machida, H. Yoshinari, A. Yahiro, Study on Fast Fracture and Crack Arrest (The 7th Report), J. Soc. Nav. Archit. Japan. 158 (1985) 610–618.
[162] S. Machida, H. Yoshinari, A. Yashiro, Crack Arrest Behavior of Fast Fracture in Steel, J. Soc. Mater. Sci. Japan. 35 (1986) 860–866.
[163] H. Mimura, Method to estimate Kca from K1a, J. High Press. Inst. Japan. 31 (1993) 58–64.
[164] N. Ogura, A Study on the Ductile Arrest of Brittle Cracks, J. Zosen Kiokai. 110 (1961) 443–453.
[165] K. Shibanuma, Y. Yamamoto, F. Yanagimoto, K. Suzuki, S. Aihara, Multiscale Model Synthesis to Clarify the Relationship between Microstructures of Steel and Macroscopic Brittle Crack Arrest Behavior - Part I : Model Presentation, ISIJ Int. 56 (2016) 341–349. doi:10.2355/isijinternational.ISIJINT-2015-450.
[166] Y. Funatsu, H. Shirahata, J. Otani, T. Inoue, Y. Hashiba, The Effect of Shear-lips on the Arrestability of Thicker Steel Plates, in: Proc. Twenty-Second Int. Offshore Polar Eng. Conf., 2012: pp. 63–66.
[167] A.S. Argon, Y. Qiao, Cleavage cracking resistance of large-angle grain boundaries in Fe-3 wt% Si alloy, Phillosophical Mag. A. 82 (2002) 3333–3347. doi:10.1080/01418610208240445.
[168] Y. Qiao, A.S. Argon, Brittle-to-ductile fracture transition in Fe – 3wt .% Si single crystals by thermal crack arrest, Mech. Mater. 35 (2003) 903–912. doi:10.1016/S0167-6636(02)00293-4.
[169] Y. Qiao, A.S. Argon, Cleavage cracking resistance of high angle grain boundaries in Fe – 3 % Si alloy, Mech. Mater. 35 (2003) 313–331.
[170] Y. Qiao, X. Kong, On size effect of cleavage cracking in polycrystalline thin films,

Mech. Mater. 39 (2007) 746–752. doi:10.1016/j.mechmat.2006.12.003.
[171] W. Lu, J. Chen, X. Kong, S.S. Chakravarthula, Y. Qiao, Nonuniform cleavage cracking across persistent grain boundary, Mech. Mater. 43 (2011) 567–573. doi:10.1016/j.mechmat.2011.07.001.
[172] S. Aihara, Y. Tanaka, A simulation model for cleavage crack propagation in bcc polycrystalline solids, Acta Mater. 59 (2011) 4641–4652. doi:10.1016/j.actamat.2011.04.010.
[173] B.D. Snartland, A. Alvaro, V. Osen, C. Thaulow, Crack arrest testing at the micro-scale, Eng. Fract. Mech. 201 (2018) 157–166. doi:10.1016/j.engfracmech.2018.06.003.
[174] M. Stec, J. Faleskog, Micromechanical modeling of grain boundary resistance to cleavage crack propagation in ferritic steels, Int. J. Fract. 160 (2009) 151–167. doi:10.1007/s10704-009-9415-7.
[175] T. Kawabata, N. Nakamura, S. Aihara, Brittle crack propagation acceleration in a single crystal of a 3% silicon-Fe alloy, Frat. Ed Integrità Strutt. 47 (2019) 416–424. doi:10.3221/IGF-ESIS.47.32.
[176] T. Iung, A. Pineau, Dynamic Crack Propagation and Crack Arrest Investigated With a New Specimen Geometry : Part II : Experimental Study on a Low-Alloy Ferritic Steel, Fatigue Fract. Eng. Mater. Struct. 19 (1996) 1369–1381.
[177] K. Sugimoto, I. Kawata, S. Aihara, H. Shirahata, Analysis of Cleavage Crack Propagation in Steels Having Anisotropy by Means of Three-Dimensional Polycrystalline Cleavage Fracture Simulation Model, Tetsu-to-Hagane. 100 (2014) 1274–1280.
[178] C. Ruggieri, R.H. Dodds, A local approach to cleavage fracture modeling: An overview of progress and challenges for engineering applications, Eng. Fract. Mech. 187 (2018) 381–403. doi:10.1016/j.engfracmech.2017.12.021.
[179] P. Haušild, I. Nedbal, C. Berdin, C. Prioul, The influence of ductile tearing on fracture energy in the ductile-to-brittle transition temperature range, Mater. Sci. Eng. A. 335 (2002) 164–174. doi:10.1016/S0921-5093(01)01913-X.
[180] P. Nilsson, P. Stahle, K.G. Sundin, On the behavior of crack surface ligaments, Nucl. Eng. Des. 184 (1998) 145–153.
[181] S. Aihara, F. Yanagimoto, K. Shibanuma, T. Namegawa, H. Nakai, T. Kawabata, H. Yoshinari, Numerical Simulation of Brittle Crack Propagation Incorporating Toughness and Residual Stress Distribution in Welds, in: 10th Int. Conf. Trends Weld. Res., 2016: pp. 420–423.
[182] K. Shibanuma, Y. Yamamoto, F. Yanagimoto, K. Suzuki, S. Aihara, H. Shirahata, Multiscale model synthesis to clarify the relationship between microstructures of steel and macroscopic brittle crack arrest behavior - Part I: Model presentation, ISIJ Int. 56 (2016). doi:10.2355/isijinternational.ISIJINT-2015-449.
[183] Y. Yamamoto, K. Shibanuma, F. Yanagimoto, K. Suzuki, S. Aihara, Multiscale Model Synthesis to Clarify the Relationship between Microstructures of Steel and Macroscopic Brittle Crack Arrest Behavior - Part II : Application to Crack Arrest Test, ISIJ Int. 56 (2016) 350–358. doi:10.2355/isijinternational.ISIJINT-2015-450.
[184] T. Kawabata, F. Tonsho, Y. Nishizono, N. Nakamura, Y. Takashima, Controlling factors for roughness increases on cleavage fracture surfaces and crack branching in polycrystalline steel, Theor. Appl. Fract. Mech. 100 (2019) 171–180. doi:10.1016/j.tafmec.2019.01.010.
[185] T. Handa, S. Igi, K. Nishimura, H. Tajika, T. Tagawa, S. Tsuyama, Effect of Toughness Distribution in the Thickness Direction on Long Brittle Crack Propagation/Arrest Behavior of Heavy Gage Shipbuilding Steel, Q. J. Japan Weld. Soc. 34 (2016) 211–217.
[186] O. Furukimi, A. Narumoto, Y. Nakano, C. Shiga, T. Tanaka, Toughness of Welded Joint and Crack Arrestability of Base in Ultra Low C-2 . 5 % Ni Steel Produced by Thermo-

mechanical Control Process, Trans. ISIJ. 27 (1987) 460–466.
[187] T. Kamo, T. Kagaya, Utilization and Standardization of Newly Developed Nickel Steel Plate for Pressure Vessel for Low Temperature Service, J. Japan Weld. Soc. 83 (2014) 459–462.
[188] J. Katsuta, M. Ueda, M. Toyosada, Brittle Crack Propagation Analysis of TMCP Steel Rolled at the Temperature of Intercritical Region, J. Soc. Nav. Archit. 167 (1990) 261–269.
[189] T. Handa, S. Igi, S. Tsuyama, T. Tagawa, F. Minami, Mechanism of Brittle Crack Arrest Toughness Improvement Due to Texture, Tetsu-to-Hagane. 98 (2012) 548–557.
[190] N. Kubo, M. Takata, M. Yamashita, D. Knowles, H. Hirose, N. Sakato, S. Muramoto, S. Hirai, M. Mitsumoto, K. Arimochi, T. Kawabata, T. Kamo, Development of 7%Ni-TMCP Steel Plato for LGN Sotrage tanks, Q. J. JAPAN Weld. Soc. 28 (2010) 130–140.
[191] A. Kubo, H. Yajima, S. Aihara, H. Yoshinari, K. Hirota, M. Toyoda, T. Kiyosue, T. Inoue, T. Handa, T. Kawabata, T. Tani, Y. Yamaguchi, Experimental study on brittle crack propagation behavior with large scale structural component model tests - Brittle crack arrest design for large container ships -5 -, in: Proc. Twenty-Second Int. Offshore Polar Eng. Conf., 2012: pp. 36–43.
[192] T. Fukui, H. Kitada, Arrestability Requirement for Crack Arrestor in Hull Structure, J. High Press. Inst. Japan. 41 (2003) 303–315.
[193] Y. Sumi, Fracture morphology and its evolution a review on crack path stability and brittle fracture along butt-weld, Frat. Ed Integrita Strutt. 9 (2015) 42–58. doi:10.3221/IGF-ESIS.34.04.
[194] H. Matsuda, H. Hiramatsu, G. Nishiyama, T. Kiyose, M. Matsuura, K. Okamoto, T. Kawabata, A. Inami, K. Onishi, S. Kubo, Investigation on the brittle crack propagation behavior of heavy thick shipbuilding steel plate (Report 6: Effect of toughness of weld metal on deviation behaviour of brittle crack initiated in weld metal), Conf. Proc. Japan Soc. Nav. Archit. Ocean Eng. 7E (2008) 51–54.
[195] U. Zerbst, R.A. Ainsworth, H.T. Beier, H. Pisarski, Z.L. Zhang, K. Nikbin, T. Nitschke-Pagel, S. Münstermann, P. Kucharczyk, D. Klingbeil, Review on fracture and crack propagation in weldments - A fracture mechanics perspective, Eng. Fract. Mech. 132 (2014) 200–276. doi:10.1016/j.engfracmech.2014.05.012.
[196] H. Yoshinari, S. Aihara, Influence of Weld Heat Input and Texture of Base Metal on Brittle Crack Propagation Behaviour along Welded Jouint -Numerical Simulation of Brittle Crack Propagation along Welded Joint (2nd Report)-, J. Japan Soc. Nav. Archit. Ocean Eng. 7 (2008) 251–258.
[197] T. Kanazawa, S. Machida, M. Matoba, Some Basic Considerations on Brittle Crack Arrester for Welded Sttel Structure (The 1st Report), J. Zosen Kiokai. 115 (1964) 78–88.
[198] T. Nishioka, T. Ooya, K. Goami, T. Fujimoto, G. Okamoto, Pure Research into Hall (Crack Arrester) for Brittleness High Speed Destruction Stop˘-The First Report Basic Experiment That Uses CGS Method And Ultra High Speed Video Camera-, J. Japanese Soc. Exp. Mech. 10 (2010) 69–73.
[199] M. Yoshiki, T. Kanazawa, S. Machida, Some Basic Considerations on Crack Arresters for Welded Steel Structures (The 3rd report) -Experimental Checks-, J. Zosen Kiokai. 118 (1965) 192–203.
[200] T. Kanazawa, S. Machida, M. Ohyagi, Some Basic Considerations on Crack Arresters (The 5th Report) -with special reference to “Ditch-type” & “Stiffener-type arresters”-, J. Zosen Kiokai. 122 (1967) 200–214.
[201] T. Kanazawa, S. Machida, M. Ohyagi, Some Basic Considerations on Crack Arresters for Welded Steel Structures (The 4 th report) -with special reference to integral stiffener type arrester model-, J. Zosen Kiokai. 121 (1967) 225–234.
[202] T. Kanazawa, S. Machida, M. Matoba, H. Tada, I. Kimpara, Some Basic Consideration

on Crack Arresters for Welded Steel Structures (The 2nd Report) -with special reference to patch type arrester model-, J. Zosen Kiokai. 116 (1964) 124–135.
[203] T. Kanazawa, S. Machida, H. Doi, Some Basic Consideration on Crack Arresters (The 6th Report) -with special reference of "Stiffeners Plate-type Arrester"-, J. Zosen Kiokai. 124 (1968) 321–330.
[204] S. Aihara, Guideline of Innovative Structural Design Standardization of Crack Arrest Evaluation Procedures, J. Japan Weld. Soc. 84 (2015) 263–269.
[205] H. Hiramatsu, H. Matsuda, K. Michiba, G. Nishiyama, T. Kiyose, M. Matsuura, K. Okamoto, T. Kabawata, T. Maeda, A. Inami, S. Kubo, Investigation on the brittle crack propagation behaviour of heavy thick shipbuilding steel plate (Report 1: The crack arrestability of brittle crack propagation in the thickness direction in steel plates), Conf. Proc. Japan Soc. Nav. Archit. Ocean Eng. 5E (2007) 131–134.
[206] T. Handa, T. Matsumoto, H. Yajima, S. Aihara, H. Yoshinari, K. Hirota, T. Kiyosue, T. Inoue, T. Tani, Effect of S tructural D iscontinuities of W elded J oints on B rittle C rack P ropagation B ehavior - Brittle C rack A rrest D esign for L arge C ontainer S hips -3 - Steel Plates Used for Tests, in: Twent. Int. Offshore Polar Eng. Conf., 2010: pp. 88–94.
[207] T. Handa, S. Igi, K. Oi, K. Nishimura, T. Tagawa, F. Minami, Brittle Crack Propagation/Arrest Behavior in Full Penetration T-joint, J. Japan Soc. Nav. Archit. Ocean Eng. 19 (2014) 179–185.
[208] T. Handa, S. Igi, K. Oi, T. Tagawa, F. Minami, Brittle crack propagation / arrest behavior in T-joint structure of heavy gauge steel plate, Weld. World. 59 (2015) 823–838. doi:10.1007/s40194-015-0242-3.
[209] T. Handa, S. Suzuki, N. Kiji, M. Toyoda, T. Miyata, Effect of Un-welded Length on Behavior of Brittle Crack Arrest in tee joint structure, Q. J. Japan Weld. Soc. 26 (2008) 124–130.

Chapter 2 Local stress evaluation in finite element analyses

2.1. Introduction

As noted in Chapter 1, the local fracture stress has been one of the most promising concept to explain brittle crack propagation and arrest behaviors. Therefore, accurate evaluation of local stresses in the vicinity of a rapidly propagating crack tip is important to study brittle crack propagation and arrest behaviors from the perspective of the local fracture stress criterion. Because this dissertation focuses on the local fracture stress criterion, the detail examination of the method to analyze the local stress is appropriate for the first content of this dissertation.

Because it is practically difficult to analytically obtain the local stress field near a propagating crack tip in elastic-viscoplastic solids like steel, numerical methods like finite element method are needed to evaluate the local stresses. Although the rapid growth of computer performance provides some method to evaluate the local stresses [1,2], the local stress evaluation in numerical methods has been merely investigated compared to vigorous researchers of numerical methods to evaluate the fracture mechanics parameters such as J and K [3,4].

In fact, numerical methods are indispensable approaches for studying rapid crack propagation problems owing to experimental difficulties. Although several numerical techniques analyzing dynamic cracks, e.g. the finite difference method [5], discrete element method [6], peridynamics [7], and element-free Galerkin method [8], have been utilized for rapid crack propagation analyses, the finite element method (FEM) is one of the most reliable and common numerical methods for dynamic crack propagation problems [3]. Based on the fundamental FEM frameworks, modifications and evolutions have been conducted for rapid crack propagation analyses. For example, XFEM, PDS-FEM, and cohesive zone model are powerful numerical methods available for analyses of dynamic crack propagation of materials [9–11]. Actually, some studies applied

them to the analyses of brittle crack propagation and arrest behavior in steels [12,13], although they could not provide sufficient explanation to the behavior.

However, almost all of the conventional studies using the numerical methods have just aimed to obtain the macroscopic fracture mechanics parameters or dissipation energy, and they have not paid attention to the accurate evaluation of the local stress in the vicinity of a propagating crack tips. Accordingly, while there have a lot of efforts to develop numerical methods which is suitable to evaluate fracture mechanics parameters and fracture energy accurately, the accuracy of the local stress evaluated by the numerical methods has not been investigated in spite of the importance of the local fracture stress to study brittle crack propagation and arrest behavior in steels. Although there are a few studies focused on local stress [1,14,15], the numerical accuracies were not sufficiently verified.

According to the above background, this chapter presents verification of the finite element analyses for rapid crack propagation based on the local fracture stress criterion as a foundational but significant investigation, and aims to propose an effective method to evaluate local stress near the crack tip with accuracy and stability. These investigation were conducted using elastic problems because there are the established theoretical local stress field in the vicinity of the dynamically propagating crack tip in elastic materials. Abaqus 6.14 was employed as a finite element analysis solver for all analyses in this chapter [16].

2.2. Nodal force release technique and finite element mesh

In this study, crack propagation is represented by the nodal force release technique [17], which is schematically illustrated in Fig. 2-1. In the nodal force release technique, the time length of the time step Δt is defined as the time it takes for a crack to pass through an element. For example, in Fig. 2-1, node A corresponds to the crack tip and the reaction force at node A is $F(t) = F_0$ at the beginning of the present step, i.e., $t = t_0$. Defining the present step, i.e., $t_0 < t < t_0 + \Delta t$, the reaction force $F(t)$ monotonically decreases from F_0 to 0. At the end of the present step, i.e., $t = t_0 + \Delta t$, $F(t)$ is zero and node B corresponds to the crack tip. Because the length of the time step Δt is the time duration for the crack to propagate through one element, Δt is determined by the mesh size and crack velocity. Therefore, the dynamic condition can be considered by setting the length of the time step needed for the crack to propagate through one element according to the crack velocity.

Although there are several methods to simulate rapid crack propagation in the FEM frameworks as described in Section 2.1, we employ the nodal force release technique because it is the simplest and most fundamental method in finite element analyses to express crack propagation [17].

The problem analyzed in this study is schematically illustrated in Fig. 2-2. The media is an infinite plate with a central crack under remotely applied tensile stress. The crack propagates only in the normal direction of the tensile stress. This is the most fundamental mode I fracture mechanics problem [18].

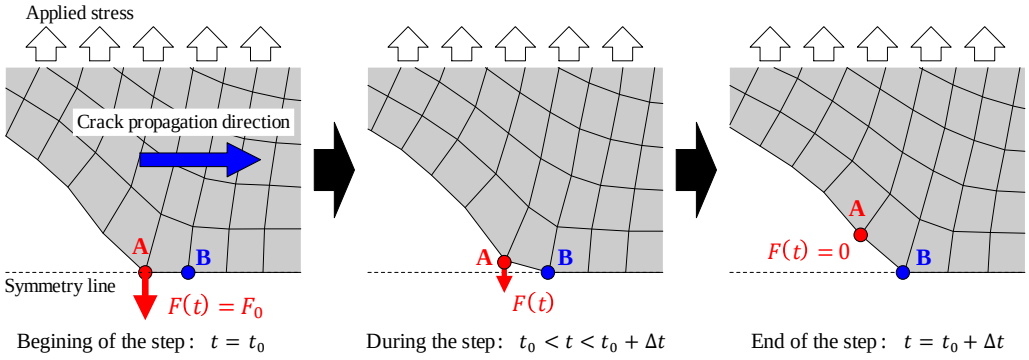

Fig. 2-1 Schematic of nodal fore release technique to simulate rapid crack propagation

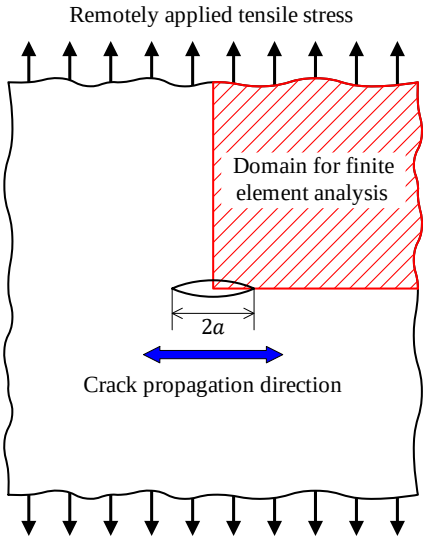

Fig. 2-2 Infinite elastic media with a center crack under remote tensile stress and the domain for finite element analyses

As this study required a series of many finite element analyses, a mesh generator that can produce reasonable finite element models to analyze the rapid crack propagation problem was developed to reduce numerical costs. This mesh generator constructs finite element models by inputting crack velocity V, final crack length a, remotely applied tensile stress σ_{app}, Young's modulus, Poisson's ratio, the mass density ρ, and minimum element size d located along the path of a crack. In all the analyses presented in this chapter, Young's modulus, Poisson's rate, and the density in all analyses were set to $E = 206\,\mathrm{GPa}$, $\nu = 0.3$, and $\rho = 7{,}800\,\mathrm{kg/m^3}$, which are those of steels, respectively, unless otherwise noted. The problems this study analyzed were 2D and plain strain. One example mesh produced by the generator is shown in Fig. 2-3. Considering its symmetry, the model is the quarter model of the media. The dimension of the longitudinal direction was set to the value larger than $\frac{V_{\mathrm{R}}}{V}\,a_{\max}$. Because the Poisson's ratio was 0.3 in this chapter, the dilatational wave velocity was about twice the Rayleigh wave velocity. Therefore, by determining the dimension of the longitudinal direction larger than $\frac{V_{\mathrm{R}}}{V}\,a_{\max}$, the dilatational wave generated at the crack tip did not return to the crack propagation path after the reflection on the model boundary, such that the model could be regarded as infinite.

Two symmetry boundary conditions are imposed on the model as shown in Fig. 2-3 considering the symmetry of the infinite elastic media with a center crack under remote tensile stress shown in Fig. 2-2. Crack propagation is represented by releasing the reaction force of the y-symmetry

boundary condition of the crack tip node (see Fig. 2-1). The plain strain and first order quadrilateral elements with full-integration were employed in the analyses although elastic analyses sometimes employ higher order elements [19]. There were two reasons why higher order elements were not employed. First, the applicability of this study to elasto-plastic analyses should be considered for future analyses of brittle crack propagation and arrest behavior in steels which deform in elasto-plastic manners. Second, the higher elements were not appropriate for the nodal force release technique because it generated a lot of vibration.

The analysis in this study included two parts. At first, the remote tensile stress was statically applied to the model. In this step, there was no crack in the model. After the loading, the dynamic analysis started and the crack began to grow. Dynamic analyses were carried out using the implicit Hilber-Hughes-Taylor (HHT) method [20], which has often been used for dynamic crack analyses [21]. This HHT method [20] is one of the most popular implicit time integration methods, which is an extension of the Newmark method.

The equation of motion in the HHT method is expressed as

$$\begin{aligned}\boldsymbol{M}\ddot{\mathbf{u}}_{t+\Delta t} + \boldsymbol{C}\{(1+\alpha_{\mathrm{HHT}})\dot{\mathbf{u}}_{t+\Delta t} - \alpha_{\mathrm{HHT}}\dot{\mathbf{u}}_t\} + \boldsymbol{K}\{(1+\alpha_{\mathrm{HHT}})\mathbf{u}_{t+\Delta t} - \alpha_{\mathrm{HHT}}\mathbf{u}_t\} \\ = \boldsymbol{F}\{t + (1+\alpha_{\mathrm{HHT}})\Delta t\}\end{aligned} \tag{2-1}$$

where $\boldsymbol{M}, \boldsymbol{C}, \boldsymbol{K}$, and $\boldsymbol{F}$ represent the mass matrix, damping matrix, stiffness matrix, and load matrix, respectively. t is the time at the beginning of the present step, Δt is the time increment, and $\mathbf{u}$ is displacement. Further, α_{HHT} is a parameter of the damping degree in the HHT method, defined as $-0.5 \leq \alpha_{\mathrm{HHT}} \leq 0$ [20]. The displacement $\mathbf{u}_t$ and velocity $\dot{\mathbf{u}}_t$ are expressed as

$$\mathbf{u}_{t+\Delta t} = \mathbf{u}_t + \Delta t\mathbf{u}_{t+\Delta t} + \{(1-2\beta_{\mathrm{HHT}})\ddot{\mathbf{u}}_t + 2\beta\ddot{\mathbf{u}}_{t+\Delta t}\}\frac{\Delta t^2}{2} \tag{2-2}$$

$$\dot{\mathbf{u}}_{t+\Delta t} = \dot{\mathbf{u}}_t + \{(\mathbf{1}-\gamma_{\mathrm{HHT}})\ddot{\mathbf{u}}_t + \gamma_{\mathrm{HHT}}\ddot{\mathbf{u}}_{t+\Delta t}\} \tag{2-3}$$

The damping parameter α_{HHT} sometimes selectively reduces the numerical vibration in analyses. To maintain the unconditional stability and second-order accuracy of the numerical analyses, β_{HHT} and γ_{HHT} are usually set as [20]

$$\beta_{\mathrm{HHT}} = \frac{1}{4}(1 - \alpha_{\mathrm{HHT}})^2 \tag{2-4}$$

$$\gamma_{\mathrm{HHT}} = \frac{1}{2} - \alpha_{\mathrm{HHT}} \tag{2-5}$$

The parameters in the HHT method were defined as $\alpha_{\mathrm{HHT}} = -0.0500$, $\beta_{\mathrm{HHT}} = 0.276$, and $\gamma_{\mathrm{HHT}} = 0.550$ unless otherwise noted, respectively, according to Czekanski *et al* [22].

Generally, crack propagation analyses can be categorized into two types. One is the generation phase analyses, and the other is the application phase analyses [23]. In the generation phase analyses, the crack velocity is an input parameter, and therefore Δt is known. Accordingly, the local stress is an output parameter obtained from the crack propagation analyses using Δt determined by the input crack velocity.

On the other hand, in the application phase analyses, the fracture criterion is an input parameter, and the crack velocity is obtained from crack propagation analyses using the input fracture criterion. Namely, Δt is an unknown parameter and can be obtained from the application phase analyses using the input fracture criterion. As explained in Section 2.1, this study employed the local stress at the characteristic distance from the crack tip as a crack propagation criterion according to the local fracture stress criterion. The crack propagation criterion employed in the application phase analyses is expressed as

$$\sigma_{\mathrm{F}} = \sigma_{yy}(r_{\mathrm{c}}) \tag{2-6}$$

where $\sigma_{yy}(r_{\mathrm{c}})$ is the local tensile stress at the characteristic distance r_{c} from the crack tip and σ_{F} is the called as the local fracture stress. σ_{F} was assumed to be constant in this study based on previous studies of the local fracture stress of brittle crack propagation and arrest behaviors in steels [24]. The validity of this assumption will be investigated in Chapter 3.

In this chapter, Section 2.3 proposes a method to evaluate local stress near the crack tip with accuracy and stability by the generation phase analyses, and Section 2.4 verifies the effectiveness of the proposed method in the application phase analyses.

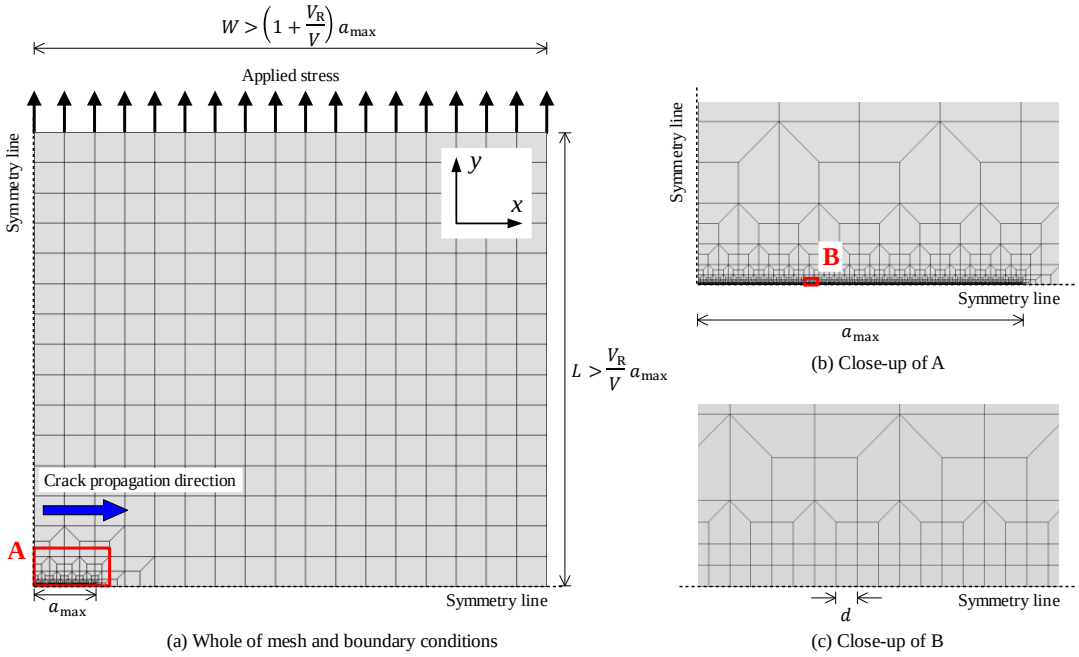

Fig. 2-3 Example of the employed finite element mesh and boundary conditions

2.3. Evaluation of local stress by generation phase

2.3.1. Numerical conditions and employed error indicators

This section verifies the evaluation accuracies of local stress near a propagating crack tip by generation phase analyses. As noted in Section 2.2, the time length for the release of the constraint of the crack tip node is determined by the mesh size and input crack velocity in this section.

The evaluated crack length was set as $a = 100$ mm. The finite initial cracks were not considered in the generation analyses. Thus, the crack length was zero before the dynamic analyses started. Two cases of the mesh size along the crack path were set as $d = 1$ mm and $d = 0.1$ mm, which are sufficiently smaller than a. Crack velocity is one of the most important factors in the verification. According to the Broberg's exact solution, the direction of the maximum circumferential stress is not coincident with the crack propagation direction when the crack velocity is more than approximately 2/3 times the Rayleigh wave velocity [25]. Therefore, the crack velocities evaluated in this verification were set as 20 levels in the range of $100\ \mathrm{m/s} \leq V \leq 2{,}000\ \mathrm{m/s}$ to ensure generality, considering the Rayleigh wave velocity of $V_R = 2980\ \mathrm{m/s}$ for employed material constants of $E = 206\ \mathrm{GPa}$ and $\rho = 7{,}800\ \mathrm{kg/m^3}$. As a result, the finite element model sizes in the cases of $V = 100\ \mathrm{m/s}$ and $V = 1{,}000\ \mathrm{m/s}$ are

$W = 3.58\,\mathrm{m}$ and $W = 0.640\,\mathrm{m}$, respectively. The number of nodes in the cases of ($V = 100\ \mathrm{m/s},\ d = 1\ \mathrm{mm}$), ($V = 1{,}000\ \mathrm{m/s},\ d = 1\ \mathrm{mm}$) and ($V = 100\ \mathrm{m/s},\ d = 0.1\ \mathrm{mm}$) are 3,072, 1,981 and 122,366, respectively. In addition, we assumed remotely applied stress as $\sigma_{yy}^{\infty} = 200$ MPa, even though it had no effect on the results because the media was elastic.

In order to verify the local stress evaluation accuracy, this chapter employs two types of error indicators. One is the norm of local stress fields against the exact solutions $H(j)$ and the other is the error of local stress at each node $\eta(x)$.

The first indicator, $H(j)$, represents the accuracy of the local stress field evaluation, which is expressed as

$$H(j) = \sqrt{\frac{1}{j}\sum_{i=1}^{j}\left(\frac{\sigma_{\mathrm{FEM}}(i\cdot d) - \sigma_{\mathrm{B}}(i\cdot d)}{\sigma_{\mathrm{FEM}}(i\cdot d)}\right)^{2}} \tag{2-7}$$

where $\sigma_{\mathrm{FEM}}(x)$ is the local stress of the node at a distance of x from the crack tip node in FEM. i means the number of nodes from the crack tip of the node of interest. In this research, the local stress was evaluated from the reaction force at each node, thus x is written as i multiplied by d. Further, $\sigma_{\mathrm{B}}(x)$ is the local stress at a distance of x from the crack tip in Broberg's exact solution. Broberg's solution provides the theoretical local tensile stress field in the vicinity of a dynamically propagating crack tip [25]. The detail of Broberg's exact solution is shown in the Appendix. j is the number of nodes that are used for the accuracy evaluation from the crack tip. j was set to 5 unless otherwise noted. Therefore, $H(j)$ denotes the absolute average difference of local stresses in FEM against Broberg's solutions for the first to the j-th nodes from the crack tip.

The second error indicator, $\eta(x)$, represents the normalized difference against Broberg's exact solution at each node, expressed as

$$\eta(x) = \frac{\sigma_{\mathrm{FEM}}(x) - \sigma_{\mathrm{B}}(x)}{\sigma_{\mathrm{B}}(x)} \tag{2-8}$$

Thus, $\eta(x)$ is an error indicator to express accuracy of the local stresses at each node although $H(j)$ is an error indicator of the averaged local stress fields.

2.3.2. Evaluation of conventional methods

There are two well-known nodal force release techniques that have been generally used for rapid crack propagation analyses [26,27] : instantaneous release, and linear release. Fig. 2-4 shows a schematic illustration of these two types of releases. Referring to Fig. 2-1, the initial reaction force of the crack tip node (equivalent to node A in Fig. 2-3) is F_0 at the beginning of the present step. The reaction force $F(t)$ immediately becomes zero in the case of the instantaneous release. On the other hand, $F(t)$ decreases linearly and becomes zero at the end of the present time step in the case of the linear release. Notwithstanding the fact that both of these release methods are often used [26,27], their accuracy of local stresses in the vicinity of rapid cracks has hardly been verified. This chapter starts from the verification of these two methods for two minimum mesh sizes from the perspective of local stress evaluation accuracy.

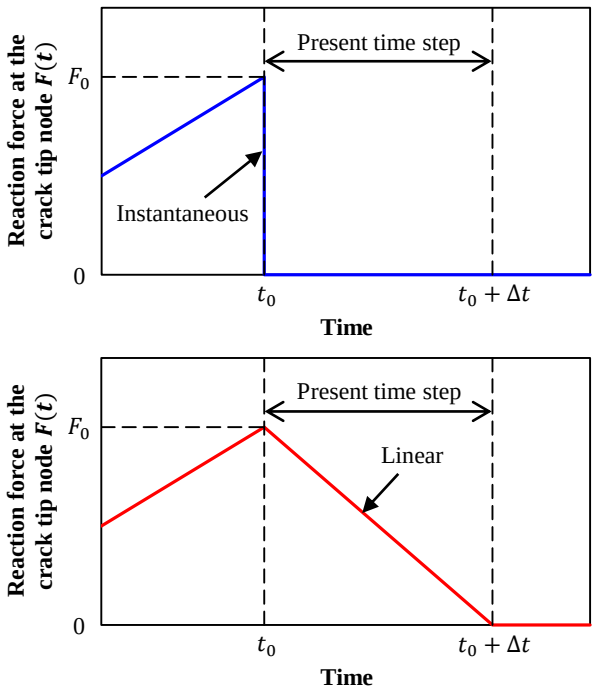

(a) Instantaneous release (b) Linear release

Fig. 2-4 Schematic illustrations of instantaneous and linear release methods

2.3.2.1. Conventional nodal force release methods for two minimum mesh sizes

At first, two mesh sizes, $d = 1\,\mathrm{mm}$ and $d = 0.1\,\mathrm{mm}$, were employed to investigate the accuracy of local stress evaluation when the conventional two nodal force release methods were used. To analyze the transition of the reaction force faithfully, the time steps determined by the crack velocity and mesh size were divided to 10 time increments.

Figure 2-5 shows $H(5)$ evaluated for two mesh sizes, i.e., $d = 1\,\mathrm{mm}$ and $d = 0.1\,\mathrm{mm}$, when the two release methods were employed respectively. Comparing the results of both mesh sizes, the small size mesh enhanced the accuracy of the linear release method especially in cases when the crack velocity was higher. However, the same trend was not found in instantaneous release. Although instantaneous release method was sometimes employed in rapid crack propagation analyses [26], the maximum error described as $H(5)$ of the instantaneous release method was 0.35. On the other hand, the linear release method provided more accurate results than the instantaneous release method as shown in Fig. 2-5. However, the error described as $H(5)$ is sometimes larger than 0.1 even in the linear release method.

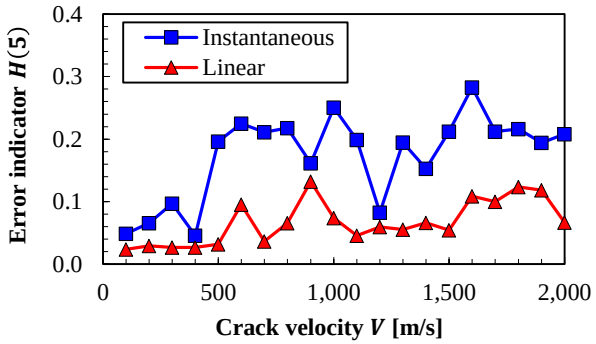

(a) $d = 1$ mm

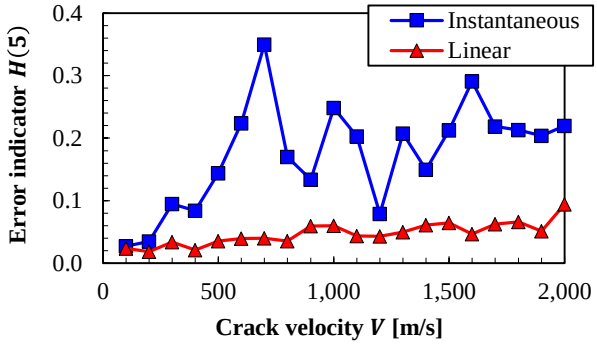

(b) $d = 0.1$ mm

Fig. 2-5 Local stress field errors with the instantaneous and linear release methods

The errors in the local stress were investigated by evaluating the error indicator of $\eta(x)$ against each mesh size and release method. The results of $\eta(x)$ in the front of crack tips in the cases of $V = 1{,}000$ m/s are shown in Fig. 2-6. The results clearly show that there were violent vibrations in local stress fields in the cases of all the mesh sizes and release methods. There was no significant difference in the values of $\eta(x)$ between the cases of the different mesh sizes. The ranges of the evaluated vibrations in the results of $\eta(x)$ were approximately 0.4 in the instantaneous release and 0.2 in the linear release, respectively. Similar vibrations were also observed under the other crack velocity conditions. There has been no serious problem in conventional studies to evaluate macroscopic fracture mechanics parameters, such as stress intensity factors and J-integral, even though the same methods were employed as node release techniques [3,26]. One of the most likely reasons is that the processes to evaluate such parameters plays a role to average the vibrations and to cancel the errors in local stress fields. However, local stress evaluation can be easily affected by the vibration and the absolute value of the local stress error $\eta(x)$. Considering that there was no significant difference of $\eta(x)$ and the degree of the

vibration between the cases of the different mesh sizes, to use fine meshes cannot sufficiently improve the local stress evaluation accuracy. Accordingly, the detailed space discretization is not effective to evaluate the local stress accurately.

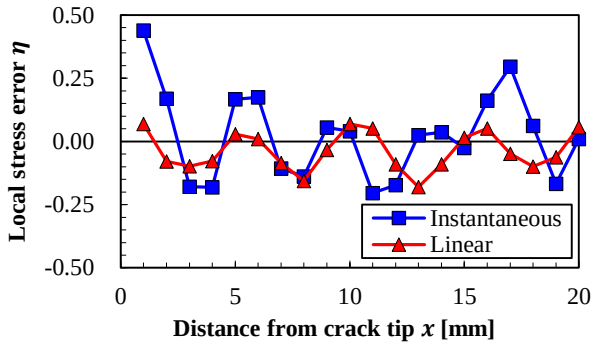

(a) $d = 1$ mm

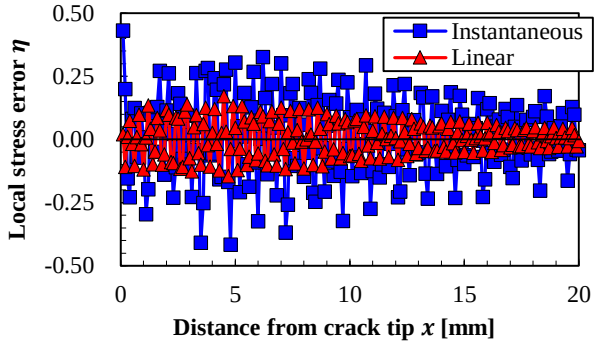

(b) $d = 0.1$ mm

Fig. 2-6 Local stress errors with the instantaneous and linear release methods ($V = 1{,}000$ m/s)

2.3.2.2. Time increment dependency

Because the analyses of this chapter employed implicit time integration method, the time increment of each step can be changed relatively freely. Generally, it is hopeful to use smaller time increment to accurately trace dynamic behaviors. Thus, the dependency of the local stress evaluation accuracy on the time increment was evaluated by dividing the time step Δt to more detailed time increments. Because no significant difference in the values of $\eta(x)$ between the

cases of the different mesh sizes was observed in Section 3.2.1, the minimum mesh size was set to 1 mm. According to the result of Section 2.3.2.1, the linear release was employed.

The number of division of time step Δt was set to 20, 40, and 80 in addition to 10, which was used in Section 2.3.2.1. Fig. 2-7 shows $\eta(x)$ of each number of time step division. Although the detailed values of $\eta(x)$ differed from one another depending on the number of time step division, the vibration of the local stress could not be suppressed in any number of time step division. In addition, we could not find any trend of local stress error against the number of time step division. The maximum values of the local stress errors of each number of time step division did not significantly differed. Thus, it can be concluded that the time discretization could not contribute to elimination of the vibration.

According to the analyses of Section 2.3.2.1 and Section 2.3.2.2, the improvement of the local stress evaluation accuracy could not be carried out by changing time and space discretization and a method to effectively suppress the vibrations is required to accurately simulate rapid crack propagations in the finite element analyses. The number of time step division were set to 10 and the minimum mesh size was 1 mm considering the above results in all analyses of this chapter.

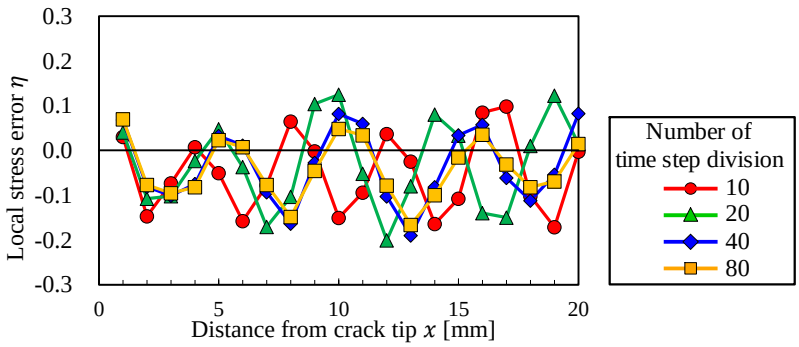

Fig. 2-7 Local stress error for the number of time step division ($d = 1$ mm, $V = 1{,}000$ m/s)

2.3.3. Optimization of nodal release path control

Nodal release path control is a method that was originally introduced to improve the accuracies of macroscopic fracture mechanics parameters, such as stress intensity factors and J-integral [28,29]. However, their studies have not systematically evaluated the effects of nodal release path control and, of course, the local stress accuracy was not considered. This section describes trials

for the optimization of the nodal release path control to suppress the vibration of local stress and improve the evaluation accuracy.

The nodal release path control in this study is defined by the nodal force at the crack tip node, as

$$F(t) = F_0 \left(1 - \frac{t - t_0}{\Delta t}\right)^n \tag{2-9}$$

where $(t - t_0)$ is time after the present step begins and Δt is the length of the present time step (see Fig. 2-1). F_0 is a reaction force at the crack tip node at the beginning of the time step, and n is an exponent to determine the nodal release path. When n approaches infinity, the nodal release path approaches the instantaneous release. When n is unity, i.e., $n = 1$, the nodal force release is coincident with the linear release. Some examples of nodal force paths with various values of n are shown in Fig. 2-8.

The error norm $H_n(j)$ is defined to optimize the nodal release path control, as

$$H_n(j) = \sqrt{\frac{1}{j}\sum_{i=1}^{j}\left(\frac{\sigma_{\mathrm{FEM}}(n, i \cdot d) - \sigma_{\mathrm{B}}(i \cdot d)}{\sigma_{\mathrm{B}}(i \cdot d)}\right)^2} \tag{2-10}$$

where j is the number of considered nodes ahead of the crack tip.

Figure 2-9 shows an example of the relationship between n and $H_n(j)$ obtained in the process of optimization ($V = 1{,}000$ m/s, $d = 1$ mm, $j = 5$). This graph shows that although the optimum value of n was determined, the sensitivity was low in the vicinity of the optimized value.

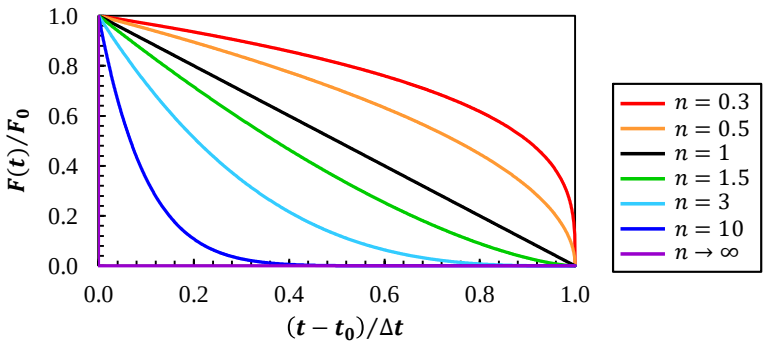

Fig. 2-8 Nodal force release paths

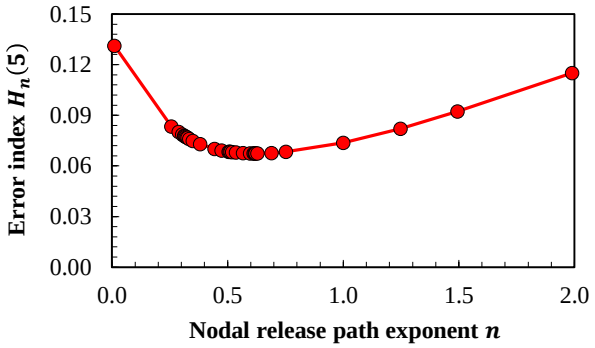

Fig. 2-9 Optimization process of nodal release path exponent n ($V = 1{,}000$ m/s, $d = 1$ mm, $j = 5$)

Figure 2-10 shows the optimized nodal release path n, which is denoted as n_{op}, for each crack velocity in the cases of $j = 5$ and $j = 20$. In addition, Fig. 2-11 shows the results of $H_n(j)$ with $n = n_{\mathrm{op}}$ compared with the linear release, i.e. $n = 1$. The results show that n_{op} is close to unity ($n_{\mathrm{op}} \approx 1$) in most cases, and therefore the results of $H_{n_{\mathrm{op}}}(j)$ with $n = n_{\mathrm{op}}$ did not deviate significantly from those with $n = 1$. The results also showed that no any clear trends of n_{op} relating to the crack velocity existed.

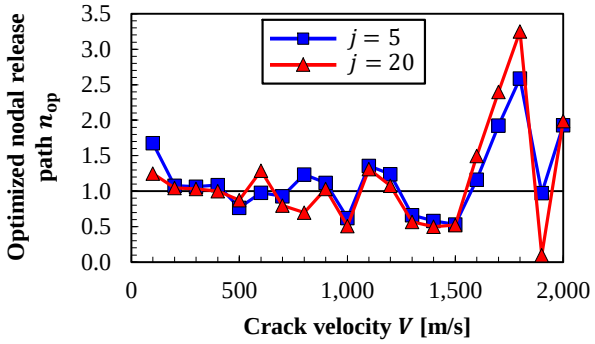

Fig. 2-10 Optimized nodal release path n_{op} for each crack velocity ($d = 1$ mm)

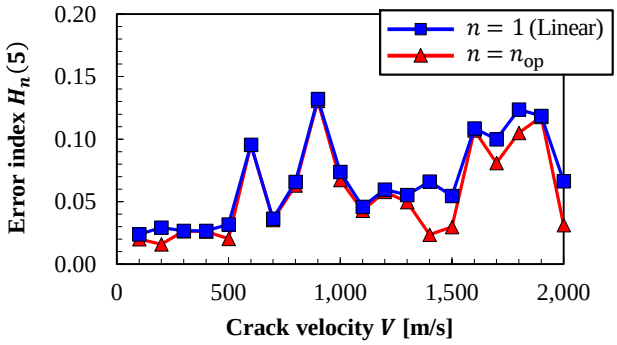

(a) $j = 5$

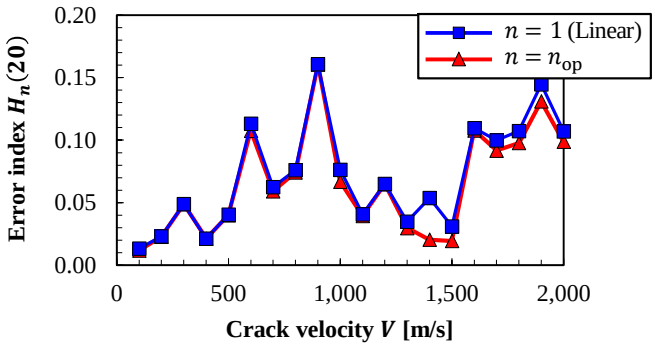

(b) $j = 20$

Fig. 2-11 Effect of optimized nodal release path for local stress field errors ($d = 1$ mm)

Figure 2-12 shows the results of the local stress error $\eta(x)$ with $n = 1$ and $n = n_{\mathrm{op}}$ in the case of $V = 1{,}000$ m/s. In these results, the numerical vibrations of local stress were found not only in the case of linear release $n = 1$, but also in the case of the optimized node release path control ($n = n_{\mathrm{op}}$). Similar vibrations were observed for any other crack velocity cases for which the nodal release path control was optimized. Therefore, although nodal release path control has frequently been employed to improve the accuracy of macroscopic parameters [3,29], the optimization of the nodal release path control cannot work as a effective method to suppress the vibration of local stress fields.

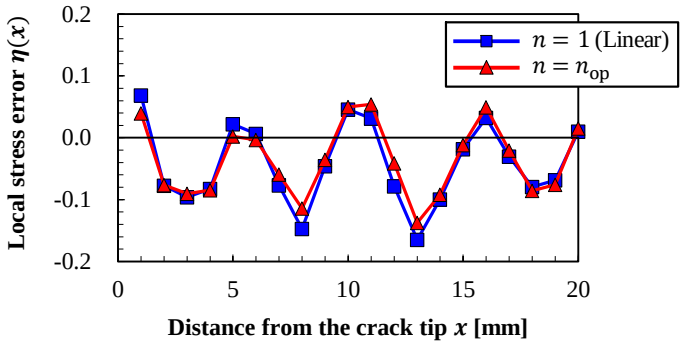

Fig. 2-12 Effect of optimized nodal release path for local stress errors ($V = 1{,}000$ m/s, $d = 1$ mm)

2.3.4. Application of artificial damping

In this section, artificial damping was applied to the rapid crack propagation analyses, as a second attempt to suppress the vibrations. Two types of artificial damping methods were evaluated, the viscous term of the HHT time integration method [20] and Rayleigh damping [30], which are some of the most popular methods generally employed in finite element analyses [31]. Considering the results in Section 2.3.3, the linear release method was used in the following analyses as the nodal release path control.

2.3.4.1. Viscous term in time integration (HHT method)

As noted in Section 2.2, the HHT method was employed as a time integration method in this study. Different from the Newmark method, an additional parameter α_{HHT} was introduced for selective reduction in the numerical vibration in the equation of motion of the HHT method. Therefore, we evaluate the ability of α_{HHT} to reduce numerical vibration of the local stress fields in the finite element analyses of rapid crack propagation. Other parameters, β_{HHT} and γ_{HHT}, followed the conditions shown in Eqs. (2-4) and (2-5) in Section 2.2.

Figure 2-13 shows the results of the local stress errors $\eta(x)$ of the analyses with various α_{HHT}. These results show only infinitesimal differences of $\eta(\mathrm{x})$ for each value of α_{HHT}. This indicated that the time integration process is not the cause of the vibration and other method should be examined to suppress the vibrations.

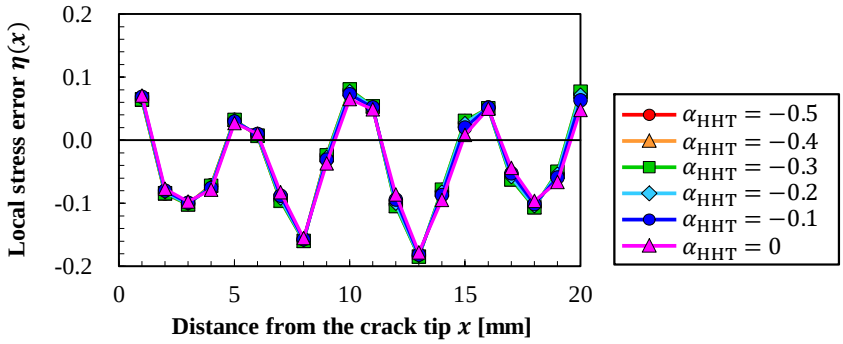

Fig. 2-13 Effect of artificial damping of the HHT method ($V = 1{,}000$ m/s, $d = 1$ mm)

2.3.4.2. Rayleigh damping

The Rayleigh damping method is one of most general artificial damping methods in finite element analyses. The damping matrix $\boldsymbol{C}$ in the Rayleigh damping method can be expressed as a linear sum of mass matrix $\boldsymbol{M}$ and stiffness matrix $\boldsymbol{K}$, as

$$\boldsymbol{C} = \alpha_{\mathrm{R}}\boldsymbol{M} + \beta_{\mathrm{R}}\boldsymbol{K} \tag{2-11}$$

where α_{R} and β_{R} are non-negative constants to represent the degrees of damping. These two parameters can be applied independently. Generally, the mass damping $\alpha_{\mathrm{R}}\boldsymbol{M}$ is effective to suppress the vibration with lower frequency and the stiffness damping β_{R} is effective to suppress the vibration with higher frequency [32].

The effect of mass damping was first evaluated. Fig. 2-14 shows the results of the local stress error $\eta(x)$ for various values of the mass damping degree α_{R} in the case of $V = 1{,}000$ m/s, $d = 1$ mm. The stiffness damping degree β_{R} was set as zero. In the case of $\alpha_{\mathrm{R}} = 100$, although the amplitude of the vibration of local stress becomes smaller compared to that in the case of $\alpha_{\mathrm{R}} = 0$, the vibration remains. In addition, in the case of $\alpha_{\mathrm{R}} = 10{,}000$, the local stress field was clearly underestimated and the state of the vibration does not greatly change compared to that in the case of $\alpha_{\mathrm{R}} = 100$. This means that the frequency of the vibration that the mass damping can reduce is significantly lower than that of the local stress fields in the rapid crack propagation analyses.

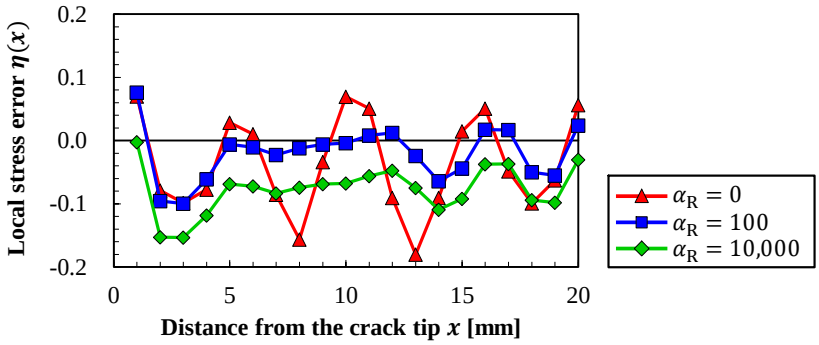

Fig. 2-14 Effect of mass damping of the Rayleigh damping method ($V = 1{,}000$ m/s, $d = 1$ mm, $\beta_R = 0$)

The effect of the stiffness damping was then evaluated. Figure 2-15 shows the results of local stress errors $\eta(x)$ for various values of the stiffness damping degree β_R in the case of $V = 1{,}000$ m/s, $d = 1$ mm. The results show that the stiffness damping can effectively suppress the numerical vibration in the local stress field in front of the crack tip and that it can determine the local stress with significantly good accuracy if β_R is appropriately defined, e.g., $\beta_R = 5 \times 10^{-7}$ in Fig. 2-15. On the other hand, if β_R is set excessively high, the local stress fields were overestimated even though the numerical vibration could be suppressed. One of the possible reasons of the overestimation was that the dynamic effect became smaller and the system in the analyses approached the static condition due to excessive stiffness damping. In other words, the local stress field approached those under slower crack velocity conditions when excessive stiffness damping occurs.

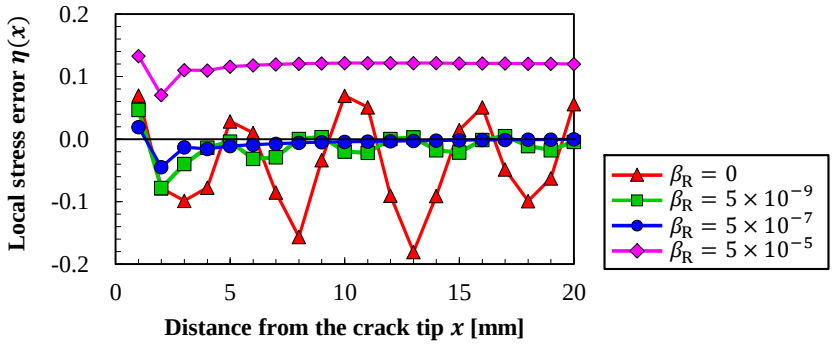

Fig. 2-15 Effect of sitiffness damping of the Rayleigh damping method ($V = 1{,}000$ m/s, $d = 1$ mm)

Figure 2-16 shows the results of the local stress field error $H(5)$ for each crack velocity with $\beta_R = 5 \times 10^{-7}$ for $d = 1$ mm and $\beta_R = 5 \times 10^{-8}$ for $d = 0.1$ mm, compared with those without Rayleigh damping. The results show that the stiffness damping provided stably accurate stress fields for all the crack velocities, which were much improved from those without the Rayleigh damping.

This introduction of the damping plays a role to reduce the kinetic energy of the analyses, although the kinetic energy was overestimated in the analyses without the damping because there were a lot of excess vibrations of nodes. Thus, the dissipated energy was underestimated in the analyses without damping. On the other hand, the appropriate damping eliminates the excess vibration and dissipates the appropriate amount of the energy along crack propagation. Therefore, to introduce the damping can contribute to appropriate energy balance of the crack propagation analyses in addition to accurate evaluation of the local stresses in finite element method.

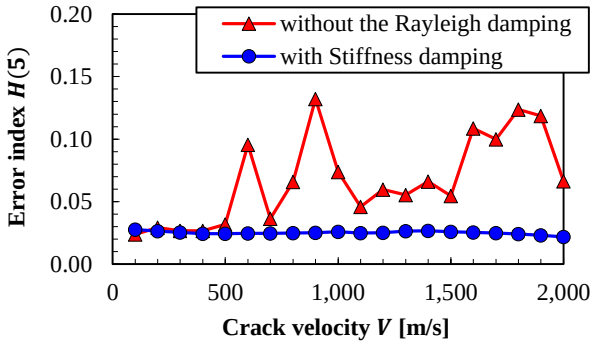

(a) $d = 1$ mm ($\beta_{\mathrm{R}} = 5 \times 10^{-7}$)

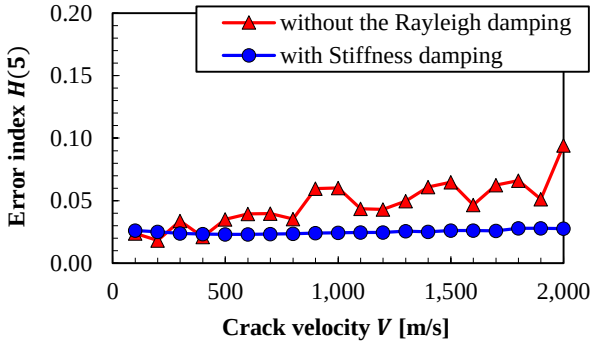

(b) $d = 0.1$ mm ($\beta_{\mathrm{R}} = 5 \times 10^{-8}$)

Fig. 2-16 Local stress field errors with sitiffness damping ($j = 5$)

Considering application phase analyses, the local stress errors $\eta(x)$ at the specified length from the crack tip was evaluated. Fig. 2-17 shows the local stress errors $\eta(x)$ at the third node from the crack tip, i.e. $x = 3d$, with stiffness damping, compared with those without Rayleigh damping. The results without Rayleigh damping showed that the accuracies of local stress fields were unstable and the ranges of the errors were $-0.17 \leq \eta(3d) \leq 0.10$ for $d = 1$ mm and $-0.10 \leq \eta(3d) \leq 0.14$ for $d = 0.1$ mm. On the other hand, the results with the stiffness damping showed that the accuracies and stability of the local stress fields were significantly improved such that the ranges of errors were $-0.019 \leq \eta(3d) \leq -0.010$ for $d = 1$ mm and $-0.020 \leq \eta(3d) \leq -0.011$ for $d = 0.1$ mm.

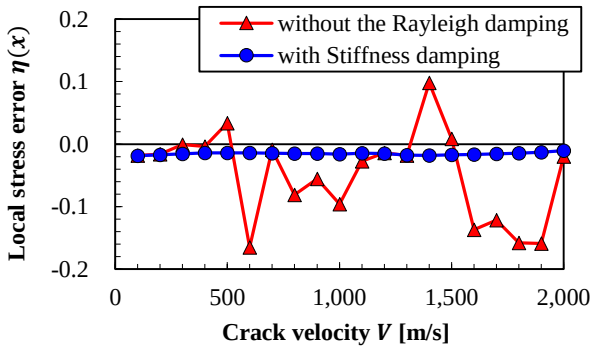

(a) $d = 1$ mm ($\beta_{\mathrm{R}} = 5 \times 10^{-7}$)

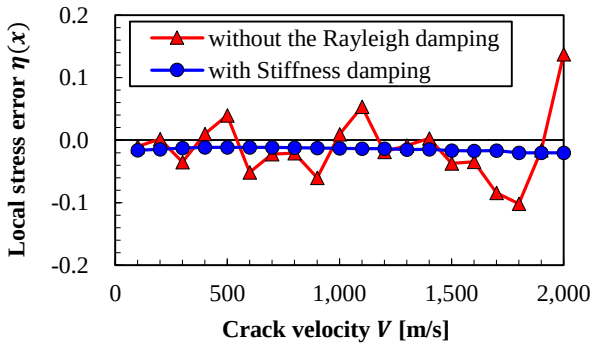

(b) $d = 0.1$ mm ($\beta_{\mathrm{R}} = 5 \times 10^{-8}$)

Fig. 2-17 Local stress errors at the distance of $x = 3d$ from the crack tip with stiffness damping

According to the above verification, stiffness damping to the Rayleigh damping method was applied to the application phase analysis with the linear release of nodal force as a suitable method to simulate rapid crack propagation by the finite element method with accuracy and stability. The appropriate determination of the stiffness damping degree β_{R} is discussed in Section 2.5.

2.4. Application phase analyses

In Section 2.3, it was shown that the application of stiffness damping in the Rayleigh damping method as a suitable method to simulate rapid crack propagation by the finite element method. This section verifies the effectiveness of the proposed method by presenting application phase analyses based on the local fracture stress criterion, which is one of the most promising concepts to explain brittle crack propagation and arrest behavior in steel.

In the application phase analysis of rapid crack propagation, the fracture criterion is an input parameter and crack velocity is an output parameter. In particular, based on the local fracture stress criterion, the local fracture stress is a fracture criterion in application phase analyses in this study as explained in Section 2.2. To perform dynamic application phase analyses, it is essential to decide a crack velocity to satisfy the fracture criterion. Most of the application phase analyses for rapid crack propagation based on macroscopic fracture mechanics parameters have been performed by using the instantaneous release method, because the crack velocity can be determined explicitly [33]. However, the instantaneous release method cannot be employed due to its extremely low accuracy to evaluate the local stress according to the results in Section 3.2.1. In order to apply the proposed method, which is a combination of the linear release of nodal force and stiffness damping in the Rayleigh damping method, an implicit calculation algorithm was developed by using a combination of the bisection and Newton methods. Based on the local fracture stress criterion, the developed algorithm carried out iterative calculations to determine the crack velocity V which satisfies the equation expressed as

$$\sigma_{yy}(V, r_{\mathrm{c}}) - \sigma_{\mathrm{F}} = 0 \tag{2-12}$$

where $\sigma_{yy}(V, r_{\mathrm{c}})$ is the local tensile stress at the characteristic distance r_{c} from the crack tip depending on the crack velocity V, σ_{F} is the local fracture stress, and r_{c} and σ_{F} are given as material constants.

Figure 2-18 shows a flowchart of the application phase analysis performed in this study. Iterative calculations are performed to search the crack velocity V to satisfy the fracture condition of Eq. (2-12) with the tolerance error set as 0.1% considering the accuracy limitation of the employed solver [16]. The iterative calculations are carried out until the crack velocity to satisfy Eq. (2-12) is found. When Eq. (2-12) is satisfied, the constraint of the crack tip node is released and the crack length is updated to start the next step.

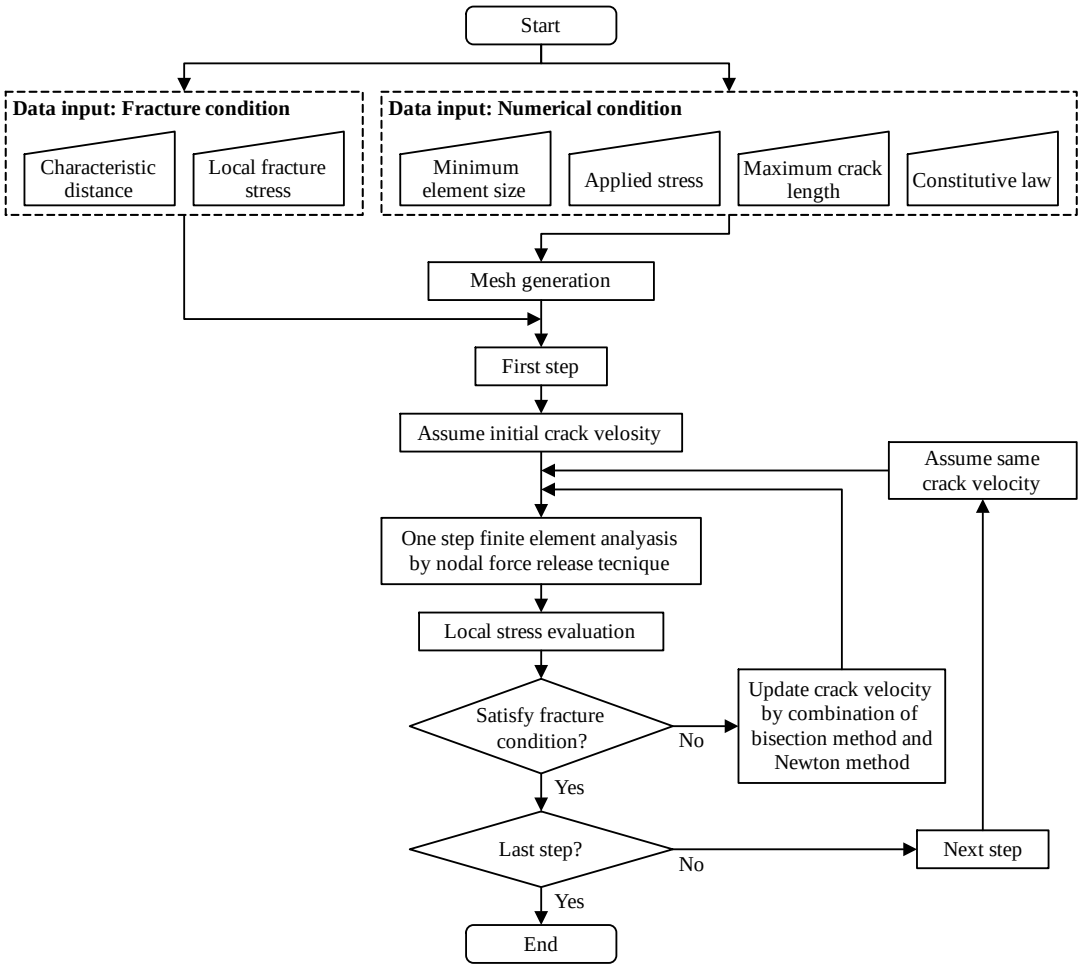

Fig. 2-18 Flowchart of the application-phase analysis

The calculation conditions for this verification are presented as follows. The range of the evaluated crack length was set as $35\ \text{mm} \leq a \leq 100\ \text{mm}$. The mesh size was set as $d = 0.1\ \text{mm}$, such that the total number of steps is 651. The remotely applied stress and the fracture stress were set as $\sigma_{yy}^{\infty} = 200\ \text{MPa}$ and $\sigma_{\text{F}} = 1{,}400\ \text{MPa}$, respectively. The characteristic length r_{c} was set as $r_{\text{c}} = 0.3\ \text{mm}$ considering previous numerical models based on the local fracture stress criterion [24]. This setting of r_{c} corresponds to the third node from the crack tip, i.e. $r_{\text{c}} = 3d$. Using the conditions of σ_{yy}^{∞}, σ_{F} and r_{c}, the exact solution of the history of the crack velocity V can be calculated from Broberg's solution for the stress field near the dynamically propagating crack tip described in Appendix. Two values of the stiffness damping degrees were used to verify the effect of the stiffness damping on the Rayleigh damping: as $\beta_{\text{R}} = 0$ (without Rayleigh damping) and $\beta_{\text{R}} = 5 \times 10^{-8}$.

The application phase analyses were performed under the above conditions. The results of the history of the crack velocity V obtained in the application phase analyses are shown in Fig. 2-19 with the crack velocity history calculated from Broberg's exact solution. Additionally, the errors of the crack velocity from the exact solution are shown in Fig. 2-20. In the analysis without Rayleigh damping, the predicted crack velocity had a significant vibration and deviated from the exact solutions shortly after the analysis started. Furthermore, the analysis terminated when the crack length reached around $a = 50$ mm. At the time, the search range of the crack velocity to satisfy the local fracture stress exceeded the Rayleigh wave velocity. This result indicated that the problem of the application phase analysis without Rayleigh damping is an impossibility of execution rather than a lack of accuracy.

On the other hand, the analysis with stiffness damping successfully duplicated the exact crack velocity history and completed the calculation to the final crack length of $a = 100$ mm, even though there was some vibration of the crack velocity. The average and maximum errors of the crack velocity V against the exact solutions in the range of the present analysis were 18 m/s and 60 m/s, respectively. Therefore, the method proposed to apply stiffness damping in the Rayleigh damping method has the potential to be the basis of rapid crack propagation analysis by the finite element method.

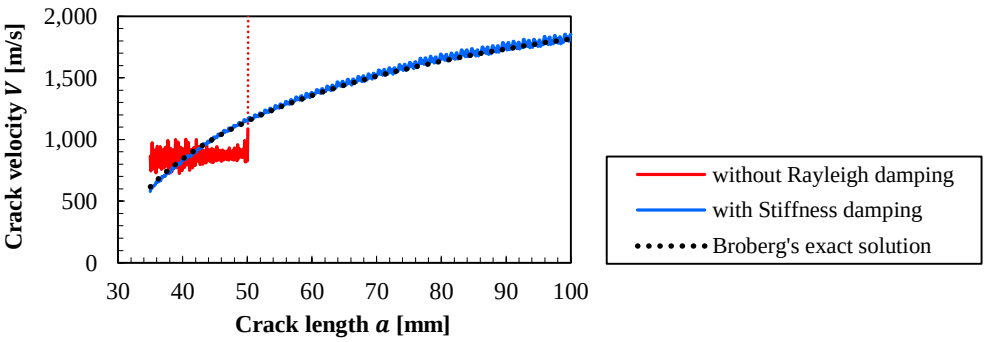

Fig. 2-19 Crack velocity history predicted by the application-phase analyses

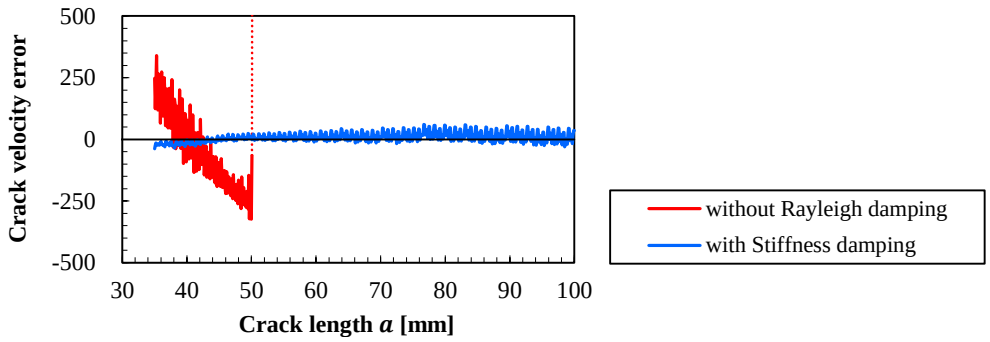

Fig. 2-20 Crack velocity differences against Broberg's solutions

2.5. Discussion

2.5.1. Generation phase analyses

As shown in Section 2.3.4, the numerical vibration could be effectively suppressed by applying stiffness damping in the generation phase analyses. On the other hand, an excessive degree of stiffness damping caused overestimation of the local stress fields even though the vibration was suppressed. Therefore, it is necessary to determine an appropriate degree of stiffness damping to accurately evaluate the local stress.

The damping ratio of stiffness damping is generally determined from the frequency of the vibrations [32]. Because the numerical vibrations in the rapid crack propagation analyses by the finite element method are caused by the dilatational elastic wave, the frequency is supposed to be determined by the mesh size and the elastic wave velocity related to Young's modulus E and density ρ. Therefore, we conducted a series of analyses with the numerical conditions of various values of Young's modulus, density, and mesh sizes and found the recommended coefficient of stiffness damping β_{rec}, expressed as

$$\beta_{\mathrm{rec}} = 2.57 \times d\ [\mathrm{m}] \times \sqrt{\frac{\rho\ [\mathrm{kg/m^3}]}{E\ [\mathrm{Pa}]}} \tag{2-13}$$

where E is Young's modulus, ρ is the density, d is the minimum element size along the crack path, and $\sqrt{E/\rho}$ is the one-dimensional elastic stress wave velocity. The recommended coefficient of the stiffness damping β_{rec} provides the equivalent results of the case of $\beta_{\mathrm{R}} = 5.0 \times 10^{-7}$ in Fig. 2-15 under any conditions of Young's modulus, density and mesh size. The

Rayleigh damping has the characteristic that the damping ratio is higher when the frequency is higher in the case of constant β_R [30]. Therefore, generally, the value of β_R required to suppress the vibration with higher frequency is lower than that with lower frequency. The trend of Eq. (2-13) that β_{rec} is larger when the element size is larger or the elastic wave velocity is slower corresponds to this general characteristic of Rayleigh damping.

This disseration could not conduct the verification of local tensile stress for elasto-plastic problems because there were no theoretical solutions of the local stresses near the dynamic crack tip in elasto-plastic materials. However, the proposed method can be considered to improve the accuracy of the local tensile stress evaluation in the elasto-plastic problem even though further investigation may be needed. This is because the deterioration of the accuracy is caused by the elastic vibration of the nodes of interest. This mechanism is considered to also work in elasto-plastic problem. Therefore, considering that the brittle crack propagation includes only small plastic region, the present investigation will be applied to the elasto-plastic problem

2.5.2. Applicaiton phase analyses

Section 2.4 shows that the application phase analysis with the stiffness damping successfully predicted the history of the crack velocity. On the other hand, the analysis without the Rayleigh damping failed when the crack velocity reached approximatedly 1,000m/s.

It means that it is impossible to simulate rapid crack propagation without Rayleigh damping. Fig. 2-21 shows the local stresses at 0.3 mm from the crack tip under various crack velocities obtained by Broberg's exact solutions, the analyses without Rayleigh damping, and the analyses with stiffness damping. According to Broberg's exact solutions, the local stress decreases monotonically when the crack velocity becomes higher. However, in the results in case which Rayleigh damping was not applied to, the local stress did not decrease monotonically. On the other hand, the results with the stiffness damping showed good agreement with Broberg's exact solutions. The reason may be the stability of the numerical results against the crack velocity as shown in Fig. 2-17. Consequently, stiffness damping effectively contributes to simulate rapid crack propagation in finite element analyses.

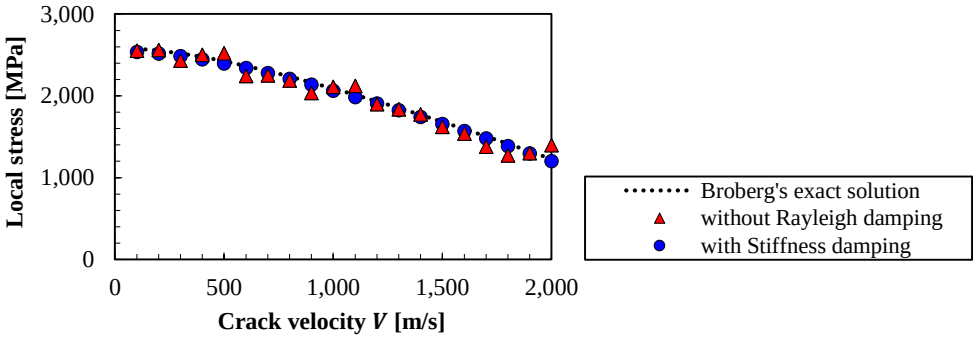

Fig. 2-21 Local stresses against crack velocity (crack length is 100 mm and $d = 0.1$ mm)

2.6. Conclusion

This chapter involved the strict verification of the finite element analyses with nodal force release technique to simulate rapid crack propagation based on the local stress criterion.

Verification of the accuracy and stability of local stress evaluation was first performed by generation phase analyses. The verification results of two conventional nodal force release techniques, instantaneous and linear release, showed that there were large errors in the local stress evaluated by conventional methods. These errors were caused by remarkable vibration in local stress fields. In addition, although nodal release path control was conducted to suppress the vibration for accurate local stress evaluation, the results of the optimized paths were close to those of linear release, and the vibration in the local stress fields could not be sufficiently suppressed by this optimization alone. Two types of artificial damping, the viscous term of the HHT time integration method and Rayleigh damping, were then applied to the rapid crack propagation analyses to improve the accuracies of local stress. The results showed that the viscous term could hardly influence the local stress. Mass damping of the Rayleigh damping could not suppress the vibration. On the other hand, the appropriate degree of stiffness damping of the Rayleigh damping successfully provided stably accurate stress fields for all the crack velocities. Consequently, this chapter proposes the application of stiffness damping in the Rayleigh damping method with the linear release of nodal force as a suitable method to simulate rapid crack propagation by the finite element method with accuracy and stability when the local stress is evaluated.

The proposed method was then verified by application phase analyses based on the local fracture stress criterion. In the analysis without Rayleigh damping, the predicted crack velocity vibrated significantly and deviated from the exact solutions shortly after the analysis started. Furthermore, the analysis terminated prematurely due to failure to find an appropriate crack velocity. This result

indicated that the problem of the application phase analysis without Rayleigh damping is an impossibility of execution as opposed to a lack of accuracy. On the other hand, analysis with the stiffness damping successfully duplicated the exact solution of crack velocity history.

Based on the above results, it is concluded that the proposed method to apply stiffness damping of the Rayleigh damping method with linear nodal force release has the potential to form the basis of rapid crack propagation from the perspective of the local fracture stress criterion analysis by the finite element method. Considering the accuracy of the generation phase analysis when the mesh is fine enough, the conventional method can be employed in the highly fine mesh in generation phase analysis. However, the proposed method is essentially needed to conduct the accurate application phase analyses as shown in Section 2.4. It is expected to predict crack arrest events in complicated circumstances such as crack arrestors by extending the proposed application phase analyses based on the local fracture stress criterion.

Appendix

The exact solution of the local tensile stress field in front of a rapidly propagating crack tip derived by Broberg [25] is expressed as

$$\begin{aligned}
&\frac{\sigma_{\mathrm{B}}(x)-\sigma_y^{\infty}}{\sigma_y^{\infty}} \\
&= -\frac{1}{\beta^2 g_1(\beta)}\Bigg\{\beta^2[4k^4+(1-4k^2)\beta^2]\boldsymbol{F}(\kappa_1,q_1) \\
&\qquad -[8k^4-4k^2(1+k^2)\beta^2+\beta^4]\boldsymbol{E}(\kappa_1,q_1) \\
&+[8k^4-4k^2(1+k^2)\beta^2+\beta^4-4k^4\beta^2(1-\beta^2)\xi^2]\frac{\sqrt{1-\frac{1}{\xi^2}}}{\sqrt{1-\beta^2\xi^2}}\Bigg\} \\
&+H_0\left(\xi-\frac{1}{k}\right)\frac{4k^2(1-\beta^2)}{\beta^2 g_1(\beta)}\Bigg\{\beta^2\boldsymbol{F}(\kappa_2,q_2)-2k^2\boldsymbol{E}(\kappa_2,q_2) \\
&\qquad +k^2(2-\beta^2\xi^2)\frac{\sqrt{1-\frac{1}{k^2\xi^2}}}{\sqrt{1-\beta^2\xi^2}}\Bigg\}
\end{aligned} \tag{2-A1}$$

$$\beta = \frac{V}{V_{\mathrm{p}}} \tag{2-A2}$$

$$\xi = \frac{V_{\mathrm{p}} a}{x + a} \tag{2-A3}$$

$$k = \sqrt{\frac{1 - 2\nu}{2\,(1 - \nu)}} \tag{2-A4}$$

$$V_{\mathrm{p}} = \sqrt{\frac{1 - \nu}{(1 + \nu)(1 - 2\nu)} \frac{E}{\rho}} \tag{2-A5}$$

$$\kappa_1 = \sin^{-1} \frac{\sqrt{1 - 1/\xi^2}}{\sqrt{1 - \beta^2}} \tag{2A6}$$

$$\kappa_2 = \sin^{-1} \frac{\sqrt{k^2 - 1/\xi^2}}{\sqrt{k^2 - \beta^2}} \tag{2-A7}$$

$$q_1 = \sqrt{1 - \beta^2} \tag{2-A8}$$

$$q_2 = \sqrt{1 - \beta^2/k^2} \tag{2-A9}$$

$$H_0(s) = \begin{cases} 0 & s \leq 0 \\ 1 & s > 0 \end{cases} \tag{2-A10}$$

$$g_1(\beta) = -4(1-\beta^2)k^2\,\overline{\boldsymbol{K}}\left(\sqrt{1-\frac{\beta^2}{k^2}}\right) + \left(4k^4+\beta^2(1-4k^2)\right)\overline{\boldsymbol{K}}\left(\sqrt{1-\beta^2}\right)$$
$$+\frac{8(1-\beta^2)k^4}{\beta^2}\overline{\boldsymbol{E}}\left(\sqrt{1-\frac{\beta^2}{k^2}}\right) \tag{2-A11}$$
$$-\frac{(\beta^4+8k^4-4\beta^2(k^2+1)k^2)}{\beta^2}\overline{\boldsymbol{E}}\left(\sqrt{1-\beta^2}\right)$$

where σ_y^{∞} is the remotely applied tensile stress, V is the crack velocity, a is the crack length, x is the distance from the crack tip, E is Young's modulus, ν is Poisson's ratio, ρ is the density, and V_{p} represents the P-wave velocity. $\boldsymbol{F}$ and $\boldsymbol{E}$ are elliptic integrals of the first and second kind, respectively. $\overline{\boldsymbol{K}}$ and $\overline{\boldsymbol{E}}$ are complete elliptic integrals of the first and second kind, respectively.

Reference

[1] B. Prabel, S. Marie, A. Combescure, Using the X-FEM method to model the dynamic propagation and arrest of cleavage cracks in ferritic steel, Eng. Fract. Mech. 75 (2008) 2984–3009. doi:10.1016/j.engfracmech.2008.01.008.

[2] C. Berdin, M. Hajjaj, P. Bompard, S. Bugat, Local approach to fracture for cleavage crack arrest prediction, Eng. Fract. Mech. 75 (2008) 3264–3275. doi:10.1016/j.engfracmech.2007.08.013.

[3] K. Kishimoto, S. Aoki, M. Sakata, Dynamic Stress Intensity Factors Using J-Integral and Finite Element Method, Eng. Fract. Mech. 13 (1980) 387–394. doi:10.1016/0013-7944(80)90067-3.

[4] J. Li, Z.S. Khodaei, M.H. Aliabadi, Dynamic dual boundary element analyses for cracked Mindlin plates, Int. J. Solids Struct. 152–153 (2018) 248–260. doi:10.1016/j.ijsolstr.2018.06.033.

[5] Y.M. Chen, Numerical Solutions of Three Dimensional Dynamic Crack Problems and Simulation Finite Difference Method, Eng. Fract. Mech. 10 (1978) 699–708.

[6] A. Coré, J.-B. Kopp, J. Girardot, P. Viot, Dynamic energy release rate evaluation of rapid crack propagation in discrete element analysis, Int. J. Fract. (2018). doi:10.1007/s10704-018-0314-7.

[7] Y.D. Ha, F. Bobaru, Studies of dynamic crack propagation and crack branching with peridynamics, Int. J. Fract. 162 (2010) 229–244. doi:10.1007/s10704-010-9442-4.

[8] A. Khosravifard, M.R. Hematiyan, T.Q. Bui, T.V. Do, Accurate and efficient analysis of stationary and propagating crack problems by meshless methods, Theor. Appl. Fract. Mech. 87 (2017) 21–34. doi:10.1016/j.tafmec.2016.10.004.

[9] D. Grégoire, H. Maigre, J. Réthoré, A. Combescure, Dynamic crack propagation under mixed-mode loading - Comparison between experiments and X-FEM simulations, Int. J. Solids Struct. 44 (2007) 6517–6534. doi:10.1016/j.ijsolstr.2007.02.044.

[10] M. Hori, K. Oguni, H. Sakaguchi, Proposal of FEM implemented with particle discretization for analysis of failure phenomena, J. Mech. Phys. Solids. 53 (2005) 681–703. doi:10.1016/j.jmps.2004.08.005.
[11] S. Salih, K. Davey, Z. Zou, Rate-dependent elastic and elasto-plastic cohesive zone models for dynamic crack propagation, Int. J. Solids Struct. 90 (2015) 95–115. doi:10.1016/j.ijsolstr.2016.04.002.
[12] N. Valoroso, G. Debruyne, J. Laverne, A cohesive zone model with rate-sensitivity for fast crack propagation, Mech. Res. Commun. 58 (2014) 82–87. doi:10.1016/j.mechrescom.2013.12.008.
[13] A. Pandolfi, P.R. Guduru, M. Ortiz, A.J. Rosakis, Three dimensional cohesive-element analysis and experiments of dynamic fracture in C300 steel, Int. J. Solids Struct. 37 (2000) 3733–3760. doi:10.1016/S0020-7683(99)00155-9.
[14] C. Berdin, 3D modeling of cleavage crack arrest with a stress criterion, Eng. Fract. Mech. 90 (2012) 161–171. doi:10.1016/j.engfracmech.2012.05.002.
[15] A. Bousquet, S. Marie, P. Bompard, Propagation and arrest of cleavage cracks in a nuclear pressure vessel steel, Comput. Mater. Sci. 64 (2012) 17–21. doi:10.1016/j.commatsci.2012.04.026.
[16] Dassault Systems, SIMULA Abaqus Analysis User's Manual, (2014).
[17] M. Kuna, Finite Elements in Fracture Mechanics Theory-Numerics-Applications, Springer, 2010.
[18] T.L. Anderson, Fracture Mechanics Fundamentals and Applircations 3rd ed., CRC Press, 2005.
[19] S.K. Chan, I.S. Tuba, W.K. Wilson, On the finite element method in linear fracture mechanics, Eng. Fract. Mech. 2 (1970) 1–17. doi:10.1016/0013-7944(70)90026-3.
[20] T.J.R. Hughes, The Finite Element Method Linear Static and Dynamic Finite Element Analysis, Prentice-Hall, 1987.
[21] E. Elmukashfi, M. Kroon, Numerical analysis of dynamic crack propagation in rubber, Int. J. Fract. (2012) 163–178. doi:10.1007/s10704-012-9761-8.
[22] A. Czekanski, N. El-Abbasi, S.A. Meguid, Optimal time integration parameters for elastodynamic contact problems, Commun. Numer. Methods Eng. 17 (2001) 379–384. doi:10.1002/cnm.411.
[23] T. Nishioka, S.N. Atluri, Numerical analysis of dynamic crack propagation: Generation and prediction studies, Eng. Fract. Mech. 16 (1982) 303–332. doi:10.1016/0013-7944(82)90111-4.
[24] K. Shibanuma, F. Yanagimoto, T. Namegawa, K. Suzuki, S. Aihara, Brittle crack propagation/arrest behavior in steel plate - Part I: Model formulation, Eng. Fract. Mech. 162 (2016) 324–340. doi:10.1016/j.engfracmech.2016.02.054.
[25] K.B. Broberg, Cracks and Fracture, Academic Press, 1999.
[26] M. Hajjaj, C. Berdin, P. Bompard, S. Bugat, Analyses of cleavage crack arrest experiments: influence of specimen vibration, Eng. Fract. Mech. 75 (2008) 1156–1170. doi:10.1016/j.engfracmech.2007.04.021.
[27] J.A. Joyce, R.E. Link, C. Roe, J.C. Sobotka, Dynamic and static characterization of compact crack arrest tests of navy and nuclear steels, Eng. Fract. Mech. 77 (2010) 337–347. doi:10.1016/j.engfracmech.2009.04.006.
[28] S. Aoki, K. Kishimoto, M. Sakata, Finite element computation of dynamic stress intensity factor for a rapidly propagating crack using J-integral, Comput. Mech. 2 (1987) 54–62.
[29] A.S. Kobayashi, K. Seo, J.Y. Jou, Y. Urabe, A Dynamic Analysis of Modified Compact-tension Specimens Using Homalite-100 and Polycarbonate Plates, Exp. Mech. (1979) 73–79.
[30] D.R.A. Mohammad, N.U. Khan, V. Ramamurti, On the role of rayleigh damping, J.

Sould Vib. 185 (1995) 207–218.
[31] J.F. Hall, Problems encountered from the use (or misuse) of Rayleigh damping, Earthq. Eng. Struct. Dyn. 35 (2006) 525–545. doi:10.1002/eqe.541.
[32] M.N. Fardis, Seismic Design, Assessment and Retrofitting of Concrete Buildings, Springer, 2009.
[33] M. Enderlein, A. Ricoeur, M. Kuna, Finite element techniques for dynamic crack analysis in piezoelectrics, Int. J. Fract. 134 (2005) 191–208. doi:10.1007/s10704-005-0522-9.
[34] K. Kishi, K. Shibanuma, F. Yanagimoto, K. Suzuki, Development of dynamic mesh superposition method for local tensile stress evaluation, in: 22nd Eur. Conf. Fract., 2018.

Chapter 3 Local tensile stress in the vicinity of the propagating crack tip

3.1. Introduction

Brittle crack propagation in steel can be expressed as cleavage crack propagation accompanying with unbroken shear lip formation. A cleavage crack generally propagates around the thickness center, and the unbroken shear lip forms the region where the cleavage crack cannot continue to propagate. The local fracture stress corresponds to the critical condition of only cleavage crack propagation and resistance due to plastic work of unbroken shear lips are not included in the local fracture stress. Therefore, to appropriately evaluate local fracture stress, other effect except the cleavage crack propagation has to be excluded.

Based on the local fracture stress criterion, the material resistance against cleavage crack propagation is written as follows:

$$\sigma_{\mathrm{F}} = \sigma_{yy}(r_{\mathrm{c}}) \tag{3-1}$$

where, σ_{F} is the local fracture stress, and $\sigma_{yy}(r_{\mathrm{c}})$ is the local tensile stress at a distance r_{c}, called the characteristic distance, from the crack tip. r_{c} was set to values between 0.1-0.3 mm in past studies [1–6]. The local fracture stress can be obtained from the finite element analyses which reproduce experimentally measured crack behaviors such as the crack velocity and crack front shape, in addition to the experimental conditions. As noted in Chapter 1, although previous studies tried to evaluate the local fracture stress by the above procedure, their evaluations did not consist with each other [3–6], and the assumption employed in the numerical models based on the local fracture stress [1,7].

One of the main reasons for this inconsistency is that, in past experimental studies conducted to

evaluate the local fracture stress, cleavage crack as a two dimensional (2D) problem, and three dimensional (3D) effects of the phenomenon have been ignored. Cleavage crack propagation in steels is strongly influenced by 3D effects, such as crack front curvatures and shear lip formations due to relaxation of plastic constraint near the surfaces [1,8]. Therefore, experimental 3D effects, such as crack front tunneling and formation of the shear lip, must be input to analyze crack propagation accurately using numerical methods. In addition, although the previous studies employed crack gauges and high speed camera to measure crack velocities, these method observes only the crack behavior emerging on the surface and therefore could not evaluate the crack velocity accurately. Nevertheless, previous studies ignored these effects and have analyzed crack propagation as a 2D problem [2,4,5]. Thus, as noted in the top of this chapter, because 3D effects change stress states significantly, local tensile stresses were not evaluated appropriately in these previous studies.

As this background discussion makes clear, it is necessary to evaluate local fracture stresses more accurately to refine the local fracture stress criterion. However, 3D effects during crack propagation in steels are difficult to observe experimentally. Therefore, this chapter presents the first evaluation of the local tensile stress in steel by means of a combination of experiments and finite element analyses of cleavage crack propagation using side-grooved specimens to minimize 3D effects. The flow of this research is presented in Fig. 3-1. This research was divided to four parts: Material preparation explained in Section 3.2, Preparation of specimen in Section 3.3, Implementation of the experiments in Section 3.3, and analyses of experiments explained in Section 3.4. The evaluations were conducted at multiple temperatures and applied stress levels to assess the validity of the local fracture stress criterion and characteristics of the local fracture stress.

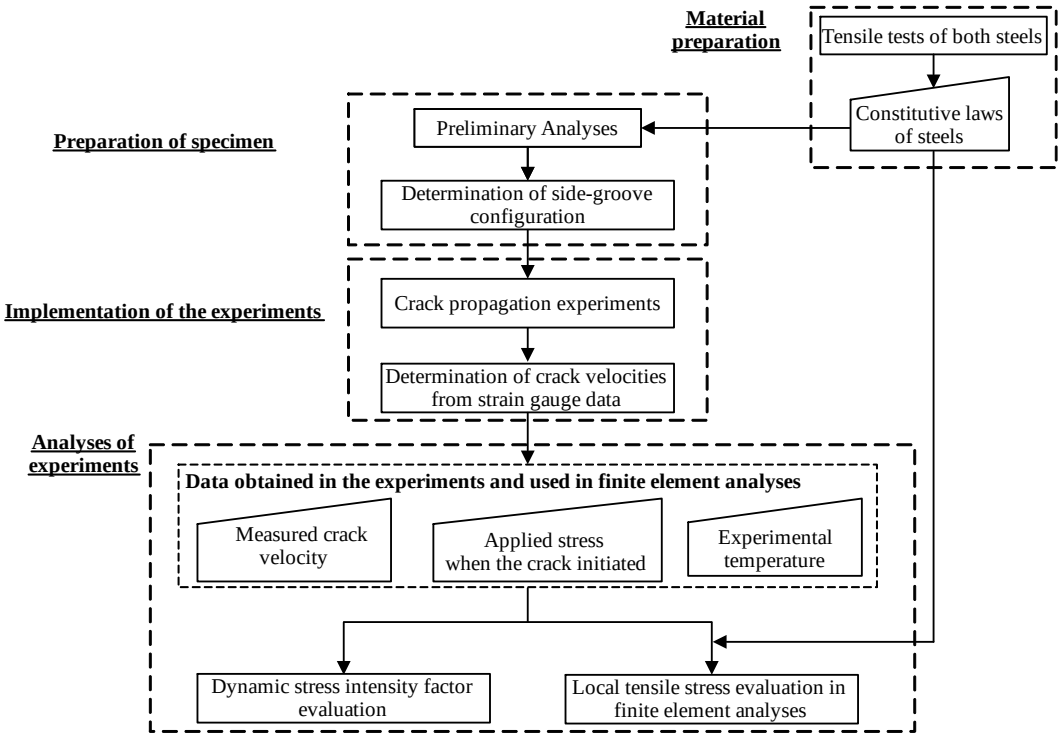

Fig. 3-1 Research flow of this chapter

3.2. Materials

Two types of ferrite-pearlite steels, steel S and steel N, were used. The chemical composition and basic mechanical properties of these steels are listed in Table 3-1 and Table 3-2, respectively. The microstructures of these steel, observed using an optical microscope, are shown in Fig. 3-2(a) and (b). The original thicknesses of each steel were 50 mm. This study employed the area average method using the electron backscattered diffraction pattern (EBSD) method to evaluate the grain sizes of the steel because it is more accurate and easy to use compared to other methods such as the optical image method [9]. According to Fig. 3-2(c), Steel N was found to have a finer grain size than steel S. The average grain sizes are listed in Table 3-2. The crack arrest toughness of steel S is too low to evaluate by the temperature gradient tests [10], but the arrest toughness of steel N was determined as $K_{\mathrm{ca}} = 107\ \mathrm{MPa}\sqrt{\mathrm{m}}$ $(3{,}370\ \mathrm{N/mm^{1.5}})$ at $-10\ ℃$ according to the results of temperature gradient crack arrest tests conducted in accordance with WES2815 [10].

The plastic deformation behaviors of the steels were characterized by conducting a series of low-temperature tensile tests and high-speed tensile tests. The stress–strain relationships obtained from the tensile tests were approximated using Swift's law [11] as follows:

$$\sigma = \sigma_{YS}\left(1 + \frac{\varepsilon_p}{\alpha}\right)^n \quad (3\text{-}2)$$

Here, σ is the flow stress, ε_p is the equivalent plastic strain, σ_{YS} is the yield stress, n is the strain hardening exponent, and α is the material constant set to a value of 0.02 [12].

Table 3-1 Chemical composition of the two steels

Steel	C	Si	Mn	P	S
S	0.15	0.17	0.68	0.016	0.003
N	0.14	0.36	1.54	0.014	0.002

Table 3-2 Mechanical properties of the two steels

Steel	Yield stress at room temperature [MPa]	Tensile strength at room temperature [MPa]	vTs [℃]	Average grain size [μm]
S	287	429	-27	31
N	368	538	-54	18

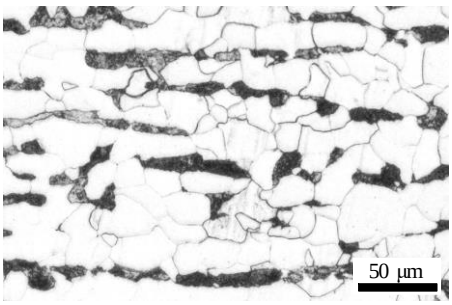

(a) Steel S

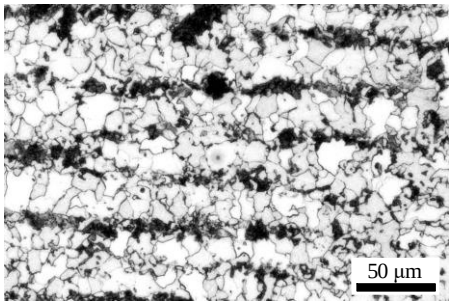

(b) Steel N

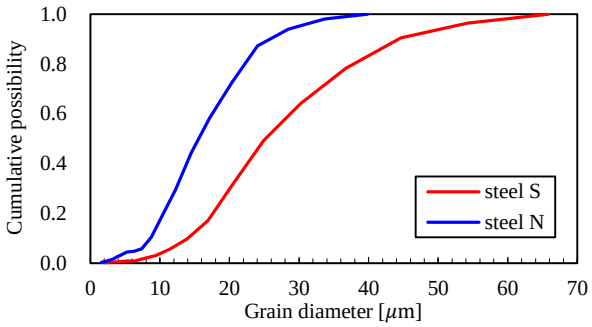

(c) Grain size distribution of the employed steels

Fig. 3-2 Optical micrographs of the two steels (polished and 2% nital etched).

Based on Bennett and Sinclair's theory that the influences of strain rates and temperatures against yield stresses were equivalent considering the dislocation mobility based on the activation energy [13], the elastic-viscoplastic deformation behaviors at each strain rate and temperature shown in Fig. 3-3 (a) and (b) were represented using the strain-rate temperature parameter R in a unified manner [14]. Therefore, the yield stresses obtained from the tensile tests were represented by parameter R as shown in Fig. 3-3(c) and approximated by R to obtain the stress–strain relationship for any arbitrary temperatures and strain rates.

The parameter R is written as follows [13,14]:

$$R = T \ln \frac{10^8}{\dot{\varepsilon}} \tag{3-3}$$

where T and $\dot{\varepsilon}$ are the temperature and strain rate, respectively. Using the R parameter, the yield stress at any arbitrary temperature and strain rate is represented as follows:

$$\sigma_{\mathrm{YS}}(T, \dot{\varepsilon}) = \sigma_{\mathrm{YS0}} \times \mathrm{Exp}\left[A \times \left(\frac{1}{R} - \frac{1}{R_0}\right)\right] \quad (3\text{-}4)$$

where σ_{YS0} A, and R_0 are fitting parameters determined from the results of the tensile tests conducted at various temperatures and strain rates using the least square method. The values determined for σ_{YS0} A, and R_0 were 320 MPa, 2,300, and 7,652 , and 368MPa, 2187, and 7548 for steel S and steel N, respectively. The fitted curves are also shown in Fig. 3-3 (c). Using the fitted curves, the plastic deformation behaviors for arbitrary strain rates and temperatures could be obtained to use in the finite element analyses as explained in Section 3.4.1 to evaluate the local tensile stresses of each experiment.

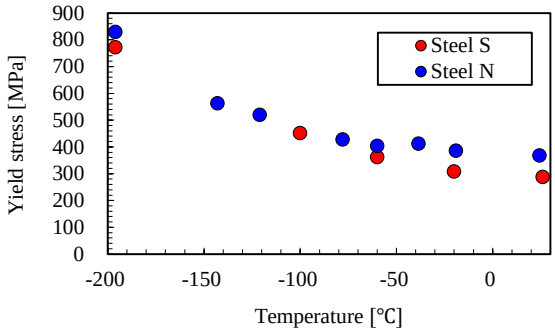

(a) Yield stress and temperature

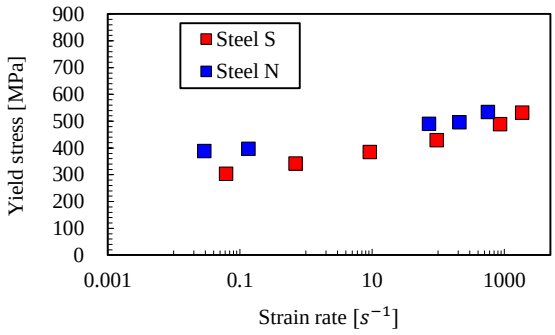

(b) Yield stress and strain rate

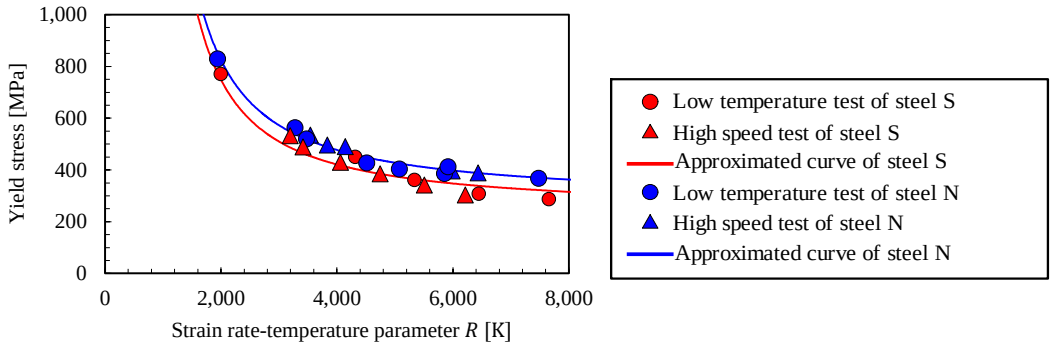

(c) Yield stress and strain-rate temperature parameter R

Fig. 3 Yield stress of steel S and steel N

3.3. Experiments

3.3.1. Concept of experiments

Side-grooved specimens were employed in cleavage crack propagation experiments to overcome 3D effects. Fig. 3-4 shows a schematic comparison between the crack front shapes of a non-side-grooved specimen and side-grooved specimen. Assuming the straight crack front, the stress triaxiality decreases monotonically with respect to the thickness and it becomes difficult to satisfy the fracture conditions near the surface in elastic-viscoplastic solids including steels [15,16]. The curved crack front gradually becomes curved to increase the local crack driving force and keep the critical condition near the surface [17]. The crack front curvature was actually shown by the 3D application phase finite element analyses that employed the local tensile stress as the critical conditions assuming the flat specimen [3]. In contrast to normal specimens, a properly designed side-groove can eliminate 3D effect by causing severe plastic constraint near the surface and preventing the crack front from curving. Thus, because the side-grooves makes it possible to regard cleavage cracks as a 2D plane strain problem, the crack front can be regarded as straight in analyses conducted to evaluate the local tensile stresses.

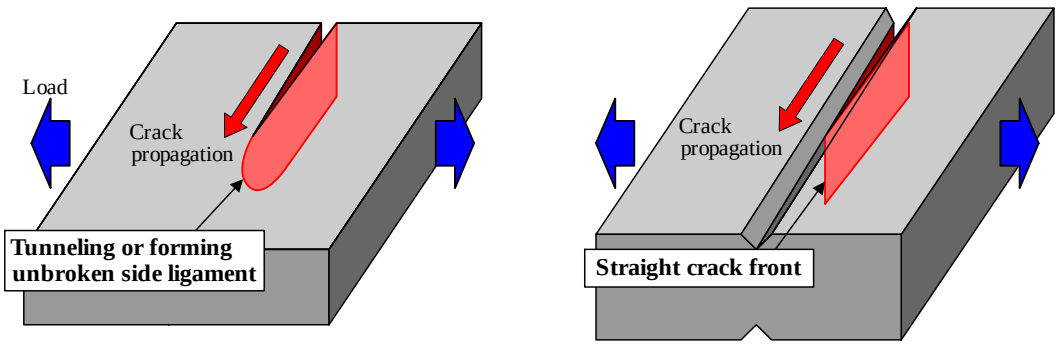

(a) Non-side-grooved specimen (b) Side-grooved specimen

Fig. 3-4 Schematic comparison of 3D effects in typical specimen and side-grooved specimen

3.3.2. Specimen

Crack propagation experiments were conducted under the tension to simplify experimental conditions. Fig. 3-5 shows the specimen configurations employed for the two steels. Although, crack propagation experiments under single tension typically require impact loading to initiate a cleavage crack [10], accurate simulation of the impact load in finite element analysis is difficult.

Therefore, embrittlement bead, NR-LS, and a mechanical notch created by erosion arc machining were employed to initiate a cleavage crack in each specimen. The length of the initial notch was 43 mm in the steel S experiments and 43 mm or 86 mm in the steel N experiments.

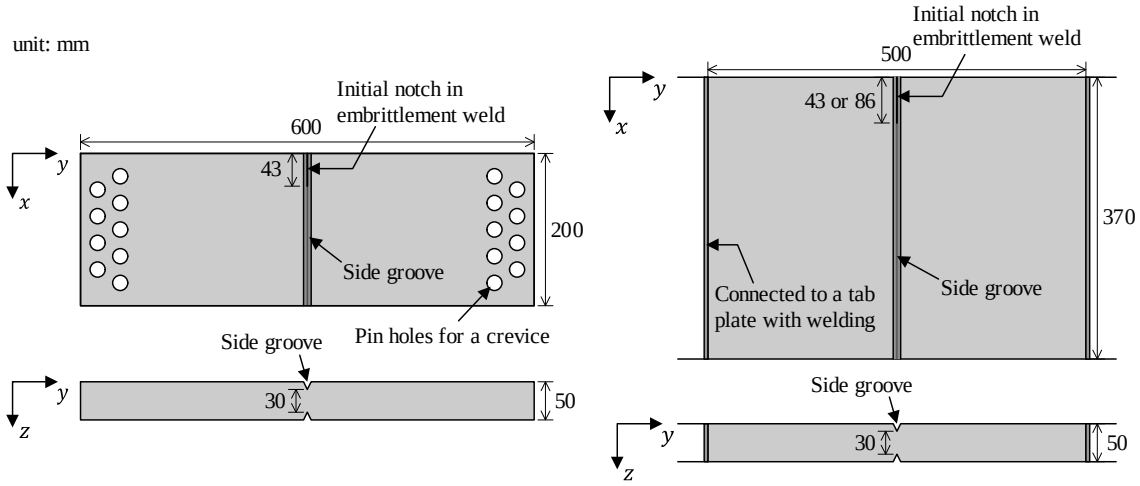

(a) Steel S (b) Steel N

Fig. 3-5 Specimen configurations

The side-groove was the focus of the experimental design. Crack front curvature and the formation of shear lips which is the region where that the critical condition cannot be satisfied and remains unbroken in the cleavage manners near the surface, are caused by monotonic decreasing of constraint along the thickness [1]. The unbroken shear lip are broken in ductile manner and become shear lip [18,19]. Because constraint is generally stronger at the center and weaker near the surface, local tensile stress is lower near the surface than at the center. Thus, a properly designed side-groove that can make the local tensile stress almost same throughout the thickness is required to regard the crack behavior as 2D plane strain. The side-groove configuration for the experimental condition was determined by preliminary finite element analyses. As Fig. 3-6 shows, the configuration was represented by three parameters: side-groove thickness t_{sl}, the angle θ_{sl}, and the root curvature of the side-groove bottom R_{sl}. For convenience in specimen preparation and strain gauge installation to the side of the side-groove bottom, constraints were set that θ_{sl} and R_{sl} were not less than $20°$ and 1 mm, respectively.

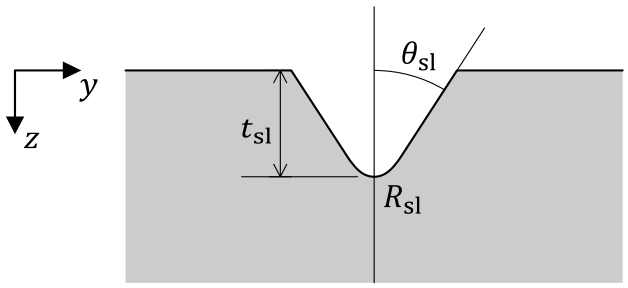

Fig. 3-6 Side-groove configuration

To determine the side groove parameters, a series of preliminary finite element analyses were conducted to assess the influence of the three parameters. The characteristic distance r_c, which is the length between the crack tip and the point of evaluating the stress, was set to 0.15 mm. The analyses were conducted by the nodal force release technique in Abaqus 6.14 [20]. The constitutive laws in the analyses were determined using the approximated curves shown in Fig. 3-3(c). The employed finite element model as shown in Fig. 3-7(a) is a quarter model considering two symmetry conditions: xz and xy planes. The crack propagates in the x direction by releasing constraint of displacement of a crack tip node in y direction. The finite element model and procedure of the preliminary finite element analyses were same as the finite element analyses presented in Section 3.4.1. Each preliminary analysis assumed constant crack velocities although experimentally measured crack velocity was input for the simulation of the experiments. The crack front was straight in the thickness direction. Fig. 3-7(b) shows an example of the plastic zone. Here, the plastic region corresponded to the zone where the equivalent plastic strain was larger than 10^{-6}. The plastic zone was confined to the region near the crack front except just near the specimen surface. The size of the plastic region in Fig. 3-7(b) was about 1.0 mm. Therefore, the stress evaluation point, which is the characteristic distance apart from the crack front, was included in the plastic region.

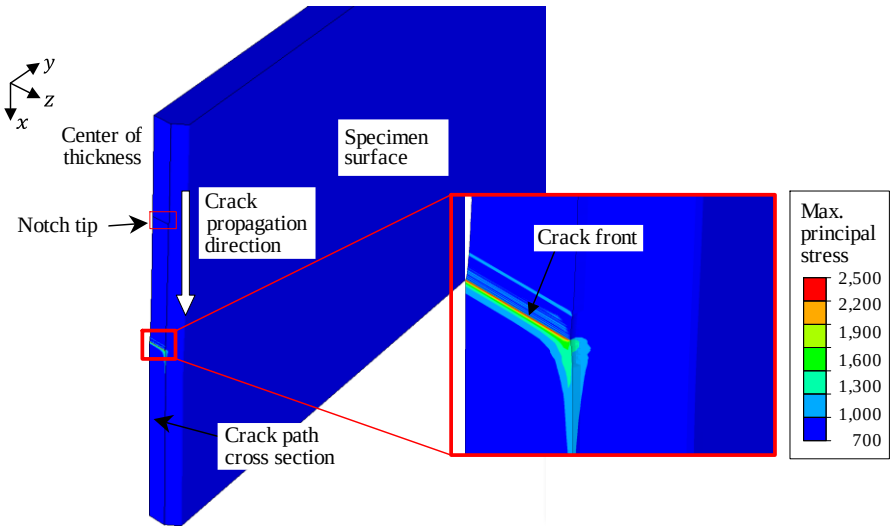

(a) Local tensile stress distribution evaluated by finite element analysis using a quarter model considering xz and xy symmetry conditions

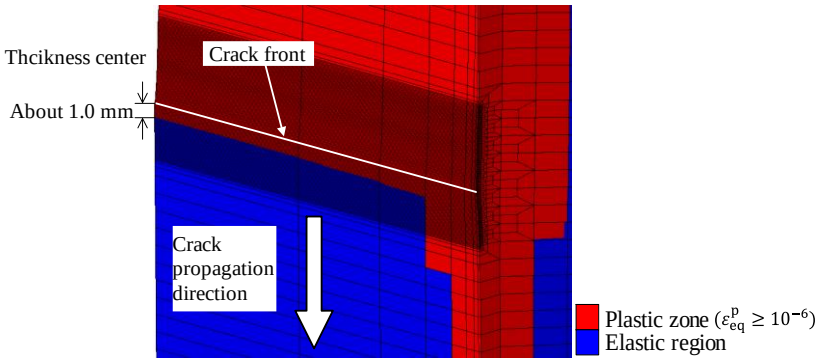

(b) Plastic region near the crack front

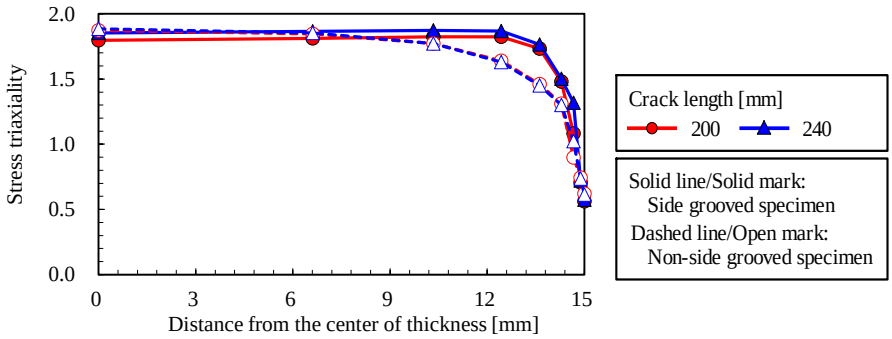

(c) Stress triaxiality distribution along the thickness direction

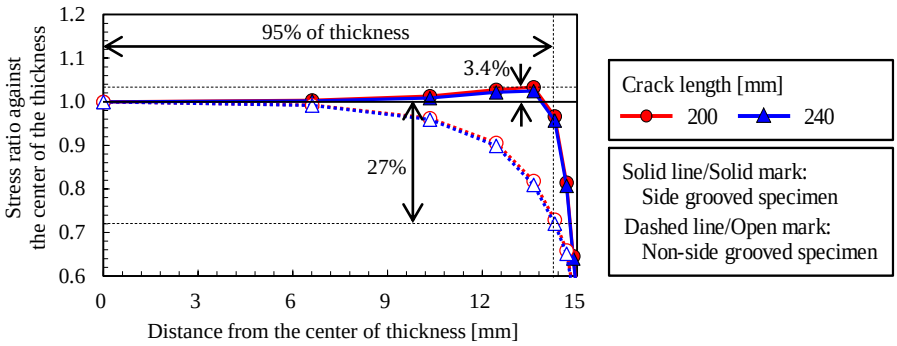

(d) Local tensile stress distribution along the thickness direction

Fig. 3-7 Comparison of the local tensile stress distribution along the thickness direction between side-grooved and non-side-grooved specimen ($T = -60$ ℃, $V = 1{,}000$ m/s, $\theta = 35°$, $\sigma_{\mathrm{eff}} = 120$ MPa)

Figure 3-7(c) shows the stress triaxiality distribution along the thickness direction. The stress applied to the crack path cross section is denoted by σ_{eff}. At the center, the stress triaxialities were approximately 1.85 with or without the side-groove. However, the triaxialities began to decrease 7 mm from the thickness center in a non-side-grooved analyses although the triaxialities were nearly constant except the region near the surface in side-grooved analyses. This trend is consistent with past analyses on static crack growth [21]. The comparison of local tensile stress ratio along the thickness direction in the both analyses is shown in Fig. 3-7(d). In this example, the local tensile stress 14 mm from the center of the thickness was 27% lower than the stress at the center in the non-side-grooved specimen. The maximum deviation of the local tensile stress distribution from the stress at the thickness center was only 3.4% in the side-grooved specimen.

Because the crack velocities and applied stresses at crack initiation could not be known prior to the experiments, analyses were conducted for the ranges of experimental temperature T, assumed crack velocities V and applied stresses. As the local tensile stress near the surface decreased even in the side-grooved specimens, the local tensile stress distribution from the center to 95% of the thickness from the center was investigated in each analysis. The side-groove parameter values that minimized the deviation of the local tensile stress distribution from the uniform distribution were determined for the ranges of supposed velocities and applied stresses considered.

Based on the results of the preliminary analyses and the constraints adopted for processing convenience, the side-groove thickness t_{sl} and root curvature of the side-groove bottom R_{sl} were set to the constant values, $t_{\mathrm{sl}} = 10$ mm and $R_{\mathrm{sl}} = 1$ mm. Only the side-groove angle θ_{sl}

was treated as a variable determined for each experimental condition.

3.3.3. Procedure

Tensile loading was applied to the specimens using the hydraulically-operated 10-MN test rig in the Kashima unit, of the Nippon Steel & Sumikin Technology Co., Ltd. An overview of the test rig is shown in Fig. 3-8 (a). Fig. 3-8 (b) shows a specimen installed in the test rig. The steel S specimens were loaded by pins and a clevis, which was connected to tab plates by welding. The tab plates were loaded by pins of the test rig. In contrast, the steel N specimens were connected directly to the tab plates by welding. Considering the provisions of crack arrest tests in WES2815[10], the spacing between the pins of the test rig was set to more than thrice the specimen width to avoid the effect of load drop due to stress wave reflection.

To compare experimental results for a range of temperatures, experimental temperature was controlled using the cooling bath covering the specimen as shown in Fig. 3-8(b). The cooling bath was separated to seven rooms and the temperature of each room can be controlled using a liquid nitrogen and compressed air splay system. The local fracture stress evaluations were conducted under the isothermal regions. In some experiments, the temperature was uniform throughout the whole specimen, but in others, because only the temperature around the notch tip was cooled to a lower temperature, the specimen partly had temperature gradient. This temperature distribution was similar to that employed in some of CAT tests [22]. The local tensile stresses were evaluated only when the crack tips were in the isothermal regions. In each experiments, the entire specimen was cooled to the target temperature isothermally, and this temperature was maintained for at least 30 min. The temperature around the notch tip was then cooled to a lower temperature if needed. After the temperature around the notch tip was lowered sufficiently, a remote load was applied until a cleavage crack was initiated. The applied stresses when the crack was initiated were varied even if the temperatures were same. Thus, the variables in the experiments were temperatures and applied stresses in addition to the type of steels.

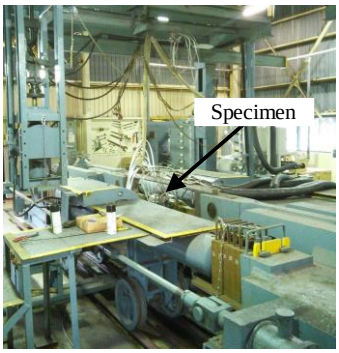

(a) 10 MN test rig

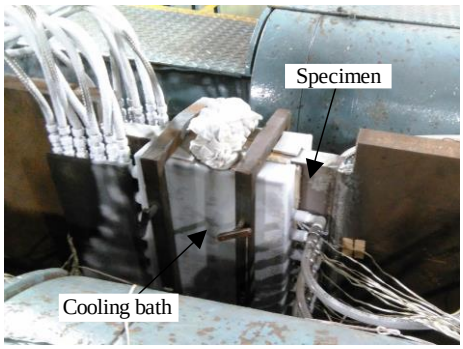

(b) Installation of specimen

Fig. 3-8 Experimental equipment

Some methods have been developed to measure the crack behaviors [4,23,24]. In many previous experiments [2,4,5], crack gauges have been employed to measure crack velocities. However, because crack gauges can only detect a crack propagating on a specimen surface, crack velocity may not be measured accurately considering that a propagating crack front at the center precedes that at the surface. Therefore, crack gauges are not appropriate to measure the velocity of cleavage crack propagation in steels. Digital image correlation (DIC) is sometime employed as the new useful method to measure the crack behaviors [23,25,26]. However, because the cooling bath prevented DIC from observing the crack behaviors in the experiments and DIC can measure only the behavior of surfaces too, DIC was not appropriate in this study.

Therefore, strain gauges were considered more appropriate to detect crack propagation for determining crack velocities [24] because the crack tip propagation changes the strain fields [24,25]. The strain gauges called as KYOWA KFL-02-120-C11 microscopic strain gauges were glued along the expected crack path of each specimen as shown in Fig. 3-9. These gauges were coupled with high-speed acquisition systems, whose time resolution of $10^{-7}\,s^{-1}$ and record duration of 0.1 s. The strain gauges were connected to the acquisition systems via the terminals and signal wires as shown in Fig. 3-9(c).

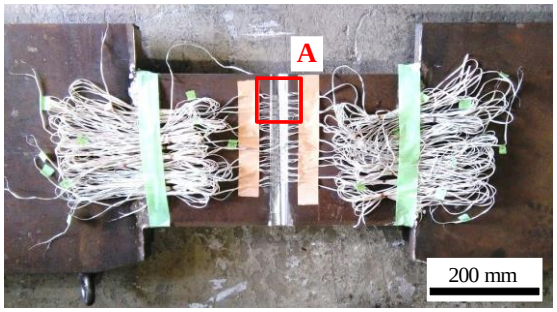

(a) Whole of specimen

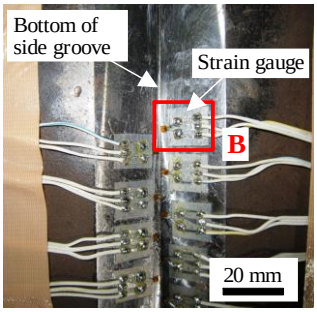

(b) Close up of A

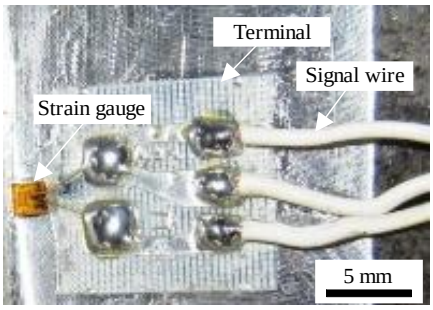

(c) Close up of B

Fig. 3-9 Instrumentation of strain gauges

3.3.4. Results

Thirty-one experiments were conducted, but because the crack location deviated considerably from the bottom of the side-groove or not all of the strain gauges could detect crack propagation, crack velocities were determined successfully in only 13. The crack deviation from the side groove caused at the initiation point in some cases, although the crack deviated from the side groove after it went through the embrittlement weld bead. Therefore, these deviations were caused by not only scatter of the crack initiation point, but also the specimen setting.

One of the fracture surfaces obtained from the experiments is shown in Fig. 3-10. The crack was initiated near the initial notch tip. All cleavage fracture appeared on the surface, and although cleavage fracture surfaces sometimes have significant macroscopic roughness with concave and convex [8], the surfaces obtained in this study were not macroscopically rough except near the initial notch tip. The cracks penetrated the specimens in all successful experiments. The experimentally obtained temperature distributions are shown in Fig. 3-11.

Temperature data of thermocouples that could not measure the temperature were omitted. Because there were local temperature gradients in some experiments, local tensile stress evaluations were

conducted only when the crack tips were in isothermal regions. The experimental conditions and specimen configurations for the 13 successful experiments are listed in Table 3-3. θ, T_{ave}, and σ_{eff} are the angle of the side-groove, average isothermal temperature, and effective stress working on the cross section of the crack path, respectively, in Table 3-3.

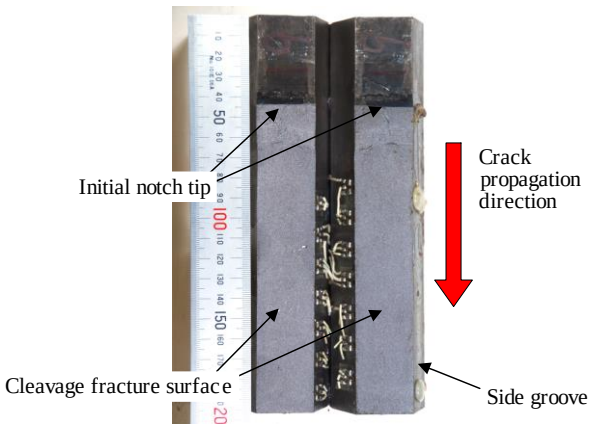

Fig. 3-10 Representative fracture surface obtained by fracture test (S19)

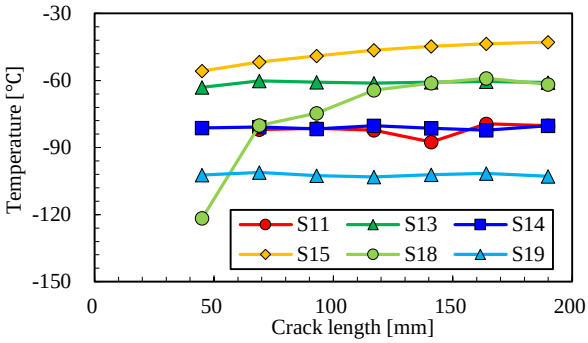

(a) Temperature distribution of steel S

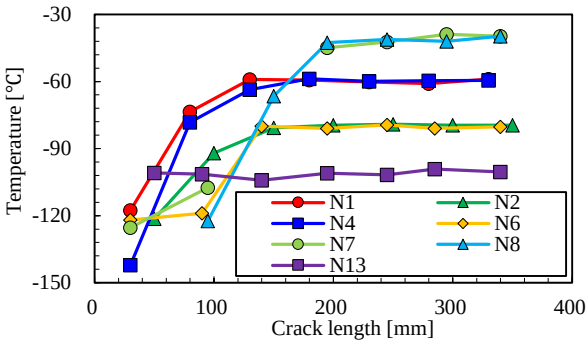

(b) Temperature distribution of steel N

Fig. 3-11 Temperature distribution

Table 3-3 Conditions of successful experiments

Steel	Mark	θ [°]	T_{ave} [℃]	σ_{eff} [MPa]
S	S12	20	-82	219
	S14	20	-61	136
	S15	40	-81	101
	S16	20	-44	174
	S18	20	-62	251
	S19	70	-102	154
N	N1	35	-60	240
	N2	50	-80	191
	N4	35	-60	257
	N6	40	-80	122
	N7	35	-41	195
	N8	35	-42	107
	N13	65	-101	116

An example of the strain data obtained is shown in Fig. 3-12. The absolute values of the strain data were not accurate or meaningful because of the limitations of the acquisition systems. Only strain transitions against time were used to determine crack velocities. The measured strains gradually increased and then suddenly decreased after reaching peak values. Considering previous studies showed that the vertical strain near the crack tip showed the steep drop after the strain peak [25,26] because the elastic strain is suddenly released just after the crack tip passes, the peaks in the measured data could be regarded as the point at which the crack tip passed just the side of the gauge. Owing to difficulties in detecting the strain transition near the bottom of the side-groove, the peaks of the strain transitions could not be determined for some gauges. Figs. 3-13(a), and (b) illustrate the relationship between the crack tip positions and time according to the strain data. This relationship can be expressed using the following equation:

$$a(t) = \alpha_V e^{\beta_V t} + \gamma_V \tag{3-5}$$

where α, β, and γ are fitting parameters and $a(t)$ [mm] is the crack length at time t [s].

The dashed lines in Figs. 3-13 (a) and (b) are curves approximated using Eq. (3-5). The values of α_V, β_V, and γ_V for each experiment are shown in Table 3-4. The crack velocities were obtained by differentiating Eq. (3-5) with respect to time. Figs. 3-13 (c) and (d) illustrate the relationship between crack tip positions and crack velocity for specimens for which the crack tip position was detected by strain gauges.

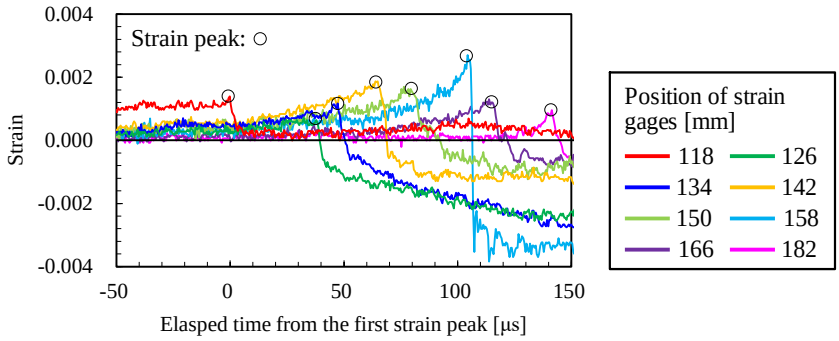

Fig. 3-12 Examples of strain transitions (case S14). The absolute values of the strain data are not accurate and do not have physical meaning.

Table 3-4 Fitting parameter values for crack tip positions versus time

	α_V	β_V	γ_V
S12	18.3	3,317	-297
S14	58.7	3,467	15
S15	41	2,038	-108
S16	31.1	2,691	-252
S18	18.6	12,179	6.56
S19	0.0763	7,886	0.1
N1	0.166	7,790	8.47
N2	57.1	1,431	-639
N4	1.18E-04	7,565	0.349
N6	8.02E-03	5,327	31
N7	983	356	-1650
N8	13.1	2,075	86
N13	0.2	3,778	0.2

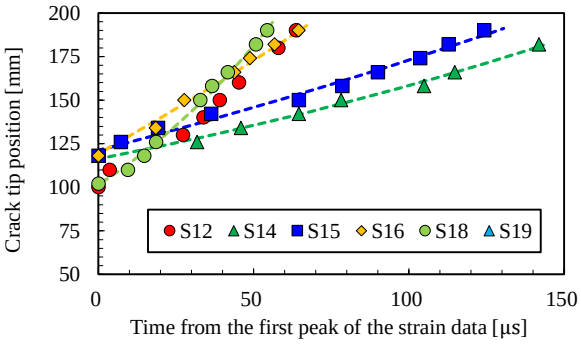

(a) Crack tip positions against time of steel S

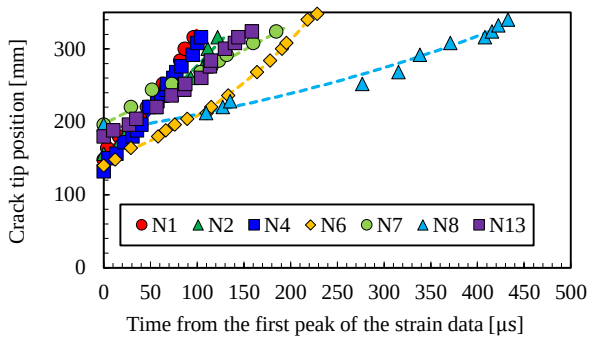

(b) Crack tip positions against time of steel N

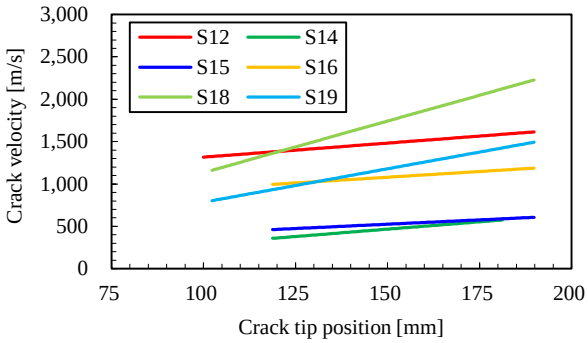

(c) Crack velocities of steel S

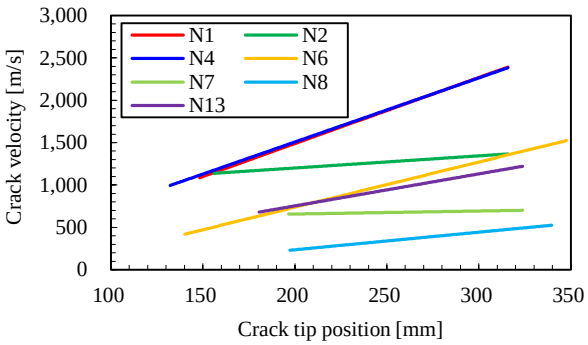

(d) Crack velocities of steel N

Fig. 3-13 Crack velocities in the experiments

3.4. Local fracture stress evaluation by finite element analysis

3.4.1. Procedure

Local fracture stresses were evaluated using crack velocity histories obtained as described in Fig. 3-13 as inputs to 3D elastic-viscoplastic finite element analyses. The analyses considered the rate and temperature dependent material plasticity because the employed constitutive laws were obtained from a series of high speed and low temperature tensile tests explained in Fig. 3-3.

The so-called generation phase nodal force release technique [27] was used in this study to represent rapid crack propagation in the analyses, because of its simplicity and robustness in comparison to other methods to analyze dynamic crack propagation problems [28]. There are in fact multiple nodal force release techniques [29,30]; in this study, linear release technique was employed, based on its previous verification in application to Broberg's reference problem in Chapter 2. The finite element analyses were conducted using Abaqus 6.14 [20]. The implicit Hilber-Hughes-Taylor (HHT) method [31] was used as the time integration method.

One of the finite element models analyzed in our study is shown in Fig. 3-14. This model is the quarter model based on symmetry of the boundary conditions of the xy and xz planes. Based on the strain data used to detect load drop due to the stress wave reflection, it was presumed that the reflected stress waves did not reach the crack propagation paths [10]. Thus, the model size in the longitudinal direction was set to be sufficiently long to prevent the reflected stress waves from reaching the crack paths. Because the local tensile stress suddenly changes near the surface as shown in Fig. 3-7, the vicinity of the model surface was divided finely using geometric progression. As explained in Section 3.3.2, t_{sl} was 10 mm.

Although the mesh size in the region of crack propagation had to be sufficiently fine to evaluate local tensile stresses at the characteristic distance from the crack tip, the computational time had to be kept within a realistic range. Thus, local fine mesh zones (LFMZ) were located along the crack propagation path at certain interval, as shown in Fig. 3-14(f), to reduce the computational time. The local tensile stresses were evaluated when the crack tip reached the center node of an LFMZ.

The minimum mesh size d of LFMZ was approximately 0.05 mm (50 μm). This size was same as those employed in previous studies to experimentally evaluate local fracture stresses using 2D finite element analyses [2,4,5]. The characteristic distance was set to 0.15 mm as same as in the preliminary analyses shown in Section 3.3.2. This characteristic distance will be discussed later.

The local tensile stresses were determined from the reaction force at the nodes located along the crack paths.

Considering that the local tensile stresses were almost constant from the center of the specimen thickness to approximately 95% of the thickness, the local tensile stresses were obtained by averaging the stresses from the thickness center to approximately 95% of the thickness. It is desirable that the local tensile stresses along the thickness are as uniform as possible. However, when the crack velocities were higher than approximately 1,700 m/s, the local tensile stresses approximately 14 mm from the center of thickness became greater than 110% of those at the center of the thickness due to the side-groove. In addition, the evaluation accuracy of the local tensile stresses decreased because of the use of LFMZ when the crack velocity was much higher. Therefore, the local tensile stresses were evaluated for crack velocities that were lower than 1,700 m/s. Actually, because the measured crack velocities were usually slower than 1,700 m/s, this limitation did not really matter.

Furthermore, because attempts have been made to use dynamic stress intensity factors to describe cleavage crack propagation and arrest behavior [32,33] as noted in Section 3.1, dynamic stress intensity factors were also determined for each experiment. The coefficient to consider the dynamic effects, $B(V)$ proposed by Broberg [34], was employed to determine the dynamic stress intensity factor from the static stress intensity factor calculated by the applied stress and crack length. This coefficient was derived considering the relative motions of semi-infinite crack propagating in constant velocity and the elastic wave [34]. The acceleration and deceleration of the crack tip does not influence the coefficient [35]. These dynamic stress intensity factors K_{d} were calculated as

$$K_{\mathrm{d}} = B(V)K_{\mathrm{s}} \tag{3-6}$$

where K_{s} is the static stress intensity factor. $B(V)$ is 1 in case of the static crack and monotonically decreases with the crack velocity and becomes zero when the crack velocity is the Rayleigh wave velocity. K_{s} was calculated from applied stress and the crack length. The detail of Broberg's coefficient is shown in Chapter 2.

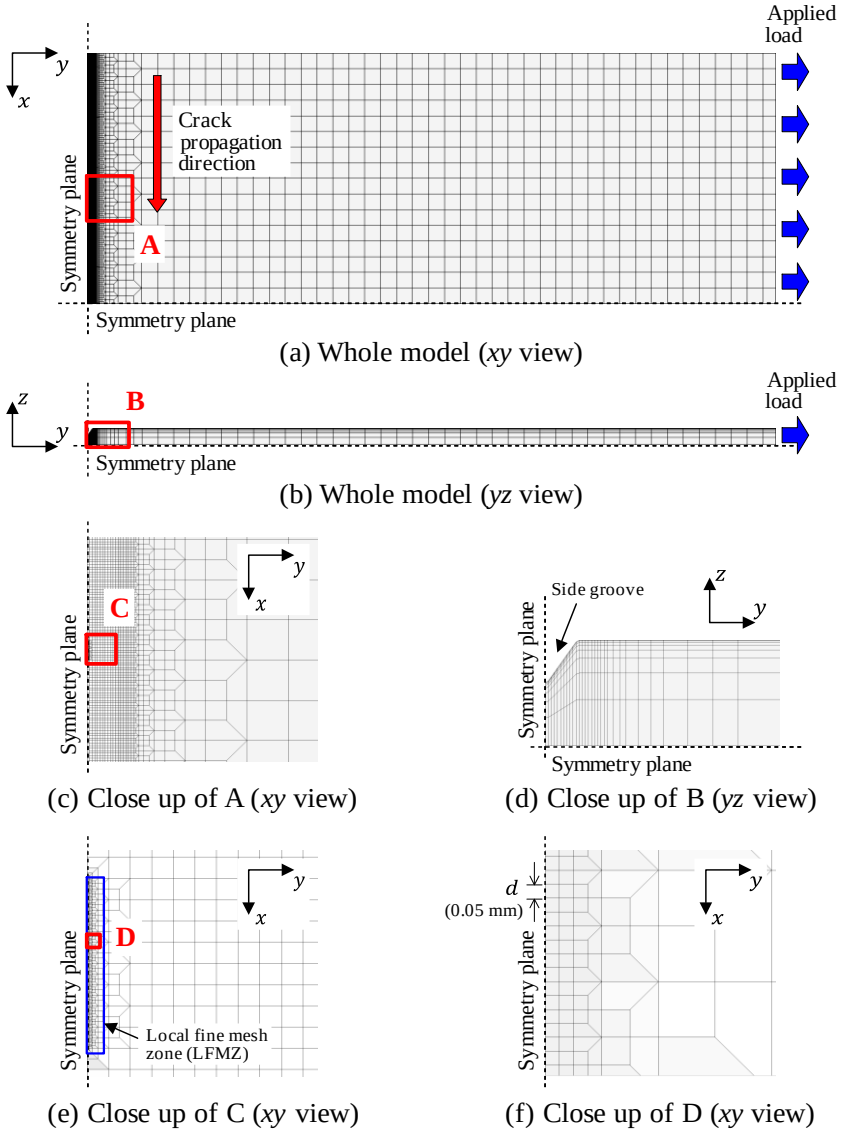

Fig. 3-14 Employed finite element model (Steel N specimen)

3.4.2. Result

The dynamic stress intensity factors of steel S and steel N obtained in our experiments are plotted with respect to crack length, temperature and crack velocity in Figs. 3-15 and 3-16, respectively. The tendency of the dynamic stress intensity factors to increase with crack velocity is consistent with the results reported by previous studies [36,37]. However, the cleavage crack propagation behavior observed in our experiments cannot be described by the dynamic stress intensity factors shown in Figs. 3-15 and 3-16. Additionally, the relationship between the dynamic stress intensity factors and crack velocities cannot be generalized because the relationship depends on the specimen geometry, temperature, and other factors [32]. The dynamic stress intensity factors obtained in this study were thus not considered for use in describing the material resistance to cleavage crack propagation in the steels tested.

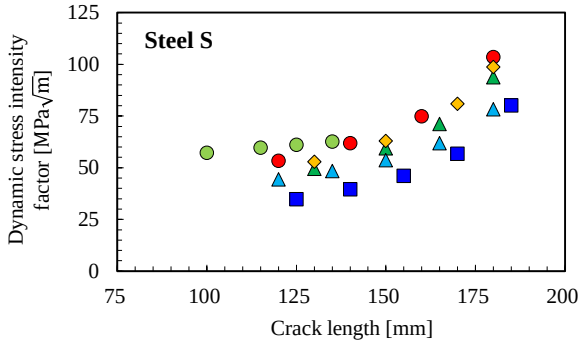

(a) Crack length (Steel S)

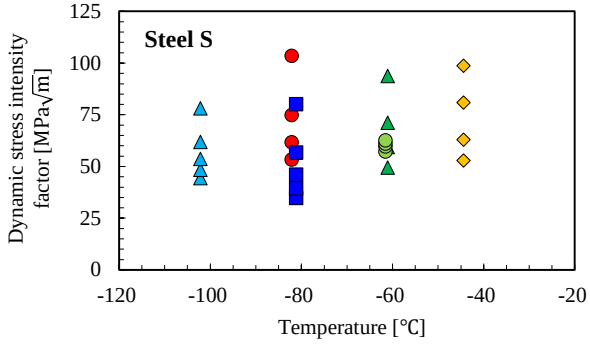

(b) Temperature (Steel S)

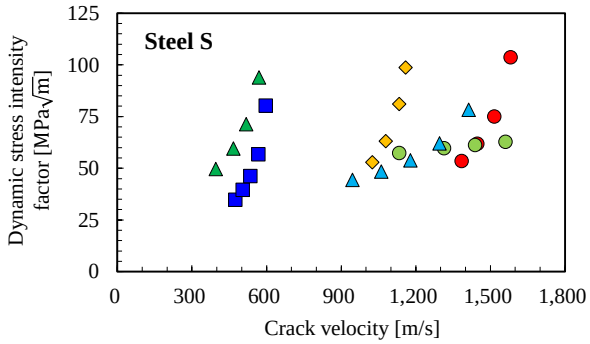

(c) Crack velcoity (Steel S)

Fig. 3-15 Dynamic stress intensity factor in steel S

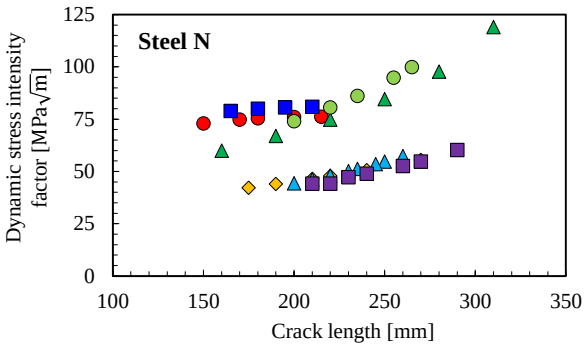

(a) Crack length (Steel N)

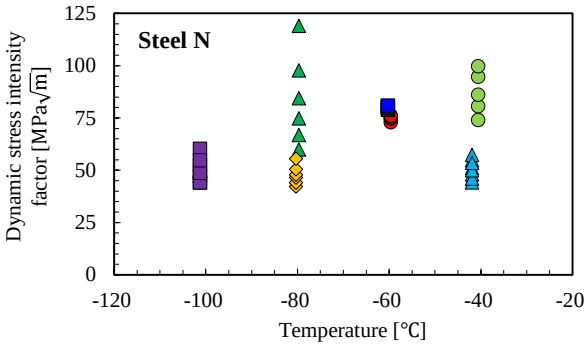

(b) Temperature (Steel N)

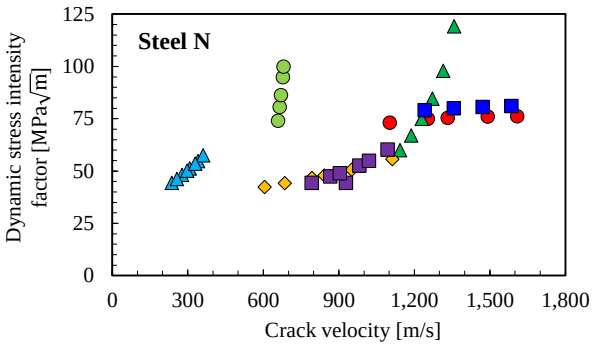

(c) Crack velocity (Steel N)

Fig. 3-16 Dynamic stress intensity factor in steel N

In contrast, the local tensile stresses were almost constant regardless of the temperatures, crack velocity, and crack length, as shown in Figs. 3-17 and 3-18. Some scatter can be observed in Figs. 3-17 and 3-18, but such scatter is inevitable in dynamic crack propagation experiments and analyses because of practical difficulties associated with conducting such experiments and analyses, as observed in previous studies [2,4,5,38]. The average values of the local tensile stresses in steel S and steel N were 1,862 MPa and 2,070 MPa, respectively. Because the crack arrest toughness of steel N is greater than that of steel S, it is to be expected that the local fracture stresses in steel N would be greater than in steel S for the same experimental conditions. The standard deviations were 130 MPa (7.0 % of the average local fracture stress of steel S) and 96 MPa (4.6 % of the average local fracture stress of steel N), respectively. The causes of the scatter are discussed in Section 3.5.2.

These results provide strong experimental evidence of the local fracture stress criterion in which local tensile stresses are regarded as representative of the material resistance to the cleavage crack propagation. Furthermore, the results showing that the local tensile stresses were nearly constant is consistent with the assumption underlying the model proposed by Shibanuma et al.[1,8].

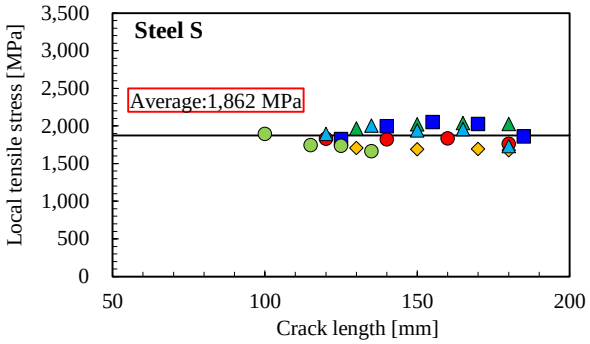

(a) Crack length (Steel S)

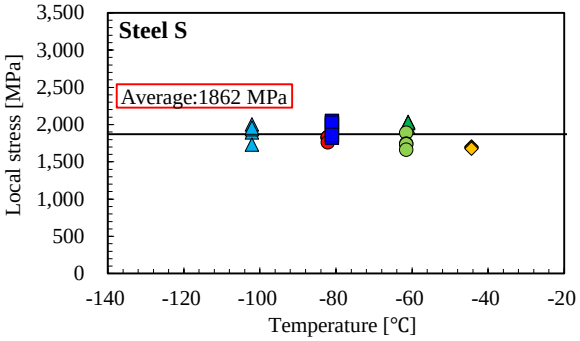

(b) Temperature (Steel S)

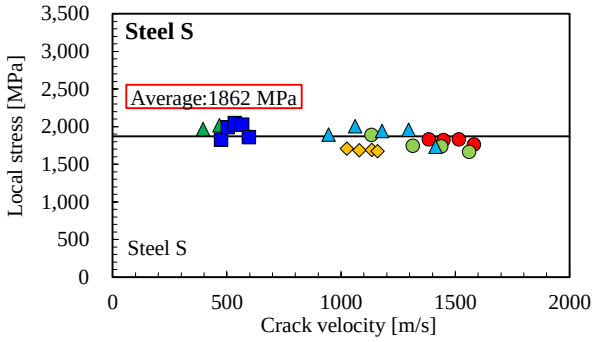

(c) Crack velocity (Steel S)

Fig. 3-17 Local tensile stress of steel S

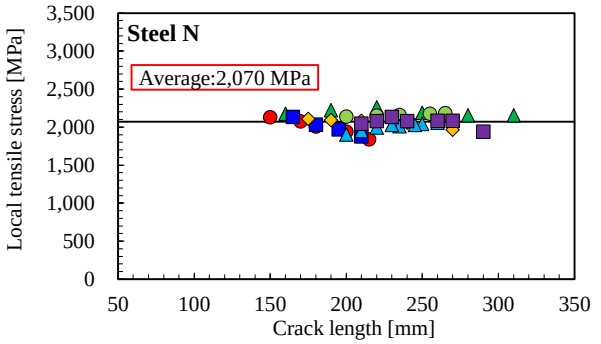

(a) Crack length (Steel N)

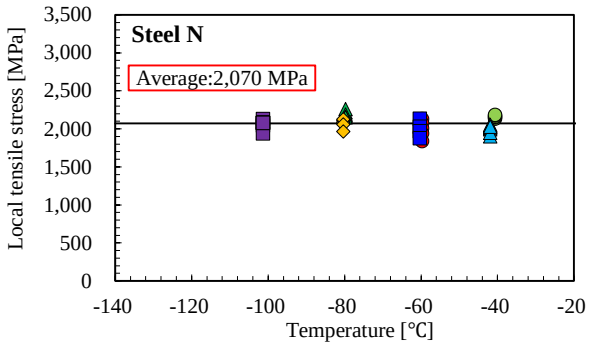

(b) Temperature (Steel N)

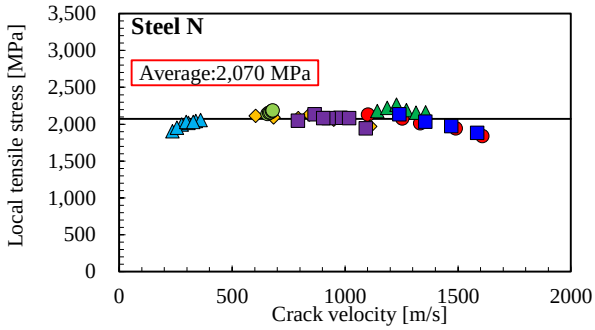

(c) Crack velocity (Steel N)

Fig. 3-18 Local tensile stress in the vicinity of propagating crack tip

3.5. Discussion

3.5.1. Characteristics of local fracture stress

Figure 3-17 and 3-18 shows that the local fracture stresses of cleavage crack propagation in each steel were nearly constant. These results are consistent with the assumption employed by the numerical model based on the local fracture stress criterion [1,8]. On the other hand, such result is different from the results of previous studies conducted by Berdin et al. [2], Prabel et al. [4], and Bousquet et al. [5]. Although, in previous studies, it was not necessarily possible to determine the crack behaviors accurately because of the lack of consideration of 3D effects. The results of these previous studies concerning the characteristics of local fracture stresses are nonetheless noteworthy.

According to Berdin et al., local fracture stresses are higher at higher temperature [2,3], and the local fracture stress can be assumed to exhibit same temperature dependency as the lower bound of the K_{Ia} arrest toughness curve. Although their experimental results suggested that the local fracture stress increases with temperature [2], this can be attributed to 3D effects which were not considered in their studies. It has been noted that because 3D effects becomes more remarkable at higher temperatures or lower crack velocities, the effective driving force of a propagating crack is lower than the apparent crack driving force. Accordingly, the local fracture stress is overestimated, especially just before crack arrest in the results obtained by Berdin et al. because their 2D analysis method could not consider this reduction of the crack driving force.

On the other hand, Prabel et al. and Bousquet et al. reported that the local fracture stress depends on the strain rates [4,5]. In their studies, the local fracture stress was higher when the strain rate was higher. However, their data included local fracture stresses determined for cases in which the strain rates were lower than 10^2 /s. The strain rates in all of our analyses were higher than 10^3 /s, even though the experiments were conducted under various applied stress and temperature conditions. Strain rates lower than 10^2 /s appear to be too low for strain rates in the vicinity of dynamically propagating cleavage crack tips. This underestimation can be attributed to the crack velocities determined in the studies being slower than the actual crack velocities (because crack gauges and high speed cameras were employed) and the fact that 3D effects were ignored.

The characteristic distance is a controversial issue in research on the local fracture stress criterion. Characteristic distances of 0.1~0.3 mm were used in previous studies [1–5,8]. In this study, the characteristic distance used was 0.15 mm, which is within this range. Fig. 3-19 shows examples of the experimentally obtained local stress distribution against the distance from the crack tip for

different temperature and crack velocity in steel N experiments. It can be found that the local stress distributions have an intersection point at about 0.15 mm from the crack tip.

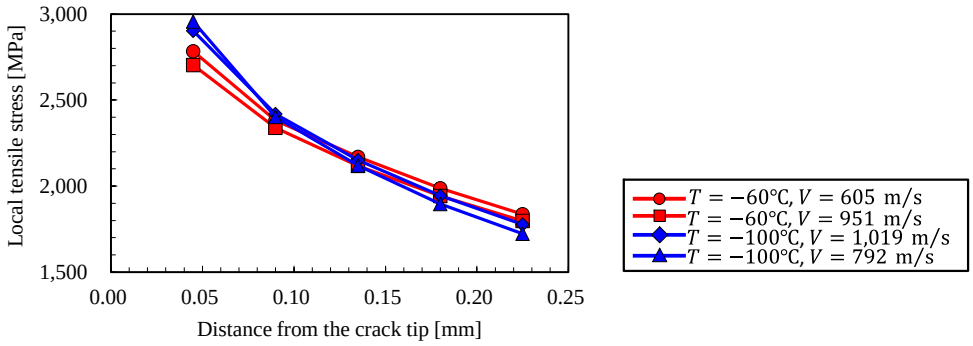

Fig. 3-19 Experimentally obtained local stress distribution (-60 ℃: N6, -100 ℃: N13)

In fact, as shown in Fig. 3-19, the local tensile stresses at distances of 0.1-0.2 mm from the crack tip exhibited trends similar to those of the local tensile stresses presented in Figs. 3-17 and 3-18, and the standard deviations were appropriately 4.7~6.1% and 7.0~8.0% for steel N steel S, respectively.

Furthermore, it is worth noting that the crack arrest toughness of steel N is much higher than that of steel S although the local fracture stress of steel N is higher than that of steel S by only approximately 10%. This gap of the crack arrest toughness of both steels may not be explained only by the gap of the local fracture stresses. The gap of the toughness can also be attributed to the rate sensitivity of yield stress. Because the yield stress of steel S is more sensitive to strain rate than that of steel N as shown in Fig. 3-3, the local tensile stress is likely to satisfy the local fracture stress even when SIF is lower. Thus, increasing the local fracture stress, and decreasing rate sensitivity of yield stresses of steels are important to improve the crack arrest toughness.

3.5.2. Microstructure and local fracture stress

In contrast to the nearly constant local fracture stresses against cleavage crack propagation shown in Figs. 3-17 and 3-18, the local fracture stress of cleavage crack initiation is known to depend on temperature [12,39]. This difference of the characteristics of the local fracture stress between cleavage crack initiation and propagation implies that the microscopic mechanism of resistance

against cleavage crack propagation differs from the microscopic mechanism of resistance against cleavage crack initiation. Most of the resistance to cleavage crack propagation can be attributed to the formation of tear ridge [40–42], as Fig. 3-20 shows, which, are ligaments broken in a ductile manner between the cleavage planes of adjacent grains. Considering this tear ridge formation does not contribute to the resistance to cleavage crack initiation, such difference in the resistance mechanism appears to lead to inconsistencies in the temperature dependency.

In fact, a relationship between microstructure and cleavage crack propagation resistance is not clear. For example, the contribution of a grain size, which is the most fundamental feature to characterize steel microstructure, is not known. Although the grain sizes of steel S and N are different, the contribution cannot be simply derived from Figs. 3-17 and 3-18 because their chemical compositions are different. Chapter 8 will show a series of examination of the local fracture stress for each grain sizes steel with same chemical composition.

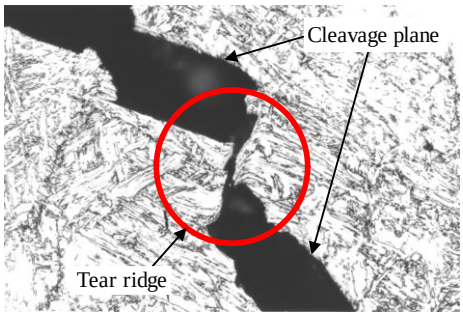

Fig. 3-20 Optical observation of the tear ridge [41]

3.5.3. Scatter of the local fracture stresses

It should be noted that there were scatters in the local fracture stress results, as shown in Figs. 3-17 and 3-18. This scatter is presumed to be associated with the accuracy of the crack velocity evaluation method, the accuracy of the finite element analysis results, and the experimental procedures used, including those for specimen installation, gauge instrumentation, and temperature control. Crack velocity determination from strain data is particularly prone to error because of the difficulty of determining the strain peak as shown in Fig. 3-12. The method used to approximate the relationship between the crack tip position and time is also a possible cause of scatter. Furthermore, a crack that appears straight macroscopically is not necessarily truly straight,

but rather may meander and branch, as can be observed microscopically. In addition, even though the side groove worked to eliminate 3D effect, the actual crack front was not perfectly straight. These complexities of crack propagation are main causes of the scatter in the local tensile stress results obtained.

Scatter in the results was also observed in previous studies of local fracture stress and other parameters like dynamic stress intensity factors [4,5,33], and such scatter is inevitable in the studies of dynamic phenomena. However, because our experiments accounted for the 3D effects and employed strain gauges instead of crack gauges, the local tensile stresses shown in Figs. 3-17 and 3-18 are regarded as more accurate than the results of previous studies, which did not consider 3D effects.

The scatter observed in the results obtained in this study also reflect intrinsic variation in the local fracture stresses due to locally inhomogeneous microstructures even though the steel plates employed were globally homogeneous. The material resistance to cleavage crack initiation is known to exhibit variation [43]. The Weibull stress concept is commonly used to characterize scatter in the critical stresses associated with cleavage fracture initiation [44] and has been applied to the cleavage crack propagation and arrest problem by Berdin [3]. However, the intrinsic variation in the local fracture stresses associated with cleavage crack propagation is considered to be much smaller than that of the local fracture stress of cleavage fracture initiation because the cleavage crack propagation process basically does not include crack nucleation in secondary phase such as cementite or pearlite, which is the trigger of cleavage crack initiation in steels [12]. In addition, because the cleavage crack propagates over the entire thickness, the local fracture stress is averaged even if some microscopic scattering of the material resistance is present. Thus, the Weibull stress concept may be not appropriate for use in describing the variation in the local fracture stress associated with cleavage crack propagation, and the variation associated with the local tensile stress evaluation process may be larger than the intrinsic scatter.

3.5.4. Temperature dependency of the local fracture stresses

Usually, K_{ca} is evaluated in the range of $-30 \sim 10$ ℃. And, the temperatures which were set in above experiments were lower than ductile-brittle transition temperature (DBTT) except N7 and N8 whose temperatures were higher than DBTT. The lower temperatures were chosen as the experimental conditions because of two reasons. One is related to temperature control. It was needed to make the temperature around the initial notch tip lower than the temperature of the

isothermal region to cause brittle fracture without impact. Therefore, if the isothermal region temperature had be set to higher than DBTT, the temperature gradient between the initial notch tip and the isothermal region would have be extremely steep or the isothermal region would be shorter. The other reason is about the measurement of crack velocity. It was needed to keep the applied stress relatively lower because the higher applied stress made fracture surfaces rough. The crack velocity measurement became hard in such cases because such rough fracture surface made the strain data much noisy. However, in particular, the brittle crack arrest toughness of steel N was higher, so the crack was arrested just after it entered the isothermal region when the applied stress was small and the temperature was high. Therefore, considering the measurement of crack velocity, the applied stress should be lower and the temperatures should be also lower. According to these two reasons, the temperatures were basically set to relatively low.

However, it is not reasonable to relate the local fracture stress to the temperature because the DBTT is determined by Charpy impact test. As noted in Section 3.5.2, the local fracture stress corresponds to the energy dissipation related to the tear ridge formation in microstructural view because the local fracture stress is the resistance against only cleavage crack propagation. On the other hand, the absorbed energy in Charpy impact test is the accumulation of the energy related to the all fracture phenomena which cause in the test. Usually, as explained in Fig. 3-21, the fracture in Charpy impact test is composed of ductile crack extension before brittle fracture initiation, brittle fracture initiation, cleavage crack propagation, shear lip formation, and ductile fracture of ligaments due to ductile fracture although some of them are not observed in the certain experimental condition [45–47]. The energy absorption due to cleavage crack propagation is small enough to be negligible compared to the other energy absorption [45,48]. The absorbed energy transition related to DBTT is attributed to the change of the absorbed energy of the fracture phenomena other than cleavage crack propagation [45] and it has not been found that energy absorption due to cleavage crack propagation has the temperature dependency as same as the whole of energy absorption in Charpy impact test. In addition, the ductile-brittle transition temperature depends on evaluation methods [49,50]. Thus, DBTT cannot be related to the temperature dependency of the local fracture stress. Accordingly, there is no necessity to evaluate the local fracture stress in the temperature higher than DBTT, and thus as Fig. 3-18 showed, it can be concluded that the local fracture stress is independent on the temperature.

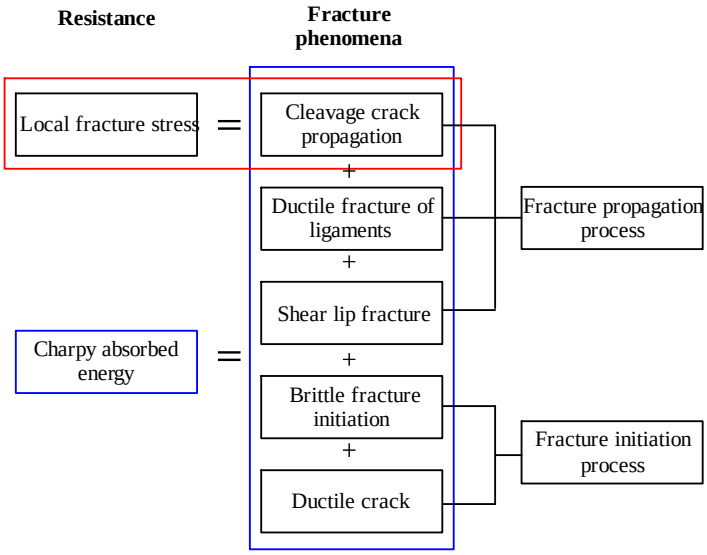

Fig. 3-21 Energy absorption in local fracture stress and Charpy absorbed energy

3.6. Conclusion

Cleavage crack propagation and arrest behavior in steel has persisted as an unsolved problem in fracture mechanics, despite its engineering importance. Given that the local fracture stress is the most promising criterion for cleavage crack propagation and arrest behavior, this study was carried out to evaluate local tensile stresses in the vicinity of the crack tip.

The evaluations were conducted using a series of cleavage crack propagation experiments and finite element analyses. Side-grooved specimens were employed to eliminate 3D effects that cause severe plastic constraint near the plate surface. Preliminary finite element analyses were conducted to design appropriate side-groove configurations. The crack velocities obtained in the experiments were used as inputs to finite element analyses to evaluate the local tensile stresses in the vicinity of the crack tip. Dynamic stress intensity factors were also calculated from the experimental results.

The dynamic stress intensity factors were found to vary with the temperature, crack velocity, and crack length. This indicates that dynamic stress intensity factors should not be used as intrinsic criteria for cleavage crack propagation and arrest behavior in steel. In contrast, the local tensile stresses were nearly constant for each steel regardless of the experimental conditions although the numerical results exhibited some scatter. These results are the first experimental evidence that strongly supports the validity of the local fracture stress criterion according to which local tensile

stresses are regarded as representative of material resistance to the cleavage crack propagation in steels. The observation that the local tensile stresses were constant is consistent with the assumption underlying the theoretical model based on the local fracture stress criterion [1,8]. Accordingly, the results of this chapter strongly support that the local fracture stress criterion is the most promising concept for explaining cleavage crack propagation and arrest behavior in steel.

Reference

[1] K. Shibanuma, F. Yanagimoto, T. Namegawa, K. Suzuki, S. Aihara, Brittle crack propagation/arrest behavior in steel plate - Part I: Model formulation, Eng. Fract. Mech. 162 (2016) 324–340. doi:10.1016/j.engfracmech.2016.02.054.

[2] C. Berdin, M. Hajjaj, P. Bompard, S. Bugat, Local approach to fracture for cleavage crack arrest prediction, Eng. Fract. Mech. 75 (2008) 3264–3275. doi:10.1016/j.engfracmech.2007.08.013.

[3] C. Berdin, 3D modeling of cleavage crack arrest with a stress criterion, Eng. Fract. Mech. 90 (2012) 161–171. doi:10.1016/j.engfracmech.2012.05.002.

[4] B. Prabel, S. Marie, A. Combescure, Using the X-FEM method to model the dynamic propagation and arrest of cleavage cracks in ferritic steel, Eng. Fract. Mech. 75 (2008) 2984–3009. doi:10.1016/j.engfracmech.2008.01.008.

[5] A. Bousquet, S. Marie, P. Bompard, Propagation and arrest of cleavage cracks in a nuclear pressure vessel steel, Comput. Mater. Sci. 64 (2012) 17–21. doi:10.1016/j.commatsci.2012.04.026.

[6] X. Yang, S. Marie, C. Jacquemoud, P. Bompard, Prediction of cleavage crack propagation path in a nuclear pressure vessel steel, Eng. Fract. Mech. (2018). doi:10.1016/j.engfracmech.2018.01.015.

[7] S. Machida, H. Yoshinari, M. Yasuda, S. Aihara, H. Mabuchi, Fracture mechanicsl modeling of brittle fracture propagation and arrest of steel (1) A fundamental model, J. Soc. Nav. Archit. Japan. 177 (1995) 243–258.

[8] K. Shibanuma, F. Yanagimoto, T. Namegawa, K. Suzuki, S. Aihara, Brittle crack propagation/arrest behavior in steel plate - Part II: Experiments and model validation, Eng. Fract. Mech. (2016). doi:10.1016/j.engfracmech.2016.02.053.

[9] K.P. Mingard, B. Roebuck, E.G. Bennett, M.G. Gee, H. Nordenstrom, G. Sweetman, P. Chan, Comparison of EBSD and conventional methods of grain size measurement of hardmetals, Int. J. Refract. Met. Hard Mater. 27 (2009) 213–223. doi:10.1016/j.ijrmhm.2008.06.009.

[10] The Japan Wedling Engineering Society, WES2815 Test method for brittle crack arrest toughness, (2014). http://www-it.jwes.or.jp/wes_ki/wesippan.jsp?arg=2815e-1.

[11] H.W. Swift, Plastic instability under plane stress, J. Mech. Phys. Solids. 1 (1952) 1–18. doi:10.1016/0022-5096(52)90002-1.

[12] K. Shibanuma, Y. Nemoto, T. Hiraide, K. Suzuki, S. Sadamatsu, Y. Adachi, S. Aihara, A strategy to predict the fracture toughness of steels with a banded ferrite–pearlite structure based on the micromechanics of brittle fracture initiation, Acta Mater. 144 (2018) 386–399. doi:10.1016/j.actamat.2017.10.046.

[13] P.E. Bennett, G.M. Sinclair, Parameter Representation of Low-Temperature Yield Behavior of Body-Centered Cubic Transition Metals, J. Basic Eng. 88 (1966) 518–524.

[14] Y. Takashima, T. Kawabata, S. Yamada, F. Minami, Observation of micro-cracks beneath fracture surface during dynamic crack propagation, Theor. Appl. Fract. Mech.

92 (2017) 178–184. doi:10.1016/j.tafmec.2017.07.013.
[15] Y. Huang, W. Zhou, Effects of crack front curvature on J-R curve testing using clamped SE(T) specimens of homogeneous materials, Int. J. Press. Vessel. Pip. 134 (2015) 112–127. doi:10.1016/j.ijpvp.2015.05.001.
[16] S.K. Kudari, K.G. Kodancha, 3D Stress intensity factor and T-stresses (T 11 and T 33) formulations for a Compact Tension specimen, Frat. Ed Integrità Strutt. 39 (2017) 216–225. doi:10.3221/IGF-ESIS.39.21.
[17] T. Handa, S. Igi, K. Oi, T. Tagawa, F. Minami, Brittle crack propagation / arrest behavior in T-joint structure of heavy gauge steel plate, Weld. World. 59 (2015) 823–838. doi:10.1007/s40194-015-0242-3.
[18] A. Pandolfi, P.R. Guduru, M. Ortiz, A.J. Rosakis, Three dimensional cohesive-element analysis and experiments of dynamic fracture in C300 steel, Int. J. Solids Struct. 37 (2000) 3733–3760. doi:10.1016/S0020-7683(99)00155-9.
[19] A. Fedoseeva, N. Dudova, R. Kaibyshev, Role of Tungsten in the Tempered Martensite Embrittlement of a Modified 9 Pct Cr Steel, Metall. Mater. Trans. A Phys. Metall. Mater. Sci. 48 (2017) 982–998. doi:10.1007/s11661-016-3926-4.
[20] Dassault Systems, SIMULA Abaqus Analysis User's Manual, (2014).
[21] H. Kordisch, E. Sommer, W. Schmitt, The Influence of Triaxiality on Stable Crack Growth, Nucl. Eng. Des. 112 (1989) 27–35.
[22] G. An, H. Bae, B. Jeong, Y. An, H. Jeong, CAT (Crack Arrest Temperature) Test Method Using Local Temperature Gradient System for Estimate of Fracture Toughness with Shipbuilding Steel, in: Proc. 28th Int. Ocean Polar Eng. Conf., 2018: pp. 107–108.
[23] K.A. Kasvayee, K. Salomonsson, E. Ghassemali, A.E.W. Jarfors, Microstructural strain distribution in ductile iron; comparison between finite element simulation and digital image correlation measurements, Mater. Sci. Eng. A. 655 (2016) 27–35. doi:10.1016/j.msea.2015.12.056.
[24] R.E. Link, J.A. Joyce, C. Roe, Crack arrest testing of high strength structural steels for naval applications, Eng. Fract. Mech. 76 (2009) 402–418. doi:10.1016/j.engfracmech.2008.11.006.
[25] B. Koohbor, S. Mallon, A. Kidane, M.A. Sutton, A DIC-based study of in-plane mechanical response and fracture of orthotropic carbon fiber reinforced composite, Compos. Part B Eng. 66 (2014) 388–399. doi:10.1016/j.compositesb.2014.05.022.
[26] S. Mallon, B. Koohbor, A. Kidane, M.A. Sutton, Fracture Behavior of Prestressed Composites Subjected to Shock Loading: A DIC-Based Study, Exp. Mech. 55 (2015) 211–225. doi:10.1007/s11340-014-9936-5.
[27] M. Kuna, Finite Elements in Fracture Mechanics Theory-Numerics-Applications, Springer, 2010.
[28] A.R. Shahani, M.R. Amini Fasakhodi, Finite element analysis of dynamic crack propagation using remeshing technique, Mater. Des. 30 (2009) 1032–1041.
[29] M. Hajjaj, C. Berdin, P. Bompard, S. Bugat, Analyses of cleavage crack arrest experiments: influence of specimen vibration, Eng. Fract. Mech. 75 (2008) 1156–1170. doi:10.1016/j.engfracmech.2007.04.021.
[30] A.S. Kobayashi, K. Seo, J.Y. Jou, Y. Urabe, A Dynamic Analysis of Modified Compact-tension Specimens Using Homalite-100 and Polycarbonate Plates, Exp. Mech. (1979) 73–79.
[31] T.J.R. Hughes, The Finite Element Method Linear Static and Dynamic Finite Element Analysis, Prentice-Hall, 1987.
[32] S. Machida, H. Yoshinari, Some recent experimental work in Japan on fast fracture and crack arrest, Eng. Fract. Mech. 23 (1986) 251–264.
[33] D.A. Shockey, J.F. Kalthoff, W. Klemm, S. Winkler, Simultaneous measurements of stress intensity and toughness for fast-running cracks in steel, Exp. Mech. 23 (1983)

140–145.
[34] K.B. Broberg, Cracks and Fracture, Academic Press, 1999.
[35] T. Nishioka, The State of the Art in Computational Dynamic Fracture Mechanics, JSME Int. J. Ser. A. 37 (1994) 313–333.
[36] N.A. Kazarinov, Y. V. Petrov, V.A. Bratov, V.Y. Slesarenko, Numerical investigation of stress intensity factor - crack velocity relation for a dynamically propagating crack, Mater. Phys. Mech. 29 (2016) 39–42.
[37] R. Yang, P. Xu, Z. Yue, C. Chen, Dynamic fracture analysis of crack-defect interaction for mode I running crack using digital dynamic caustics method, Eng. Fract. Mech. 161 (2016) 63–75.
[38] X. Deng, A.J. Rosakis, Dynamic crack propagation in elastic-perfectly plastic solids under plane stress conditions, J. Mech. Phys. Solids. 39 (1991) 683–722. doi:10.1016/0022-5096(91)90047-R.
[39] J.I. San Martin, J.M. Rodriguez-Ibabe, Determination of energetic parameters controlling cleavage fracture in a Ti-V microalloyed ferrite-pearlite steel, Scr. Mater. 40 (1999) 459–464.
[40] R.G. Hoagland, A.R. Rosenfield, G.T. Hahn, Mechanisms of fast fracture and arrest in steels, Metall. Trans. 3 (1972) 123–136. doi:10.1007/BF02680591.
[41] K. Shibanuma, Y. Yamamoto, F. Yanagimoto, K. Suzuki, S. Aihara, Multiscale Model Synthesis to Clarify the Relationship between Microstructures of Steel and Macroscopic Brittle Crack Arrest Behavior - Part I : Model Presentation, ISIJ Int. 56 (2016) 341–349. doi:10.2355/isijinternational.ISIJINT-2015-450.
[42] T. Iung, A. Pineau, Dynamic Crack Propagation and Crack Arrest Investigated With a New Specimen Geometry : Part II : Experimental Study on a Low-Alloy Ferritic Steel, Fatigue Fract. Eng. Mater. Struct. 19 (1996) 1369–1381.
[43] F.M. Beremin, A Local Criterion for Cleavage Fracture of a Nuclear Pressure Vessel Steel, Metall. Trans. A. 14 (1983) 2277–2287.
[44] A. Pineau, A.A. Benzerga, T. Pardoen, Failure of metals I: Brittle and ductile fracture, Acta Mater. 107 (2016) 424–483. doi:10.1016/j.actamat.2015.12.034.
[45] T. Kobayashi, K. Takai, H. Maniwa, Transition Behaviours and Estimation of Fracture Toughness in the Charpy Impact Test, J. Japan Inst. Met. Mater. 30 (1966) 700–706.
[46] M. Tanaka, S. Umekawa, On the Brealing Behaviours in Charpy Impact Bending Tests, J. Japan Inst. Met. Mater. 21 (1957) 221–225.
[47] T. Yagi, A. Itoh, M. Nagumo, Resistance against the Stable Crack Growth and Brittle Fracture Initiation Site Controlling the Ductile-Brittle Fracture Transition Behaviors of Low Carbon Steels, Tetsu-to-Hagane. 81 (1995) 225–230.
[48] H. Shirahata, T. Okawa, T. Inoue, K. Ushida, Simplified Evaluation Method for Brittle Crack Arrest Toughness of Steel Plates Exploiting Charpy Impact Test, Tetsu-to-Hagane. 104 (2018) 155–165.
[49] B. Tanguy, J. Besson, R. Piques, A. Pineau, Ductile to brittle transition of an A508 steel characterized by Charpy impact test Part I: Experimental results, Eng. Fract. Mech. 72 (2005) 49–72. doi:10.1016/j.engfracmech.2004.03.010.
[50] L.C.A. Folch, F.M. Burdekin, Application of coupled brittle-ductile model to study correlation between Charpy energy and fracture toughness values, Eng. Fract. Mech. 63 (1999) 57–80. doi:10.1016/S0013-7944(99)00009-0.

Chapter 4 Governing factors of local stresses in the vicinity of the running crack tip in elastic- viscoplastic solids

4.1. Introduction

Chapter 3 presented the experimental evidence to strongly support the local fracture stress criterion in brittle crack propagation/arrest behaviors. Because this study attempts to model brittle crack propagation and arrest behaviors, the local tensile stress in the vicinity of a rapidly propagating crack tip is needed to appropriately understand. In fact, the local stress field near the crack tip is one of the most attractive issues in dynamic fracture mechanics and studied by previous literatures [1,2]. In linear elastic problems, the local stress field follows $1/\sqrt{r}$ singularity even in rapid crack propagation as mentioned in Chapter 2. However, although several studies analysed the local tensile stresses in elastic-viscoplastic solids based on some simplifications [3,4], it is practically difficult to establish accurate asymptotic equations of the local tensile stresses in the complicated elastic-viscoplastic solids like steels. Therefore, a numerical method is vital to accurately evaluate the local tensile stresses.

Although some studies using numerical methods were devoted to investigate the local tensile stresses, viscoplastic effect has been mainly considered to evaluate the energy balance of the crack tip and thus examination of the features of the local tensile stress have not been carried out based on the local fracture stress criterion [5–7] . Numerical methods such as finite element method were applied to analyse viscoplastic effect to crack tip energy balance and thus the effect to the local tensile stresses is not sufficiently understood [8,9]. In particular, it is essential to clarify how the local tensile stresses are influenced by the crack propagation conditions, such as the crack velocity and stress intensity factor (SIF), to appropriately model the local tensile stresses.

Previous studies attempted to relate the local tensile stress to the macroscopic crack parameters to explain brittle crack propagation and arrest behaviors [10–12,4,13]. For example, a conventional numerical model based on the local fracture stress assumed that the determinants of local tensile stress were SIF, temperature, and crack velocity when the constitutive law was same [10]. This assumption, however, did not result from findings obtained from detail investigation and thus, further inspection is needed.

In addition to the aforementioned macroscopic parameters (SIF, crack velocity, and temperature), the crack velocity history including unsteady effect (non-constant crack velocity) is also important to understand the brittle crack propagation and arrest behavior although such an effect has been hardly considered for elastic-viscoplastic solids. When it is needed to evaluate the local fracture stress, it is necessary to measure the crack velocity and temperature in order to simulate the crack behavior in finite element analyses [14,15]. In reality, it is difficult to measure the crack velocity history and temperature distribution perfectly because of limitations in the measurement tools of crack velocity histories. As a result, these quantities are usually only measured in the range of interest. However, because it is not clear whether the crack velocity history and temperature distribution before the crack enters the range of interest influences the local tensile stresses in the range of interest, the measured local tensile stresses cannot be regarded as an accurate value. This unsteady effect is an important topic in elastic fracture mechanics [16,17], but it has rarely been considered in elastic-viscoplastic solids like steel.

Although there are some numerical methods developed to analyze rapid crack propagation problems, this chapter also employed finite element method as same as Chapter 2 and 3. In addition, to accurately distinguish what parameter influences the local tensile stress, it was needed to conduct accurate evaluation of the local tensile stress. Therefore, based on the results of Chapter 2, the Rayleigh damping was applied. The used FEM software was Abaqus 6.14 [18].

As indicated in the above discussion, it is important to determine and investigate the parameters that influence the local tensile stress in the vicinity of a rapidly propagating crack tip for further understanding of the brittle crack propagation and arrest behaviors in steel from the perspective of the local fracture stress criterion. A series of finite element analyses were carried out in this chapter, in which crack propagation was categorized as follows: steady state crack propagation (crack velocity is constant during crack propagation), and unsteady state crack propagation (crack velocity changes during crack propagation). Based on the assumption of the proposed numerical model based on the local fracture stress criterion [10], the candidates for the factors that determine the local tensile stress were the SIF, crack velocity, and temperature including temperature

gradient in steady state crack propagation. These steady state crack propagation analyses are described in Section 4.3. In addition, the analyses in which the crack velocity is not constant during crack propagation are described in Section 4.4. Section 4.5 discusses the results obtained in Sections 4.3 and 4.4, before Section 4.6 concludes this chapter.

4.2. Method

The analyses in this chapter used FEM to evaluate the local tensile stresses in the vicinity of a rapidly propagating crack tip. In particular, the nodal force release technique was employed to represent rapid crack propagation in FEM, as the accuracy of local stress evaluation in the nodal force release technique is known to be sufficient for our purpose based on Chapter 2 [19]. Herein, the implicit HHT method was employed to solve dynamic problems.

The problem dealt with in this chapter is a propagating crack located in the center of an infinite plate under remotely applied tensile stress, as shown in Fig. 4-1. The direction of the tensile stress is normal to the direction of crack propagation. This is one of the most typical problems in fracture mechanics [20] and same as the problem analysed in Chapter 2.

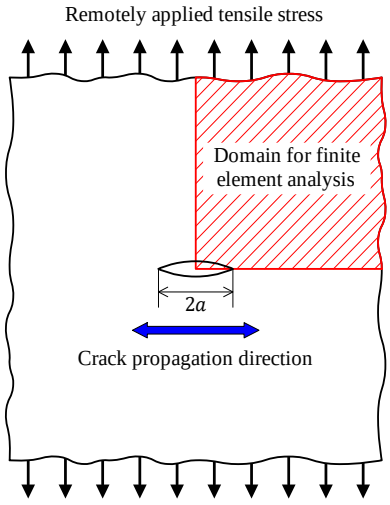

Fig. 4-1 Infinite media with a center crack under remotely applied tensile stress and the domain for finite element analyses

The mesh generator employed in Chapter 2 was also used to construct finite element models for use in a series of crack propagation analyses. As shown in Fig. 4-1, the symmetries of the problem mean that the employed mesh is a quarter model. In the mesh generator, the crack velocity V, minimum mesh size along a crack path d, crack length a, remotely applied stress σ_{app}, Young's modulus E, Poisson's ratio ν, and density ρ are input parameters. In all analyses described in this study, the Young's modulus, Poisson's ratio, and density are set to $E = 206$ GPa, $\nu = 0.3$, and $\rho = 7{,}800$ kg/m^3. These material constants are the same as those of steel.

In order to regard the finite element model as practically infinite, the finite element model dimensions were set to be sufficiently large so that the reflected stress waves did not reach the crack path before the crack reached the final crack length. In addition, the final crack length was much smaller than the model dimension so that the SIF was not influenced by the finite width effect. Therefore, the dimensions of the model varied in terms of the input parameters such as the crack velocity to keep the model infinite.

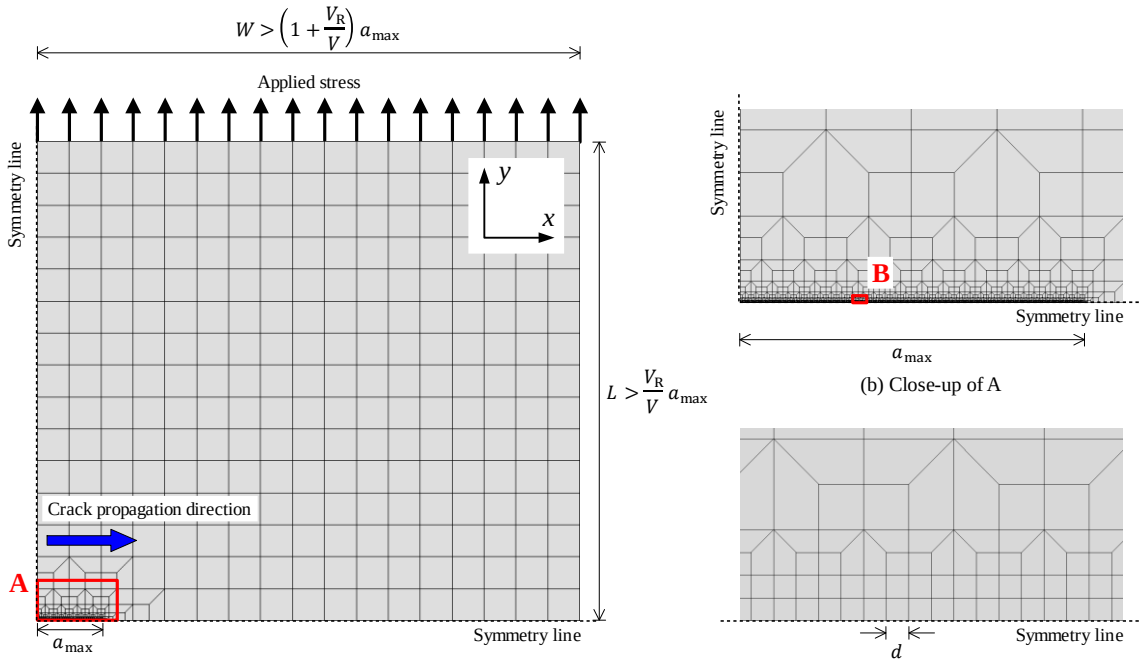

Fig. 4-2 Example of the employed finite element mesh and boundary conditions made by the mesh generator

One example of the finite element models produced by the mesh generator is shown in Fig. 4-2.

V_R, V, and a_{max} denote the Rayleigh wave velocity, crack velocity, and final crack length, respectively.

Two boundary conditions were imposed on the model, as shown in Fig. 4-2, according to the symmetry of the model. W and L were width and length of the finite element model, respectively. The plain strain and first-order quadrilateral elements with full-integration were employed in all analyses reported in this chapter. CPE4 was employed as the element in Abaqus 6.14 [18]. These fundamental information of employed meshes was same as those employed in Chapter 2.

Unless otherwise noted, the minimum mesh size d was 0.05 mm and the local tensile stresses were evaluated at a point 0.15 mm away from the crack tip, based on the experimental results explained in Chapter 3. In other words, the characteristic distance was 0.15 mm, which is equal to $3d$. Therefore, herein, the local tensile stress was defined as the maximum principal stress evaluated using the reaction forces at the third node from the crack tip.

The yield point of steel is strongly dependent on temperature and strain rate [21]. Although such a dependency varies for the type of steels, the dependency expressed by the empirical equation shown below was employed because this chapter does not deal with any specific steel.

The empirical equation was proposed by Gotoh et al. [22,23] based on the strain rate-temperature parameter [21] to express the yield point σ_{YS} at an arbitrary temperature T $[K]$ and strain rate $\dot{\varepsilon}$ $[s^{-1}]$ as

$$\sigma_{YS} = \sigma_{YS0}\exp(497.5 - 68.90\ \ln\sigma_{YS0})\left(\frac{1}{T}\frac{18.42 - \ln\dot{\varepsilon}_0}{18.42 - \ln\dot{\varepsilon}} - \frac{1}{T_0}\right) \quad (4\text{-}1)$$

where σ_{YS0} is the yield point at the reference temperature [Pa] and strain rate, T_0 is the reference temperature $[K]$ (set to 293 K), and $\dot{\varepsilon}_0$ is the reference strain rate (set to $5.0 \times 10^{-5}\ s^{-1}$). In these elastic-viscoplastic analyses, σ_{YS0} was set to 400 MPa. The relationship between strain rate and yield stress expressed by Eq. (4-1) is shown in Fig. 4-3 for $\sigma_{YS0} = 400$ MPa. Because Eq. (4-1) was obtained by averaging the relationship between strain rate, temperature, and yield stress of various types of steels, it can be regarded as an average relationship of strain rate, temperature, and yield stress of various steels. It was also employed to express the average relationship in previous studies [10,11].

The stress–strain relationship was modelled using Swift's law [24] expressed as

$$\sigma = \sigma_{YS}\left(1 + \frac{\varepsilon_p}{0.02}\right)^n \tag{4-2}$$

where ε_p , σ_{YS}, and n are the plastic strain, yield stress, and hardening exponent, respectively. The hardening law was isotropic. According to a series of tensile tests of steels [22,23], n can be empirically expressed by the yield stress for certain strain rate and temperature as

$$n = 0.471\, e^{-0.00219\sigma_{YS}} \tag{4-3}$$

where σ_{YS} is the yield stress.

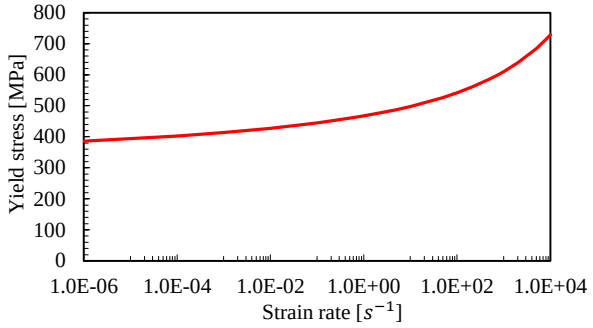

Fig. 4-3 Dependency of yield stress on strain rate ($\sigma_{YS0} = 400$ MPa)

4.3. Steady state crack propagation

Using the method described in Section 4.2, the steady state crack propagation was analysed to investigate the effect of the SIF, crack velocity, temperature, and temperature gradient. All the analyses reported in this section were carried out in the elastic-viscoplastic condition.

Conventionally, the crack tip local tensile stress field of a rapidly propagating crack in steel has been regarded as being in the small-scale yielding condition, because the strain rate near the crack tip is extremely high [10,25–27]. This suggests that the SIF could describe the amplitude of the local tensile stress field around a rapidly propagating crack tip.

Although previous studies regarded that the local tensile stress field is a function of SIFs [10,12,13], there have been no rigorous investigations on how SIF influences the local tensile

stresses. Thus, the first investigation in this chapter considers the relationship between the local stresses and the SIFs (see Section 4.3.1). Here, because the crack length is sufficient small for the finite effect on SIF to be much small, SIF is expressed as

$$K = \sigma_{\mathrm{app}}\sqrt{\pi a} \tag{4-4}$$

where K is SIF, σ_{app} is the remotely applied stress, and a is the crack length.

Furthermore, the crack velocity provides inertia to the body containing the crack and determines the amplitude of the local stress field around the crack tip [28]. Although experiments have found a wide range of velocities of brittle cracks (approximately $100–2{,}000\,\mathrm{m/s}$) [29–32], the influence of the crack velocity on the crack tip stress fields has not been evaluated quantitatively in elastic-viscoplastic materials such as steel. Therefore, Section 4.3.2 explores how the crack velocity influences the local tensile stress. Finally, for steady state crack propagation, the effects of the temperature and temperature gradients are investigated in Section 4.3.3. Because the temperature is a determinant of the yield stress of steel, it is expected to strongly influence the local tensile stresses. As the temperature gradients are used in crack arrest tests [33], they are also examined in Section 4.3.3.

4.3.1. Stress intensity factor

As noted before, this section aims to clarify the influence of SIF on the local tensile stress. Four amplitudes of applied stresses (160, 200, 300, and 360 MPa) were considered in the crack propagation analyses. The comparison of the local tensile stresses for each applied stress is shown in Fig. 4-4. When SIFs were same, the crack length was different for each applied stress. For example, when the stress intensity factor was $100\ \mathrm{MPa}\sqrt{\mathrm{m}}$, the crack lengths were 124.3, 79.5, 35.3, and 24.5 mm at $\sigma_{\mathrm{app}} = 160, 200, 300, \text{and } 360$ MPa, respectively.

The local tensile stresses increase with the SIF, but the rate of increase gradually becomes smaller as the SIF becomes larger (see Fig. 4-4). In particular, even when the crack length becomes extremely large and the SIF is much higher than approximately $150\ \mathrm{MPa}\sqrt{\mathrm{m}}$, the rate of increase of the stress is smaller than increase ratio of SIF. Note that this gradual decline in the rate of increase of the local tensile stress with respect to SIF contributes to the “long brittle crack problem” [10,34], because the local tensile stress barely rises as the SIF becomes much higher. Namely, it can be said that the local tensile stress approaches saturation as the stress intensity factor rises.

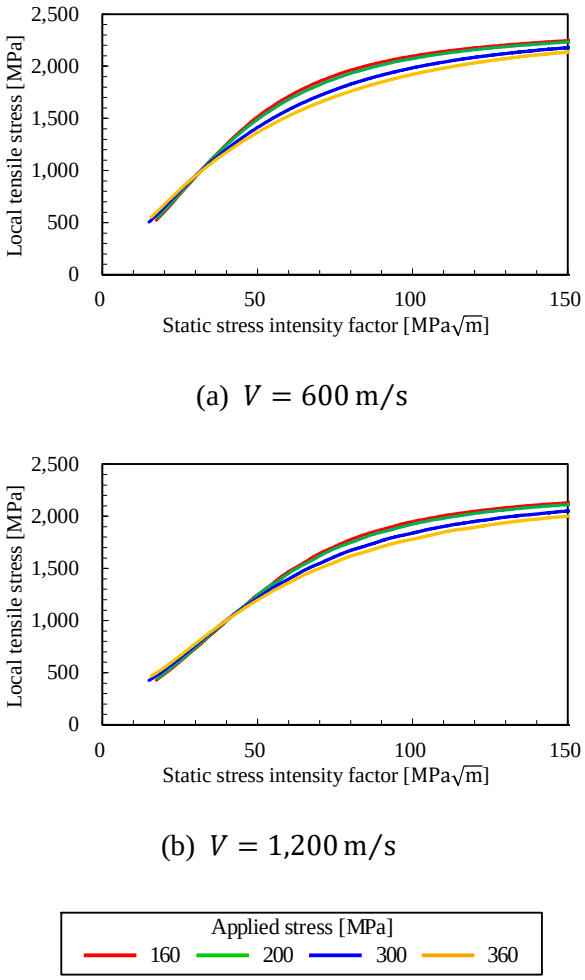

Fig. 4-4 Relationships between stress intensity factors and local tensile stresses

Under the assumption of small-scale yielding, the crack tip stress field is regarded to be characterized by SIF. However, Fig. 4-4 clearly shows that the local tensile stresses are not same with respect to the applied stresses when the SIF is the same. To make the difference clear, the local tensile stresses for $\sigma_{\mathrm{app}} = 200, 300, \mathrm{and}\ 360$ MPa were normalized by the local tensile stress for $\sigma_{\mathrm{app}} = 160$ MPa. Fig. 4-5 shows these normalized results. While the SIFs are less than 30 MPa$\sqrt{\mathrm{m}}$, the local tensile stresses are higher in cases of higher applied stress conditions. Once the SIF exceeds 30MPa$\sqrt{\mathrm{m}}$, the local tensile stresses are higher in cases of lower applied stresses than higher applied stresses. Once this condition occurs, the minimum normalized local tensile stress becomes 0.89 in the case of $V = 600\ \mathrm{m/s}$ and $\sigma_{\mathrm{app}} = 360$ MPa (see Fig. 4-5).

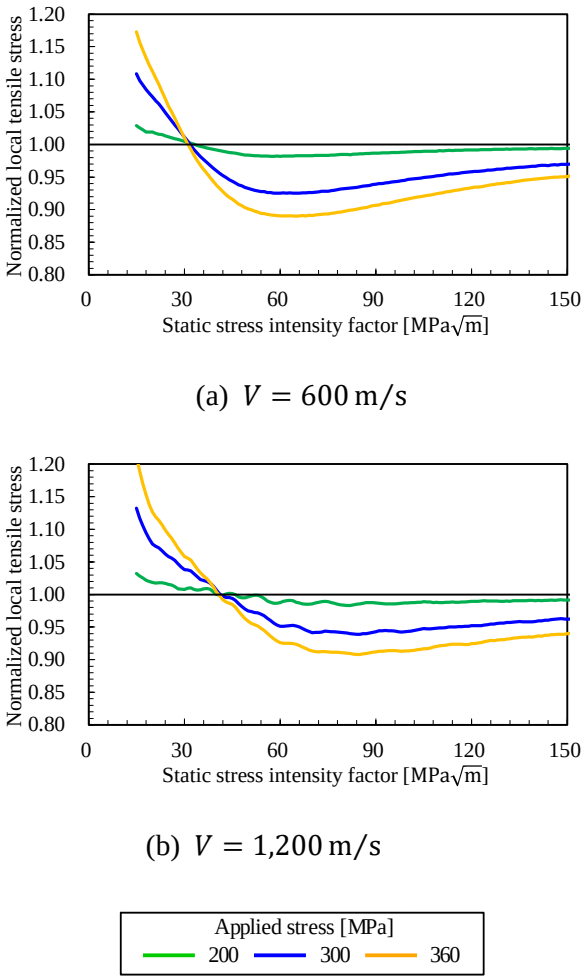

Fig. 4-5 Normalized local tensile stresses against stress intensity factors

To investigate the reason for the local tensile stresses being different for different tensile stresses even for the same SIFs, the equivalent plastic strains at the characteristic distance (0.15 mm) from the crack tip were investigated for each applied stress. The equivalent plastic strains are shown in Fig. 4-6. The equivalent plastic strains are higher when the applied stresses are lower, even for the same SIFs. Assuming that the SIFs are the same, the crack lengths are longer in cases of lower applied stresses.

This difference in the plastic strains was caused by the degree of accumulation of plastic strains. To clarify the reason why different plastic strains were observed, the plastic strain accumulation history at a certain position was investigated. Fig. 4-7 shows the plastic strain at the position of interest with respect to the distance from the crack tip. The crack velocity was 600 m/s. The position of interest was located 0.15 mm from the crack tip when SIF = 89.7 MPa$\sqrt{\text{m}}$. Namely,

the accumulations of the plastic strain were observed along crack propagation until the SIFs reached $89.7\ \mathrm{MPa}\sqrt{\mathrm{m}}$. According to Fig. 4-7, the accumulation behavior of the plastic strain depended on the level of the applied stresses. Because the plastic strain accumulated as the crack approached the position of interest, longer crack lengths produced higher plastic strains than shorter crack length for the same SIF. The plastic strain in cases of lower applied stress conditions clearly started to accumulate earlier than in cases of the higher applied stress conditions. This accumulation of plastic strain led to higher local tensile stresses near the crack tip. Therefore, it can be concluded that the differences of the local tensile stresses are caused by the different behaviors of the plastic strain accumulation.

When the SIF is $50-60\ \mathrm{MPa}\sqrt{\mathrm{m}}$, the differences in the local tensile stresses due to the plastic strain accumulation was remarkable (Fig. 4-5(a)). This is because the plastic strains in cases of higher applied stresses remained negligible after the plastic strains at lower applied stresses began to increase ($K = 50-60\ \mathrm{MPa}\sqrt{\mathrm{m}}$). In the cases of higher crack velocities, the differences in the local tensile stresses were maximized when SIFs are $80-90\ \mathrm{MPa}\sqrt{\mathrm{m}}$, as shown in Fig. 4-5(b). This is because a higher SIF was needed to generate the plastic strain when the crack velocity was higher, as shown in Fig. 4-6(b).

Accordingly, the conventional assumption that the SIF can be used to describe the local tensile stress in the vicinity of the rapidly propagating crack tip in elastic-viscoplastic materials such as steel is invalid and thus the applied stress and crack length have to be separately considered to describe the local tensile stresses.

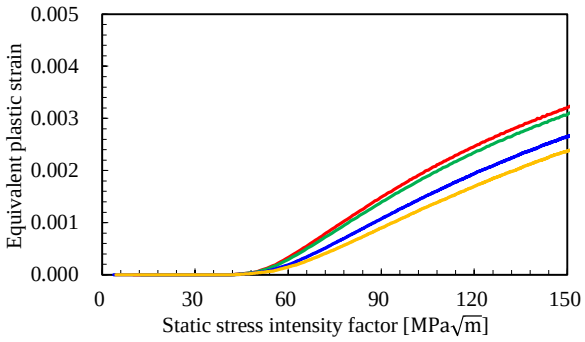

(a) $V = 600\,\mathrm{m/s}$

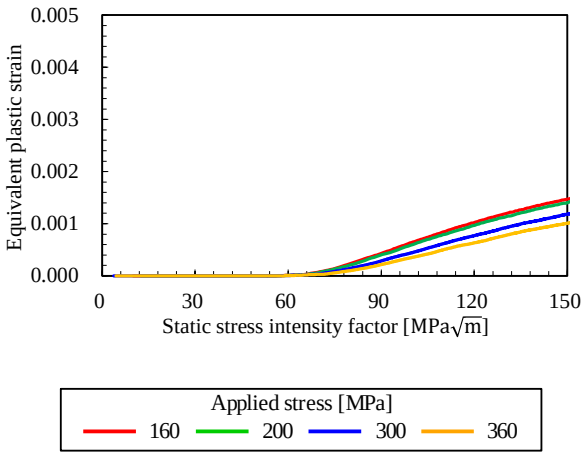

(b) $V = 1{,}200\,\mathrm{m/s}$

Fig. 4-6 Equivalent plastic strain

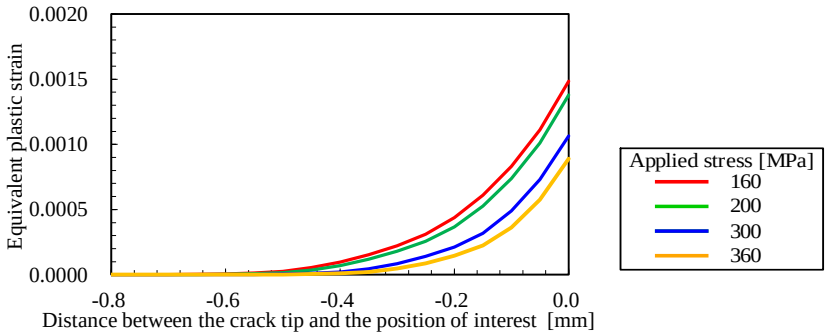

Fig. 4-7 Accumulation of equivalent plastic strains at the point of interest

4.3.2. Crack velocity

The local tensile stresses in the vicinity of the crack tip for $V = 100–1{,}000$ m/s are shown in Fig. 4-8. The remotely applied stress was uniformly set to 200 MPa. Fig. 4-8(a) shows the relationships between the local tensile stress and the crack velocities, and Fig. 4-8(b) shows the local tensile stresses for each crack velocity normalized by the local tensile stress when $V = 100$ m/s. Although elastic materials tend to display a higher local tensile stress for lower crack velocities [28], such monotonic relationship is not observed in Fig. 4-8.

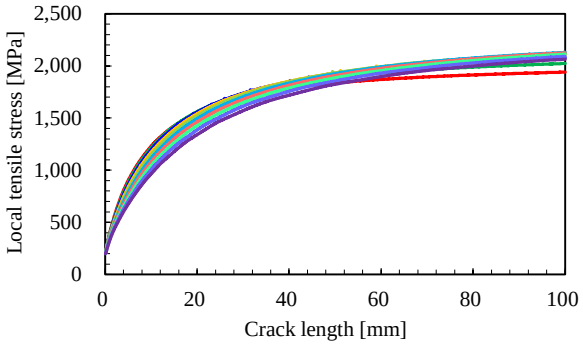

(a) Local stress

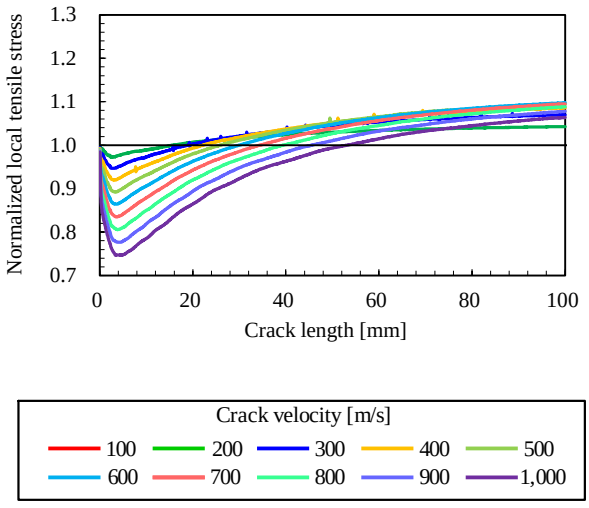

(b) Local stress normalized by that of $V = 100$ m/s

Fig. 4-8 Relationships between the local tensile stresses and the crack velocities ($\sigma_{app} = 200$ MPa)

According to Fig. 4-8, when the SIF was relatively small, the lower crack velocity provided higher local tensile stresses. This is because the plastic region of the crack tip was much smaller, and the condition near the crack tip was similar to that in elastic solids. However, higher crack velocities gradually provided higher local tensile stresses as the crack grew. In general, because the kinetic energy around the propagating crack is larger when the crack velocity is higher, the energy available for the crack tip stress field decreases and the opening displacement behind the crack tip becomes smaller when the crack velocity is higher. Therefore, in elastic solids, the local tensile stress decreases as the crack velocity becomes higher. However, in elastic-viscoplastic solids, the plastic strain rate influences the crack tip field in addition to available energy.

Figure 4-9 shows the equivalent plastic strain rates for each crack velocity. When $V = 100$ m/s, the strain rate is remarkably low and the yield stress does not rise significantly than the yield stresses of the higher crack velocity. When the crack velocity is higher, the strain rates gradually increase and the yield stress near the crack tip rises once the plastic region of the crack tip is sufficiently large. This effect due to strain rate leads to higher local tensile stresses at higher crack velocities. However, because the energy available for the crack tip stress field is smaller when the crack velocity is higher, the monotonic relationship between the local stress and crack velocity cannot be found and it can be found that a certain crack velocity shows the maximum local tensile stress. Accordingly, the local tensile stress in elastic-viscoplastic solids is determined by the balance between the plastic strain rate and energy available for the crack tip field.

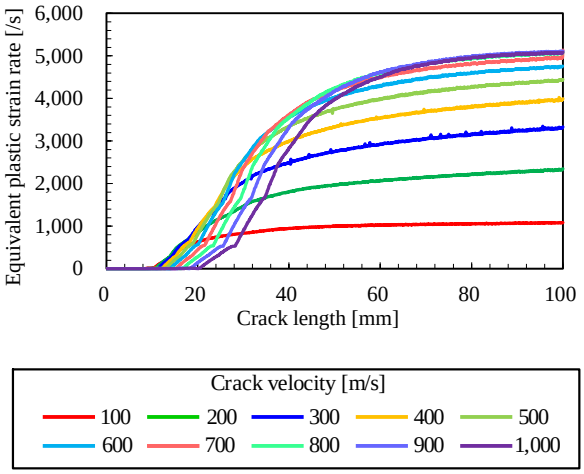

Fig. 4-9 Equivalent plastic strain rates and crack velocity

4.3.3. Temperature and temperature gradient

Temperature is one of the most important factors influencing the behavior of a propagating crack in elastic-viscoplastic solids. In crack propagation and arrest experiments, both the uniform temperature distribution and the temperature gradient should be considered to evaluate the crack arrest toughness K_{ca} [33]. Thus, in addition to temperature effects, it is important to investigate how the temperature gradient influences the local tensile stresses in the vicinity of the crack tip. For all analyses reported in this section, the crack velocity was set to 600 $\mathrm{m/s}$.

Figure 4-10 shows the temperature dependency of the local tensile stresses in the vicinity of the crack tip. At the beginning of crack propagation, the local tensile stresses were higher for higher temperatures than for lower temperatures. This can be explained by that the plastic strain rate near the crack tip is higher in lower SIF because the plastic region does not grow under lower temperature in lower SIF. Once the plastic zone has grown sufficiently even under low temperature, the local tensile stress becomes higher at lower temperatures. According to Fig. 4-10(b), the normalized local tensile stress at lower temperatures increased as the crack became longer. When the temperature is relatively high, the plastic region absorbs more energy available for the crack tip local stress fields than when the temperature is lower.

Next, the influence of temperature gradients is investigated. To consider the influence of temperature gradients, the temperature distribution along the crack path is expressed as

$$T(x) = \begin{cases} T_0 - \Delta T \times (a_{\mathrm{ref}} - x) & (x \le a_{\mathrm{ref}}) \\ T_0 & (x > a_{\mathrm{ref}}) \end{cases} \tag{4-5}$$

where x is the crack length, T_0 is the reference temperature, ΔT is the temperature gradient, and a_{ref} is the reference crack length. Namely, the temperature increases linearly for $0 \le x \le a_{\mathrm{ref}}$ and reaches the constant reference temperature when $a_{\mathrm{ref}} < x$. T_0 was set to $20℃$ in all the analyses.

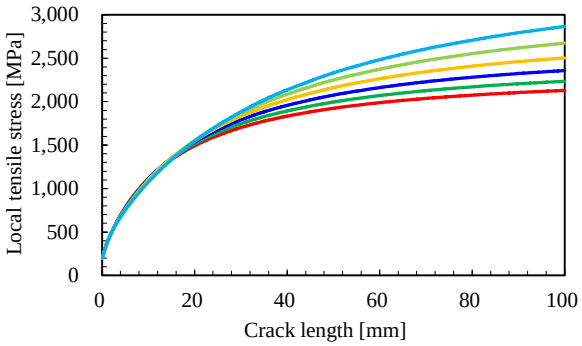

(a) Local tensile stress of each temperature

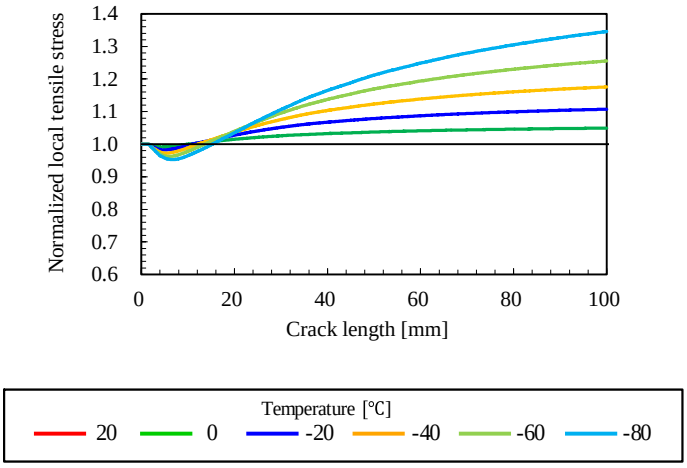

(b) Normalized local tensile stress

Fig. 4-10 Temperature dependency of the local tensile stress ($V = 600$ m/s, $\sigma_{\mathrm{app}} = 200$ MPa)

Three levels of temperature gradient are considered: $\Delta T = 500, 1{,}000$ and $2{,}000\,℃/\mathrm{m}$. Considering that ΔT is often set to $300\,℃/\mathrm{m}$ in crack arrest tests [33], the values of ΔT employed in this study are sufficiently high to investigate the influence of the temperature gradient on the local stresses.

Figure 4-11 compares the local tensile stresses under each temperature gradient for the same reference crack length. The influence of the reference crack length under the same temperature gradient is shown in Fig. 4-12. Figs. 4-11(b) and 4-12(b) show the local tensile stresses at $x = a_{\mathrm{ref}}$ normalized by the local tensile stress when the temperature distribution was uniform. These figures clearly show that the temperature gradient did not influence the local tensile stresses in the vicinity of a rapidly propagating crack tip in elastic-viscoplastic solids. Accordingly, the temperature gradient can be ignored in evaluating the local tensile stresses, whereas the temperature at the position of interest is critical.

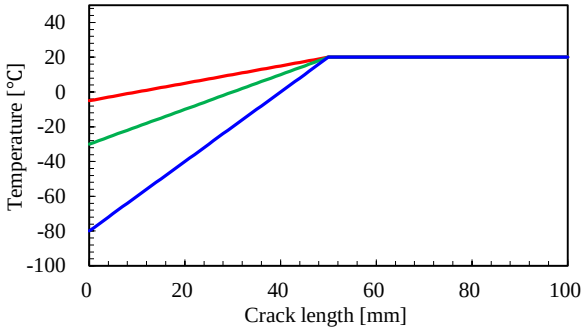

(a) Temperature distribution

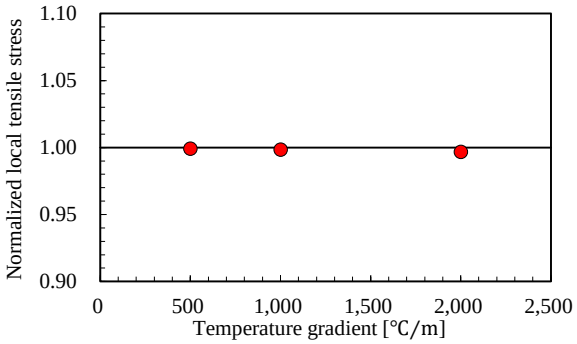

(b) Normalized local stress at the reference crack length

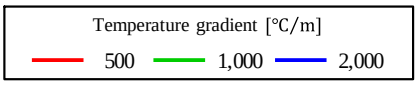

Fig. 4-11 Local stress for each reference temperature gradient in case of the same reference crack length ($a_{\mathrm{ref}} = 50$ mm)

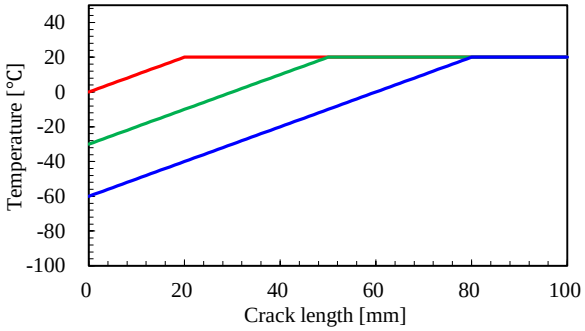

(a) Temperature distribution

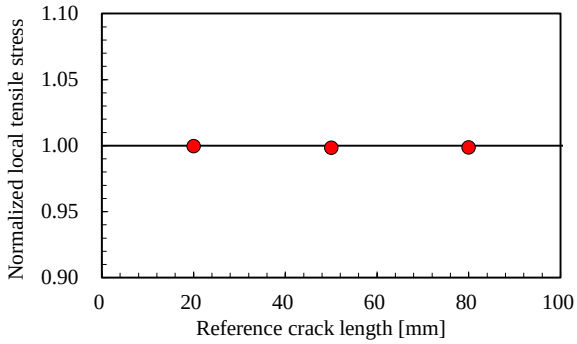

(b) Normalized local stress at the reference crack length

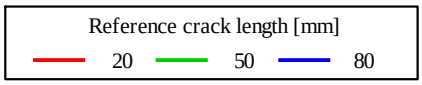

Fig. 4-12 Local stress for each reference crack length in case of the same temperature gradient ($\Delta T = 1{,}000$ ℃/m)

4.4. Unsteady state crack propagation

The crack velocity is not necessarily constant in actual crack propagation phenomena. Namely, the crack is unsteady in real phenomena. In particular, crack arrest experiments have shown that the crack experiences some deceleration prior to a crack arrest event [25,35]. Chapter 3 showed crack acceleration under isothermal conditions. Thus, it is important to investigate the effects of unsteady phenomena on the crack propagation and arrest behaviors in elastic-viscoplastic solids.

In elastic solids, Nishioka [36] conducted asymptotic analyses of unsteady crack propagation which showed that the local stress field in the vicinity of a crack tip is not influenced by unsteady effects. Considering this asymptotic solution, the model proposed by Shibanuma et al. [10]

ignored the acceleration and deceleration when it evaluated the local stresses. However, dynamic elastic finite element analyses have shown that the deceleration influences the dynamic SIF just before a crack arrest event [33]. Additionally, crack propagation experiments indicate that crack acceleration and deceleration influences the experimentally obtained critical dynamic SIFs in elastic polymers [16,37]. Accordingly, Section 4.4.1 analysed unsteady crack propagation in elastic solids before investigating the unsteady effects in elastic-viscoplastic solids because elastic-viscoplastic solids are usually complicated than elastic solids. After that, elastic-viscoplastic solids were analysed from the perspective of unsteady crack propagation.

The unsteady crack velocity history is described as a function of the acceleration k, maximum crack velocity $V_{\max}$, minimum velocity $V_{\min}$, and reference crack velocity V_{ref}. In the analyses, the reference crack velocity was defined as the crack velocity when the crack length reached the reference crack length a_{ref}. After the crack reached the reference crack length, the crack velocity became constant value, equal to the reference crack velocity. Unless otherwise noted, the reference, maximum, and minimum crack velocities were set to 600 m/s, $2{,}000\ \mathrm{m/s}$ and $400\ \mathrm{m/s}$, respectively. $k = 0\ \mathrm{m/s^2}$ means that the crack velocity is constant. Fig. 4-13 shows the crack velocity histories in which the reference crack length was 100 mm employed to evaluate the influence of unsteady effects on the local tensile stresses.

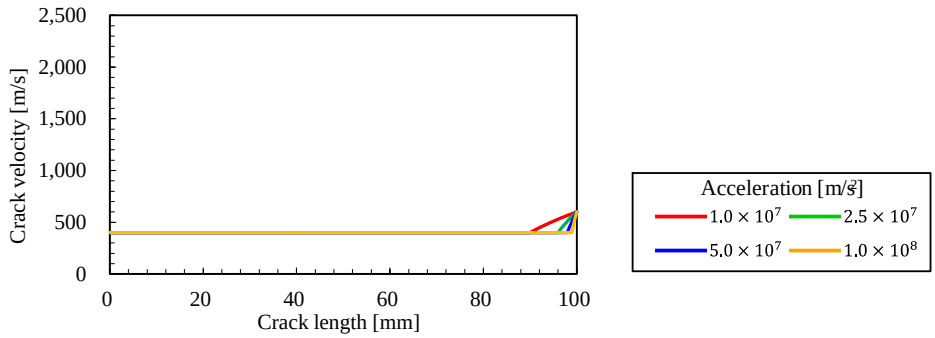

(a) Positive acceleration

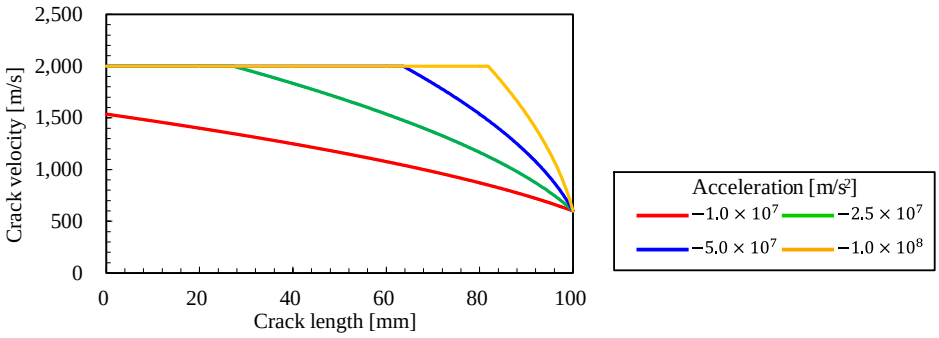

(b) Negative acceleration

Fig. 4-13 Crack velocity histories employed for unsteady effect evaluations

($V_{\mathrm{ref}} = 600$ m/s, $V_{\max} = 2{,}000$ m/s, $V_{\min} = 400$ m/s, $a_{\mathrm{ref}} = 100$ mm)

4.4.1. Linear elastic problem

First, the unsteady crack propagation was analysed in linear elastic solids. The local tensile stresses when the crack reached the reference crack length for each crack acceleration are shown in Fig. 4-14. The normalized local tensile stress means that the local tensile stress is normalized by the local tensile stress when the crack velocity was constant in this section. The crack velocity histories were the same as those shown in Fig. 4-13. When the acceleration was positive, the normalized local tensile stress was slightly less than 1.00, but the variations were very small. When the acceleration was negative, the normalized local tensile stress was negative except when $k = -1.0 \times 10^7$ m/s^2. In the negative acceleration analyses, the greater the acceleration was, the lower the normalized local tensile stress was.

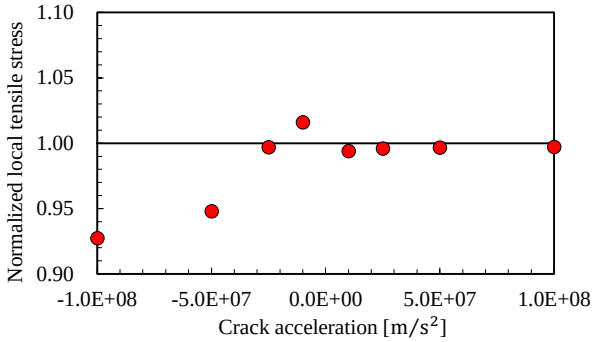

Fig. 4-14 Normalized local tensile stress transition for each acceleration in linear elastic solids

In order to investigate the causes of above unsteady effect shown in Fig. 4-14, the analyses which had the accelerations from the beginning of crack propagation to the middle of crack propagation were carried out. The crack velocity is expressed as

$$V(x) = \begin{cases} \sqrt{V_{\mathrm{ref}} - 2kx} & (x \le a_{\mathrm{ref}}) \\ V_{\mathrm{ref}} & (x > a_{\mathrm{ref}}) \end{cases} \tag{4-6}$$

where V_{ref} is the reference crack velocity, x is the crack length, and a_{ref} is the reference crack length. As for the analyses shown in Fig. 4-15, the maximum and minimum crack velocities are 2,000 and 400 m/s; the reference crack length is 80 mm. After the crack length reached the reference crack length, the crack propagation became steady state and the crack velocity became constant. Thus, these analyses whose crack velocity histories were expressed by Eq. (4-6) are named partly unsteady crack propagation analyses which were composed of both unsteady crack propagation (until the reference crack length) and steady crack propagation (after the reference crack length). In contrast, the analyses shown in Fig. 4-14 reflect fully unsteady crack propagation.

Figure 4-15 shows the normalized local tensile stresses under acceleration from the beginning of crack propagation to the reference crack length in the partly unsteady crack propagation analyses. In the case of positive acceleration (Fig. 4-15(a)), the normalized local tensile stresses after the crack velocity reached the reference crack velocity were almost the same, regardless of acceleration. However, as shown in Fig. 4-15(b), the normalized local tensile stresses after the crack velocity reached the reference crack velocity exhibited some variation. Note that the normalized local tensile stresses after the crack velocity reached the reference crack velocity were greater than 1.00, even when the normalized local tensile stress at $x = a_{\mathrm{ref}}$ was less than 1.00.

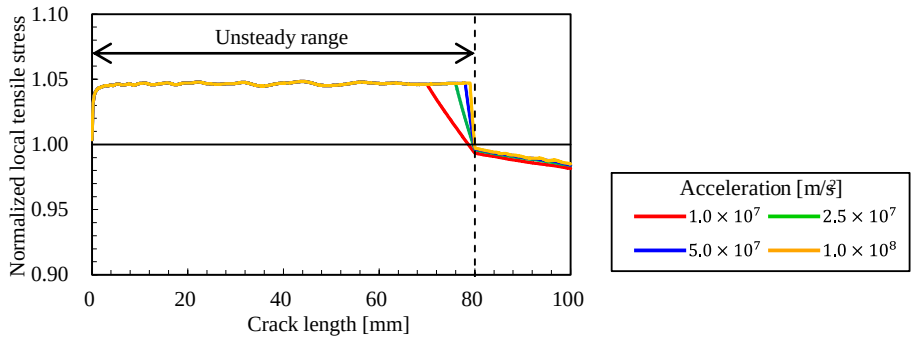

(a) Positive acceleration

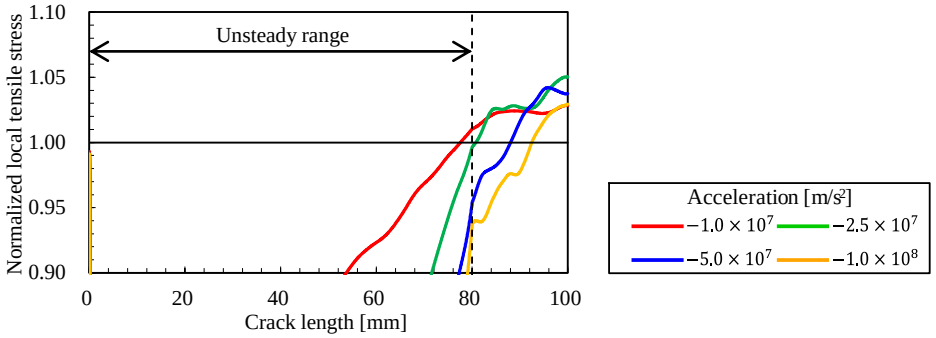

(b) Negative acceleration

Fig. 4-15 Normalized local tensile stresses for the partly unsteady crack propagation analyses which have accelerations in case of $a_{\mathrm{ref}} = 80$ mm

According to the results shown in Fig. 4-15, the normalized local tensile stresses were less than 1.00 in the case of positive acceleration and greater than 1.00 in the case of negative acceleration after the crack lengths reached the reference crack length. This indicates that the energy influx and outflow played a role to change the normalized local tensile stress during unsteady crack propagation in linear elastic solids. Namely, the strain energy near the crack tip leaks from that region to become kinetic energy for the positive acceleration cases, and the kinetic energy flows in the region near the crack tip become the elastic strain energy in the negative acceleration cases. However, when the negative acceleration is very high, the normalized local tensile stresses were less than 1.00 just when the crack length reached the reference crack length in all cases except $k = -1.0 \times 10^7$ m/s^2. This is because the influx of energy is delayed with respect to the change in crack velocity by the sudden change of crack velocity. Therefore, the influx of energy increased the local tensile stresses after the crack velocity became constant.

The above explanation based on the energy influx and outflow is supported by the results shown in Fig. 4-16, which compares the normalized local tensile stress history for each maximum crack velocity under partly unsteady crack propagation ($k = -1.0 \times 10^7$ m/s^2, $a_{\mathrm{ref}} = 80$ mm). The lower maximum crack velocity produces a smaller variation in the normalized local tensile stress than the longer reference crack length. This difference is caused by the differences in the energy influx to the crack tip field. Therefore, the reason why the unsteady effect is not observed in the cases of positive acceleration in Fig. 4-14 is that the variation in the crack velocity is small.

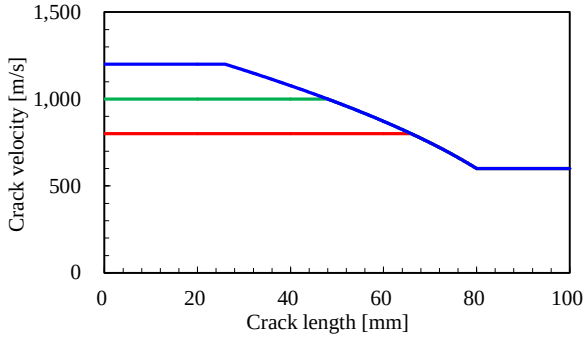

(a) Crack velocity history

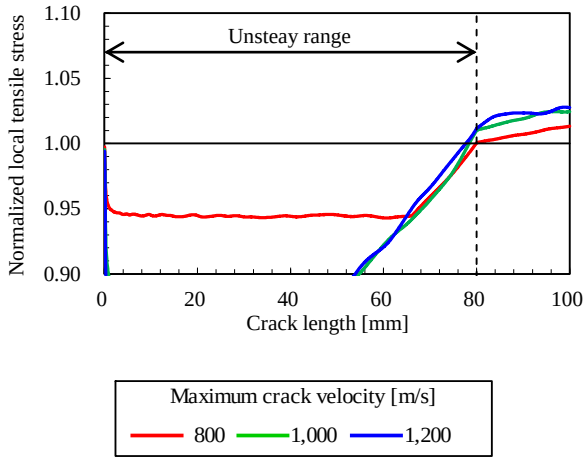

(b) Normalized local stress

Fig. 4-16 Local stress transition against each maximum crack velocity ($k = -1.0 \times 10^7$ m/s^2, $V_{\mathrm{ref}} = 600$ m/s)

Considering above results, the crack velocity history itself plays a critical role in determining the variation in the local tensile stress. The rise and decline of the local tensile stress are caused by the influx and outflow of energy in the vicinity of the crack tip. Therefore, to investigate unsteady effects in linear elastic solids, it is necessary to consider not the acceleration, but the crack velocity history itself.

In fact, according to Nishioka and Kondo [38], the singularity of the crack tip local stress field is not influenced by crack acceleration in linear elastic crack propagation, which seems to be inconsistent with above result. However, their analysis considered only the acceleration and did not take care of crack velocity history. As Fig. 4-16 shows, even when the crack acceleration is higher, the local stress variation is small if the change of crack velocity is small. Thus, above result is not inconsistent with analytical solutions obtained by Nishioka and Kondo [38].

4.4.2. Elastic-viscoplastic problem

This section investigates the influence of unsteady effects on the local tensile stresses in elastic-viscoplastic solids by following the results of Section 4.4.1. As described in Section 4.4.1, the crack velocity history influences the local tensile stresses in the vicinity of the propagating crack tip in elastic solids through the influx or outflow of energy. As noted in Section 4.3, the contribution of the available energy to the local tensile stresses is relatively small in elastic-viscoplastic solids because the strain rate and accumulation of plastic strain also influence the local tensile stresses. Therefore, the influence of unsteady effects in elastic-viscoplastic solids is expected to differ from that in elastic solids.

Figure 4-17 shows the normalized local tensile stresses for each rate of acceleration when the crack length reached 100 mm under fully unsteady crack propagation. Just like in Section 4.4.1, the local tensile stresses are normalized by the local tensile stress of steady state crack propagation in this section. In the same way as the analyses shown in Fig. 4-14, this figure uses the crack velocity histories shown in Fig. 4-13. In these analyses, the crack continued to experience acceleration until the crack length reached 100 mm, at which point the crack velocity remained at 600 m/s. Although the normalized local tensile stresses exhibited a similar trend to those for linear elastic solids (see Fig. 4.14), the variation in the normalized local tensile stresses was smaller than in linear elastic solids, especially for larger negative accelerations.

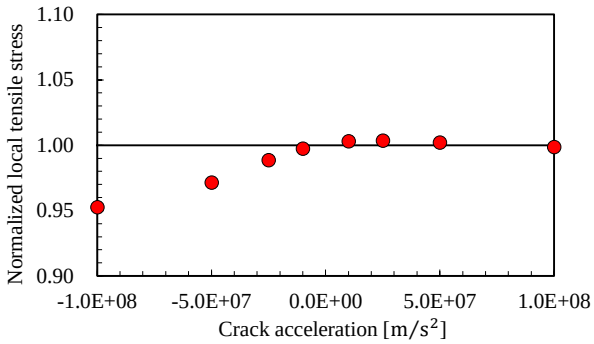

Fig. 4-17 Normalized local tensile stress transition for each acceleration in elastic-viscoplastic solids

As same as in Fig. 4-15, Fig. 4-18 shows the normalized local tensile stress histories for partly unsteady crack propagation analyses in elastic-viscoplastic solids, where the acceleration ran from the beginning of crack propagation to the middle of crack propagation. The reference crack length was again set to 80 mm. Unlike the linear elastic cases shown in Fig. 4-15, Fig. 4-18 exhibits only small deviations after the crack length reached the reference crack lengths. In particular, although the normalized local tensile stresses for negative acceleration in the elastic analyses deviated from 1.00 significantly after the crack length reached the reference crack length (Fig. 4-15(b)), the normalized local stresses shown in Fig. 4-18(b) seemed to converge to 1.00 after the reference crack length was reached.

These results indicate that the energy influx and outflow are not the dominant influences on the unsteady effect in elastic-viscoplastic solids. This explanation is supported by Fig. 4-19, which shows the normalized local tensile stress histories for different maximum crack velocities in elastic-viscoplastic solids. The normalized local tensile stresses after the crack length reached the reference crack length were not influenced by the maximum crack velocity. Therefore, the energy influx and outflow should not be regarded as the dominant unsteady effects in elastic-viscoplastic solids.

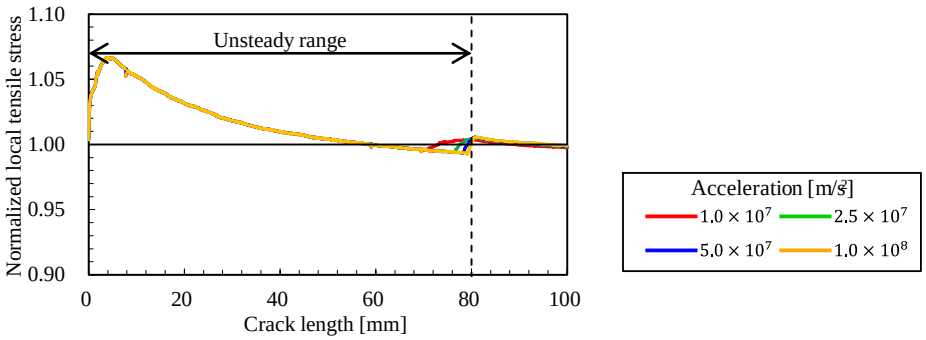

(a) Positive acceleration

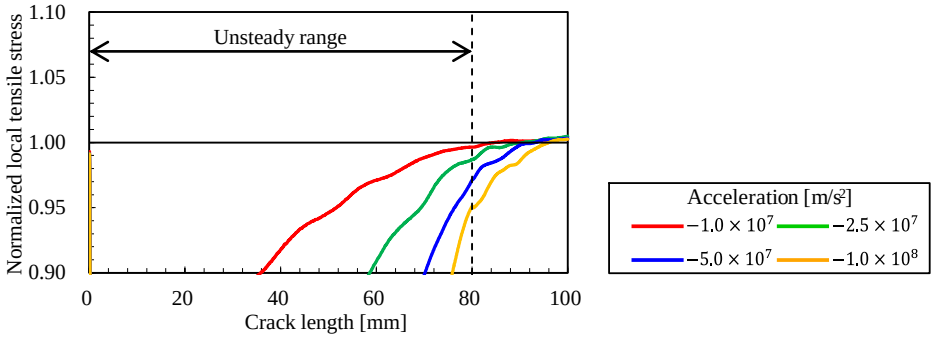

(b) Negative acceleration

Fig. 4-18 Normalized local tensile stress histories for each acceleration in the elastic-viscoplastic solids

This difference between the elastic and elastic-viscoplastic solids is caused by the strain rate dependency. As discussed in Section 3.2, the local tensile stress is determined by the combination of the energy available for the crack tip field and the strain rate in the elastic-viscoplastic solids. Even when the crack experiences acceleration, the unsteady effects are small in elastic-viscoplastic solids than in elastic solids because the strain rate is determined by the present crack velocity. Therefore, the reference crack velocity is expected to influence the variation in local tensile stresses because the growth of the plastic region depends on the crack velocity. Namely, when the reference crack velocity is high, the plastic region is small and the crack tip region is relatively similar to the elastic condition. Fig. 4-20 compares the variations of the local tensile stresses for three reference crack velocities with each crack velocity history. The analyses were carried out assuming fully unsteady crack propagation. The variations were represented by the local tensile stresses normalized by those in steady state crack propagation with each reference crack velocity. The normalized local tensile stresses shown in Fig. 4-20 are consistent with the above mentioned trend whereby the variation with high crack velocity is larger.

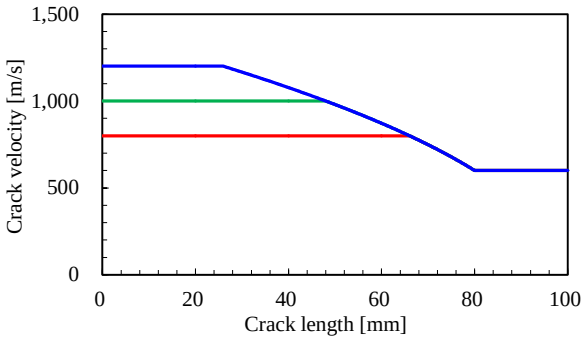

(a) Crack velocity history

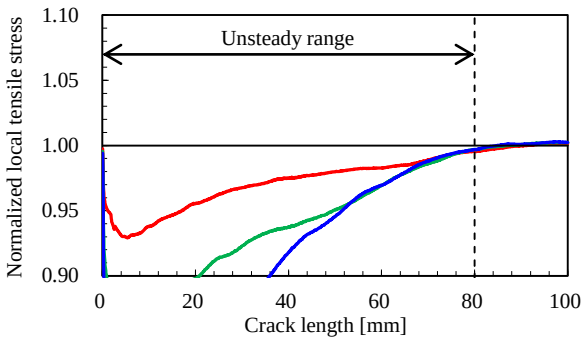

(b) Normalized local stress

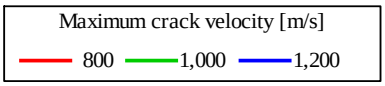

Fig. 4-19 Normalized local tensile history for each maximum crack velocity

($k = -1.0 \times 10^7$ m/s^2, $a_{\mathrm{ref}} = 80$ mm)

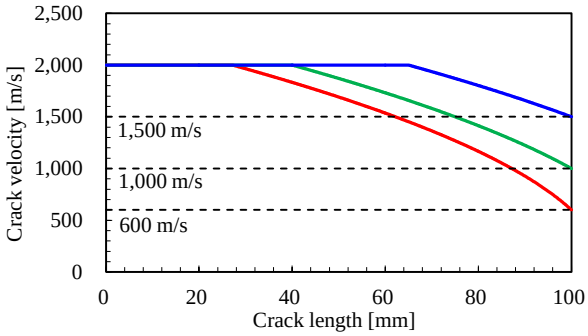

(a) Crack velocity hisotry

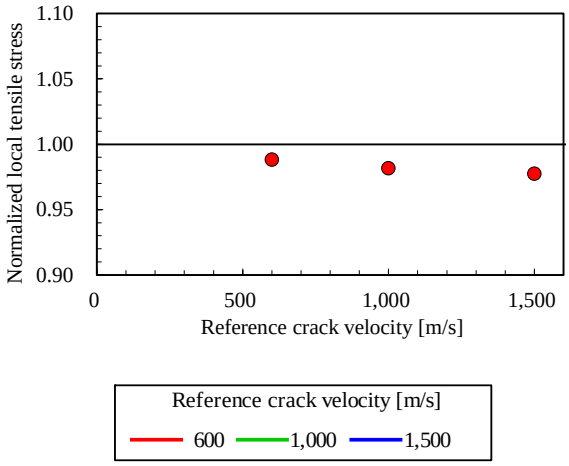

(b) Normalized local tensile stress

Fig. 4-20 Normalized local tensile stresses for three levels of reference crack velocities ($k = -2.5 \times 10^7$ m/s^2)

Therefore, because the contribution of the energy influx and outflow to the local tensile stress variation is small in elastic-viscoplastic solids, it is reasonable to consider that there are other causes of the variation in local tensile stresses in elastic-viscoplastic solids. To investigate the underlying cause of the variation, the plastic strain accumulation was examined. The accelerations were negative in the all analyses here.

Figure 4-21 shows the plastic strain at the position of interest with respect to the distance from the crack tip in case of fully unsteady crack propagation analyses. The position of interest was 0.15 mm away from the crack tip when the crack length reached 100 mm. Namely, this position was located at $(100.15, 0)$ in the coordinate shown in Fig. 4-2. In these analyses, the reference crack velocity was 600 m/s. The plastic strain accumulation at the position of interest decreased

in the cases of the higher accelerations because the crack velocity was high just before the crack length reached the reference crack length. Therefore, the local tensile stress became smaller. Namely, the crack velocity just before the crack reaches the reference crack length is important when the variation of the local tensile stresses is considered under unsteady effects in elastic-viscoplastic solids. Although the same mechanism is expected to act when the acceleration is positive, the local tensile stresses are almost the same regardless of the values of the positive acceleration. This is because there is no significant difference in the accumulation of plastic strain between the cases when $V = 400\ \mathrm{m/s}$ and $V = 600\ \mathrm{m/s}$.

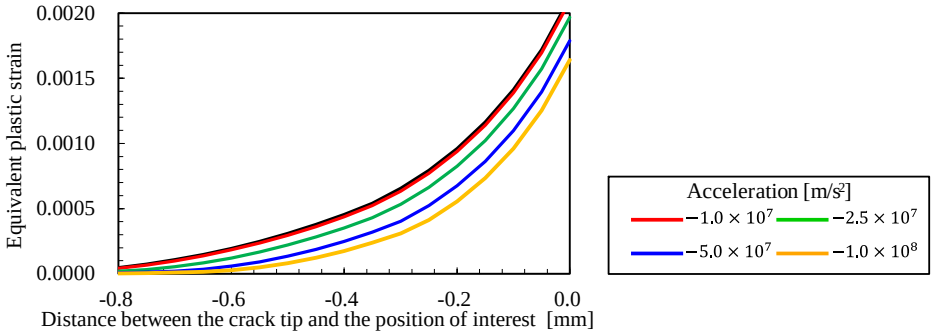

Fig. 4-21 Equivalent plastic strain at 0.15 mm from the crack tip when the crack reached the reference crack length

($V_{\mathrm{ref}} = 600\ \mathrm{m/s}$)

4.5. Discussion

4.5.1. Factors governing the local tensile stresses

Sections 4.3 and 4.4 presented results from a series of systematic analyses to investigate how various factors influence the local tensile stress in the vicinity of a propagating crack tip in elastic-viscoplastic solids. Section 4.3 clearly showed that the crack length, applied stress, crack velocity, and temperature determine the local tensile stresses. Section 4.3 also indicated that the local tensile stress is not influenced by temperature gradients. It is worth noting that SIF cannot be applied to characterize the local tensile stress because plastic strain accumulations depend on the combination of the applied stress and the crack length. Therefore, the applied stress and crack length should be separately considered as the determinants.

According to Section 4.4.1, the unsteady effects are sometimes remarkable in elastic analyses, because the energy influx and outflow near the crack tip directly influence the local tensile stresses in the vicinity of the crack tip. On the other hand, the unsteady effects in the elastic-viscoplastic solids are smaller than the effects in elastic solids according to Section 4.4.2. Although Section 4.4.2 shows that the unsteady effects cannot be ignored when the acceleration is extremely high, e.g., -1.0×10^8 m/s^2, such extremely high acceleration is hardly observed in the actual crack propagation and arrest behaviors. For example, the acceleration measured in crack propagation experiments to evaluate the local fracture stress was 2.1×10^7 m/s^2 at most in Chapter 3. The measured crack velocity histories in previous studies suggest that the maximum accelerations were approximately -1.0×10^7 m/s^2 [39], -9.0×10^6 m/s^2 [40], -2.5×10^6 m/s^2 [34], and -2.3×10^6 m/s^2 [41]. Although these accelerations are just examples and depend on experimental conditions and materials, it can be said that the accelerations are usually less than $\pm 1.0 \times 10^7$ m/s^2 and seldom exceed $\pm 2.5 \times 10^7$ m/s^2 [42,43]. Therefore, it is reasonable to consider the actual unsteady effects as being weaker than those shown in Fig. 4-17, and so the variation of the local tensile stresses due to unsteady effects are no more than 2–3%.

Although the variation depends on the reference crack velocity (because the degree of plastic region growth is determined by the crack velocity, as mentioned in Section 4.4.2), the variation is only 2.3% when the reference crack velocity is 1,500 m/s (see Fig. 4-20). The crack velocity seldom exceeds 1,500 m/s [34]. According to the above discussion, because it is difficult to distinguish such variation from errors in local stress evaluations, considering the accuracy of dynamic elastic-viscoplastic analyses in FEM, it is reasonable to regard the unsteady effects as sufficiently small to be practically negligible in elastic-viscoplastic analyses.

Therefore, when the constitutive law does not change, the local tensile stress σ_{yy} at the characteristic distance from a propagating crack can usually be described as

$$\sigma_{yy} = f\left(a, \sigma_{\mathrm{app}}, V, T\right) \tag{4-7}$$

Namely, when brittle crack propagation and arrest behaviors are simulated, instantaneous temperature and crack velocity at the time of interest have to be considered and their histories do not have to be incorporated.

However, it is worth noting that extremely high acceleration can occur in so-called duplex crack arrest tests. Specimens employed in duplex tests are composed of a crack running plate and a test plate [33]. Because the crack running plate is much more brittle than the test plate, the crack

velocity can suddenly decrease when the crack enters the test plate from the crack running plate [11]. Therefore, unsteady effects may influence the local tensile stresses in duplex crack arrest tests when the toughness of the two plates are much different.

4.5.2. Maximum stress velocity

In Section 4.3.2, the monotonic relationship between the crack velocity and the local tensile stress observed in linear elastic solids could not be found in elastic-viscoplastic solids. Instead, Fig. 4-8 indicates that the crack velocity which provides the maximum local tensile stress is determined by the crack length and the applied stress. This crack velocity is called as the "maximum stress velocity" here. One example of this maximum stress velocity is shown in Fig. 4-22 for an applied stress of 360 MPa and a temperature of 20℃. As noted in Section 4.3.2, this maximum stress velocity is determined by the balance of the strain rate and the energy available to the crack tip field. As shown in Fig. 4-22, when the crack length is short, the plastic zone is small and the energy available for the crack tip field is dominant, and so the maximum stress velocity is lower. Namely, the circumstances around the crack tip is similar to the elastic condition. As the crack length becomes longer and the crack tip plastic zone grows, the strain rate contributes to the determination of the maximum stress velocity and the higher crack velocity becomes the maximum stress velocity.

According to some previous crack arrest experiments, it has been reported that there is a lower limit crack velocity for brittle crack propagation in steel [34,44,45]. Namely, the crack velocity of a brittle crack suddenly drops to zero from the lower limit crack velocity at the crack arrest event. The existence of this lower limit crack velocity was known in crack arrest experiments, although the reason for this lower limit remains unclear from the perspective of the energy balance approach [45]. However, based on the local fracture stress criterion, the existence of the lower limit crack velocity can be explained by the maximum stress velocity. Therefore, the existence of the maximum stress velocity supports the validity of the local fracture stress criterion as the theory explaining brittle crack propagation and arrest behavior in steel.

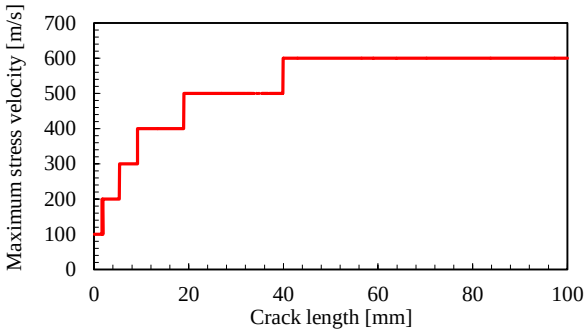

Fig. 4-22 Maximum crack velocity ($\sigma_{\mathrm{app}} = 360$ MPa, $T = 20$℃)

4.6. Conlusion

In this chapter, a series of systematic finite element analyses were conducted to investigate the factors governing the local tensile stress in the vicinity of a rapidly propagating crack tip. This chapter aims to deepen the understanding of the local fracture stress criterion for brittle crack propagation and arrest behaviors in steel through investigations of the local tensile stress amplitude.

Steady state crack propagation was first analysed to investigate the influence of the SIF, crack velocity, temperature, and temperature gradient. It was found that, even for the same SIF, the local tensile stresses vary according to the combination of the crack length and applied stress. These differences are caused by the accumulation of plastic strain in the vicinity of the crack tip. This finding may provide new perspectives for interpreting past crack arrest experiments, because conventional studies assumed that the same SIF provided the same local tensile stress [10]. The crack velocity is important in considering the local tensile stresses, but the monotonic relationship between the crack velocity and the local tensile stress found in elastic solids is not valid in elastic-viscoplastic solids. This is because the plastic strain rate influences the local tensile stresses in rate-dependent elastic-viscoplastic solids. Therefore, there is a “maximum stress velocity” which provides the maximum local tensile stress when all other conditions are equal. The existence of this maximum stress velocity corresponds to the lowest crack velocity for brittle crack propagation in steel found by previous experiments as noted above. Temperature was also found to influence the local tensile stresses. Temperature was a critical factor in determining the local tensile stress and the rate of change in tensile stress with respect to crack length. However, the temperature gradient has no effect on the local tensile stresses.

In addition to steady state crack propagation, the influence of unsteady effects in both linear elastic

and elastic-viscoplastic solids were also investigated. This is the first systematic evaluation of the unsteady effects with respect to local tensile stresses. The results showed that the crack velocity history changed the local tensile stress remarkably in elastic solids, but the unsteady effects were practically negligible in the typical crack propagation process in elastic-viscoplastic solids because the contribution of the energy influx and outflow to the local tensile stress was small. However, because extremely high crack acceleration influences the local tensile stress, unsteady effects could influence the crack behavior in duplex crack arrest tests which is usually composed of two types of steels. These results on unsteady effects in elastic-viscoplastic solids were considered for the first time and shown to be significantly important to interpret actual crack behaviors.

The systematic crack propagation analyses conducted in this study showed that the local tensile stress in the vicinity of a rapidly propagating crack tip in rate-dependent elastic-viscoplastic homogeneous materials like steel was governed by the crack length, applied stress, crack velocity, and temperature. Furthermore, findings based on the relationships identified by the above analyses between the local tensile stresses and the macroscopic crack behavior will be beneficial for understanding brittle crack propagation and arrest behaviors in steel based on the local fracture stress criterion.

Reference

[1] T. Nishioka, The State of the Art in Computational Dynamic Fracture Mechanics, JSME Int. J. Ser. A. 37 (1994) 313–333.

[2] B. Jia, Z.Q. Wang, Y.D. Li, W.Y. Liang, Viscoplastic solution to field at steadily propagating crack tip in linear-hardening materials, Appl. Math. Mech. 27 (2006) 527–533. doi:10.1007/s10483-006-0413-1.

[3] W. Zhen-qing, Z. Bo, S.U. Juan, Perfect elastic-viscoplastic field at mode I dynamic propagating, Appl. Math. Mech. 28 (2007) 495–500.

[4] P. Ståhle, Dynamic crack tip fields at steady growth and vanishing strain-hardening, J. Mech. Phys. Solids. 41 (1993) 919–936. doi:10.1016/0022-5096(93)90005-Z.

[5] C.H. Popelar, Y.C. Sheu, The characteristics of viscoplastic effects in dynamic crack propagation in nuclear reactor pressure vessel steels, Nucl. Eng. Des. 133 (1992) 411–418. doi:10.1016/0029-5493(92)90166-S.

[6] L.B. Freund, J.W. Hutchinson, P.S. Lam, Analysis of high-strain-rate elastic-plastic crack growth, Eng. Fract. Mech. 23 (1986) 119–129. doi:10.1016/0013-7944(86)90181-5.

[7] L.B. Freund, Y.J. Lee, Observations on high strain rate crack growth based on a strip yield model, Int. J. Fract. 42 (1990) 261–276. doi:10.1007/BF00013217.

[8] S. Ostlund, On Numerical Modeling and Fracture Criteria of Dynamic Elastic-Viscoplastic Crack Growth, Int. J. Fract. 44 (1990) 283–299. doi:10.1007/BF00036169.

[9] S. Yoshimura, G. Yagawa, S.N. Atluri, Generation and Propagation Analyses of High-Strain-Rate Dynamic Crack Propagation in A Visco-Plastic Solid, Nucl. Eng. Des. 111

(1989) 273–289.
[10] K. Shibanuma, F. Yanagimoto, T. Namegawa, K. Suzuki, S. Aihara, Brittle crack propagation/arrest behavior in steel plate - Part I: Model formulation, Eng. Fract. Mech. 162 (2016) 324–340. doi:10.1016/j.engfracmech.2016.02.054.
[11] K. Shibanuma, F. Yanagimoto, T. Namegawa, K. Suzuki, S. Aihara, Brittle crack propagation/arrest behavior in steel plate - Part II: Experiments and model validation, Eng. Fract. Mech. (2016). doi:10.1016/j.engfracmech.2016.02.053.
[12] J.D. Achenbach, M.F. Kanninen, C.H. Popelar, Crack-tip fields for fast fracture of an elastic-plastic material, J. Mech. Phys. Solids. 29 (1981) 211–225. doi:10.1016/0022-5096(81)90027-2.
[13] X. Deng, A.J. Rosakis, A finite element investigation of quasi-static and dynamic asymptotic crack-tip fields in hardening elastic-plastic solids under plane stress - Part I: Crack growth in linear hardening materials, Int. J. Fract. 57 (1992) 291–308. doi:10.1007/BF00013054.
[14] A. Bousquet, S. Marie, P. Bompard, Propagation and arrest of cleavage cracks in a nuclear pressure vessel steel, Comput. Mater. Sci. 64 (2012) 17–21. doi:10.1016/j.commatsci.2012.04.026.
[15] F. Yanagimoto, K. Shibanuma, K. Suzuki, T. Matsumoto, S. Aihara, Local stress in the vicinity of a propagating cleavage crack tip in ferritic steel, Mater. Des. 144 (2018) 361–373.
[16] K. Arakawa, T. Mada, Unsteady dynamic crack propagation in a brittle polymer, Exp. Mech. 47 (2007) 609–615. doi:10.1007/s11340-006-9020-x.
[17] E. Sharon, S.P. Gross, J. Fineberg, Energy dissipation in dynamic fracture, Phys. Rev. Lett. 76 (1996) 2117–2120. doi:10.1103/PhysRevLett.76.2117.
[18] Dassault Systems, SIMULA Abaqus Analysis User's Manual, (2014).
[19] F. Yanagimoto, K. Shibanuma, Y. Nishioka, Y. Shirai, K. Suzuki, T. Matsumoto, Local stress evaluation of rapid crack propagation in finite element analyses, Int. J. Solids Struct. 144–145 (2018) 66–77. doi:10.1016/j.ijsolstr.2018.04.014.
[20] T.L. Anderson, Fracture Mechanics Fundamentals and Applircations 3rd ed., CRC Press, 2005.
[21] P.E. Bennett, G.M. Sinclair, Parameter Representation of Low-Temperature Yield Behavior of Body-Centered Cubic Transition Metals, J. Basic Eng. 88 (1966) 518–524.
[22] M. Toyosada, K. Gotoh, The Estimating Method of Critical CTOD and J integral at Arbitrary Crosshead Speed, J. Soc. Nav. Archit. Japan. 172 (1992).
[23] K. Gotoh, H. Hirasawa, M. Toyosada, A Simple Estimating Method of Constitutive Equation for Structural Steel as a Function of Strain Rate and Temperature, J. Soc. Nav. Archit. Japan. 176 (1994) 501–507.
[24] H.W. Swift, Plastic instability under plane stress, J. Mech. Phys. Solids. 1 (1952) 1–18. doi:10.1016/0022-5096(52)90002-1.
[25] B.R. Bass, C.E. Pugh, J.K. Walker, Elastodynamic fracture analysis of large crack-arrest experiments, Nucl. Eng. Des. 98 (1987) 157–169. doi:10.1016/0029-5493(87)90164-6.
[26] J.A. Joyce, R.E. Link, C. Roe, J.C. Sobotka, Dynamic and static characterization of compact crack arrest tests of navy and nuclear steels, Eng. Fract. Mech. 77 (2010) 337–347. doi:10.1016/j.engfracmech.2009.04.006.
[27] L.B. Freund, J.W. Hutchinson, High strain-rate crack growth in rate-dependent plastic solids, J. Mech. Phys. Solids. 33 (1985) 169–191.
[28] K.B. Broberg, Cracks and Fracture, Academic Press, 1999.
[29] T. Akiyama, A. Katoh, I. Watanabe, M. Kawahara, A Study for the Evaluation of Brittle Crack Arrestability by the WIde Plate Duplex Esso Test, J. Soc. Nav. Archit. Japan. 152 (1983) 412–418.
[30] H. Jaeckels, T. Iung, A. Pineau, Dynamic Crack Propagation and Crack Arrest

Behaviour in Relation To Brittle Intergranular and Cleavage Fracture, Fatigue Fract. Eng. Mater. Struct. 17 (1994) 1281–1293. doi:10.1111/j.1460-2695.1994.tb00216.x.
[31] T. Kawabata, Y. Nishizono, S. Aihara, Brittle crack propagation behavior in a member subjected to bending load, Theor. Appl. Fract. Mech. 92 (2017) 266–275. doi:10.1016/j.tafmec.2017.09.005.
[32] R.E. Link, J.A. Joyce, C. Roe, Crack arrest testing of high strength structural steels for naval applications, Eng. Fract. Mech. 76 (2009) 402–418. doi:10.1016/j.engfracmech.2008.11.006.
[33] The Japan Wedling Engineering Society, WES2815 Test method for brittle crack arrest toughness, (2014). http://www-it.jwes.or.jp/wes_ki/wesippan.jsp?arg=2815e-1.
[34] S. Machida, H. Yoshinari, Some recent experimental work in Japan on fast fracture and crack arrest, Eng. Fract. Mech. 23 (1986) 251–264.
[35] A.T. Zehnder, A.J. Rosakis, Dynamic fracture initiation and propagation in 4340 steel under impact loading, Int. J. Fract. 43 (1990) 271–285. doi:10.1007/BF00035087.
[36] T. Nishioka, Computational dynamic fracture mechanics, Int. J. Fract. 86 (1997) 127–159. doi:10.1023/A:1007376924191.
[37] L. Cheng, A.J. Rosakis, L.B. Freund, The interpretation of optical caustics in the presence of dynamic non-uniform crack-tip motion histories: A study based on a higher order transient crack-tip expansion, Int. J. Solids Struct. 30 (1993) 875–897. doi:10.1016/0020-7683(93)90017-2.
[38] T. Nishioka, K. Kondo, Derivation of In-plane Mixed-Mode Asymptotic Solutions ofr an Unsteadily Fast-Propagating Crack Tip Using a Sympolic Manipulation System, Trans. Japan Soc. Mech. Eng. Ser. A. 62 (1996) 945–952. doi:10.1248/cpb.37.3229.
[39] T. Inoue, Y. Yamaguchi, H. Yajima, S. Aihara, H. Yoshinari, K. Hirota, T. Kiyosue, T. Tani, Required Brittle Crack Arrest Toughness Kca Value with Actual-scale Model Tests -Brittle Crack Arrest Design for Large Container Ships -4-, in: Proc. Tweintieth Int. Offshore Polar Eng. Conf., 2010: pp. 95–101.
[40] B. Prabel, S. Marie, A. Combescure, Using the X-FEM method to model the dynamic propagation and arrest of cleavage cracks in ferritic steel, Eng. Fract. Mech. 75 (2008) 2984–3009. doi:10.1016/j.engfracmech.2008.01.008.
[41] Y. Nakano, M. Tanaka, Crack Arrest Toughness of Structural Steels Evaluated by Compact Test, Trans. ISIJ. 22 (1982) 147–153.
[42] B. Brickstad, A Viscoplastic Analysis of Rapid Crack Propagation Experiments in Steel, J. Mech. Phys. Solids. 31 (1983) 307–327.
[43] Y. Yamaguchi, H. Yajima, S. Aihara, H. Yoshinari, K. Hirota, T. Kiyosue, T. Tani, Development of G uidelines on Brittle Crack Arrest Design - Brittle Crack Arrest Design for Large Container Ships -1 -, in: Proc. Twent. Int. Offshore Polar Eng. Conf., 2010.
[44] A.J. Rosakis, J. Duffy, L.B. Freund, The determination of dynamic fracture toughness of AISI 4340 steel by the shadow spot method, J. Mech. Phys. Solids. 32 (1984) 443–460. doi:10.1016/0022-5096(84)90030-9.
[45] S. Machida, M. Matoba, H. Yoshinari, C. Tone, A Model for Brittle Crack Propagation and Arrest in Structural Steel, J. Soc. Nav. Archit. Japan. 172 (1992) 637–647.

Chapter 5 Brittle crack propagation/arrest behaviors under high stress intensity factor and isothermal conditions

5.1. Introduction

As noted in previous chapters, the local fracture stress criterion is promising concept to explain brittle crack propagation and arrest behaviors in steel. According to the numerical model based on the local fracture stress criterion, the growth of unbroken shear lip is a key factor of so called "Long brittle crack problem" [1–3]. This problem is that the brittle crack can be arrested under extremely high stress intensity factor conditions even when the stress intensity factor (SIF) is higher than K_{ca} at the temperature. Although this problem has been interpreted as the saturation of SIF [4], the cause of the problem had not been explained. This "Long brittle crack problem" is also important from the perspective of engineering because the required brittle crack arrest toughness is determined based on "Long brittle crack problem". According to literatures, the steel plates for large container ships is required to have K_{ca} at the design temperature $>$ 190 MPa$\sqrt{\mathrm{m}}$ ($6{,}000\mathrm{Nmm}^{-3/2}$) when the plate thickness is smaller than 80 mm [5] although the supposed SIF in actual ship structures is much high. This requirement is justified by crack arrest phenomena called as "Long brittle crack problem" and the cracks with higher SIF were actually arrested in large size crack arrest experiments when K_{ca} was larger than 190 MPa$\sqrt{\mathrm{m}}$. Therefore, considering that the requirement is related to "Long brittle crack problem" and the required value depends on plate thickness, examination of brittle crack propagation and arrest behaviors under high SIF conditions is important to legislate rational requirements [6].

According to the model, the crack arrest at high SIF conditions is explained by the rise of closure effect makes the SIF smaller so as to make the crack arrested, or the strong plastic constraint is

lost along the crack front through thickness due to increasing SIF. The model assumed that the thickness of unbroken shear lips t_{sl} is expressed as

$$t_{sl} = \frac{k_{sl}}{6\pi}\left(\frac{K_{app}}{\sigma_{YS}(T,\dot{\varepsilon})}\right)^2 f_{sl}(V) \tag{5-1}$$

where K_{app} is stress intensity factor due to the applied stress ($= \sigma_{app}\sqrt{\pi a}$), $\sigma_{YS}(T,\dot{\varepsilon})$ is the yield stress at temperature T and strain rate $\dot{\varepsilon}$, $f_{sl}(V)$ is a function to express shear lip thickness coefficient determined by crack velocity V, and k_{sl} is a constant, set to 2. Namely, shear lip thickness is determined by stress intensity factor. The numerical mode noted that "Long brittle crack problem" was caused by shear lip thickness growth due to rise of stress intensity factor.

In addition, the $K_{ca} - T$ relationship predicted by the model is composed of a lower curve and upper curve, which are connected at a bending point as shown in Fig. 5-1 although conventional studies thought that $K_{ca} - T$ relationship is approximated by an exponential function (which is almost equal to "lower curve" in Fig. 5-1). However, the existence of the bending point and upper curve is concerned because they have not been examined experimentally in detail.

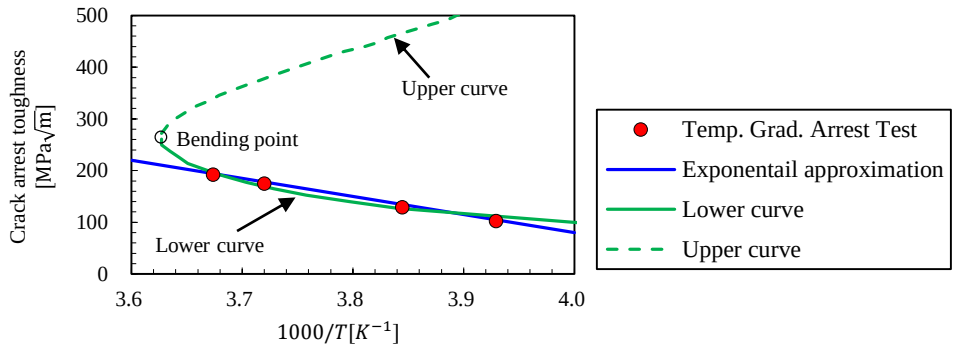

Fig. 5-1 $K_{ca} - T$ relationship example

Although the numerical model showed above crack behaviors under high SIF conditions, crack behaviors under high SIF conditions have not been clear. In fact, some literatures investigated the crack behaviors under high SIF conditions. However, these experiments often employed duplex crack arrest test specimen shown in Fig.5-2 [4,7,8]. Duplex type specimen includes weld and is composed of a crack running plate and a test plate, which causes material discontinuity

and has residual stress. Because residual stress strongly influences brittle crack arrest phenomena [9,10], duplex type tests are not suitable to examine only SIF effect. And, duplex type test is usually conducted to judge whether a brittle crack is arrested or not at predetermined SIF [11] and thus it is not intended to investigate the crack behaviors in detail.

Accordingly, because such studies may be influenced by some additional factors such as residual stress, mismatch of strength and so on in duplex type tests [10], their experimental data are not suitable for investigation of crack behaviors under high SIF conditions in detail. Thus, detail investigation of crack behaviors under high SIF is meaningful to investigate whether Eq. (5-1) is reasonable or not in order to develop a new simulation model attempting to explain brittle crack propagation and arrest behaviors. Although some experiments carried out using wide specimen with temperature gradient and without welded section, temperature gradient also makes the interpretation of experimental results complicated [12] because temperature strongly influences crack behaviors [7].

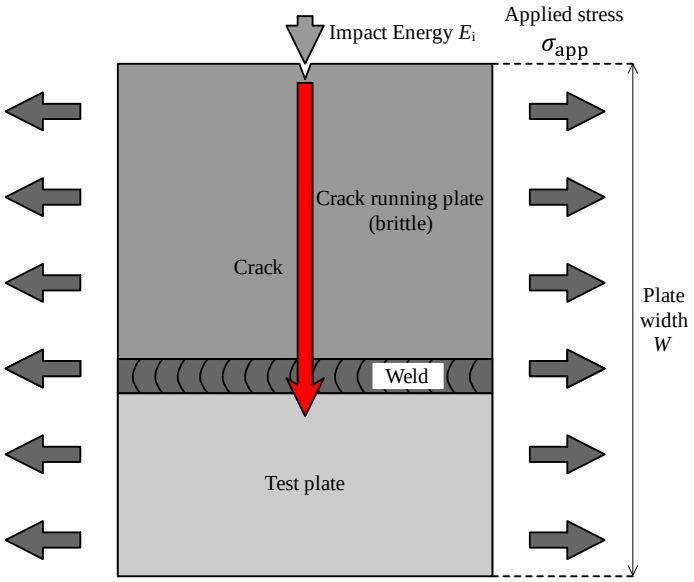

Fig. 5-2 Duplex type specimen

Because of importance of brittle crack behaviors under high SIF condition from the scientific and engineering perspectives, this chapter experimentally investigated brittle crack propagation and arrest behaviors under high SIF conditions based on preliminary calculation using the numerical model. The experiments were conducted in wide specimen to increase SIF under isothermal conditions. The experimental conditions were determined using the model so as to

make SIF is always larger than K_{ca} and reached the upper curve. SIF transition in these experiments is schematically illustrated in Fig. 5-3. According to the model prediction, the crack is arrested when SIF reaches the upper curve.

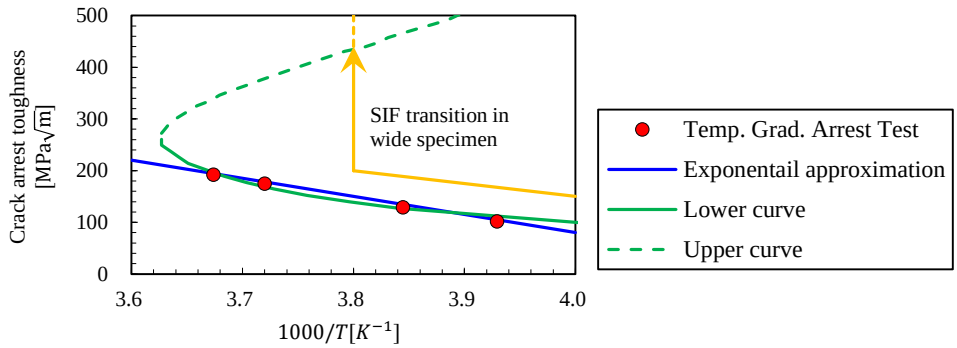

Fig. 5-3 SIF transition in wide specimen

The experimental temperatures were kept isothermal except a region near crack initiation (this region had to be lower temperature to cause brittle fracture). The experiments under high SIF were carried out by 2,000 ton test rig in Amagasaki Unit, Nippon Steel & Sumikin Technology Co. Ltd.

5.2. Preparation of experiments

5.2.1. Material

A ferrite-pearlite steel with 30 mm thickness was employed for this chapter. This steel was a normalized and did not experience TMCP or other techniques to generate a strong anisotropic texture in its microstructure. Thus, the steel was dealt with an isotropic material. The chemical composition is shown in Table 5-1. The fundamental mechanical properties are shown in Table 5-2. This steel is same as the steel employed in literature [13].

Table 5-1 Chemical composition of the steel employed (mass%)

C	Si	Mn	P	S
0.14	0.41	1.45	0.017	0.003

Table 5-2 Mechanical properties of the steel employed

Thickness [mm]	Yield stress at room temperature [MPa]	Tensile strength at room temperature [MPa]	vTs [℃]
30	364	540	-40

5.2.2. Specimen and experimental environment

Although, in order to test higher SIF condition, it is desirable to make the specimen width longer, due to limitation of original plate configuration, the specimen width was set to 1,500 mm. The specimen was joined to tab plates by welding. Two specimens were prepared for this chapter. The first and second experiments are called as Wide2016 and Wide2017, respectively.

Figure 5-4 shows both the specimen and the tab plates. Three tab plates (named A, B, and C, respectively as shown in Fig. 5-4) with different thickness were joined by welding to constitute the large tab plate. Because the tab plates were once separated after Wide2016 and connected against for Wide2017, the detail configurations of tab plates were different in Wide2016 and Wide2017. There was side groove on one side of the specimens to make crack propagation straight. An initial machine notch was also processed to cause brittle fracture. The configuration of the notch was same as that usually employed in the temperature gradient crack arrest test [11]. To avoid stress reflection effect, the distance between pin holes should be kept long enough [14]. The distance was set to about 6,000 mm, which was the maximum value of the test rig.

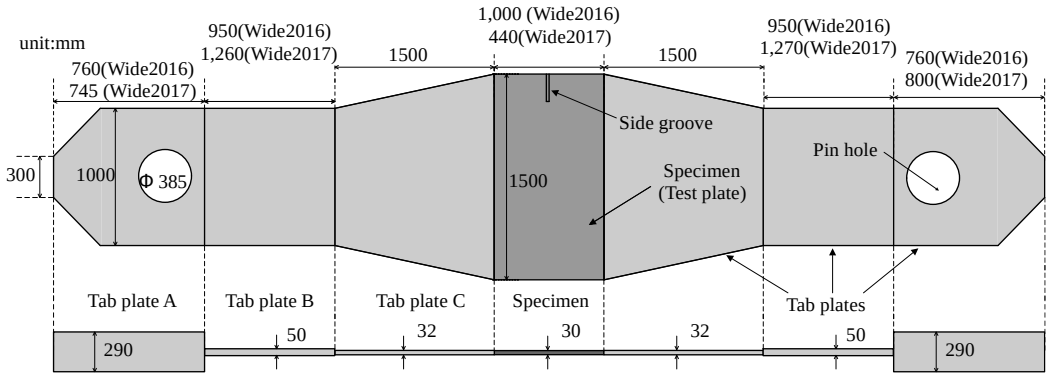

Fig. 5-4 Specimen and tab plate

Because the force capability of the test rig was about 16 MN and the static yield stress at room temperature of the steel employed was 364 MPa, the applied stress was set to 315 MPa (the force was about 14.2 MN). The steel for tab plates was HT60 grade, which was much stronger than the specimen steel.

Although it was desirable to keep whole of the specimen isothermal, there were temperature gradients between the top of the specimens and 280 mm from the top to cool a region where brittle fracture was initiated. Temperature distributions were measured by thermocouples. The temperatures were controlled using liquid nitrogen and compressed spray system in the cooling bath (Fig. 5-5). Strain gauges were also glued on the surface of the specimens and they were connected to the high speed acquisition systems, which were same as those employed in Chapter 3. The interval between strain gauges was about 30 mm in Wide2016 and 19 mm in Wide2017 in the region whose distance from the top of the specimen was shorter than a half of the specimen width. In the latter half of the specimen width, the interval was longer because of the limitation of data recording. The last strain gauge was glued at 1,200 mm from the top.

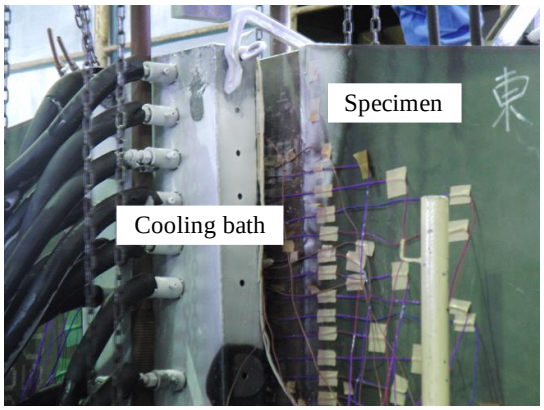

Fig. 5-5 Specimen and cooling bath

5.2.3. Preliminary model calculation

As noted in Section 5.1, the experimental conditions were decided so that the SIF of the brittle crack was always larger than the lower curve and reached the upper curve. Therefore, although the upper curve had to be calculated by the model, the brittle crack arrest toughness of the employed steel was needed to conduct the model calculation. This was obtained by the temperature gradient crack arrest tests. The experimental procedure of the temperature gradient crack arrest tests is shown in WES2815 [11]. The results of these temperature gradient crack arrest tests are shown in Table 5-3. Totally, 9 crack arrest data were obtained. 3 of them were carried out by Shimada et al.(No.1, 2, and 3 in Table 5-3) [15], and Tonsho et al. (No.4, 5, and 6 in Table 5-3)[16], respectively. 3 new experiments (No. 7, 8, and 9 in Table 5-3) were newly carried out by this study in Kashima Unit, Nippon Steel & Sumikin Technology. The Arrhenius plot of the results is shown in Fig. 5-6.

To predict the upper curve and lower curve by the conventional model [1], it is needed to identify the local fracture stress, which is a unique fitting parameter in the model, beforehand [1]. This local fracture stress was identified to 4,410 MPa from one of the $K_{\mathrm{ca}} - T$ relationships shown in Fig. 5-6. The predicted curve is also shown in Fig. 5-6. This curve was predicted by a series of calculation assuming temperature gradient crack arrest test with standard width (500 mm) under a remotely applied stress from 90 to 500 MPa.

Table 5-3 Results of temperature gradient crack arrest tests

No.	Applied stress [MPa]	Temperature gradient [℃/m]	Temperature at crack arrest [℃]	Crack arrest length [mm]	K_{ca} [MPa$\sqrt{m}$]
1	102	300	-18.5	230	96
2	205	300	-0.8	230	192
3	131	300	-12.9	245	129
4	178	300	-10	225	150
5	178	300	-1.0	323	179
6	200	300	10.9	315	199
7	115	300	-10.0	293	132
8	300	300	8.79	302	355
9	315	300	13	338	422

It is worth noting that there was inconsistency between the model calculation and the experimental results in higher temperature and higher K_{ca} conditions although they agreed well in lower temperature and lower K_{ca} conditions in Fig. 5-6. This inconsistency appeared as the location of the bending point. Namely, although the bending point was found in the model prediction, three experimental points were located in the region where the temperature was higher than the bending point. The location of the bending point and crack behaviors around the bending point remains controversial in the papers in which the model was proposed [1,2]. Because these experimental data which did not consist with the model prediction were under high SIF conditions, the following investigations would provide relevant findings to these deviation. Therefore, the local fracture stress was set to 4,410 MPa in subsequent calculations.

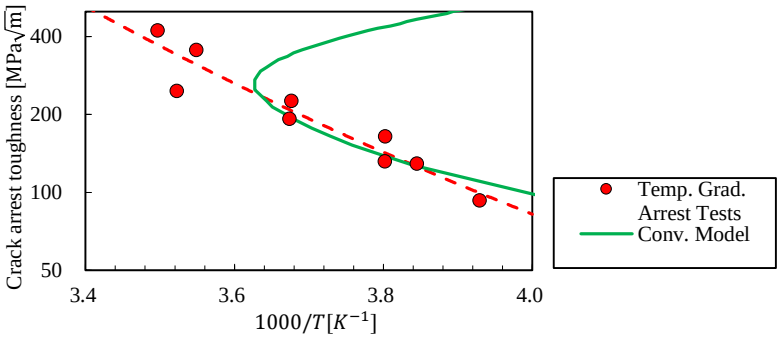

Fig. 5-6 $K_{ca} - T$ relationship of the employed steel with model calculation

5.2.4. Determination of experimental conditions

Using the local fracture stress identified in Section 5.2.3, the model calculation was carried out to decide the experimental conditions. These calculations assumed the expected SIF transitions and temperature distributions in the specimen shown in Section 5.2.2. Thus, the isothermal temperature began from 280 mm from the top of the specimen and the input applied stress was 315 MPa according to Section 5.2.2. The detail calculation procedure is shown in the literature [1]. The isothermal temperatures were set to $2 \sim -25$ ℃ to predict the crack arrest length for each temperature. The predicted crack arrest lengths were shown in Fig. 5-7.

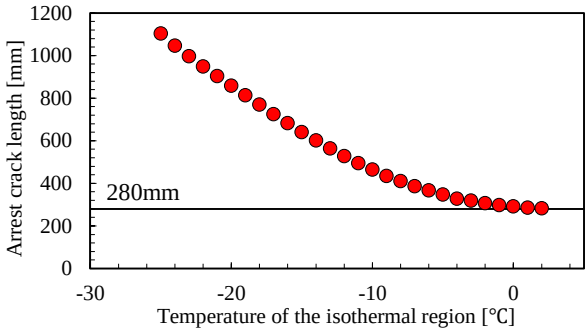

Fig. 5-7 Crack arrest length prediction

In the experiments in this chapter, it was desirable to exclude unnecessary factors, In particular, stress wave reflection frequently influences the experiments where the crack can become longer

[14,17]. Therefore, from the perspective of conservative thought, the experimental temperatures were determined so as that the predicted crack arrest length were not longer than 600 mm because the stress wave reflected at the pin reached the crack path when the crack length reached 600 mm if it was assumed that the crack velocity was $600\ \mathrm{m/s}$. This calculation considered that the distance between pins was about 6 m and the stress wave velocity is approximately $6{,}000\ \mathrm{m/s}$. In addition, it was desirable for the brittle crack ran a certain distance in the isothermal region. Therefore, because the temperature was gradient from the top of specimen to 280 mm, the predicted crack arrest length was desirable to be longer than 300 mm for the experimental temperature.

According to Fig. 5-7 and above limitation of the predicted crack arrest length, the experimental temperatures were set to -3 and -13 ℃ because the predicted crack arrest lengths under both temperatures were longer than 300 mm and shorter than 600 mm. The SIFs at crack arrest were predicted as 312 and 415 $\mathrm{MPa}\sqrt{\mathrm{m}}$ under -3 and -13 ℃, respectively.

5.3. Experiments under high SIF conditions

5.3.1. Experimental procedure

The experimental procedure is below;

(1) Specimen was cooled to the target isothermal temperature. At this step, the specimen was made isothermal.

(2) The temperature was kept for 30 minutes after the temperature became isothermal.

(3) The remote stress was statically applied until it reached 315 MPa.

(4) The temperature around the region near the initial notch tip was additionally cooled to scheduled temperature (about -90℃) to cause brittle fracture by impact energy as small as possible. At this step, the temperature gradient was made from the top to the beginning of the isothermal region.

(5) The temperature distribution was kept for 10 min.

(6) Brittle fracture was initiated by impact and the brittle crack started to propagate.

Although the stress is usually applied after the temperature distribution including temperature gradient is completely made, the applied stress was loaded before the further cooling, not to cause brittle fracture naturally, before the applied stress became the scheduled magnitude. The impact energy was set to 2,000 J, which followed the requirement in WES2815 [11] and was the minimum amount in the employed impact machine.

The target temperature distributions are shown in Fig. 5-8. Ten thermocouples per one side of the specimen were installed to measure the temperature at each point. The lowest temperature was set to $-90℃$ around the initial notch tip. Although the temperature gradients were basically same in both Wide2016 and Wide2017, the gradient was steeper in Wide2016 just before the temperature became isothermal.

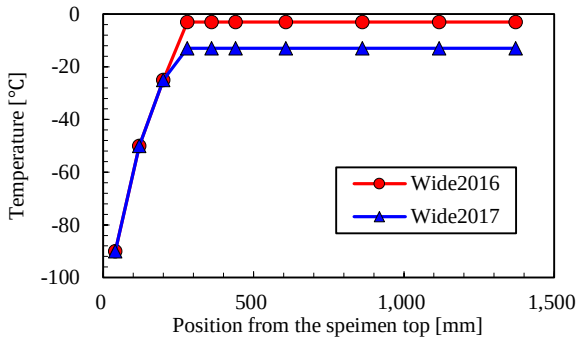

Fig. 5-8 Target temperature distributions

5.3.2. Experimental results

The experimental results of Wide2016 and Wide2017 are shown in Table 5-4. The static SIF was evaluated by the static finite element analysis in Section 5.3.3.

Although the Static SIF at crack arrest in Wide2016 was much larger than K_{ca} at the test temperature, the crack was arrested as predicted by the model calculation. On the other hand, although the model predicted that the brittle crack was arrested under $-13℃$, the crack went through the specimen in Wide2017. After the experiment of Wide2016, the ligament was broken by causing brittle fracture under tensile loading after the temperature was cooled to $-196\ ℃$.

Table 5-4 Experimental results

	Applied stress [MPa]	Test temperature [℃]	K_{ca} at test temperature [MPa$\sqrt{m}$]	Crack arrest length [mm]	Static SIF at arrest [MPa$\sqrt{m}$]
Wide2016	315	-3.0	184	303	364
Wide2017	315	-13.9	146	Propagate	N.D.

The measured temperature distributions are shown in Fig. 5-9. Although there were some deviations of the measured temperature from the target temperatures, the temperatures were almost kept as scheduled.

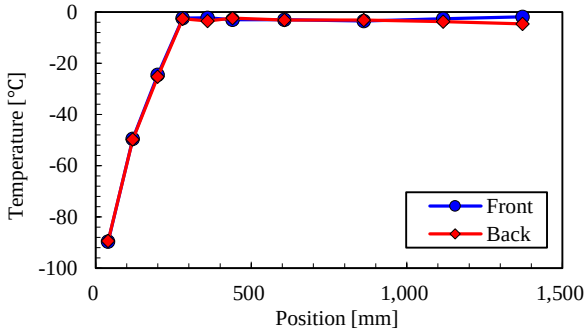

(a) Wide2016

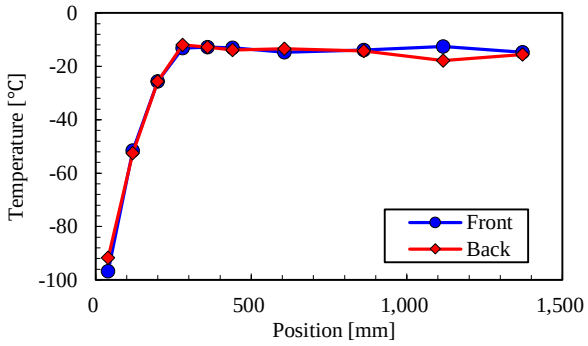

(b) Wide2017

Fig. 5-9 Temperature distributions

The fracture surfaces obtained in the experiments were shown in Fig. 5-10. In Fig. 5-10(a), which is a fracture surface of Wide2016, the shear lip started to grow after the crack reached the isothermal region and the crack was arrested. Fig. 5-10(b) showed the fracture surface of Wide2017. Around about 680 mm from the top of the specimen, the crack deviated from the original straight path. The crack was slant from 680mm to 740 mm and became straight after it reached 740 mm. After that, the crack propagated in straight path until it reached the end of the specimen width.

Crack velocities in both experiments were determined from strain transition data obtained by strain gauges. The obtained strain data were shown in Fig. 5-11. As same as the procedure in Chapter 3, the strain peaks were regarded to mean that the crack propagated just side of the strain gauge at that time. After the peak was found in each strain transition, the strains were scaled out in some strain gauges. This may be explained by the destruction or spallation of strain gauges because the strain gauges whose data were scaled out were located in the latter part of specimen width where the crack tip plastic zone was large.

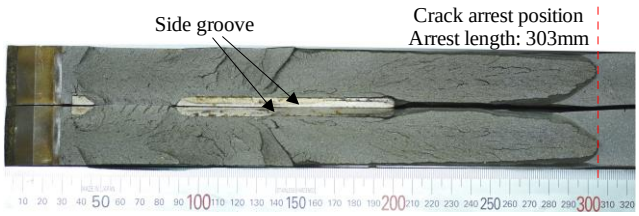

(a) Wide2016

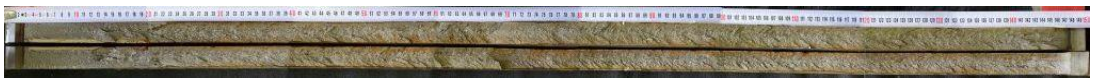

(b) Wide2017

Fig. 5-10 Fracture surface

Fig. 5-12 is the relationship between the crack length and time. In Wide2016, only 4 gauges successfully detected the crack passing near the gauges because the crack was arrested in relatively shorter length. On the other hand, a lot of strain gauges could detect the crack passing near the gauges in Wide2017 because the crack was not arrested. The relationship between the crack length and time was almost linear in Wide2017 as shown in Fig. 5-12. Namely, because the crack velocity is a slope of this relationship, the crack velocity was almost constant in Wide2017. This crack velocity was approximately 486 m/s. Any strain gauge was glued in the region where the distance from the top of the specimen was longer than 1,200 mm.

As noted above, the Wide2017 result that the crack was not arrested defied the prediction in Section 5.2.4. Therefore, as the detail investigation of the result of Wide2017, finite element analyses were carried out to obtain the detail SIF transition.

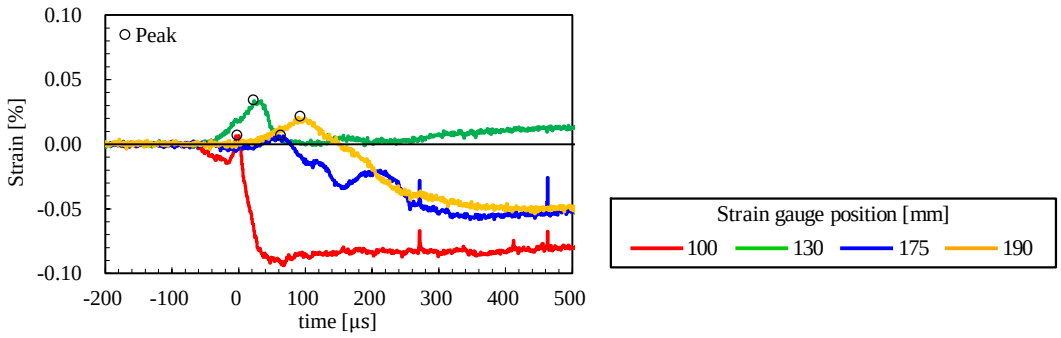

(a) Wide2016

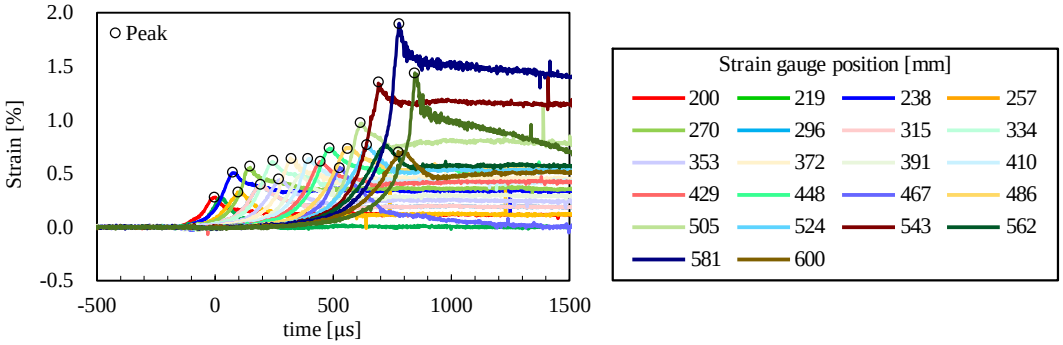

(b) Wide2017 (0~600 mm)

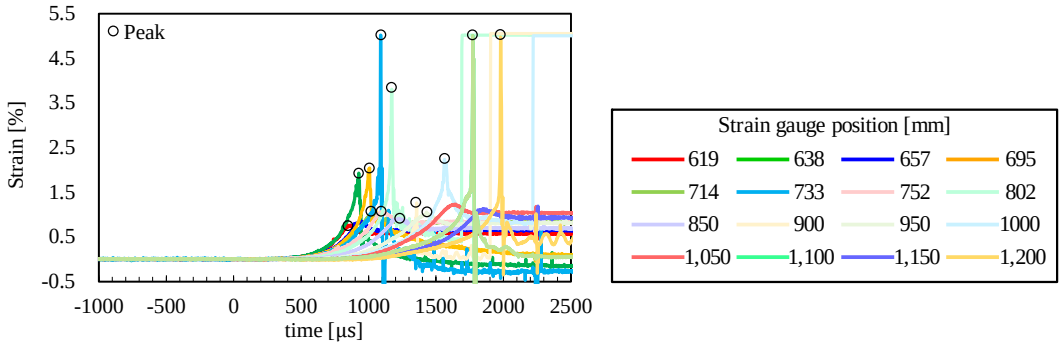

(c) Wide2017 (600 mm~1200 mm)

Fig. 5-11 Strain data example

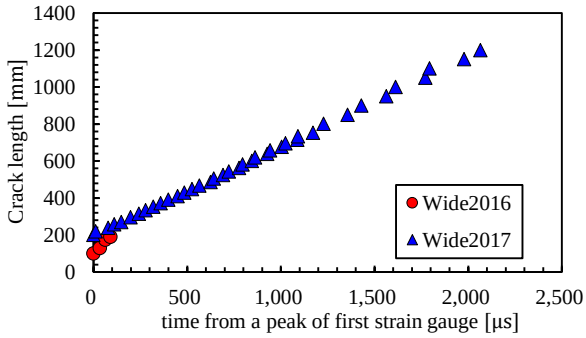

Fig. 5-12 Crack length-time relationship obtained by strain gauges

5.3.3. Finite element analysis

To obtain SIF transitions, stress wave reflection had to be take into account in FEM. Dynamic elastic condition was assumed because these analyses aimed to calculate SIF transition.

The stress wave reflection mainly causes at pins, but the stress wave also reflects at the boundary of different thickness plates. As shown in Fig. 5-4, the tab plate thicknesses were not uniform and thus had to be considered in FEM. Finite element analyses were conducted using implicit dynamic analysis in Abaqus 6.14 [18].

The finite element model was 2D plain strain. The model is shown in Fig. 5-13. It was a half model that the crack path corresponded to the symmetry line. The differences of tab plate thickness were taken into account by using the element thickness. All elements were full-integration quadrilateral elements. The element size along the crack path, d, was set to 1 mm. In order to consider the stress wave reflection, the fixed displacement was provided. Although the displacement was provided to the specimen via pins, to include contact between pins and inner of the pin hole of the specimen model may worsen the convergence of the analyses. Therefore, the fixed displacement was directly provided to the nodes around the pin holes. The amount of the displacement was determined so that the average tensile stress of the crack path reached 315 MPa. Although the stress field around the pins was different from that when the pins was accurately modelled, it was reasonable to consider that the stress distribution along the crack path was not influenced because the pin hole was far from the crack path.

The crack propagation was represented using nodal force release technique in generation phase analysis where the crack velocity was input. As noted in Section 5.3.2, the crack velocity after the crack length reached 200 mm. It was needed to assume the initial crack velocity from the specimen top to 200 mm from the top because there were no strain gauge data in that range. This initial crack velocity was assumed to be 1,000 m/s. Although the analysis with other initial crack velocity was also carried out, the change of the crack velocity influenced the result only a little.

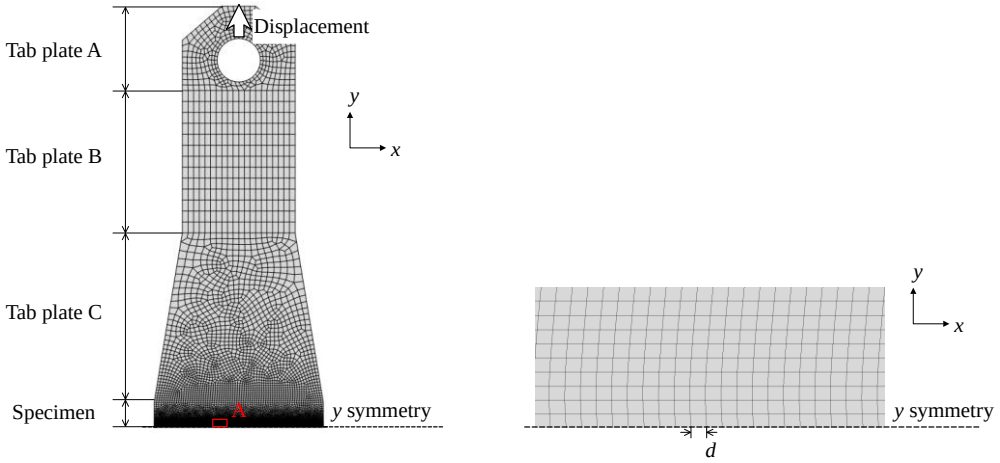

(a) Finite element model (b) Close up of A

Fig. 5-13 Finite element analysis

At the first of the analysis, the forced displacement was statically applied. The tensile stress distribution under this static loading is shown in Fig. 5-14. The applied stress was not uniform along the crack path. The stress was higher around the center and lower near the edge of the crack path. This non-uniform stress distribution was caused because the specimen width was wider than that of tab plate A and B, and the distance between the pin and the crack path was not long enough. Therefore, the SIF was expected to be different from SIF calculation using $\sigma_{\mathrm{app}}\sqrt{\pi a}$ where σ_{app} and a are the applied stress and the crack length, respectively. The SIF at crack arrest in Wide2016 shown in Table 5-4 is obtained by static finite element analysis using the mode of Fig. 5-13 to take the above non-uniform tensile stress distribution into account. After this static loading, the generation phase crack propagation analysis was carried out by releasing the nodal constraint following the prescribed crack velocity.

It is known that the local stress field near the crack tip has $1/\sqrt{r}$ singularity in a rapidly propagating crack tip as same as in a stationary crack tip [19]. The dynamic SIF was determined from the crack tip local tensile stress field as conducted in previous studies [13,20]. And then, using the coefficient to express dynamic effect, the static SIF was calculated from the dynamic SIF. This coefficient is explained in Chapter 2 in detail. These SIFs are shown in Fig. 5-15 from 200 mm to 1,450 mm. The SIFs monotonically increased at first, but they became the maximum values when the crack length was 1,055 mm and started to decrease. These transitions were caused because the reflected stress wave reached the crack path. According to Fig. 5-15, the maximum static SIF was $637\ \mathrm{MPa}\sqrt{\mathrm{m}}$ when the crack length reached 1,055 mm. This SIF is

larger than the predicted arrest SIF (415 MPa$\sqrt{m}$). Even if the SIF became smaller than above FEM value due to crack deviation, the static SIF at crack deviation (the crack length was 680 mm) was 545 MPa$\sqrt{m}$, which is also larger than the predicted arrest SIF. Therefore, if the model correctly represented the actual crack behaviors, the brittle crack should be arrested even under Wide2017 condition. This result indicated the necessity of the model modification according to the experimental result.

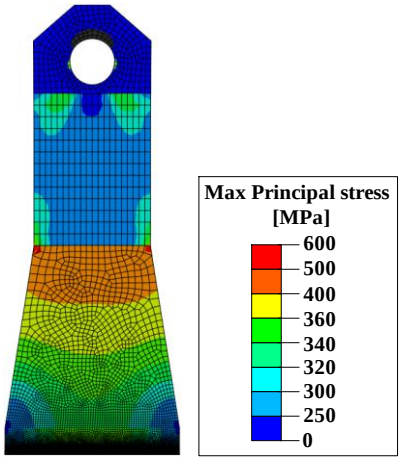

Fig. 5-14 Tensile stress distribution under the initially loading

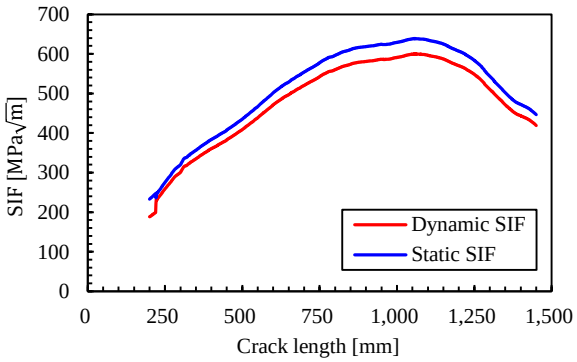

Fig. 5-15 SIF transition of Wide2017 calculated by FEM

5.4. Model modification

To reconsider the formulation in the model, shear lip was focused on because shear lip formation was considered a key to explain Long brittle crack problem. As noted in Chapter 1, the formulation related to shear lip of the model was not supported by detail experimental or numerical investigations. Therefore, each formulation might be inappropriate to reproduce shear lip effects. The shear lip effect can be divided to two factors: closure stress and shear lip thickness. Although the closure stress evaluation method similar to the model has been employed in other studies [21,22], formulation of shear lip thickness can merely be found in literature. Thus, this section focuses on the shear lip thickness.

The calculated SIF in Fig. 5-15 was used to simulate Wide2017 by the conventional model. Fig. 5-16 shows the shear lip thickness in this model simulation of Wide2017. In this calculation, the SIF shown in Fig. 5-15 was used as SIF transition for the model calculation. As mentioned in Section 5.3.3, the tensile stress along the crack path was not uniform, so the arrested crack length in this calculation differed from the crack arrest length predicted in Section 5.2.3. The crack was arrested because the shear lip thickness reached the plate thickness in this simulation. Comparison of this result with Fig. 5-10(b) clearly points out that the shear lip thickness was much overestimated in the conventional model calculation.

The shear lip thickness was evaluated by Eq. (5-1) in the conventional model calculation. This equation was developed based on an idea that the degree of the plastic constraint relaxation was correlated to the plastic zone size of the crack tip. Because the plastic zone size is determined by the crack's SIF, the shear lip thickness was expressed by Eq. (5-1). However, considering that the plastic zone size should be related to the amplitude of the crack tip stress field, it is reasonable to regard that the K_{app} is not appropriate to represent the crack's SIF. On the other hand, the effective SIF, which is a difference between the K_{app} and the closure effect, is suitable to express the amplitude of the crack tip stress field. Therefore, the Eq. (5-1) is modified as

$$t_{\mathrm{sl}} = \frac{k_{\mathrm{sl}}}{6\pi}\left(\frac{K_{\mathrm{eff}}}{\sigma_{\mathrm{YS}}(T,\dot{\varepsilon})}\right)^2 f_{\mathrm{sl}}(V) \tag{5-2}$$

where K_{eff} is the effective SIF.

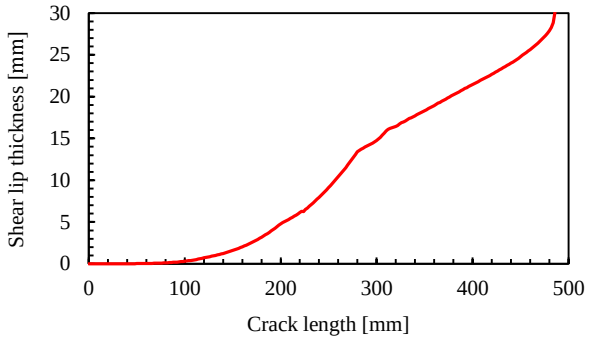

Fig. 5-16 Shear lip thickness predicted by the conventional model in Wide2017 condition

The modified model using Eq. (5-2) was used to carry out a series of simulations of the temperature gradient crack arrest tests, Wide2016, and Wide2017. As same as in the calculation of the conventional model explained in Section 5.2.3, the local fracture stress was identified to 4,450 MPa. The simulated results are shown in Fig. 5-17.

As shown in Fig. 5-17, it is worth noting that the bending point moved to the higher temperature and higher K_{ca} region in the model calculation. As a result of it, the simulated $K_{\mathrm{ca}} - T$ curve (blue line in Fig. 5-17) agreed well with the experimental $K_{\mathrm{ca}} - T$ relationship obtained by the temperature gradient crack arrest tests. The simulated SIF at crack arrest under Wide2016 condition was relatively similar to the experimental result. On the other hand, the crack was not arrested in the modified model simulation under Wide2017 condition. This result consisted with the experimental result of Wide2017. The reason why the crack was not arrested in the modified model simulation is because the shear lip could not growth as predicted by the conventional model because the shear lip growth makes SIF decrease, which lead to thinner shear lip.

As noted above, the modified model successfully simulated the experimental result although the conventional model could not reproduce some of the experimental results such as Wide2017 and the bending point location. Therefore, considering the above reason about relationship between SIF and shear lip thickness and this model simulation results, Eq. (5-2) should be employed as a formula to express the shear lip thickness in subsequent studies.

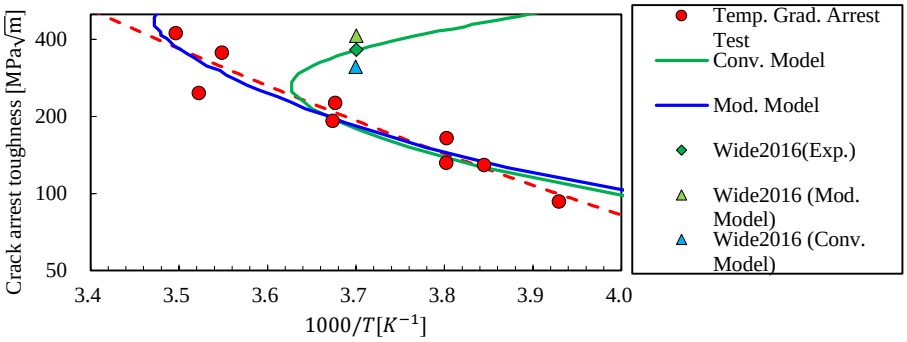

Fig. 5-17 Calculation results of the modified model

5.5. Discussion

5.5.1. Crack arrest SIF of Wide2016

As noted in Section 5.4, the modified model successfully reproduced Go/NoGo results of Wide2016 and Wide2017. However, there was difference between SIF at arrest in the experiment and model simulation of Wide2016. It is hard to conclude the reason why this difference was observed, but it is worth noting that the impact energy was ignored in the finite element analysis to evaluate SIF at crack arrest shown in Table 5-4. The model calculation did not also consider the impact effect. As noted in Section 5.3.1, the brittle crack was initiated by impact device. The impact energy was set to 2,000J in both Wide2016 and Wide2017. Although this impact energy was much smaller than the limitation defined by WES2815, 50% increase of SIF is expected at most even when the impact energy is in the range of the limitation [11]. Although considering that the crack arrest length was larger than 300 mm and the applied stress was 315 MPa, the increase rate of SIF is expected to be relatively smaller compared to the usual temperature gradient crack arrest test [23–25], it is reasonable to regard that the actual SIF at crack arrest in Wide2016 was higher than the value shown in Table 5-4. Therefore, the overestimation of the simulated result of SIF at crack arrest in the modified model corresponds to the above consideration of impact effect. On the other hand, the SIF at crack arrest predicted by the conventional model was lower than the experimental SIF at crack arrest in Wide2016. This is also unreasonable considering the above impact effect.

5.5.2. Required K_{ca}

In fact, the results that the crack was arrested under -3 ℃ but was not arrested under -13 ℃ consists with the conventional finding that the long brittle crack is arrested when K_{ca} at the test condition is larger than 190 MPa$\sqrt{\text{m}}$ in the steel plate whose thickness is not larger than 75 mm [3]. Considering that K_{ca} at -3 ℃ was almost 190 MPa$\sqrt{\text{m}}$, the crack arrest in Wide2016 corresponded to the conventional findings.

According to the modified model, SIF decreasing due to shear lip growth and SIF increasing due to crack length extension can be in harmony or increasing SIF can precede under lower temperature because shear lip growth prevents the shear lip from growing further. Namely,

Therefore, the crack cannot be arrested under lower temperature in the modified model. From the perspective of this finding, the K_{ca} required to cause brittle crack arrest under Long brittle crack problem conditions is related to judgment whether the shear lip growth precedes or not. Thus, the conventional regulation which requires enough K_{ca} at the design temperature is reasonable from the perspective of above idea about relationship between shear lip growth and crack length extension.

In fact, the required K_{ca} depends on plate thickness [6]. In thicker plates, higher K_{ca} is required. Based on the above idea on required K_{ca}, this dependency on the plate thickness is essential because the closure effect due to same shear lip thickness is lower at the thickness center in the thicker plates than in thinner plate [1]. Namely, thicker shear lip is required to arrest the brittle crack in thicker plates. As the result, the required K_{ca} becomes higher for thicker plates.

5.6. Conclusion

In order to investigate brittle crack propagation and arrest behaviors under high SIF conditions, two experiments were carried out using wider specimens under isothermal conditions. The experimental conditions were designed based on the upper curve of $K_{ca} - T$ relationship proposed by the model based on the local fracture stress criterion. SIFs were designed to be always larger than the lower curve of $K_{ca} - T$ relationship based on the model calculation. Two experiments using wider specimens were called Wide2016 and Wide2017, respectively. By a series of the model calculations, the applied stress and temperatures were determined. The applied stress was set to 315 MPa in both experiments, The isothermal experimental

temperatures were -3 and -13 ℃, respectively. These temperatures were determined based on the crack arrest length under various temperatures in the wider specimen predicted by the model.

Two experiments showed that the crack was arrested under -3 ℃ as predicted the model, but the crack went through the specimen under -13 ℃ contrary to the model prediction that the crack was arrested under -13 ℃. Finite element analyses were carried out and showed that the maximum SIF in Wide2017 was much larger than the SIF needed for crack arrest in the prediction.

Based on the inconsistency between the experiments and the model calculation, the formula of shear lip thickness in the model was focused to modify the model. Although the conventional model assumed that the shear lip thickness was governed by applied SIF, the modified model considered that the shear lip thickness was expressed by effective SIF based on the idea of plastic constraint relaxation. This modified model successfully simulated Go/NoGo of Wide2016 and Wide2017. In addition, although the conventional model could not accurately predict $K_{\mathrm{ca}} - T$ relationship in higher temperature and higher K_{ca} region, the modified model prediction consisted with the experimental results of $K_{\mathrm{ca}} - T$ relationship in higher temperature and higher K_{ca} region. These results of the modified model simulation strongly support the hypothesis Long brittle crack problem can be explained by the shear lip formation to cause closure effect.

As noted above, a series of experiments in this chapter provided new findings of the model formulation, especially shear lip formulation. However, shear lip thickness including crack velocity coefficient, $f_{\mathrm{sl}}(V)$, still based on invalid assumption and the necessity of detail examination of shear lip thickness formulation still remains. In addition, although the closure stress was not discussed in this chapter, the previous studies including the conventional model employed elastic perfect-plastic deformation to calculate the closure stress. This also remains to be investigated in detail. Therefore, in next chapter, these factors related to shear lip will be investigated and discussed.

Reference

[1] K. Shibanuma, F. Yanagimoto, T. Namegawa, K. Suzuki, S. Aihara, Brittle crack propagation/arrest behavior in steel plate - Part I: Model formulation, Eng. Fract. Mech. 162 (2016) 324–340. doi:10.1016/j.engfracmech.2016.02.054.

[2] K. Shibanuma, F. Yanagimoto, T. Namegawa, K. Suzuki, S. Aihara, Brittle crack propagation/arrest behavior in steel plate - Part II:Experiments and model validation, Eng. Fract. Mech. 162 (2016) 341–360. doi:10.1016/j.engfracmech.2016.02.054.

[3] T. Inoue, Recent Topics in Large Scale Fracture Test, J. Japan Weldi. 86 (2017) 159–163.

[4] T. Kanazawa, S. Machida, H. Yajima, M. Aoki, Study on Brittle Crack Arrestter - Considerations on the Arrest of a Very Long Crack-, Sel. Pap. from J. Soc. Nav. Archit. Japan. 11 (1973) 135–147. doi:10.1029/2005RG000183.Gajardo.

[5] International Association of Classification Societies, UR S33 Requirements for Use of Extremely Thick Steel Plates, (2014).

[6] K. Matsumoto, T. Fukui, S. Nanno, S. Aihar, T. Kawabata, K. Shibanuma, T. Inoue, T. Okawa, T. Tagawa, H. Tajika, H. Imamura, Brittle Crack Arrest Toughness for Extremely Thick Steel Plates -Required Kca Value of Steel Plates with Thickness of 100 mm Used in Ultra-Large Container Ships-, in: Proc. 28th Int. Ocean Polar Eng. Conf., 2018: pp. 91–97.

[7] S. Machida, H. Yoshinari, Some recent experimental work in japan on fast fracture and crack arrest, Eng. Fract. Mech. 23 (1986) 251–264.

[8] A. Kubo, H. Yajima, S. Aihara, H. Yoshinari, K. Hirota, M. Toyoda, T. Kiyosue, T. Inoue, T. Handa, T. Kawabata, T. Tani, Y. Yamaguchi, Experimental study on brittle crack propagation behavior with large scale structural component model tests - Brittle crack arrest design for large container ships -5 -, in: Proc. Twenty-Second Int. Offshore Polar Eng. Conf., 2012: pp. 36–43.

[9] U. Zerbst, R.A. Ainsworth, H.T. Beier, H. Pisarski, Z.L. Zhang, K. Nikbin, T. Nitschke-Pagel, S. Münstermann, P. Kucharczyk, D. Klingbeil, Review on fracture and crack propagation in weldments - A fracture mechanics perspective, Eng. Fract. Mech. 132 (2014) 200–276. doi:10.1016/j.engfracmech.2014.05.012.

[10] H. Kihara, T. Kanazawa, K. Ikeda, H. Maenaka, M. Kinoshita, R. Nagamoto, H. Yajima, Effectiveness of Crack Arrester (First Report), J. Zosen Kiokai. 122 (1967) 191–199.

[11] The Japan Wedling Engineering Society, WES2815 Test method for brittle crack arrest toughness, (2014). http://www-it.jwes.or.jp/wes_ki/wesippan.jsp?arg=2815e-1.

[12] T. Kanazawa, Recent Studies on Brittle Crack Propagation in Japan, J. Japan Weilding Soc. 42 (1973) 68–84.

[13] T. Kawabata, Y. Nishizono, S. Aihara, Brittle crack propagation behavior in a member subjected to bending load, Theor. Appl. Fract. Mech. 92 (2017) 266–275. doi:10.1016/j.tafmec.2017.09.005.

[14] T. Handa, S. Igi, S. Endo, S. Tsuyama, H. Shiomi, Effect of Distance of Loading Points on Long Brittle Crack Propagation / Arrest Behavior, Q. J. Japan Weld. Soc. 30 (2012) 213–219.

[15] Y. Shimada, T. Inoue, T. Kawabata, T. Handa, M. Kaneko, K. Sugimoto, S. Aihara, K. Shibanuma, Effect of Stress Reflection on Dynamic Stress Intensity Factor of Crack Arrest Toughness Specimen - Study on Standard Test Method for Crack Arrest Toughness , Kca -4 -, in: 24th Int. Ocean Polar Eng. Conf., 2014: pp. 130–136.

[16] F. Tonsho, T. Kawabata, S. Aihara, Investigation of Driving Force for Crack Propagation around the Arrest Point On Temperature-Gradient Crack Arrest Tests in Steels, CAMP-ISIJ. 28 (2015) 768.

[17] S. Machida, Y. Kawaguchi, M. Tsukamoto, An Evaluation of the Crack Arrestability of

9% Ni Steel Plate to a Extremely Long Brittle Crack, J. Japan Soc. Nav. Archit. 150 (1981) 511–517.
[18] SIMULIA, Abaqus Analysis User's Guide Version 6.14, Dassault Systemes, 2014.
[19] K.B. Broberg, Cracks and Fracture, Academic Press, 1999.
[20] T. Handa, S. Igi, K. Oi, K. Nishimura, T. Tagawa, F. Minami, Brittle Crack Propagation/Arrest Behavior in Full Penetration T-joint, J. Japan Soc. Nav. Archit. Ocean Eng. 19 (2014) 179–185.
[21] D. Nakanishi, T. Kawabata, S. Aihara, Effect of dispersed retained γ-Fe on brittle crack arrest toughness in 9% Ni steel in cryogenic temperatures, Mater. Sci. Eng. A. 723 (2018) 238–246. doi:10.1016/j.msea.2018.03.056.
[22] H. Mimura, Method to estimate Kca from K1a, J. High Press. Inst. Japan. 31 (1993) 58–64.
[23] T. Kawabata, M. Kaneko, S. Aihara, Effect of Impact Energy in the Esso Test (Part 1 : Basic Experiments and Validation of FEM Analysis), J. Test. Eval. 46 (2018). doi:10.1520/JTE20170045.
[24] M. Kaneko, T. Kawabata, S. Aihara, Effect of Impact Energy in ESSO Test ((Part 2: Proposal of Validity Criteria of Impact Condition in ESSO Test by FEM Crack Propagation Analysis), J. Test. Eval. 47 (2019) 20170151. doi:10.1520/JTE20170150.
[25] M. Kaneko, T. Kawabata, S. Aihara, Effect of Impact Energy in ESSO Test (Part 3: Experimental Validation for New Validity Criteria of Impact Condition Giving Constant Evaluation in ESSO Test), J. Test. Eval. 47 (2019) 20170150. doi:10.1520/JTE20170150.

Chapter 6 Shear lip closure stress and its formation

6.1. Introduction

Formation of unbroken shear lip is an important factor for brittle crack propagation and arrest behaviors in steels. Unbroken shear lip works to decrease the SIF of the crack until it is broken in ductile manner. This contribution is called as closure effect and the stress working on the unbroken shear lip is called as the closure stress. The closure effect has been widely known to contribute to the crack arrest and considered by previous studies [1–4]. However, the closure stress and shear lip thickness have merely been investigated in detail.

In the conventional model based on the local fracture stress criterion [5], the closure stress was regarded to be equal to the yield stress considering the temperature and strain rate based on an assumption that the shear lip deformation was perfectly plastic. This assumption on deformation is not realistic because the strain rate was assumed to be $10^4\ \mathrm{s}^{-1}$ in the unbroken shear lips, which is higher than the strain rate near the crack tip. Thus, the assumed strain rate also deviated from the actual crack behaviors. Other studies which modelled the closure stress also employed similar unrealistic strain rate ($10^3 \sim 10^4\ \mathrm{s}^{-1}$) of unbroken shear lip deformation [6,7]. Accordingly, it is needed to quantitatively evaluate the closure stress to accurately model the closure effect caused by the unbroken shear lip.

On the other hand, the thickness of shear lip has not been appropriately modelled as pointed in Chapter 5 in spite of its importance. In Chapter 5, the formulation of shear lip thickness was modified to consider effective SIF, but the crack velocity coefficient was not investigated. This crack velocity coefficient was determined from a distribution of plastic strain in thickness direction of each crack velocity against the static case in the conventional model [5], and thus such crack velocity dependency was not supported experimentally. In particular, it is unknown

whether the shear lip thickness has crack velocity dependency in the first place. Although there have been some studies to measure shear lip thickness in brittle crack propagation in steels [8–11], their methods to measure the thickness were not mentioned and their data were not enough to evaluate relationships between the shear lip thickness and other parameters such as SIF and crack velocity.

In fact, previous literatures also mentioned shear lip thickness associated with brittle fracture initiation toughness [12–14]. They indicated that shear lip thickness was related to plastic zone size near the crack tip, which was determined based on the small scale yielding concept [12,14–17]. The formulation of shear lip thickness in the conventional model was based on this idea which originated from the above measurements of shear lip thickness observed in the brittle fracture initiation test such as Charpy impact test. However, as noted above, the systematic measurements of shear lip thickness during brittle crack propagation have not been carried out.

As discussed above, instead of their importance in brittle crack propagation and arrest behaviors, formulations of closure stress and shear lip thickness have hardly progressed. Therefore, this chapter shows quantitative evaluation of the closure stress using 3D finite element analyses and systematic experiments to investigate and formulate shear lip thickness in brittle crack propagation in steels.

6.2. Closure stress

6.2.1. Calculation of closure effect

The closure stress works as shown in Fig. 6-1. The closure effect due to the closure stress working on the unbroken shear lips is expressed in the form of SIF as [5]

$$K_{\mathrm{cl}} = \int_{\Omega_{\mathrm{sl}}} \frac{\sqrt{2}\sigma_{\mathrm{cl}}}{(\pi|x|)^{3/2}\left\{1+\left(\frac{z}{x}\right)^2\right\}} d\Omega_{\mathrm{sl}} \tag{6-1}$$

where K_{cl} is the closure effect, Ω_{sl} is the region of the shear lip, and σ_{cl} is the closure stress. This equation was derived by integrating the closure stress σ_{cl} working on (x, z) over the unbroken shear lip region.

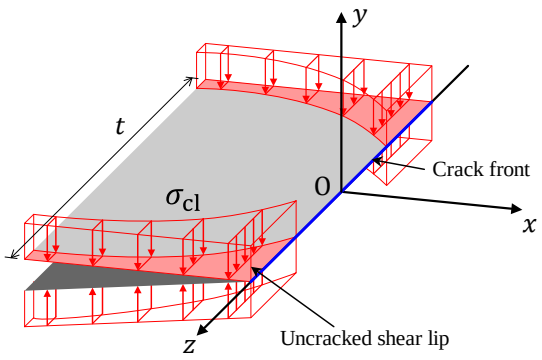

Fig. 6-1 Closure stress working on the unbroken shear lip

As noted above, the closure stress was assumed to be equal to the yield stress at high strain rate $10^3 \sim 10^4\ s^{-1}$ in previous studies without any detail investigation. Therefore, this study systematically analyzed the influence of the crack length, crack velocity, the unbroken shear lip thickness, the applied stress, and the temperature against the closure stress. Because the closure stress is regarded to be equal to the maximum principal stress working on the unbroken shear lips, a series of finite element analyses were conducted to evaluate the maximum principal stress in the unbroken shear lip. In these analyses, crack propagation was represented by the nodal force release technique, and the unbroken shear lip was expressed by leaving the unreleased nodes near the surface behind the crack tip which most advanced in the thickness center. The region of unbroken shear lip is defined prior to the analysis.

In this calculation, the cleavage surface and unbroken shear lips were supposed as shown in Fig. 6-2. The crack front was straight and the plate thickness was set to 50 mm. This is because these analyses assumed steel N employed in Chapter 3 and 7. The constitutive law was also same as that of steel N. The cleavage surface and unbroken shear lips were expressed by rectangles for simplification. The shear lip thickness, t_{sl}, was a variable and constant during an analysis for simplification. In addition, ductile fracture of the end of unbroken shear lip was not considered to make the finite element analysis easy. Therefore, the unbroken shear lip length, l_{sl}, was always equal to the crack length, a.

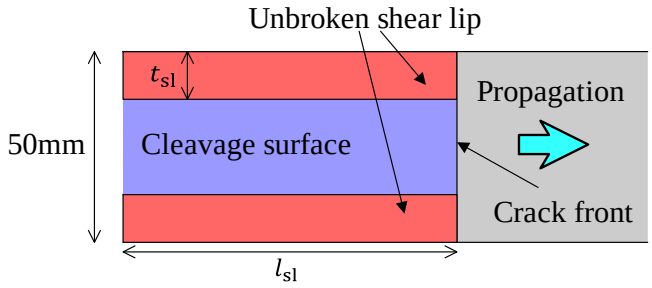

Fig. 6-2 Supposed fracture surface of the finite element model

6.2.2. Finite element analyses to evaluate the closure stress

6.2.2.1. Finite element model and analysis conditions

The employed finite element model is shown in Fig. 6-3. This model is an infinite 3D model which was extended from the infinite 2D model employed in Chapter 2 and 4. The analyses were carried out in dynamic implicit conditions. The all element was 3D hexahedral full-integration. This model corresponds to a quarter model of the infinite plate with a center crack. Therefore, the thickness of the model was 25 mm.

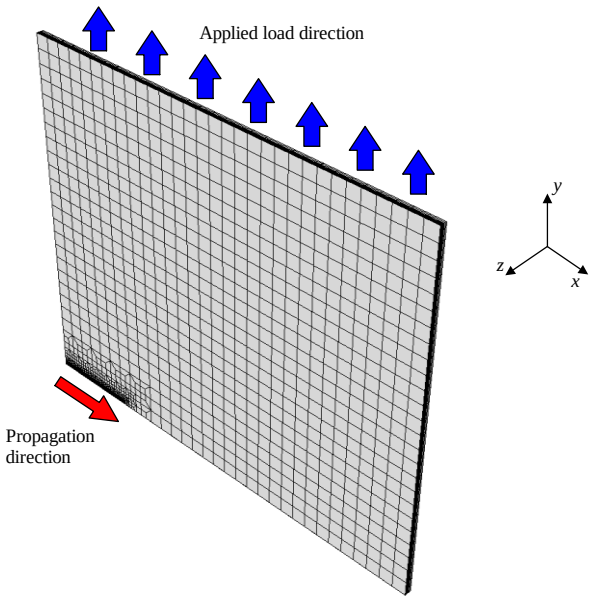

(a) Overview

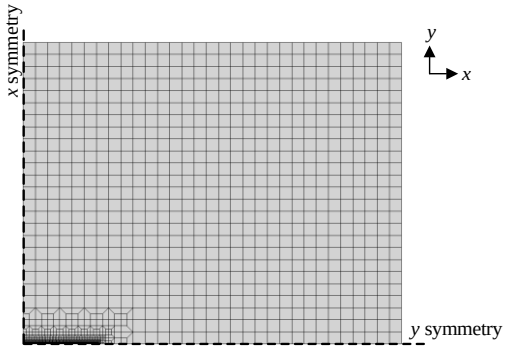

(b) $x-y$ view

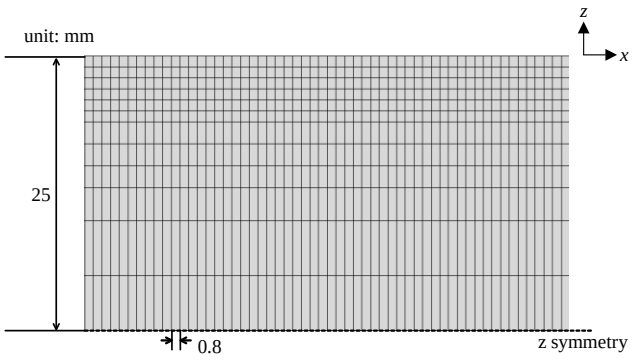

(c) $x-z$ view

Fig. 6-3 Finite element model

The element size in x direction along the crack path was set to 0.8 mm. Although it is desirable to employ fine meshes in finite element analyses, the element size was set to 0.8 mm considering that the numerical cost restricts the element size. The element division in the thickness direction was also shown in Fig. 6-3(c). Because the accuracy of the analyses is relatively low when the crack length is much short, the closure stress was evaluated when the crack length was from 80 to 200 mm. In the analyses, the crack velocity, V, the unbroken shear lip thickness, the applied stress, σ_{app} were variables to change for the analysis condition. The temperature, T, was basically set to -10 ℃. The closure stress was calculated from the reaction force distributing the unbroken shear lips. In addition, equivalent plastic strain was also evaluated in the unbroken shear lips.

6.2.2.2. Analysis results

The unbroken shear lip formation in the finite element analyses is shown in Fig. 6(a). Although the crack front advances, the unbroken shear lip remains an unbroken ligament. One example of the maximum principal stress in the analysis, which corresponds to the closure stress, is shown in Fig. 6-4(b). Although the closure stress is not uniformly distributed in the unbroken shear lip as shown in Fig. 6-4(b), the mean value of the maximum principal stress in the unbroken shear lip was regarded to represent the closure stress of a certain analysis condition.

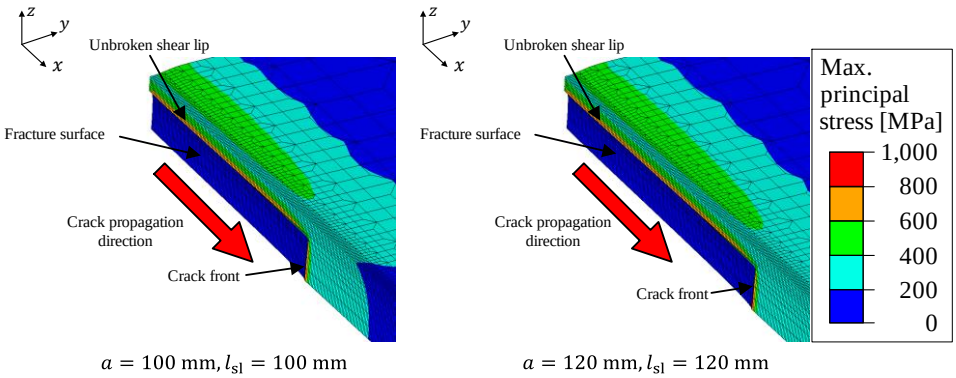

(a) Unbroken shear lip in finite element analyses

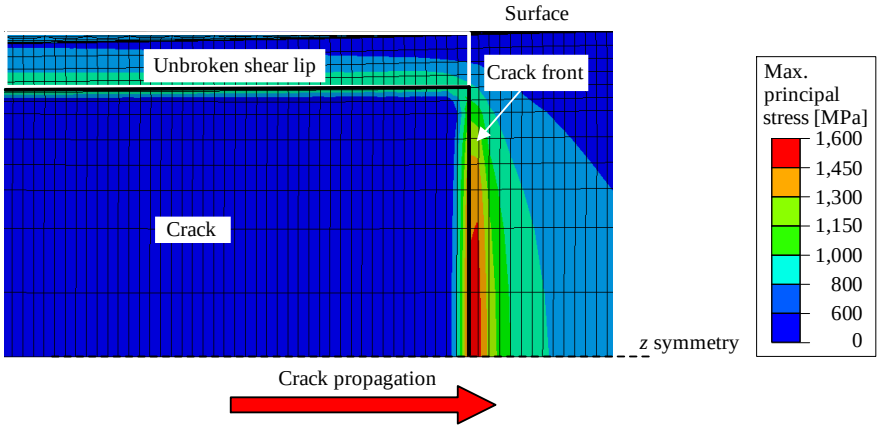

(b) Maximum principal stress distribution in finite element analysis

Fig. 6-4 Maximum principal stress distribution in finite element analysis

The closure stresses calculated from the finite element analyses are shown in Fig. 6-5. They clearly showed that the closure effect hardly depends on the crack velocity, but is strongly influenced by the shear lip thickness and the applied stress. Namely, when the shear lip thickness is thinner and the applied stress is larger, the closure stress becomes larger. According to these trends, the assumption that the closure stress depended only on the temperature in the conventional model [5], does not consist with the actual closure stress.

Because the stress is generally related to strain, the closure stress is considered to be related to the equivalent plastic strain. The maximum plastic strains in the unbroken shear lips are shown in Fig. 6-6. These strain data are under same conditions of those shown in Fig. 6-5. Fig. 6-6 shows that the closure stress is associated with the plastic strain. In other words, the closure stress is larger in the condition in which the plastic strain is larger.

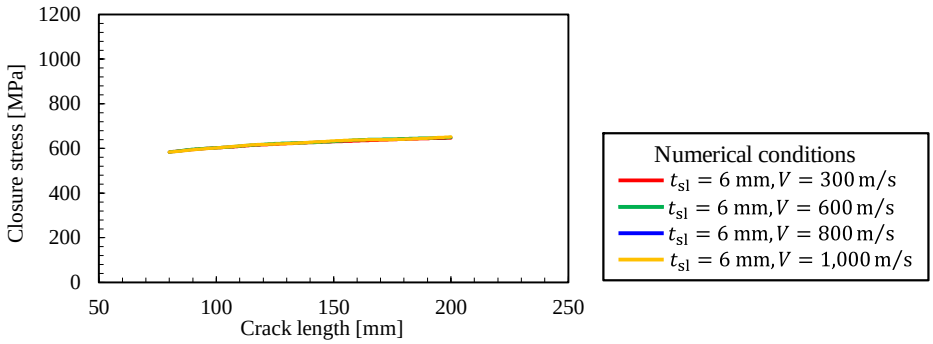

(a) Influence of crack velocity ($T = -10$ ℃, $\sigma_{app} = 184$ MPa)

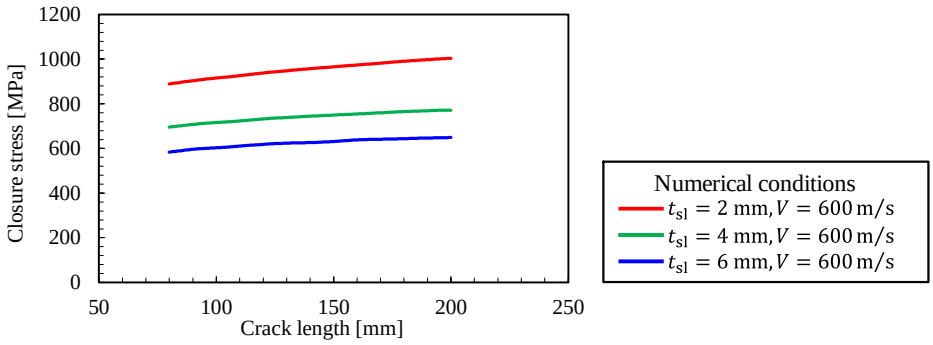

(b) Influence of the unbroken shear lip thickness ($T = -10$ ℃, $\sigma_{app} = 184$ MPa)

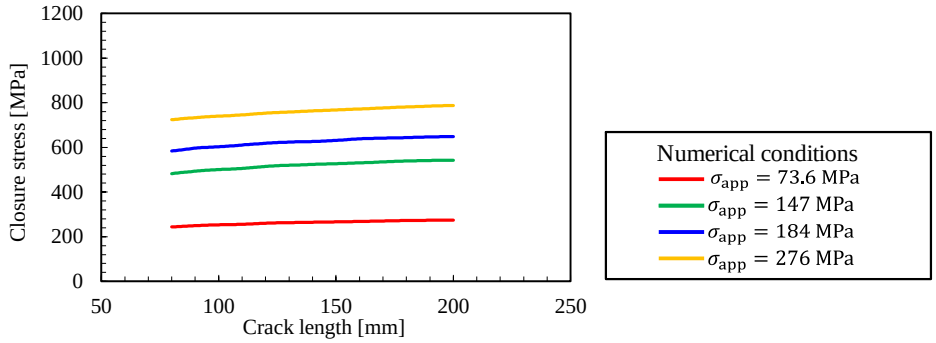

(c) Influence of the applied stress ($T = -10$ ℃, $t_{sl} = 6$ mm, $V = 600$ m/s)

Fig. 6-5 Closure stress against finite element analysis variables

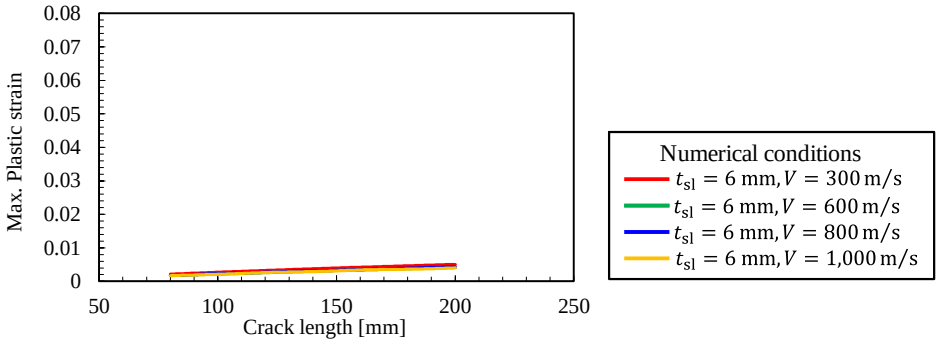

(a) Influence of crack velocity ($T = -10$ ℃, $\sigma_{app} = 184$ MPa)

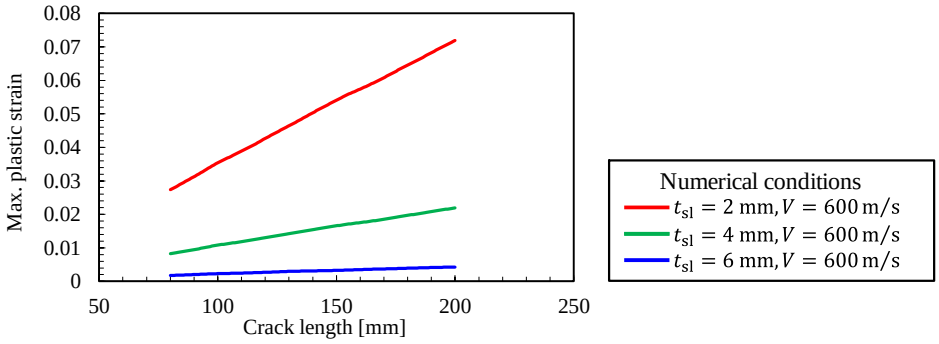

(b) Influence of the unbroken shear lip thickness ($T = -10$ ℃, $\sigma_{app} = 184$ MPa)

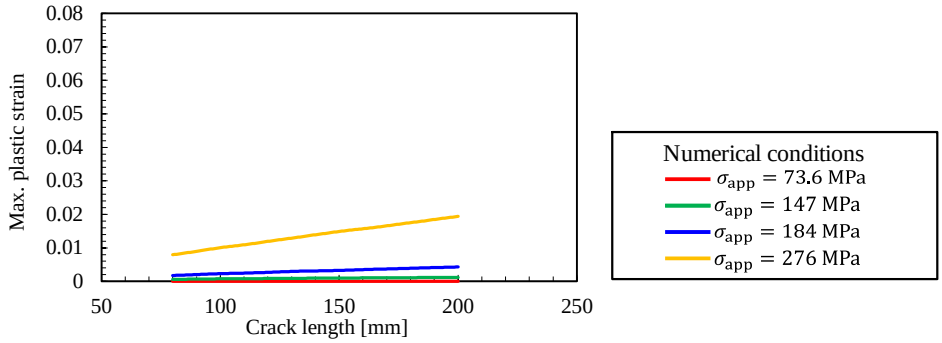

(c) Influence of the applied stress ($T = -10$ ℃, $t_{sl} = 6$ mm, $V = 600$ m/s)

Fig. 6-6 Plastic strain in the unbroken shear lips

Here, using the above finite element analysis results shown in Fig. 6-5 (b), (c), Fig. 6-6 (b), and (c), the closure stresses were organized against the maximum equivalent plastic strain in the unbroken shear lips as shown in Fig. 6-7. The same plastic strain generates the almost same closure stress and thus the unique relationship can be roughly found between the closure stress and the plastic strain in Fig. 6-7 although there are some scatters. This finding is a useful to formulate the closure stress from the crack behaviors.

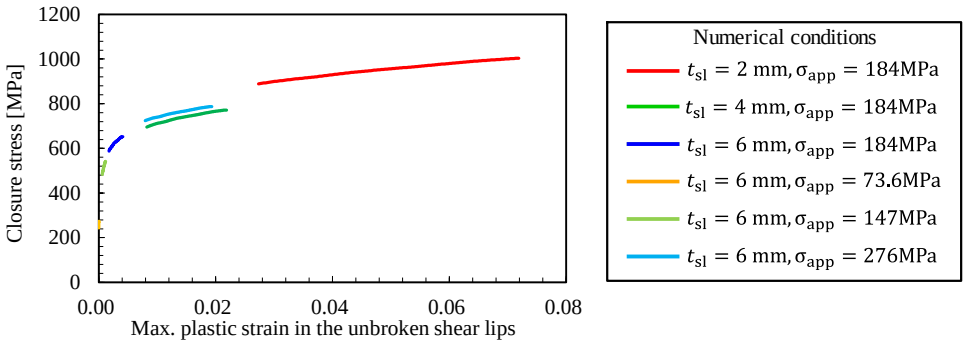

Fig. 6-7 Relationship between the closure stress and the plastic strain in the unbroken shear lips under $T = -10$ ℃ and $V = 600$ m/s

6.2.3. Closure stress approximation

As noted above, the closure stress was not quantitatively investigated and the previous studies had no choice but to regard the yield stress at much high strain rate ($10^3 \sim 10^4$ s^{-1}) as the closure stress. Therefore, the closure stress has been regarded as independent on the factors other than the temperature. However, as shown in Section 6.2.2.2, the closure stress is influenced by the shear lip thickness and the applied stress in addition to the temperature. Accordingly, although it is needed to formulate the closure stress based on the above findings, it is difficult to derive the closure stress analytically. Thus, by focusing on the relationship between the plastic strain and the closure stress as shown in Fig. 6-7, it was attempted to make approximation functions the closure stress from the results of the finite element analyses. In fact, to express the closure stress by the plastic strain in the unbroken shear lips is convenient because the strain in the unbroken shear lip is calculated in the conventional model using opening displacement behind the crack tip [5].

Here, although some relationships between the closure stress and the plastic strain were obtained as shown in Fig. 6-7, a series of analyses explained in Section 6.2.2.1 to evaluate the closure stress for each numerical condition were carried out more to add the data. In these analyses, the applied stress was set to from 37 MPa to 350 MPa, and the shear lip thickness was set to from 2 mm to 15 mm. Because the crack velocity hardly influences the closure stress as noted in Section 6.2.2.2, the crack velocity was basically set to 600 m/s in the all analyses of this section.

Considering that the plastic strain is associated with the amplitude of the closure stress, the reference stress, which is expressed by the plastic strain, was employed to evaluate the closure stress. This reference stress is expressed as

$$\sigma_{\mathrm{ref}} = \sigma_{\mathrm{YS}}(T, \dot{\varepsilon}) \left(1 + \frac{\varepsilon_{\mathrm{p}}}{0.02}\right)^{n} \tag{6-2}$$

where $\sigma_{\mathrm{YS}}(T, \dot{\varepsilon})$ is an yield stress at temperature T and strain rate $\dot{\varepsilon}$, ε_{p} is plastic strain, and n is a hardening exponent. Namely, Eq. (6-2) means a stress-strain relationship expressed by the Swift equation [18].

The closure stress and the plastic strain were obtained from these analyses, and the relationships between the closure stress and the reference stress were made for each analysis. These relationships under -10 ℃ were shown in Fig. 6-8.

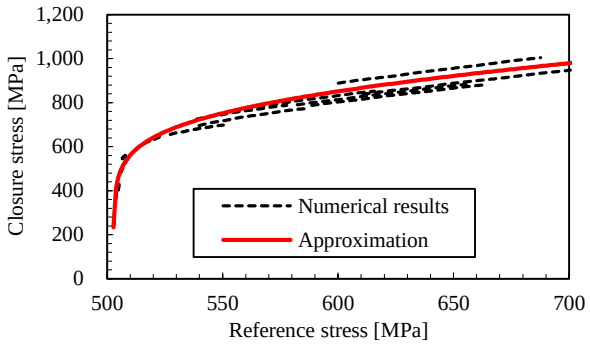

Fig. 6-8 Approximation of relationship between the closure stress and the reference stress under -10 ℃ (black dashed line: approximated curve)

In these relationships, the strain rate in Eq. (6-2) was set to $100\ \mathrm{s}^{-1}$ for simplicity because the actual strain rate in the analyses were almost in the order of $10^{1}\sim10^{2}\ \mathrm{s}^{-1}$. Although there are some separations of each relationship, it can be said that the closure stress has a unique relationship with the reference stress and thus it is well expressed by the reference stress. Therefore, the closure stress was approximated by the reference stress as

$$\sigma_{\mathrm{cl}} = 1.42\left\{360\left(1+\frac{\sigma_{\mathrm{ref}}(T,\dot{\varepsilon},\varepsilon_{\mathrm{p}})-\sigma_{\mathrm{ref}}(T,\dot{\varepsilon},0)}{0.050}\right)^{n(T)} + 0.3\left(\sigma_{\mathrm{ref}}(T,\dot{\varepsilon},\varepsilon_{\mathrm{p}})-750\right)\right\}-150 \tag{6-3}$$

where $n(T)$ is a parameter depending on the temperature. $n(T)=0.101$ under -10 ℃,. Here, it is worth noting that the form of Eq. (6-3) does not have any physical meaning. It is just an equation approximating the relationship shown in Fig. 6-8.

Same procedures as above were applied to other temperatures and it was shown that form of Eq. (6-3) could be applied to the other temperatures. Although the shear lip is sometimes observed in much low temperature in the brittle fracture surface of higher crack arrest toughness steels [2,19], the studied temperatures were $-40,\ -30,\ -20,\ -10,\ 0,\ 10$ ℃ because the shear lip is usually observed in usual steels like steel N when the temperature is higher than $-30\sim-20$ ℃ in brittle crack propagation [20,21].

As the result, only $n(T)$ and the reference stress were changed by the temperature and other values could be regarded as constants. The values of $n(T)$ is shown in Fig. 6-9. $n(T)$ is a

monotonically decreasing against temperature. These findings about the closure stress is used in next section, and the simulation model development in Chapter 7.

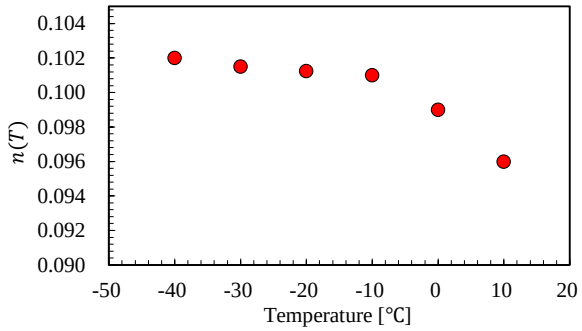

Fig. 6-9 $n(T)$ for each temperature

6.3. Shear lip thickness

6.3.1. Conventional formulation

The shear lip thickness is also an important factor to determine the amplitude of the closure effect. Although there have not been attempts to measure the thickness systematically, some studies pointed out the thickness was related to the plastic zone size near the crack tip [5,22]. Following them, Chapter 5 expressed the shear lip thickness in one side is expressed based on the small scale yielding concept as

$$t_{\mathrm{sl}} = \frac{k_{\mathrm{sl}}}{6\pi}\left(\frac{K_{\mathrm{eff}}}{\sigma_{\mathrm{YS}}(T,\dot{\varepsilon})}\right)^2 f_{\mathrm{sl}}(V) \tag{6-4}$$

where K_{eff} is the effective SIF, k_{sl} is a coefficient set to 2, and $f_{\mathrm{sl}}(V)$ is a coefficient depending on the crack velocity, which was proposed by the conventional numerical model of brittle crack propagation and arrest behaviors in steels [5]. Excluding $f_{\mathrm{sl}}(V)$, the expression of shear lip thickness similar to Eq. (6-4) can be found in previous literatures [12–14].

The crack velocity coefficient, $f_{\mathrm{sl}}(V)$, was derived by a series of 3D dynamic elastic-viscoplasitc finite element analyses in the conventional model [5]. Fig. 6-10 shows the schematic illustration to determine the crack velocity coefficient. Here, the shear lip thickness at the static condition, $t_{\mathrm{sl}}^{V=0}$ was expressed as

$$t_{\mathrm{sl}}^{V=0} = \frac{2}{6\pi}\left(\frac{K_{\mathrm{eff}}}{\sigma_{\mathrm{YS}}(T,\dot{\varepsilon})}\right)^2 \tag{6-5}$$

Here, $\varepsilon_{zz}^{\mathrm{sl}}$ is the plastic strain at the boundary between the shear lip and cleavage fracture surface. In the static cases, the boundary is located from $t_{\mathrm{sl}}^{V=0}$ in the thickness direction from the surface. According to the conventional model [5,23], the depth from the surface at which the plastic strain in thickness direction satisfy $\varepsilon_{zz}^{\mathrm{sl}}$ at each crack velocity correspond to the shear lip thickness. For example, $t_{\mathrm{sl}}^{V=400}$ is the shear lip thickness at $V = 400$ m/s in Fig. 6-10. Namely, $t_{\mathrm{sl}}^{V=400}/t_{\mathrm{sl}}^{V=0}$ is the crack velocity coefficient, $f_{\mathrm{sl}}(400)$. Thus, the conventional model supposed that the plastic strain represented the state of the plastic constraint. The previous study carried out a series of finite element analyses to obtain $f_{\mathrm{sl}}(V)$ for each crack velocity for the wide range of SIF. One of these results are shown in Fig. 6-11 [5]. The results indicated that the lower crack velocity made the shear lip thicker although the coefficient was not uniquely determined. The conventional model approximated the model as

$$f_{\mathrm{sl}}(V) = \cos\left(\frac{\pi}{2}\frac{V}{V_{\mathrm{R}}}\right)^{23.9} \tag{6-6}$$

where V_{R} is the Rayleigh wave velocity, which is the theoretical upper limit of fast crack propagation in solid [24].

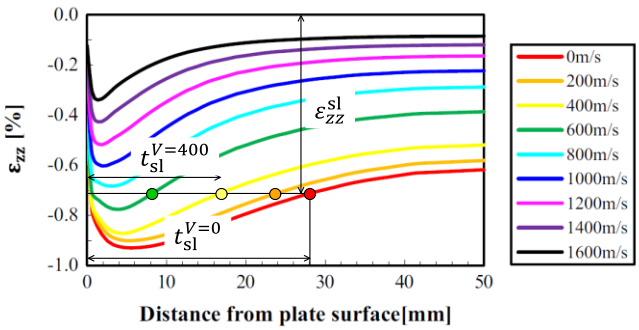

Fig. 6-10 Schematic illustration to decide the crack velocity coefficient [5]

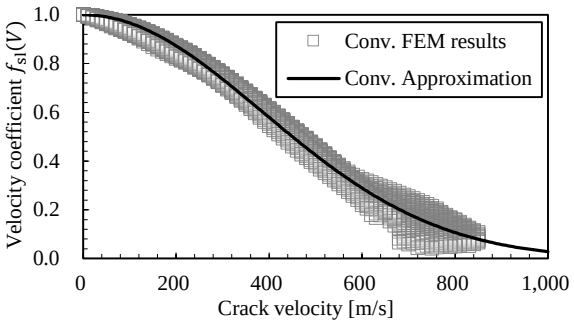

Fig. 6-11 Crack velocity coefficients and the approximation [5]

Although above formulation of the shear lip thickness is the first attempt to consider the crack velocity effect in brittle crack propagation in steels, there is no any experimental evidence to support the trend of shear lip thickness on the crack velocity. Therefore, to make shear lip thickness formulation supported by the physical meaning and experimental results, this section carried out systematic experiments and analyses of brittle crack propagation accompanying with the shear lip formation.

6.3.2.Shear lip formation experiments

Although Chapter 3 carried out crack propagation experiments preventing the shear lip from forming, it was needed to form shear lips in the experiments of this section. Thus, the experiments were carried out under relatively high temperatures ($-30\sim-10$ ℃). In addition, the applied stress when the brittle fracture started to run should be controlled because the shear lip thickness is expected to be thin or zero when the SIF is much low. So, on the contrary to the use of embrittlement bead to cause natural brittle fracture initiation without impact in Chapter 3, the impact was needed to employ to cause brittle fracture initiation under the aimed applied stress. The experiments were designed by considering these circumstances.

6.3.2.1. Specimen and experimental procedure

The employed steel was steel N explained in Chapter 3. The overview of the specimen is shown in Fig. 6-12. The configuration basically followed a specimen for the temperature gradient crack arrest test [25]. It was also similar to the specimen of steel N shown in Chapter 3. The specimen

was composed of a test plate and a dummy plate as shown in Fig. 6-12(a). This dummy plate was used to prevent the test rig from getting damage due to rapid change of the load, which was caused by fracture of specimens. The dummy plate was 5 mm apart from the test plate. Although it is desirable to keep higher temperature to promote shear lip formation, the top of the specimen had to be kept low temperature to make the brittle fracture initiation easy. Therefore, there was the temperature gradient from the specimen top to 210 mm from the top. To prevent shear lip formation in the temperature gradient region, the side groove was processed in the region. This side groove is expressed in Fig. 6-12(b). The shear lip formation was evaluated only in the isothermal region, which started from 210 mm from the specimen top. The temperatures were controlled by same method as explained in Chapter 3. Fig. 6-12(c) shows the photo of the specimen with strain gauges, which were used to measure crack velocities.

These experiments were conducted by the 10MN test rig in Kashima Unit, Nippon Steel & Sumikin Technology. The distance between pins was set to follow WES2815 [25], which was long enough not to cause the stress wave reflection effect.

As explained above, the impact was used to cause brittle fracture. The impact energy was set to 1,200 J, which was the minimum value of the employed impact machine. In addition, because the impact effect was relatively large until the crack length was shorter than 150 mm, the crack behaviors before it entered the isothermal region were not considered.

The isothermal temperatures were set to $-30, -20, \text{and} -10$ ℃ under the same applied stress. In addition, at -10 ℃, three levels of the applied stress were tested to change SIF. The crack velocity was also measured by the strain gauges, which were glued on the plate surface. However, it is worth noting that the strain gauge in these experiments could not detect crack tip position in the thickness center because of the unbroken shear lips and crack front tunneling although the strain gauges could be used to obtain the crack velocity in the thickness center in the side grooved specimen explained in Chapter 3 [8].

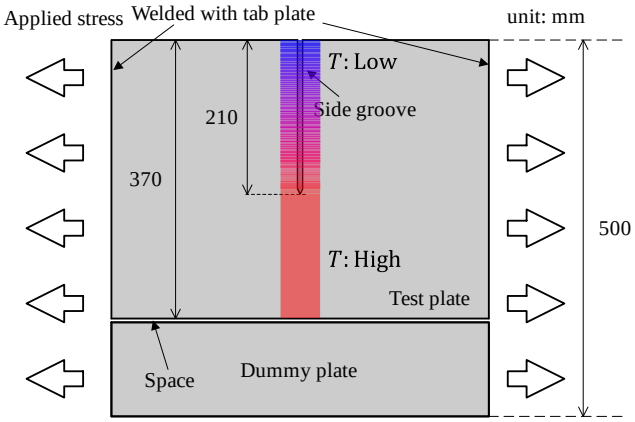

(a) Top view

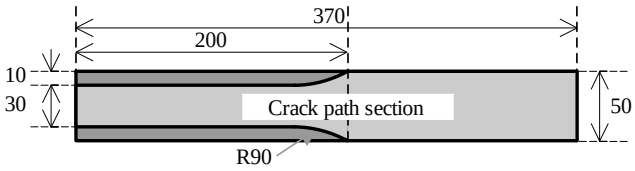

(b) Cross section of the test plate

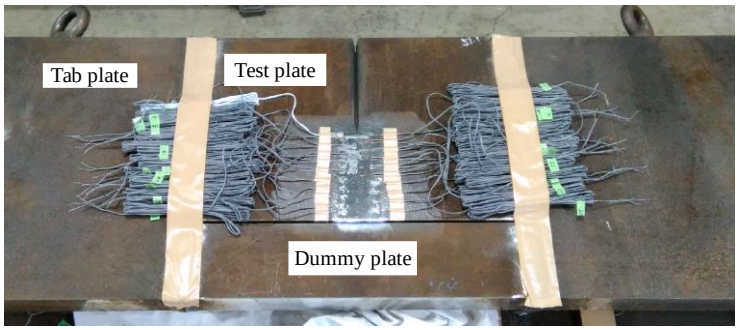

(c) Specimen photo

Fig. 6-12 Specimen

6.3.2.2. Experimental results

The experimental results are shown in Table 6-1. Totally, five experiments were conducted. SL1, SL2, and SL5 were under same temperature (−10 ℃). The applied stress was maximum in SL5 and minimum in SL1. Although as noted above, the impact was basically used to cause brittle crack initiation, the crack was naturally initiated to propagate in SL2 while the applied stress was increasing before the impact was applied. The measured average temperature was the mean value of the temperatures in the isothermal region. Four thermocouples were attached to this isothermal region in addition to three thermocouples in the temperature gradient region. After the experiment ended, the dummy plate and the tab plates were cut from the test plate. The fracture surfaces obtained in each experiment are shown in Fig. 6-13.

Table 6-1 Experimental conditions

No.	Initiation	Measured average temp. [℃]	Load [kN]	Remotely applied stress [MPa]
SL1	Impact	-10.4	4310	174
SL2	Natural	-10.2	5093	205
SL3	Impact	-31.6	5079	205
SL4	Impact	-21.3	5090	206
SL5	Impact	-11.4	6200	251

The crack velocities for each experiment were obtained from the time of the strain peak of each strain gauge. It should be paid attention to that these corresponded to mean velocities of the cleavage crack fronts as noted in Section 6.3.2.1. The relationships between the crack tip and time are shown in Fig. 6-14. The time of first observed peak was set to zero. These relationships were approximated by polynomials and differentiated to obtain the crack velocities. These crack velocities were used to evaluate the displacement behind the crack tip in Section 6.3.4 to calculate plastic strains in the unbroken shear lip.

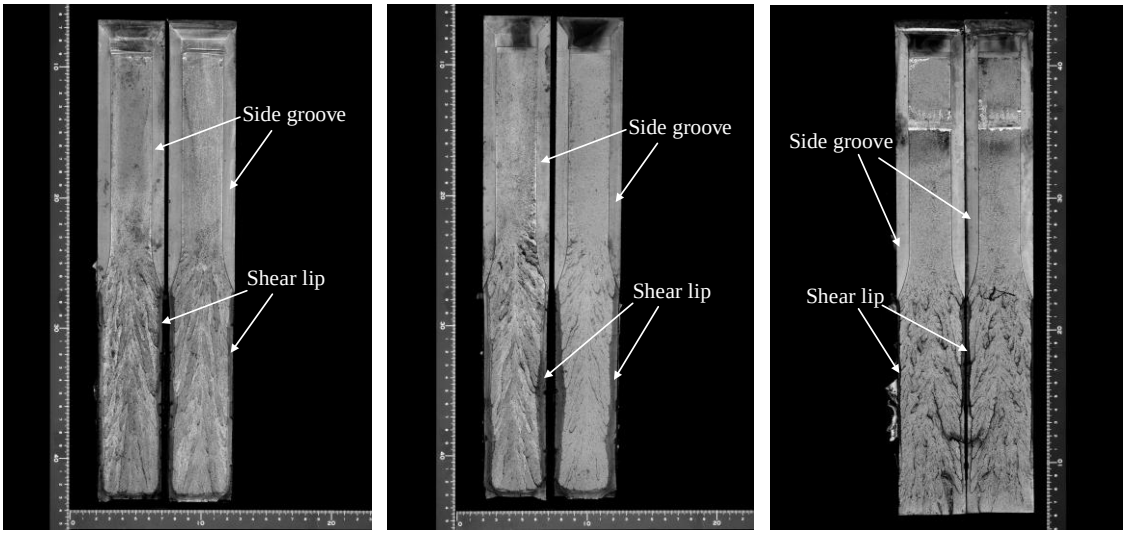

(a) SL1 (b) SL2 (c) SL3

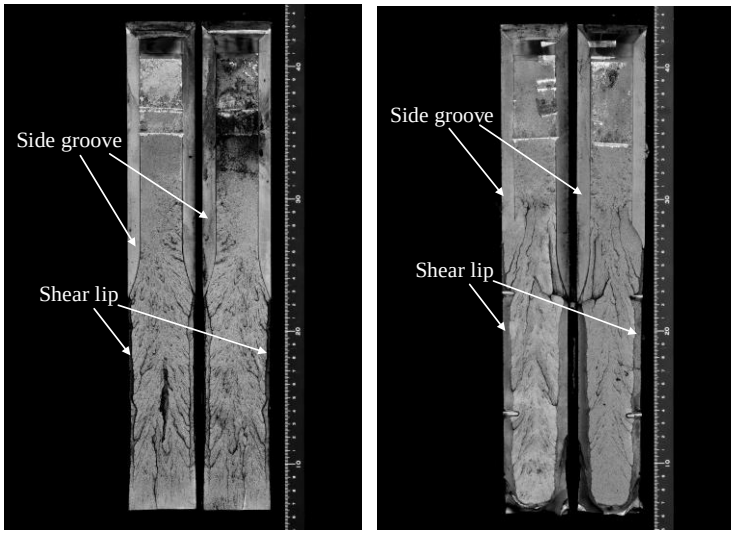

(d) SL4 (e) SL5

Fig. 6-13 Fracture surface of experiments.

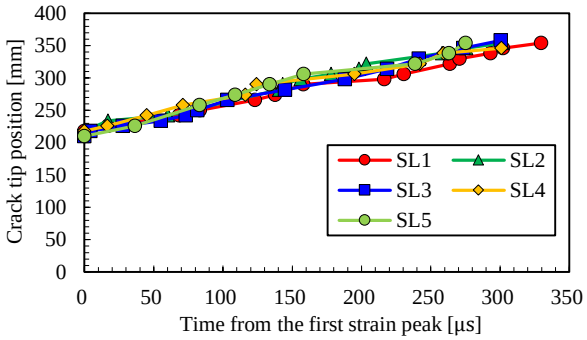

Fig. 6-14 Crack tip position-time relationship from strain data

6.3.3. Shear lip thickness measurement

In fact, there are no established methods to measure the shear lip thickness. There have been some literatures to attempt to measure shear lip thickness which formed not only during brittle crack propagation in steel but also in other fracture phenomena. The methods were not explained in detail in those literatures [8,9,26–28] although the optical measurement was conducted [13]. Therefore, the method to measure shear lip thickness was firstly examined.

At first, the most fundamental method is a visual measurement with ruler, which was usually conducted [13]. However, such measurement cannot be expected to have high accuracy, and, because the fracture surface has 3D configuration, such 2D method is not suitable to accurately evaluate the fracture surface including shear lip thickness. Using image processing from the fracture surface images as shown in Fig. 6-13 is a similar method and not suitable because of same reason. Therefore, the 3D measurement tools were promising to measure the shear lip thickness accurately. Aikawa et al. measured shear lip thickness which formed in a temperature gradient crack arrest test using a lazer 3D measurement system [29]. Although this method could reproduce the trend of shear lip thickness along the crack length, its resolution was doubtful to be enough to quantitatively measure the shear lip thickness. In addition, measurement speed of such system was very low. Therefore, the other 3D measurement tool was looked for, and the non-contact 3D configuration measurement tool, called One-shot machine [30], was employed.

Each specimen was cut to three small blocks with about 60 mm width and the surface 3D image was measured by the One-shot machine, VR-3000&3200 [30]. Because the visual field of the machine was smaller than each block's surface, some 3D images were measured respectively, and they were automatically integrated in the 3D image processing software. One example of the integrated 3D image of a block is shown in Fig. 6-15. The morphology including surface

roughness can be clearly observed in Fig. 6-15 by using the One-shot machine.

And then, the cross section morphology was obtained from the 3D image to evaluate the cleavage fracture thickness, t_{cl} as shown in Fig. 6-15. t_{cl} was determined based on the idea that the ductile fracture surface of shear lip tilted $45°$ against the flat cleavage fracture surface. This evaluation of the cross section morphology was conducted at 2~4 mm intervals. This process was conducted using a VR-3000 G2 analysis software.

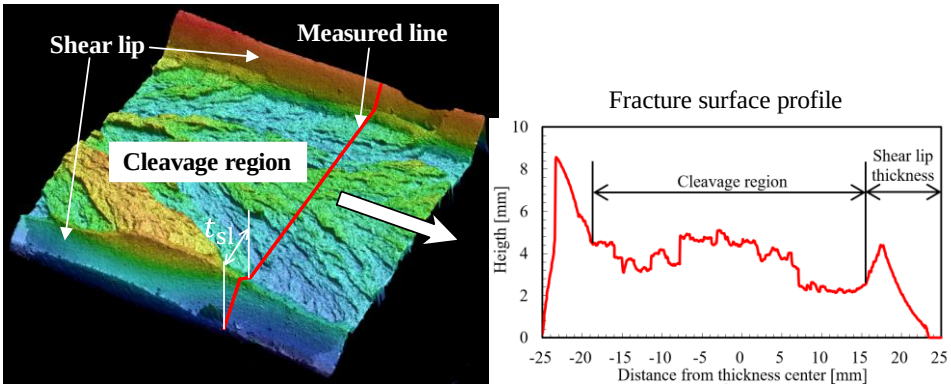

Fig. 6-15 3D image and the cross section morphology

Because of the plastic deformation due to brittle crack propagation, the specimen plate became thinner than the original condition near the crack path. Thus, it was concerned that the direct measurement of the shear lip may underestimate the thickness [31]. Therefore, the shear lip thickness, t_{sl}, was expressed as

$$t_{sl} = \frac{t - t_{cl}}{2} \tag{6-7}$$

where t is an original thickness (50 mm).

These measurements were carried out from 210 to 330 mm from the top of the specimens considering that the finite width effect may become too much when the crack tip approached to the end of the test plate. The measured shear lip thicknesses were shown in Fig. 6-16. The shear lip vanished after the crack length reached about 310 mm in SL3. These were the shear lip thickness data for the first time. Then, these shear lip thickness is used to formulate the shear lip

thickness in next section by interpolating the shear lip thickness against the crack length although the shear lip thickness data were discretely obtained.

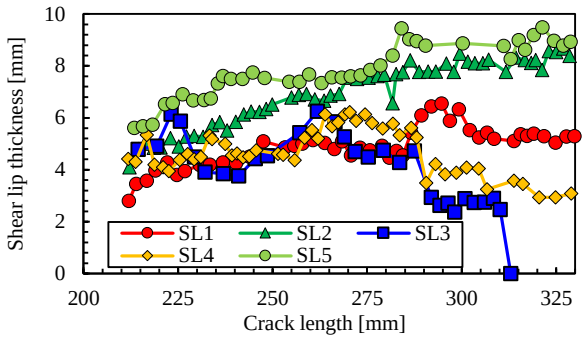

Fig. 6-16 Measured shear lip thickness

6.3.4. Formulation of shear lip thickness

This section aims to formulate the shear lip thickness using the above experimental data. The detail procedure is shown below;

(1) Effective SIFs for each measured shear lip thickness were calculated considering the closure effect. To calculate the closure effect due to the unbroken shear lip, strain values across the unbroken shear lip were evaluated to determine the closure stresses and the location where the unbroken shear lip broke due to shear.

(2) From the experimental data, the shear lip thickness at the static case, $t_{\mathrm{sl}}^{V=0}$, was calculated by Eq. (6-5) for each experimental shear lip thickness. $t_{\mathrm{sl}}^{V=0}$ was used to calculate $t_{\mathrm{sl}}^{\mathrm{ratio}}$, which is a ratio of the experimentally measured shear lip thickness against $t_{\mathrm{sl}}^{V=0}$.

(3) By using the calculated effective SIFs, the crack velocities at the thickness center were evaluated against the measured shear lip thickness from the response surfaces of local tensile stresses constructed.

(4) $t_{\mathrm{sl}}^{\mathrm{ratio}}$ for the crack velocity at the thickness center was calculated using the crack velocity determined in Step (3)

(5) $t_{\mathrm{sl}}^{\mathrm{ratio}}$ obtained in Step (4) were approximated to propose a new formulation for crack velocity coefficient.

6.3.4.1. Calculation of effective SIFs

As noted in Section 6.3.1, the shear lip thickness has been often expressed based on the plastic zone size of the crack tip [12,13]. Therefore, the plastic zone size based on the small scale yielding concept was calculated for each crack length. The effective SIF was needed to calculate the plastic zone size. This procedure corresponds to Step (1).

As shown in Chapter 5, the effective SIF should be considered to relate the SIF and the shear lip thickness. Thus, the effective SIFs were calculated for each experiment. The effective SIF, K_{eff}, is calculated as

$$K_{\mathrm{eff}} = K_{\mathrm{app}} - K_{\mathrm{cl}} \tag{6-8}$$

where K_{app} is the static SIF due to the applied stress and crack length, and K_{cl} is the closure effect defined in Eq. (6-1). Here, K_{app} was calculated by using 3D elastic finite element analyses considering the dummy plate and side-groove. To calculate K_{cl}, the shear lip thickness, length, and the closure stress have to be known. Although the shear lip thickness is known as shown in Fig. 6-16, the shear lip length at a certain crack length could not be determined from the fracture surfaces. In addition, although the closure stress is calculated from plastic strain in the unbroken shear lips to use the approximated formula of the closure stress proposed in Section 6.2, plastic strain was not also obtained from the fracture surfaces. Thus, the same procedure as the conventional model [5] was used to determine the plastic strain in the unbroken shear lips for evaluation of the shear lip end and closure stress in the unbroken shear lips.

In this procedure, a displacement behind a crack tip δ in crack opening direction is considered. δ is calculated under a closure stress by the equation proposed by Embley and Sih [32]. Because δ is a function of the crack velocity, the crack velocities measured in Section 6.3.2.2 were used to determine δ. Because the crack velocity suitable for calculating δ corresponds to the averaged velocity of the crack front, the crack velocities measured in Section 6.3.2.2 are appropriate to use here. The unbroken shear lip can be schematically illustrated as shown in Fig. 6-17. Assuming unbroken shear lip shows $45°$ shear deformation to break in ductile manner, the strain in the unbroken shear lip, $\varepsilon_{\mathrm{sl}}$, is simply written as

$$\varepsilon_{\mathrm{sl}} = \frac{\delta}{2t_{\mathrm{sl}}} \tag{6-9}$$

The strain distribution in the unbroken shear lip can be derived from Eq. (6-9). Here, because elastic strain is relatively small after it starts plastic deformation, this strain distribution was regarded to correspond to the plastic strain. Thus, the closure stress distribution can be evaluated using $\varepsilon_{\mathrm{sl}}$. In addition, the unbroken shear lip is broken in ductile manner at which $\varepsilon_{\mathrm{sl}}$ satisfies

$$\varepsilon_{\mathrm{sl}} = \varepsilon_{\mathrm{cr}} \tag{6-10}$$

where $\varepsilon_{\mathrm{cr}}$ is a failure strain which was set to 0.1 following the previous studies [5,33]. The unbroken shear lip length for each crack length was determined to satisfy Eq. (6-10). This means that the unbroken shear lip contributes to the closure effect until the strain in the unbroken shear lip reaches 0.1.

Accordingly, the above procedure enabled to determine the closure stress distribution and shear lip length. Namely, the closure effect could be calculated using Eq. (6-1). In addition, it is worth noting that the impact energy is not negligible even when the experiments followed the regulation in WES2815 [25]. Although the impact energy employed was small enough to follow the regulation, SIFs were expected to be 1.5 times at most according to WES2815 [25]. Because the impact effect depends on crack velocity, applied stress, and the crack length in addition to the amount of the impact energy itself, the effect cannot be simply calculated [34]. Therefore, this study considered that the impact made the applied SIF 1.3 times according to the previous studies [34–36]. This reason will be discussed in detail in Chapter 7. Of course, such impact energy was not introduced to SL2 because the impact was not used to initiate the brittle fracture in SL2. By following above procedure, the effective SIFs of the five experiments were calculated as shown in Fig. 6-18. These SIFs were applied to evaluate $t_{\mathrm{sl}}^{V=0}$ by using Eq. (6-5) as noted in Step (2).

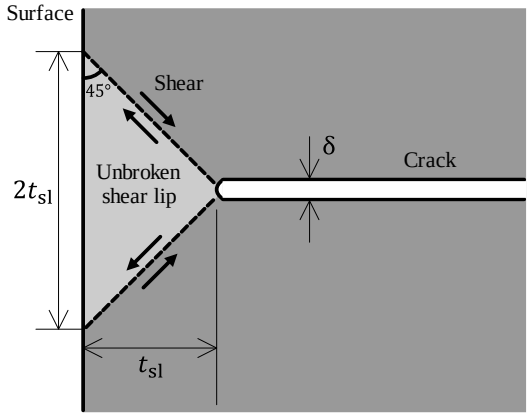

Fig. 6-17 Schematic illustration of shear lip shear deformation

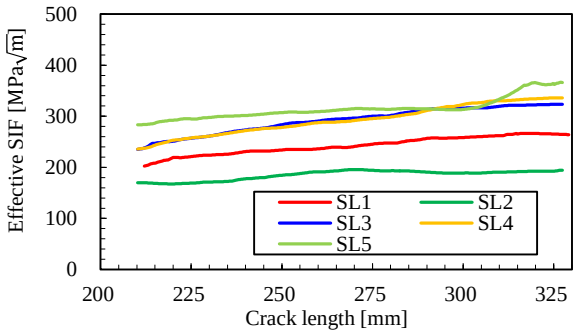

Fig. 6-18 Effective SIFs

6.3.4.2. Crack velocity coefficient

Next, Step (3) was carried out. Here, $t_{sl}^{V=0}$ could be obtained by using Eq. (6-2) and the effective SIFs shown in Fig. 6-18 and thus t_{sl}^{ratio}, which is the ratio of the experimentally measured shear lip thickness against $t_{sl}^{V=0}$, was calculated at each SIFs. However, the crack velocity has to be known at a certain SIF to determine $f_{sl}(V)$. Because the crack velocity to express $f_{sl}(V)$ is the crack tip velocity at the thickness center based on the previous model [5], the crack velocities obtained in Section 6.3.2.2 were not appropriate because these were the averaged velocities of the crack fronts. Thus, the crack velocity at the thickness center was evaluated using the response surface of the local tensile stresses made in Chapter 7. Although the detail procedure and characteristics of this response surface will be noted in Chapter 7, the local tensile stress σ_{yy} at the characteristic distance from the crack tip can be expressed as

$$\sigma_{yy} = f(V, T, a, \sigma_{\mathrm{app}}^{\mathrm{eff}}) \tag{6-11}$$

where V, T, a, and $\sigma_{\mathrm{app}}^{\mathrm{eff}}$ are crack velocity, temperature, crack length, and the applied stress which reflects the effective SIF, respectively. Based on the local fracture stress criterion, σ_{yy} always equal to the local fracture stress, σ_{F}, during crack propagation. σ_{F} of steel N is 2,070 MPa as noted in Chapter 3. Because temperature, crack length, and the applied stress which reflects the effective SIF are known in all experiments in this chapter, the crack velocity was derived by solving Eq. (6-11) about the crack velocity. The obtained crack velocities while the shear lip existed are shown in Fig. 6-19. The crack velocity is not changed a lot during crack propagation in each experiment. This is because increase rate of the local tensile stress against SIF becomes much smaller after SIF reaches a certain value as noted in Chapter 4. In addition, $t_{\mathrm{sl}}^{\mathrm{ratio}}$ is shown in Fig. 6-20 against SIF. The data shown in Fig. 6-20 are the shear lip thickness experimentally measured in Section 6.3.3. The overall trend that the shear lip thickness is thicker in lower crack velocity is elucidated experimentally for the first time and consisted with the prediction of the previous studies [5,21]. This process to obtain Fig. 6-20 corresponds to Step (4).

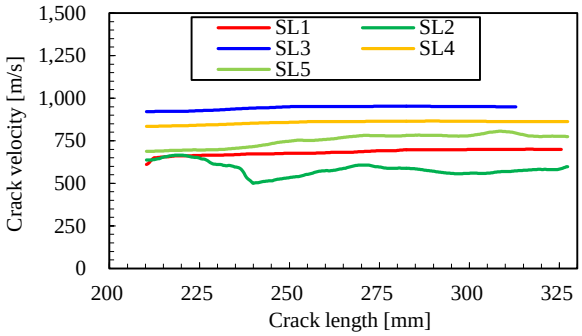

Fig. 6-19 Crack velocity at the thickness center

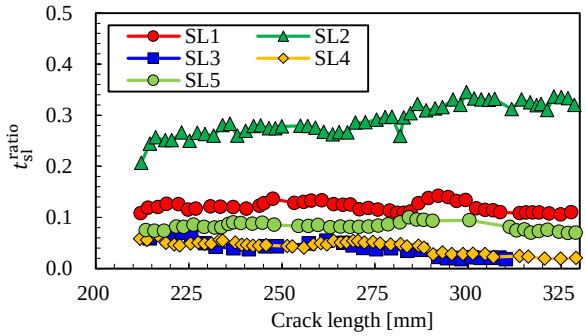

Fig. 6-20 t_{sl}^{ratio}

According to the above procedure, Step (5) was carried out to construct relationships between each experimental t_{sl}^{ratio} and the estimated crack velocity. These relationships are show in Fig. 6-21(a) with the conventional crack velocity coefficients and the approximation. The experimental t_{sl}^{ratio} are roughly included in the conventional crack velocity coefficients calculated from 3D finite element analyses, and thus, it can be said that the conventional method to determine the crack velocity coefficient in particular, about the trend against the crack velocity, was reasonable. In addition, Fig. 6-21(a) indicates the idea that the shear lip thickness is related to the plastic zone size is appropriate to be applied also to brittle crack propagation and arrest behaviors in steels.

However, the conventional approximation overestimated the experimental t_{sl}^{ratio}, so here, experimental t_{sl}^{ratio} is approximated by the same form of the function anew. The approximation with the experimental data is shown in Fig. 6-21(b). The approximation function, $f_{sl}(V)$, is expressed as

$$f_{sl}(V) = \cos\left(\frac{\pi}{2}\frac{V}{V_R}\right)^{28.6} \tag{6-12}$$

where V_R is the Rayleigh wave velocity. This approximation is the first expression to evaluate shear lip thickness based on the experimental results of brittle crack propagation in steels.

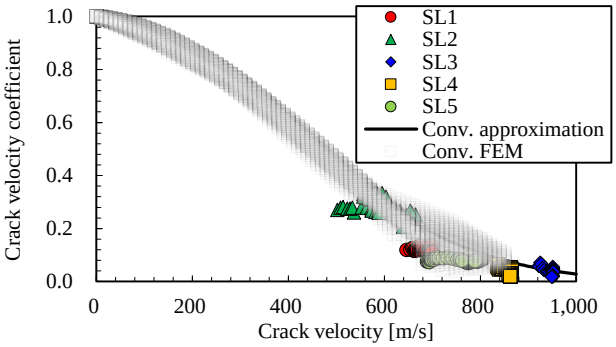

(a) Experimental data with the conventional approximation

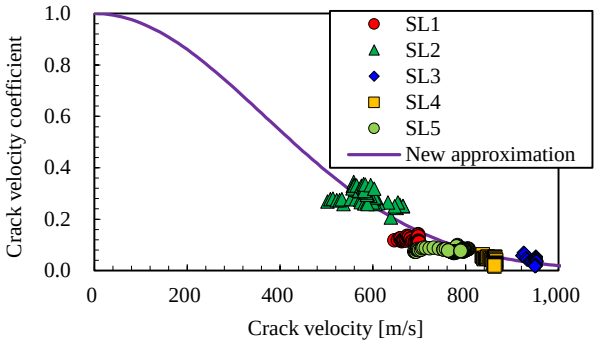

(b) New approximation

Fig. 6-21 Crack velocity coefficient of the shear lip thickness

6.4. Discussion

According to Section 6.2, the closure stress depends on the plastic strain. This means that the thicker unbroken shear lip has lower closure stress. When closure stresses are constant regardless of the plastic strain distribution as assumed in previous studies [5], the closure effect is a little overestimated in the thicker unbroken shear lip compared to the present formulation of the closure stress.

As noted above, the shear lip thickness can be expressed by a combination of the plastic zone size of the crack tip and the crack velocity coefficient. This study analyzed the experimental data and made the function to express the crack velocity effect to the shear lip thickness as shown in Fig. 6-21. Fig. 6-21 does not include the experimental data whose crack velocity is lower than 400 m/s, and therefore the approximation was carried out without the experimentally obtained shear lip thickness data whose crack velocity is lower than 400 m/s. However, as previously pointed in Chapter 4, the brittle crack hardly continues to propagate to keep its velocity lower

than $400\ \mathrm{m/s}$ [37,38]. This phenomenon can be explained from the local fracture stress criterion because the local tensile stress at a certain temperature and SIF becomes maximum when the crack velocity is 400~700 m/s as discussed in Chapter 4. This means that the shear lip thickness data when the crack velocity is lower than 400 m/s is difficult to obtain in the crack propagation experiments. And, because of the same reason, to simulate actual brittle crack propagation and arrest behaviors, the lack of the data whose crack velocity is lower than $400\ \mathrm{m/s}$ does not matter practically.

As shown in Fig. 6-21(a), the experimentally obtained crack velocity coefficients were approximated included in the conventional FEM range, which was evaluated from ε_{zz} distribution along the crack front. Although its physical basis of such evaluation has not been clarified, the amplitude of plastic deformation is associated with the amplitude of the plastic constraint in the thickness direction. Thus, the same plastic strain expresses the same amplitude of the plastic constraint along the crack front. Therefore, to determine the crack velocity effect, the conventional approach, which looked for the same ε_{zz} positions for each crack velocity, is considered as an appropriate way to determine the shear lip thickness.

On the other hand, it is worth noting that based on the local fracture stress criterion, the shear lip region is the region where the local fracture stress cannot be satisfied because the plastic constraint is lower near the surface. Therefore, the above approach which related the shear lip thickness to the size of the plastic region is an indirect and may be not applicable to the steel plates with gradient mechanical properties in thickness direction [39]. However, because there is no method to accurately evaluate the shear lip thickness based on the local fracture stress criterion, the above approach based on the experimental data is useful and meaningful to characterize the shear lip formation.

6.5. Conclusion

The unbroken shear lip which forms during brittle crack propagation in steels has not been investigated despite of its importance. The previous studies had no choice but to depend some assumptions, some of which were unrealistic. Therefore, in addition to Chapter 5 which modified the formulation of the shear lip thickness using effective SIF based on the experimental observation, systematic analyses on shear lip contributions were conducted in this chapter to appropriately model shear lip effect for accurate and physically-reasonable simulation of brittle crack propagation and arrest behaviors.

The contents of this chapter is divided to two studies because the shear lip contribution is attributed to two factors: the closure stress and the shear lip thickness. One is to investigate the characteristics of the closure stress by using 3D dynamic elastic visco-plastic finite element analyses as shown in Section 6.2. This section also modelled the closure stress based on a series of the analyses. On the other hand, Section 6.3 showed the study which attempted to formulate the shear lip thickness based on the crack propagation experiments accompanying with the shear lip formation.

In Section 6.2, a series of finite element analyses were carried out and showed that the closure stress is independent on crack velocity, and the contribution of other factors such as the applied stress can be introduced to evaluate the closure stress by focusing on the plastic strain. This section also showed that the closure stress can be expressed by the reference stress, which was derived using plastic strain. Following these findings, the approximated function to evaluate the closure stress was proposed in this section.

On the other hand, Section 6.3 measured the shear lip thickness from the fracture surface obtained in brittle crack propagation experiments by the One-shot 3D measurement machine. The measured results were used to relate the shear lip thickness with the plastic region size expressed by effective SIF based on the small scale yielding concept. The crack velocity coefficients were derived from these relationship for each experimentally obtained data. In this procedure, the effective SIF was calculated from the applied SIF, the unbroken shear lip length, and thickness. These crack velocity coefficients for each crack velocity were approximated by a function depending on the crack velocity. This approximation was carried out by referring the previous formulation of the shear lip thickness using the crack velocity.

Above two studies were first attempts to provide the characteristics and the contributions of the shear lips to brittle crack propagation and arrest behaviors in steel from the systematic experiments and numerical analyses. To model the closure stress and the shear lip thickness in this chapter will be applied to the numerical model development to simulate brittle crack propagation and arrest behaviors in steel, which will be explained in Chapter 7.

Reference

[1] H. Mabuchi, T. Hasegawa, T. Ishikawa, Metallurgical Features of Steel Plates with Ultra Fine Grains in Surface Layers and their Formation Mechanism, ISIJ Int. 39 (1999) 477–485. doi:10.2355/isijinternational.39.477.

[2] Y. Funatsu, H. Shirahata, J. Otani, T. Inoue, Y. Hashiba, The Effect of Shear-lips on the Arrestability of Thicker Steel Plates, in: Proc. Twenty-Second Int. Offshore Polar Eng.

Conf., 2012: pp. 63–66.
[3] T. Ishikawa, Y. Nomiyama, I. Hagiwara, S. Aihara, Study on Unstable Brittle Crack Arrest Toughness of Newly Developed Steel with Surface Layers with Ultra FIne Grain Microstructures-Improvement of Arrest Toughness by Enhanced Shear-lips Formation-, J. Soc. Nav. Archit. Japan. (1995) 259–267.
[4] A.H. Priest, An energy balance in crack propagation and arrest, Eng. Fract. Mech. 61 (1998) 231–251. doi:10.1016/S0013-7944(98)00075-7.
[5] K. Shibanuma, F. Yanagimoto, T. Namegawa, K. Suzuki, S. Aihara, Brittle crack propagation/arrest behavior in steel plate - Part I: Model formulation, Eng. Fract. Mech. 162 (2016) 324–340. doi:10.1016/j.engfracmech.2016.02.054.
[6] H. Mimura, Method to estimate Kca from K1a, J. High Press. Inst. Japan. 31 (1993) 58–64.
[7] D. Nakanishi, T. Kawabata, S. Aihara, Effect of dispersed retained γ-Fe on brittle crack arrest toughness in 9% Ni steel in cryogenic temperatures, Mater. Sci. Eng. A. 723 (2018) 238–246. doi:10.1016/j.msea.2018.03.056.
[8] N. Ogura, A Study on the Ductile Arrest of Brittle Cracks, J. Zosen Kiokai. 110 (1961) 443–453.
[9] Y. Akita, K. Ikeda, On the Brittle Crack Propagation and Arrest with Special Reference to ESSO Test with Temperature Gradient, J. Zosen Kiokai. 112 (1962) 153–162.
[10] S. Machida, H. Yoshinari, A. Yahiro, Study on Fast Fracture and Crack Arrest (The 7th Report), J. Soc. Nav. Archit. Japan. 158 (1985) 610–618.
[11] A.T. Zehnder, A.J. Rosakis, On the temperature distribution at the vicinity of dynamically propagating cracks in 4340 steel, J. Mech. Phys. Solids. 39 (1991) 385–415. doi:10.1016/0022-5096(91)90019-K.
[12] M.O. Lai, W.G. Ferguson, Relationship Between the Shear Lip Size and the Fracture Toughness., Mater. Sci. Eng. 45 (1980) 183–188. doi:10.1016/0025-5416(80)90224-4.
[13] J.R. Matthews, C.V. Hyatt, J.F. Oorter, K.J. Karisallen, Effect of Thickness on the Relationship between Shear Lip and Energy in Dynamic Tear Specimen, Eng. Fract. Mech. 60 (1998) 539–542. doi:10.1016/0013-7944(95)00258-8.
[14] Q.Q. Duan, R.T. Qu, P. Zhang, Z.J. Zhang, Z.F. Zhang, Intrinsic impact toughness of relatively high strength alloys, Acta Mater. 142 (2018) 226–235. doi:10.1016/j.actamat.2017.09.064.
[15] H.F. Li, Q.Q. Duan, P. Zhang, R.T. Qu, Z.F. Zhang, A new method to estimate the plane strain fracture toughness of materials, Fatigue Fract. Eng. Mater. Struct. (2018) 1–10. doi:10.1111/ffe.12919.
[16] A. Uguz, J.W. Martin, Plastic zone size measurement techniques for metallic materials, Mater. Charact. 37 (1996) 105–118. doi:10.1016/S1044-5803(96)00074-5.
[17] T.S. Koko, J.R. Matthews, Plastic zone development in dynamic tear-type test specimens, Finite Elem. Anal. Des. 37 (2001) 997–1012. doi:10.1016/S0168-874X(01)00045-2.
[18] H.W. Swift, Plastic instability under plane stress, J. Mech. Phys. Solids. 1 (1952) 1–18. doi:10.1016/0022-5096(52)90002-1.
[19] S. Machida, Y. Kawaguchi, M. Tsukamoto, An Evaluation of the Crack Arrestability of 9% Ni Steel Plate to a Extremely Long Brittle Crack, J. Japan Soc. Nav. Archit. 150 (1981) 511–517.
[20] S. Machida, H. Yoshinari, A. Yashiro, Crack Arrest Behavior of Fast Fracture in Steel, J. Soc. Mater. Sci. Japan. 35 (1986) 860–866.
[21] S. Machida, H. Toshinari, T. Miyahara, G. Nishiyama, Study on Fast Fracture and Crack Arrest (6th Report), J. Soc. Nav. Archit. Japan. 156 (1984) 550–557.
[22] A. Uguz, J.W. Martin, Plastic zone size measurement techniques for metallic materials, Mater. Charact. 37 (1996) 105–118. doi:10.1016/S1044-5803(96)00074-5.

[23] K. Shibanuma, F. Yanagimoto, T. Namegawa, K. Suzuki, S. Aihara, Brittle crack propagation/arrest behavior in steel plate - Part II: Experiments and model validation, Eng. Fract. Mech. (2016). doi:10.1016/j.engfracmech.2016.02.053.
[24] K.B. Broberg, Cracks and Fracture, Academic Press, 1999.
[25] The Japan Wedling Engineering Society, WES2815 Test method for brittle crack arrest toughness, (2014). http://www-it.jwes.or.jp/wes_ki/wesippan.jsp?arg=2815e-1.
[26] Y. Hagiwara, S. Tsukamoto, T. Otani, G. Arakane, K. Matsuda, Toughness Evaluation by Means of Side-notched Charpy Test, Tetsu-to-Hagane. 90 (2004) 76–82.
[27] V. Granados-Alejo, C. Rubio-González, C.A. Vázquez-Jiménez, J.A. Banderas, G. Gómez-Rosas, Influence of specimen thickness on the fatigue behavior of notched steel plates subjected to laser shock peening, Opt. Laser Technol. 101 (2018) 531–544. doi:10.1016/j.optlastec.2017.12.011.
[28] H. Yajima, M. Tada, S. Yamagata, A. Deguchi, J. Imai, J. Katsuta, A Consideration on Surface-Notched Double Tension Test, Trans. West-Japan Soc. Nav. Archit. 72 (1986) 327–333.
[29] T. Aikawa, S. Aihara, T. Kawabata, F. Yanagimoto, K. Shibanuma, Computer simulation of cleavage fracture surface morphologies in steel plates, in: 22nd Eur. Conf. Fract., 2018: p. 19.
[30] KEYNCE, VR-3200, (n.d.). https://www.keyence.co.jp/products/microscope/roughness-measure/vr-3000/models/vr-3200/ (accessed October 10, 2018).
[31] J. Zuidema, F. Veer, C. Van Kranenburg, Shear lips on fatigue fracture surfaces of aluminum alloys, Fatigue Fract. Eng. Mater. Struct. 28 (2005) 159–167. doi:10.1111/j.1460-2695.2004.00837.x.
[32] G.T. Embley, G.C. Sih, Plastic flow around an expanding crack, Eng. Fract. Mech. 4 (1972) 431–442. doi:10.1016/0013-7944(72)90055-0.
[33] S. Machida, H. Yoshinari, M. Yasuda, S. Aihara, H. Mabuchi, Fracture mechanicsl modeling of brittle fracture propagation and arrest of steel (1) A fundamental model, J. Soc. Nav. Archit. Japan. 177 (1995) 243–258.
[34] T. Kawabata, M. Kaneko, S. Aihara, Effect of Impact Energy in the Esso Test (Part 1 : Basic Experiments and Validation of FEM Analysis), J. Test. Eval. 46 (2018). doi:10.1520/JTE20170045.
[35] M. Kaneko, T. Kawabata, S. Aihara, Effect of Impact Energy in ESSO Test ((Part 2: Proposal of Validity Criteria of Impact Condition in ESSO Test by FEM Crack Propagation Analysis), J. Test. Eval. 47 (2019) 20170151. doi:10.1520/JTE20170150.
[36] M. Kaneko, T. Kawabata, S. Aihara, Effect of Impact Energy in ESSO Test (Part 3: Experimental Validation for New Validity Criteria of Impact Condition Giving Constant Evaluation in ESSO Test), J. Test. Eval. 47 (2019) 20170150. doi:10.1520/JTE20170150.
[37] S. Machida, M. Matoba, H. Yoshinari, C. Tone, A Model for Brittle Crack Propagation and Arrest in Structural Steel, J. Soc. Nav. Archit. Japan. 172 (1992) 637–647.
[38] I. Watanabe, M. Suzuki, Y. Matsuda, S. Yamagata, H. Yajima, The Crack-Arrest Properties of 9%Ni Steel and its Weldment (1st Report), J. Soc. Nav. Archit. Japan. 155 (1984) 368–379.
[39] T. Handa, S. Igi, K. Nishimura, H. Tajika, T. Tagawa, S. Tsuyama, Effect of Toughness Distribution in the Thickness Direction on Long Brittle Crack Propagation/Arrest Behavior of Heavy Gage Shipbuilding Steel, Q. J. Japan Weld. Soc. 34 (2016) 211–217.

Chapter 7 Development of a numerical model to simulate brittle crack propagation and arrest behaviors in steel

7.1. Introduction

The theories based on the local fracture stress have developed to explain brittle crack propagation and arrest behaviors in steel from 1995 to 2016 [1–5]. Although the conventional model recently showed simulated results which agreed well with the experimental results, each element models in the conventional model were not physically meaningful and not supported by the detail investigations, and in particular, the identified local fracture stresses in the conventional simulations were far from the supposed value. This study aimed to refine the theory to explain brittle crack propagation and arrest behaviors in steel based on a series of experiments and numerical analyses described above.

From Chapter 3 to Chapter 6, a series of experiments and numerical analyses have been carried out. These studies showed

(1) The local tensile stresses at the characteristic distance, which corresponds to the local fracture stress, are almost constant. This result strongly supports the validity of the local fracture stress criterion. In addition, the brittle crack arrest toughness of a steel is determined by not only the local fracture stress, but also constitutive law. (Chapter 3)

(2) The local tensile stress can be expressed by a function of the crack length, applied stress, temperature, and crack velocity. Unsteady effect is practically negligible (Chapter 4)

(3) By regarding the shear lip thickness is governed by the effective SIF, whether the crack can be arrested or not is appropriately simulated based on the local fracture stress (Chapter 5)

(4) The closure stress can be calculated by the reference stress, which considers the plastic strain of the unbroken shear lip. In addition, the shear lip thickness can be expressed by the plastic region size and the crack velocity (Chapter 6)

These findings can replace the assumptions in the conventional model, which were not supported by physical background [1,5]. Therefore, this chapter develops a new simulation model to predict brittle crack propagation and arrest behaviors in steel based on the local fracture stress criterion. The validity of this model is tested by comparison with the temperature gradient crack arrest test results. Through this validation process, the validity of the local fracture stress evaluated in Chapter 3 is also tested by comparing the experimentally evaluated value in Chapter 3 and the identified value in the model simulation.

7.2. Model development concept

According to previous studies, brittle crack propagation and arrest behaviors in steel can be expressed based on the local fracture stress criterion by three element models as schematically shown in Fig. 7-1: (i) the local stress near the crack tip, (ii) the closure effect of the unbroken shear lip, and (iii) shear lip thickness. To evaluate the local tensile stress in the model, systematic finite element analyses were carried out to make response surfaces to relate the local stress with macroscopic parameters. Second, the closure effect is evaluated by using the approximation formula of the closure stress proposed in Section 6.2. And then, the shear lip thickness is determined using the formulation proposed in Section 6.3.

Based on the local fracture stress criterion, the critical condition of brittle crack propagation is expressed as

$$\begin{aligned} \sigma_{\mathrm{F}} = \sigma_{yy}(r_{\mathrm{c}}) &: \text{continue to propagate} \\ \sigma_{\mathrm{F}} > \sigma_{yy}(r_{\mathrm{c}}) &: \text{arrest} \end{aligned} \tag{7-1}$$

where $\sigma_{yy}(r_{\mathrm{c}})$ is the local tensile stress at the characteristic distance, r_{c}, from the crack tip, and σ_{F} is the local fracture stress. According to Chapter 3, the local fracture stress is set to constant value depending of the material. σ_{yy} depends on the material's constitutive law, so the constitutive law of the material used in crack arrest experiments for model validation should be employed to evaluate σ_{yy}.

Here, the model employs two assumptions following the conventional model: (a) the crack front shape is straight, and (b) the critical condition is evaluated at the thickness center [5]. Although the crack front curvature cannot be accurately predicted, the fracture surface observation indicated that the crack front curvature was not remarkable and SIF reduction due to 3D effect was dominantly caused by the unbroken shear lips [5]. And, (b) is employed because the stress state except the thickness center is not known and thus the local stress along the crack front cannot be evaluated by the response surface made by parametric finite element analyses although the thickness center is regarded to be plain strain.

In addition, because this model development aims to establish theoretical explanation of brittle crack propagation and arrest behaviors in steel, the developed model does not suppose its application to the steels with complex textures, which are recently developed to improve its brittle crack arrest toughness [6–8].

From next section, the above three factors are respectively modelled based on the findings shown in previous chapters. And then, these are integrated to the numerical model simulating brittle crack propagation and arrest behaviors.

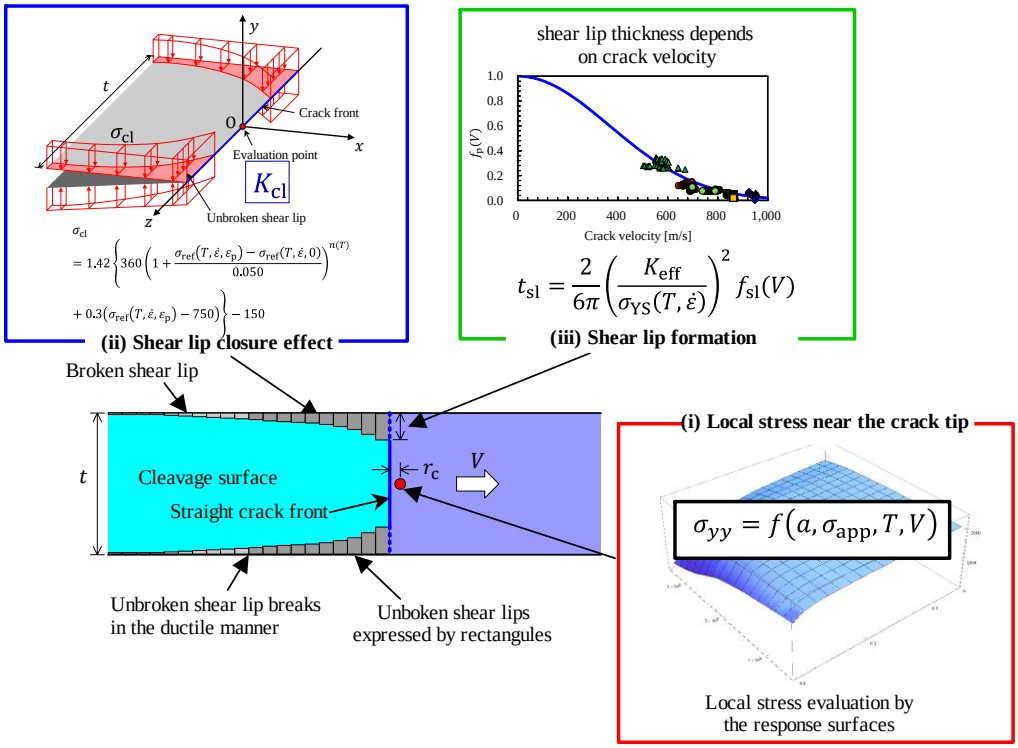

Fig. 7-1 Model concept

7.3. Element models

7.3.1. Local tensile stress

The local tensile stress in the vicinity of a rapidly propagating crack tip is the most important factor in the local fracture stress criterion. According to Chapter 4, the local tensile stress σ_{yy} at the characteristic distance r_c from the crack tip is expressed as

$$\sigma_{yy}(r_c) = f(\sigma_{app}, a, T, V) \tag{7-2}$$

where σ_{app}, a, T, V are the applied stress, the crack length, the temperature, and the crack velocity, respectively.

As noted in Chapter 2 and 4, it is difficult to evaluate the local tensile stress without any numerical methods like finite element method. Although the conventional models evaluated the local tensile stress by combination of some analytical solutions, such simplified method overestimated the local tensile stress and provided an unrealistic value [1,5]. Therefore, the local tensile stresses were evaluated to make the response surface using a series of finite element analyses. The response surface was made by interpolating the local tensile stresses evaluated in each numerical condition by finite element analyses. By modifying the mesh generator explained in Chapter 2 and 4, finite element models for crack propagation analyses were constructed. Fig. 7-2 shows an example of the finite element model made by the mesh generator. The model is 2D semi-infinite and the crack was supposed to be edge crack. The model was infinite in the crack propagation direction and applied stress direction to exclude the stress wave reflection effects. This is because the model simulation supposed the temperature gradient crack arrest test in that the single edge crack specimen is employed. This experiment will be noted in detail later. The crack propagation is expressed by generation phase nodal force release technique.

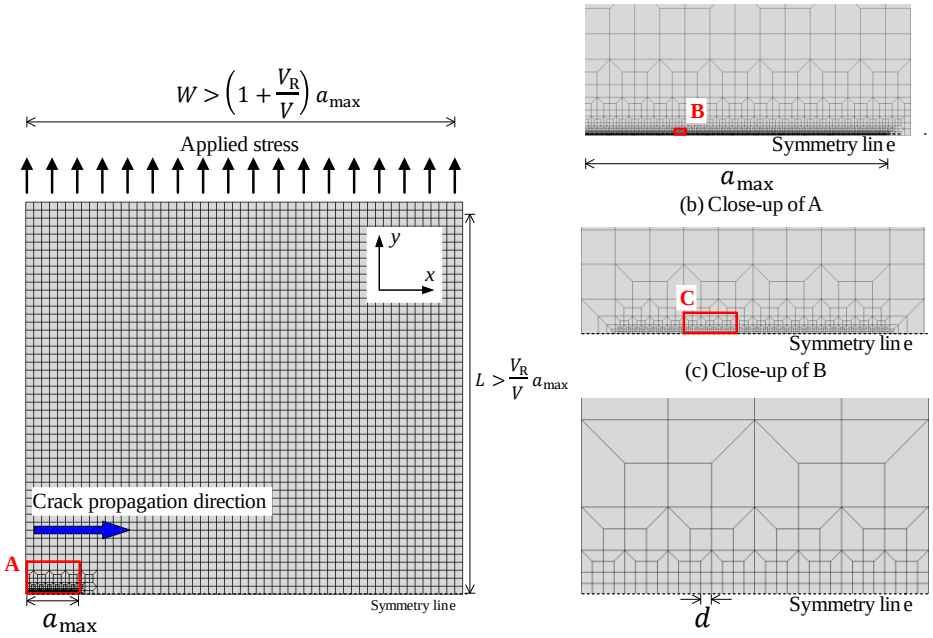

Fig. 7-2 Finite element model

Because to make the response surface accurately required a lot of analysis results, the fine mesh zones were located at a certain interval along the crack path in the finite element models as shown in Figs. 7-2(b) and (c). The local stresses were evaluated when the crack tip reached the center node along the crack path of this zone. The minimum mesh size of this zone, d, was set to 0.05 mm, and the minimum mesh size along the crack path except the fine mesh zone was set to 0.8 mm. The elements of which the finite element model was composed were fully integration and plain strain. Finite element analyses were carried out under implicit dynamic elastic viscoplastic condition using Abaqus 6.14 [9].

The constitutive law of steel N, which was shown in Chapter 3, was input to the analyses. Numerical conditions are shown in Table 7-1. The yield stress at static and room temperature conditions of steel N is 368 MPa, so the applied stresses were smaller than 368 MPa in all analyses. Because the model validation will be conducted for the normal width temperature gradient crack arrest test, the maximum crack length was set to 500 mm. The temperatures around the crack arrest temperature were emphatically employed in the analyses. Similarly, the crack velocities which have been frequently observed in actual crack propagation were primarily analyzed. The finite element model in each analysis was set to isothermal. The characteristic distance was set to 0.15 mm according to Chapter 3.

Table 7-1 Numerical conditions

Variable	σ_{app} [MPa]	a [mm]	T [℃]	V [m/s]
Value	60, 114, 184, 242, 300, 300	15, 30, 45, 60, 90, 100, 120, 150, 200, 250, 300, 350, 400, 450, 500	-90, -60, -30, -20, -10, 0, 10	100, 200, 300, 400, 450, 500, 550, 600, 650, 700, 800, 1200

The obtained local stresses from a series of finite element analyses were linearly interpolated to make the response surfaces. Fig. 7-3 shows examples of the response surfaces. The overall trend of the local stress against the four parameters consisted with that shown in Chapter 4. As noted, these response surfaces were applied in Section 6.3 to determine the crack velocity in the thickness center.

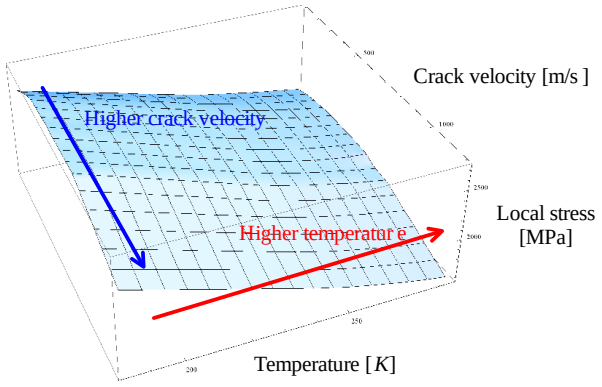

(a) Temperature and crack velocity vs. local stress

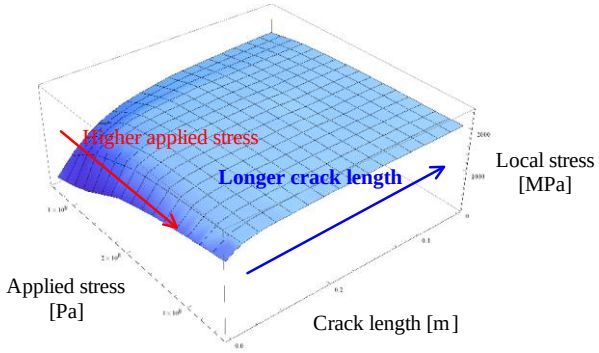

(b) Applied stress and crack length vs. local stress

Fig. 7-3 Response surfaces

7.3.2. Closure effect

As it is widely known, the unbroken shear lip, which is a region where the cleavage crack cannot continue to propagate in, forms near the surface. The closure effect is caused by this unbroken shear lip until it is broken in ductile manner to become shear lip.

The closure stress was discussed in Section 6.2 and the procedure to calculate follows the conventional model [5]. The closure stress works on the unbroken shear lip as schematically illustrated in Fig. 7-4. The effective SIF, K_{eff}, is expressed as

$$K_{\mathrm{eff}} = \sigma_{\mathrm{app}}\sqrt{\pi a} - K_{\mathrm{cl}} \tag{7-3}$$

where K_{cl} is the closure effect expressed in terms of stress intensity factor.

Then, K_{cl} is calculated as

$$K_{\mathrm{cl}} = \int_{\Omega_{\mathrm{sl}}} \frac{\sqrt{2}\sigma_{\mathrm{cl}}}{(\pi|x|)^{3/2}\{1+(z/x)^2\}}\mathrm{d}\Omega \tag{7-3}$$

where Ω_{sl} is the area of unbroken shear lip and σ_{cl} is the closure stress. In the model calculation, the closure effect was calculated by rectangular integration.

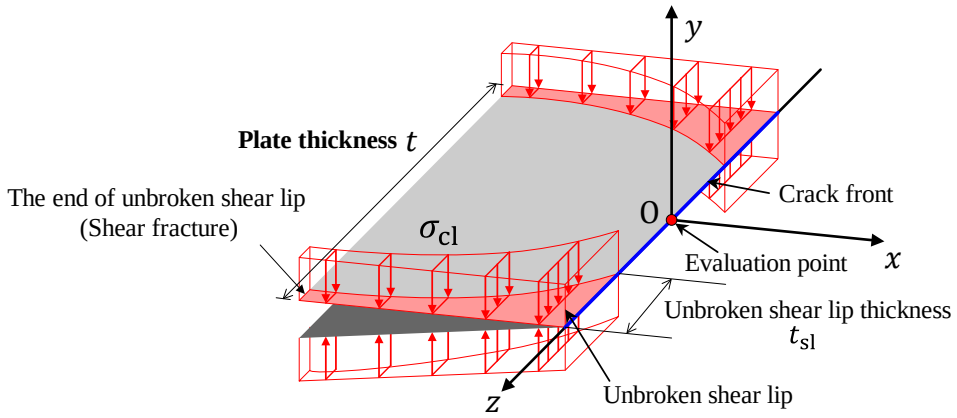

Fig. 7-4 Schematic illustration of closure stress calculation

σ_{cl} is formulated by approximating results of a series of 3D finite element analyses in Section 6.2. One example is shown in Fig. 7-5. The approximated formula is written as

$$\sigma_{cl} = 1.42\left\{360\left(1+\frac{\sigma_{\mathrm{ref}}(T,\dot{\varepsilon},\varepsilon_p)-\sigma_{\mathrm{ref}}(T,\dot{\varepsilon},0)}{0.050}\right)^{n(T)} + 0.3\left(\sigma_{\mathrm{ref}}(T,\dot{\varepsilon},\varepsilon_p)-750\right)\right\}-150 \tag{7-4}$$

where $\sigma_{ref}(T,\dot{\varepsilon},\varepsilon_p)$ is a reference stress calculated from Swift's equation at the temperature T, strain rate $\dot{\varepsilon}$, and plastic strain ε_p. The strain rate was set to $100\ s^{-1}$. $n(T)$ is coefficient determined for each temperature, T, shown in Fig. 7-6. To obtain $n(T)$ for arbitrary temperature, the discretely obtained value of $n(T)$ was linearly interpolated against temperature.

The mode employed same procedure to evaluate the plastic strain as explained in Section 6.3. Namely, the plastic strain, ε_p, was calculated as

$$\varepsilon_{\mathrm{p}} = \frac{\delta}{2t_{\mathrm{sl}}} \tag{7-5}$$

where δ is the crack opening displacement behind the crack tip, and t_{sl} is the shear lip thickness. Although the conventional model used this plastic strain only as indicator which decided the unbroken shear lip length, this present model utilized the plastic strain to evaluate

the closure stress. The crack opening displacement, δ, is calculated by a method proposed by Embley and Shih [10]. Fig. 7-7 shows the closure stress for plastic strain for each temperature. Basically, the closure stress is larger in lower temperature.

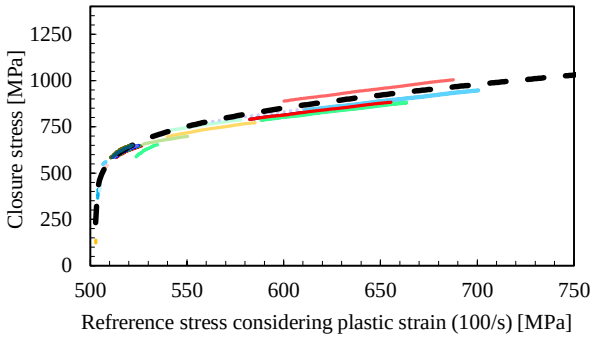

Fig. 7-5 Approximation of relationship between the closure stress and the reference stress under -10 ℃ (black dashed line: approximated curve)

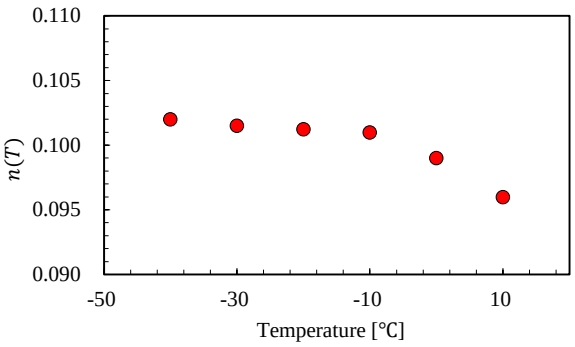

Fig. 7-6 Hardening coefficient of closure stress for each temperature

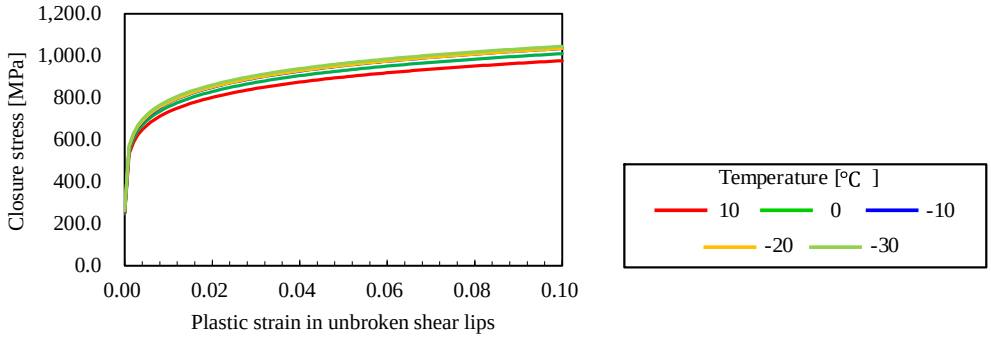

Fig. 7-7 Closure stress for each temperature

Because the unbroken shear lip is regarded to break in ductile manner, it is required to set failure criterion in ductile manner of the unbroken shear lip. Although the ductile fracture is simulated by some numerical methods [11–13], they make the numerical cost too large, and are much complicated to introduce in the present theoretical simulation model. Therefore, as a simple criterion, the critical strain concept was employed in this present model, following past studies on ductile fracture and the conventional models [1,5,14,15]. Thus, the unbroken shear lip breaks in shear fracture when the plastic strain in the unbroken shear lip reaches the failure strain, ε_{f}. Namely, the fracture condition of unbroken shear lips is expressed as

$$\varepsilon_{\mathrm{p}} = \varepsilon_{\mathrm{f}} \tag{7-6}$$

Here, the failure strain was set to 0.1 following the previous study [5].

7.3.3. Shear lip thickness

The formulation of shear lip thickness was described in Section 6.3. According to a series of the experiments and their analyses, the shear lip thickness, t_{sl}, can be expressed by

$$t_{\mathrm{sl}} = \frac{k_{\mathrm{sl}}}{6\pi}\left(\frac{K_{\mathrm{eff}}}{\sigma_{\mathrm{YS}}(T,\dot{\varepsilon})}\right)^2 f_{\mathrm{sl}}(V) \tag{7-7}$$

where k_{sl}, $\sigma_{\mathrm{YS}}(T,\dot{\varepsilon})$, and $f_{\mathrm{sl}}(V)$ are constant set to 2, yield stress at temperature T and strain rate $\dot{\varepsilon}$, set to $10^{-3}\ \mathrm{s}^{-1}$, and function to express crack velocity coefficient. Eq. (7-7) depends on the idea that the depth of surface region where the plastic constraint becomes small enough not

to cause cleavage fracture is twice the plastic region of the crack tip [1]. This idea is also supported by the experimental results in Section 6.3.

$f_{\mathrm{sl}}(V)$ is derived by approximating the experimental results as shown in Fig. 7-8. The experiments named SL1 , 2, 3, 4, and 5 were described in Section 6.3 in detail. $f_{\mathrm{sl}}(V)$ is expressed as

$$f_{\mathrm{sl}}(V) = \cos\left(\frac{\pi}{2}\frac{V}{V_{\mathrm{R}}}\right)^{28.6} \tag{7-8}$$

where V_{R} is Rayleigh wave velocity.

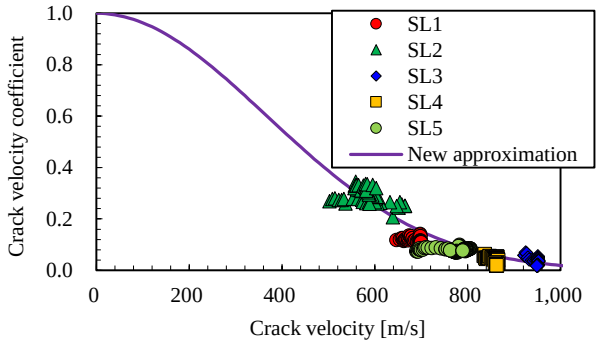

Fig. 7-8 Crack velocity coefficient of the shear lip thickness

7.4. Model formulation

7.4.1. Model integration

By integrating the element models to express each physical phenomenon shown in Section 7.3, the present simulation model is formulated. This model is described by simultaneous equations composed of two equations expressed as

$$\sigma_{\mathrm{F}} = f(\sigma_{\mathrm{eff}}, a, T, V) \tag{7-9}$$

$$t_{\mathrm{sl}} = \frac{2}{6\pi}\left(\frac{K_{\mathrm{eff}}}{\sigma_{\mathrm{YS}}(T,\dot{\varepsilon})}\right)^2 f_{\mathrm{sl}}(V) \tag{7-10}$$

where $f(\sigma_{\text{eff}}, a, T, V)$ is the function composed of the response surfaces made in Section 7.3.1 and unknown variables are the crack velocity and the shear lip thickness at the crack tip. This formulation composed of two equations is simpler than that of the conventional model, whose simultaneous equations were composed of four equations and four unknown variables.

Because SIF cannot express the local tensile stresses, the applied stress and the crack length are separately introduced in this model although the closure effect is expressed in terms of SIF. Therefore, the effective applied stress, σ_{eff}, and the effective crack length, a_{eff}, are introduced for convenience instead of σ_{app} and a. These are used to express the change of SIFs due to impact effect, finite width correction, and the closure effect. σ_{eff} is expressed as

$$\sigma_{\text{eff}} = F\sigma_{\text{app}} \tag{7-11}$$

a_{eff} is expressed as

$$a_{\text{eff}} = \frac{K_{\text{eff}}}{\sigma_{\text{eff}}\sqrt{\pi}} \tag{7-12}$$

Therefore, σ_{eff} reflects the impact effect and a_{eff} considers the finite width correction and the closure effect for convenience.

7.4.2. Simulation procedure

The model simulation procedure is shown in Fig. 7-9. The input parameters are the plate thickness t, width W, temperature distribution, applied stress σ_{app}, initial crack length a_0, crack length increment Δa, and the local fracture stress σ_{F}, which is an adjustable parameter determined by one of the experimental data. The unbroken shear lip length l_{sl} is set to 0 at the beginning of calculation.

In actual crack propagation in specimens, finite width correction has to be considered [16]. The model employed so called tangent formula to express SIF change due to the finite width correction.

The initial crack length is usually set to 150~200 mm. Although it is desirable to keep the initial crack length as short as possible to simulate actual crack propagation, the initial crack length does not influence the simulation results when the temperature until the initial crack length is

low enough to generate only negligible unbroken shear lips. Therefore, the initial crack length is basically set to 150 mm, but it was set to up to 200 mm as necessary because there are some cases that the fracture condition cannot be satisfied at the short initial crack length.

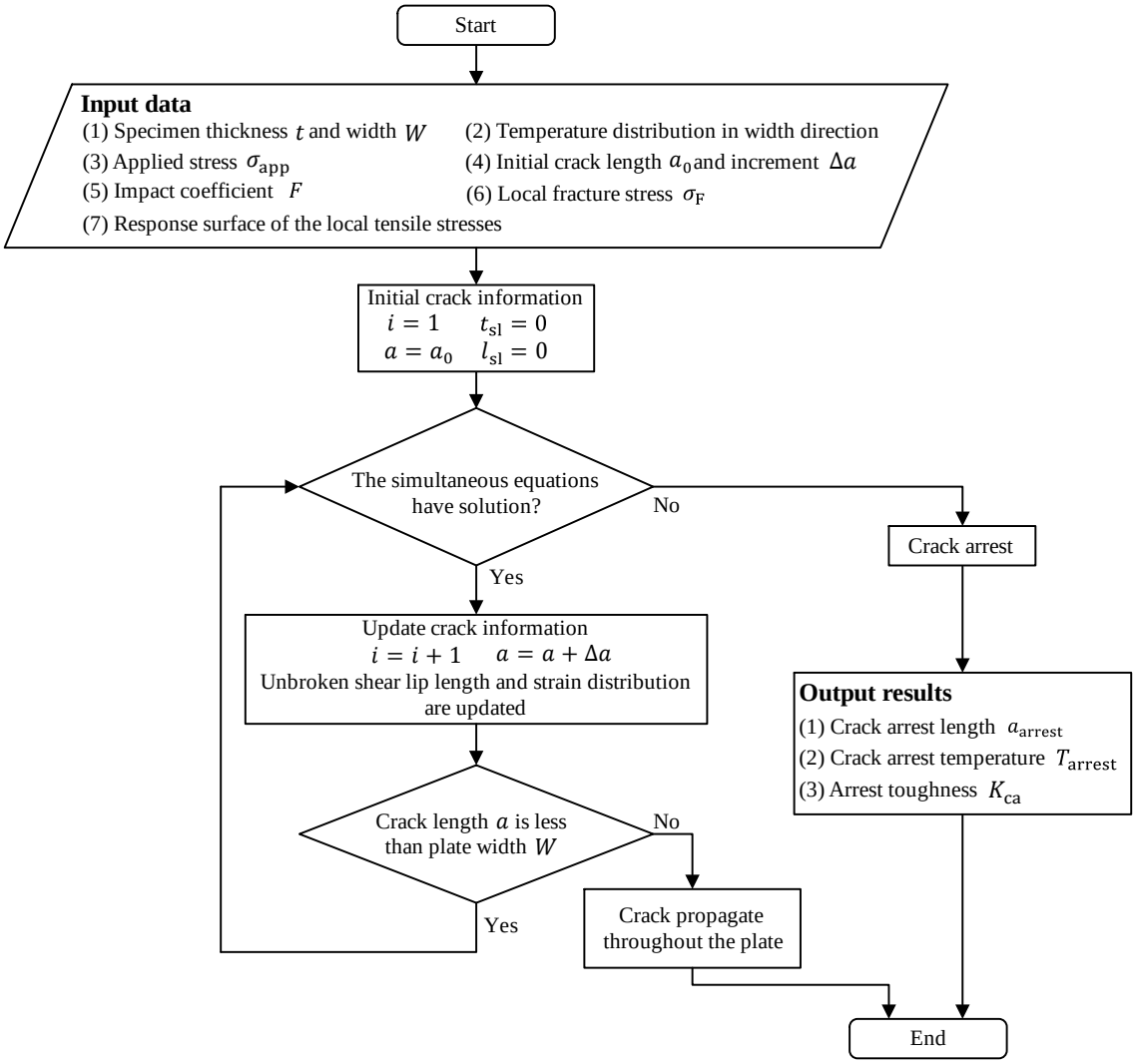

Fig. 7-9 Simulation procedure

The temperature distribution is described by a temperature of the specimen top T_0 and a temperature gradient $\Delta T/\Delta x$. Although the temperature from the top to 150 mm is usually set to lower temperature to cause brittle fracture initiation easily in actual tests [17], the temperature gradient was set to uniform because the crack propagation during the top to 150 mm was not simulated in this present study.

The simulation is discretized by the crack length increment. Namely, the simultaneous equations composed of Eqs. (7-9) and (7-10) is solved at every crack length. The crack length increment was set to 0.2 mm. When the solutions of the unknown variables are found, the crack length is updated by adding the crack length increment to the original crack length for the next step calculation. When one or both of the unknown variables are not found to satisfy the simultaneous equations, the crack is regarded to be arrested. When this model simulation is applied to actual experimental data, it is required to identify the local fracture stress beforehand. As same as in the conventional simulation model [5], the local fracture stress is a fitting parameter to characterize the crack arrest toughness of the simulated steels. Because there is no changeable parameters other than the local fracture stress in this model, this is a unique parameter of the simulated steel.

7.5. Validation

In order to investigate the validity of the above proposed model, the model simulation was applied to the actual $K_{\mathrm{ca}} - T$ relationship and crack arrest tests. As noted in Chapter 2, the crack arrest toughness is strongly related to not only the local fracture stress, but also the steel's constitutive law. Considering that the constitutive law of steel N was used in Section 7.3.1 because it was known in detail, and the crack arrest toughness data of steel N were fully accumulated, the crack arrest data of steel N were employed to validate the simulation model in this section. In addition, steel N is suitable for the validation because the steel N was normalized and did not have particular microstructures like anisotropy. The mechanical properties and chemical compositions are shown in Chapter 3.

As noted in Chapter 1, there are some methods to evaluate brittle crack arrest toughness of steels. This section employed temperature gradient crack arrest test and so called Arrhenius type $K_{\mathrm{ca}} - T$ relationship [17] for model validation because this evaluation method is widely employed.

7.5.1. Temperature gradient crack arrest test

Temperature gradient crack arrest test is schematically illustrated in Fig. 7-10. The temperature is controlled to have the fixed temperature gradient, which is around $300\ ℃/\mathrm{m}$. Brittle crack is initiated by impact and runs under remotely applied stress. Brittle crack arrest toughness K_{ca} is evaluated from the experiments by using the expression called the tangent formula as

$$K_{\mathrm{ca}} = \sigma_{\mathrm{app}}\sqrt{\pi a_{\mathrm{arrest}}}\sqrt{\frac{2W}{\pi a_{\mathrm{arrest}}}\tan\frac{\pi a_{\mathrm{arrest}}}{2W}} \tag{7-13}$$

where a_{arrest} is the crack arrest length. $K_{\mathrm{ca}} - T$ relationship is expressed by using Eq. (7-13) and reciprocal number of the temperature at crack arrest T_{k}. $K_{\mathrm{ca}} - T$ is usually expressed by Arrhenius type function and thus K_{ca} is approximated as

$$K_{\mathrm{ca}} = K_0 \exp\left(\frac{C}{T_{\mathrm{k}}}\right) \tag{7-14}$$

Where K_0 and C are fitting parameters. According to linear fracture mechanics, the crack propagation/arrest is judged by the comparison between a crack tip K and the steel's K_{ca}. Therefore, in the region below the curve approximated by Eq. (7-14), the crack should be arrested. On the other hand, when SIF is located in the region above the curve, the crack cannot be arrested and continue to propagate according to linear fracture mechanics. In addition, WES2815 tolerates the error of $\pm 15\%$ of $K_{\mathrm{ca}} - T$ relationships [17].

One example of specimen joined to tab plates is shown in Fig. 7-11. The distance between the pin holes is kept longer than three times the specimen width to avoid reflected stress wave effect. Specimen width is frequently set to 500 mm. The pin hole and tab plate configurations depend on a test rig.

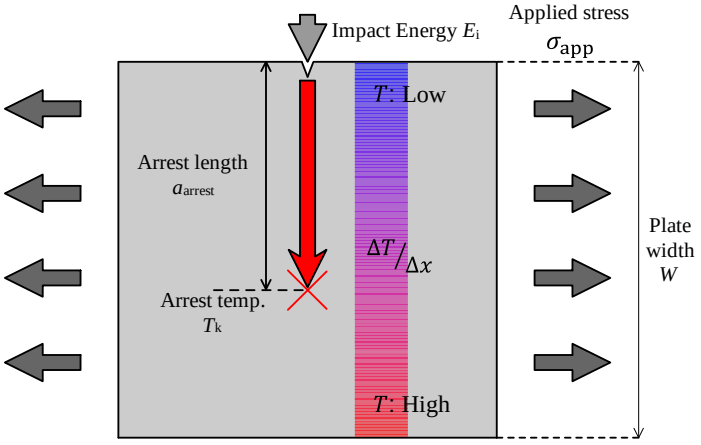

Fig. 7-10 Temperature gradient crack arrest test

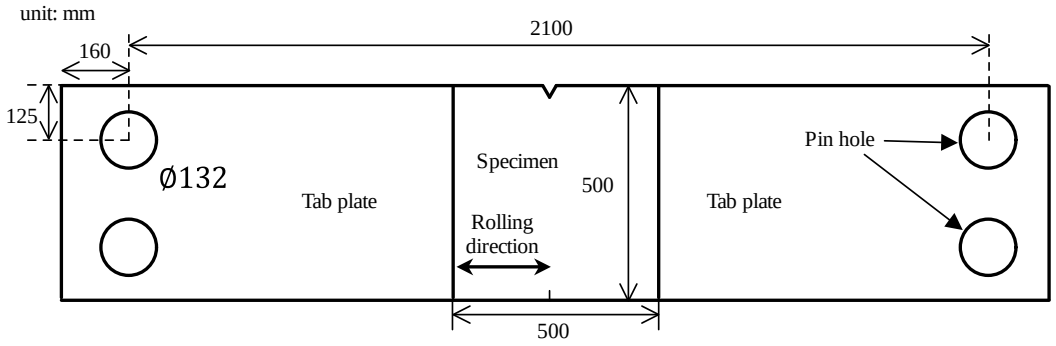

Fig. 7-11 Specimen with tab plates for temperature gradient crack arrest tests

The temperature gradient crack arrest tests of steel N were carried out in the round robin test for standardization of temperature gradient crack arrest test as WES2815 [17,18]. Therefore, although the specimens were basically similar to that shown in Fig. 7-11, the detail configurations were different and depended on which test rig was used to evaluate it. Therefore, the detail procedures of the tests such as temperature control were different from each other. According the result of a series of the round robin tests, the differences among the experimental procedure did not influence the experimental results [19].

The test results are shown in Table 7-2. The plate thickness was 50 mm and the specimen widths were set to 500 mm in all tests. The temperature gradient and impact energy were not uniform, but it followed a regulation in WES2815. Fig. 7-12 shows the $K_{\mathrm{ca}} - T$ relationship of steel N, which is shown in Table 7-2. This relationship agreed well with the Arrhenius type approximation.

Table 7-2 Crack arrest results of steel N [16]

Mark	σ_{app} [MPa]	Impact energy [J]	Temp. gradient [℃/m]	Crack arrest length [mm]	Crack arrest temperature [℃]	$1{,}000/T_k$	K_{ca} [MPa$\sqrt{m}$]
1	200	1040	280	185	-0.8	3.67	162
2	110	1040	300	254	-14	3.86	111
3	220	1040	340	234	5.8	3.59	209
4	80	1040	320	247	-20	3.95	79
5	112	1078	310	252	-4.4	3.72	113
6	186	1078	310	221	1.1	3.65	170
7	80	1078	270	243	-16.8	3.90	78
8	148	1999	300	247	-2.2	3.69	147
9	256	2999	330	241	5.4	3.59	249
10	99	1744	310	248	-8.6	3.78	98
11	296	2999	300	223	9.4	3.54	272
12	190	2940	300	293	3.9	3.61	218
13	120	2940	300	264	-9.8	3.80	125
14	155	2940	250	280	4.3	3.61	170
15	80	2940	330	319	-9.8	3.80	100

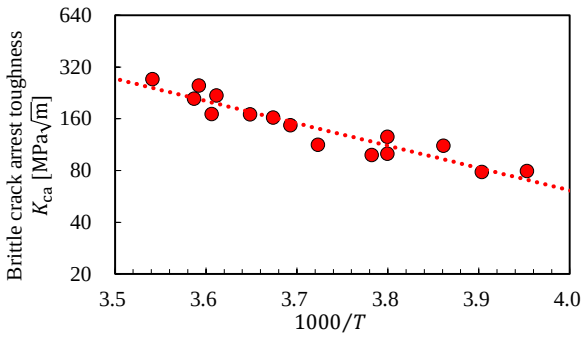

Fig. 7-12 $K_{ca} - T$ relationship of steel N

7.5.2. Impact effect

To interpret crack arrest experiments, impact effect is not negligible. Although double tension system is sometimes employed in brittle crack arrest tests not to cause impact effects, brittle fracture initiation by double tension [20–22] is lack of certainty and frequently leads to failure of experiments. Accordingly, to easily initiate brittle crack in crack arrest tests, impact is usually used in temperature gradient crack arrest test [17].

A systematic experiments and simulations by Kaneko and his co-workers showed that the variation of $K_{ca} - T$ relationship is within the range of $\pm 15\%$ error, which was acceptable to WES2815, when the dynamic SIF at crack arrest with impact is not larger than 1.5 times dynamic SIF without impact at crack arrest [23–25]. They also noted that the impact effect during crack propagation depended on crack velocity, applied stress, crack length, and the impact energy. One example of dynamic SIF transition with and without impact is shown in Fig. 7-13 [23], which was evaluated by 2D linear elastic finite element analyses. These impact effects were considered by multiplying the applied SIFs by impact coefficients. Thus, the SIF when the impact load is applied is expressed in infinite plates as

$$K_{app} = F\sigma\sqrt{\pi a} \tag{7-15}$$

where F is an impact coefficient to express amplitude of SIF increase due to the impact load. When the plate is finite, K_{app} is expressed as

$$K_{app} = F\sigma_{app}\sqrt{\pi a}\left(\frac{2W}{\pi a}\tan\frac{\pi a}{2W}\right)^{1/2} \tag{7-16}$$

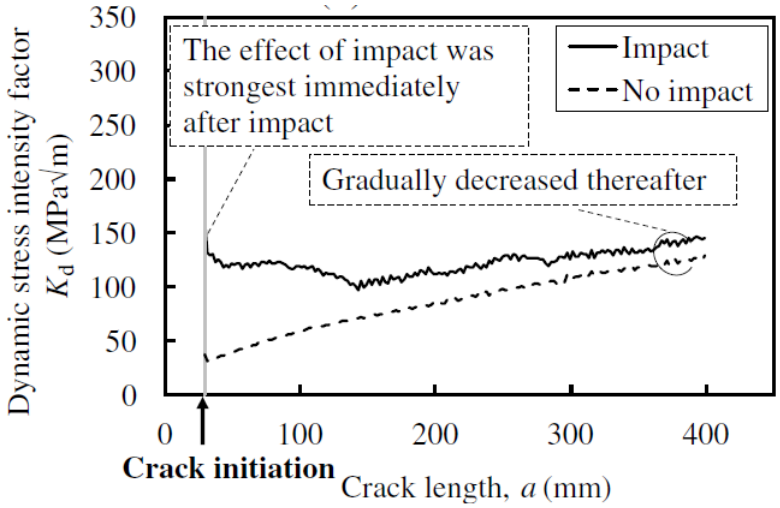

Fig. 7-13 Example of impact effect [23]

($\sigma_{app} = 0.3\sigma_{YS}, V = 600$ m/s, Impact energy: 40 J per thickness)

As shown in Table 7-2, the impact energies employed in the experiments which are used to validate the present model are not uniform. Furthermore, as indicated by Fig. 7-13, the impact effect varies during crack propagation. Therefore, because it is practically difficult to determine the value of F in each test as noted above, the impact coefficients were uniformly set to 1.3 in the simulation regardless of the test conditions shown in Table 7-2. This value of the coefficient was determined based on the assumption that the error of the $K_{ca} - T$ relationship is caused by the change of impact effect. According to this assumption, the maximum impact effect as long as WES2815 allows causes the maximum overestimation of $K_{ca} - T$ relationship. Namely, when the maximum impact coefficient ($= 1.5$) in WES2815 is applied, apparent K_{ca} becomes 0.85 times according to WES2815 [17]. In this case, the average $K_{ca} - T$ relationship appears when the impact coefficient is approximately 1.3 ($\fallingdotseq 0.85 \times 1.5$). Therefore, the impact coefficient in the model simulation was usually set to 1.3.

7.5.3. Model simulation

At first, the present model simulation was applied to $K_{ca} - T$ relationship shown in Fig. 7-12. Input information for the model simulations is shown in Table 7-3. The temperature of the specimen top was set to -90 ℃. The temperature gradient was set to 300 ℃/m. The applied stresses were set to in the range of 86-230 MPa at 1~5MPa interval. The local fracture stress was identified by making the simulated K_{ca} same as the experimental K_{ca} in Mark 15. The identified value was 2,035 MPa, which was almost equal to the local fracture stress experimentally evaluated in Chapter 3. Fig. 7-14 shows the simulation results where the above identified local fracture stress was applied. The simulated $K_{ca} - T$ relationship agreed well with the experimental relationship although the experimental data have some scatters, which may be due to impact effect or other experimental procedures. As noted, WES2815 allows ± 15 % errors in evaluation of brittle crack arrest toughness [17].

Table 7-3 Input data for model simulations

Applied stress	Temperature		Initial crack length	Local fracture stress
σ_{app} [MPa]	T_0 [℃]	$\Delta T/\Delta x$ [℃/m]	a_0 [mm]	σ_F [MPa]
86~230 (31 levels)	-90	300	150~200	2,035

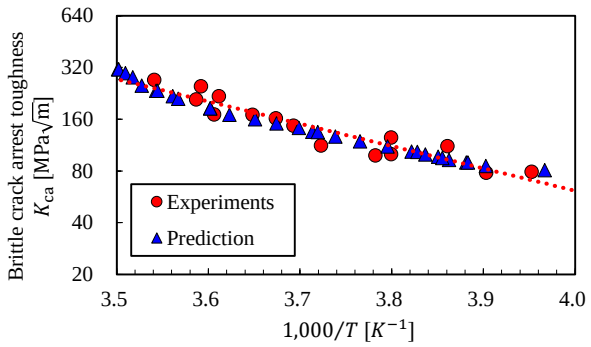

Fig. 7-14 Model simulation results with the test results ($K_{ca} - T$ relationship)

Each test was also simulated by the present model. The numerical condition of the simulation for each test followed each experimental condition shown in Table 7-2. Although the impact effect at the crack arrest varied in each experimental condition, the impact coefficient was uniformly set to 1.3 in all simulation because it was difficult to identify the impact effect in each test. As noted in Section 7.5.1, the top of specimen was in the lower temperature to cause brittle fracture. However, because the temperature distribution until the initial crack length did not influence the simulation results, the temperatures of the specimen top were determined from the temperature gradient and the temperature at the crack arrest length.

Figure 7-15 shows relationships between each experimental and simulated crack arrest lengths. The dashed line means that the simulated crack arrest length agrees perfectly with the experimental crack arrest length. Because any initial crack length to satisfy the fracture condition could not be found in Mark 4 and 7, the model simulation results are blank in Mark 4 and 7. These non-occurrences of initial brittle fracture in the simulations indicate that the local fracture stress was coincidently lower or the impact effect was larger than that supposed in the simulations. In particular, the impact effect should be larger when the crack length is shorter. In the experiments of Mark 4 and 7, the critical conditions were satisfied during the impact effects were larger and the cracks were arrested as the impact effects became small in the experiments. Therefore, by providing appropriate transitions of the impact effects along crack propagation, the model may be also able to reproduce the crack behaviors of Mark 4 and 7. However, such transitions cannot be known, so this section does not care the results of them.

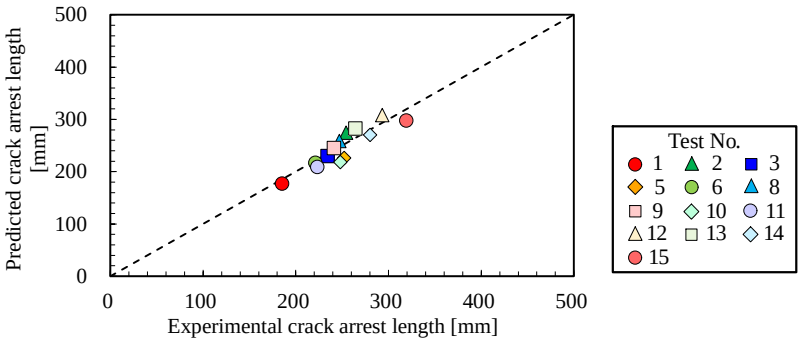

Fig. 7-15 Simulated and experimental crack arrest lengths

Apart from Mark 4 and Mark 7, considering that the maximum gap of the crack arrest lengths was -29.6 mm in Mark 10, the simulated crack arrest lengths agreed well with the experimental crack arrest lengths. In particular, the previous studies to model brittle crack propagation and arrest behaviors including the conventional model showed larger gaps between the experiments and simulations than the present simulations [4,26–28]. The differences of the simulated and experimental results shown in Fig. 7-15 are due to some reasons. One main reason is the scatter of the local fracture stress. Although the scatter of brittle crack arrest toughness is supposed to be relatively smaller than brittle crack initiation toughness, the local fracture stress is not perfectly uniform due to steel microstructures. The above simulations supposed the local fracture stress is constant, which is not necessarily realistic assumption and caused the differences of the crack arrest lengths between the experimental and simulated results. However, considering that the $K_{\mathrm{ca}} - T$ relationship as shown in Fig. 7-14 is the averaged result of the experiments, the consistency between the experiments and simulation of Fig. 7-14 indicated the validity of the proposed simulation model. And the impact effect assumption is also a main reason to cause the difference because the impact effect is assumed to be uniform in all experiments although it should depend on experimental conditions and the crack behaviors such as crack velocity history. However, considering that it is practically difficult to incorporate accurately both of the local fracture stress scatters and the impact effect difference, the agreement between the experimental and simulated results in Figs. 7-14 and 7-15 is enough to validate the present simulation model.

7.6. Discussion

7.6.1. Local fracture stress criterion

A series of above studies showed the local fracture stress criterion can uniformly explain brittle crack propagation and arrest behaviors by just one parameter, the local fracture stress. The numerical model simulations shown in this chapter successfully reproduced the experimental results accurately. The model simulation incorporated the shear lip formations and their closure effects in addition to the local tensile stress in the vicinity of the crack tip. These modellings were based on systematic investigation using crack propagation experiments and finite element analyses. These detail and sophisticated modellings were physically-meaning and therefore the model was much refined compared to the conventional numerical model.

The local fracture stress identified in Section 7.5.3 was 2,035 MPa, which is almost equal to the experimentally evaluated local fracture stress of steel N in Chapter 3 although the identified value was a little bit smaller than the experimentally evaluated value. This consistency strongly supports the validity of the present model simulation. This very small gap between the experimental one and the identified one may be attributed to the errors of the crack velocity evaluation, finite element analyses, and scatters of the material microstructures. On the other hand, the local fracture stress of steel N was identified as about 4,500 MPa by the conventional model. This inconsistency between the identified value by the conventional model and the experimentally evaluated value suggests the model formulation of the conventional model is inappropriate and cannot reproduce the actual crack behaviors.

The characteristics of the local fracture stress had been conventionally controversial as noted in Chapter 1. However, in addition to the experimental evaluation of the local fracture stress in Chapter 3, this chapter shows the simulation using the local fracture stress which is independent on the temperature and strain rate successfully reproduced the experimental results. This strongly supports such idea of the local fracture stress. It is worth noting that the local fracture stress evaluated in Chapter 3 can be applied to the model simulation supposing temperatures higher than those in the experiments of Chapter 3 although the $K_{\mathrm{ca}} - T$ relationship was evaluated under the temperatures higher than DBTT and the experimental conditions in Chapter 3 were basically lower than DBTT. Thus, above model simulation results were supportive for the discussion in Section 3.5.4.

The characteristic distance is a controversial problem in the local fracture stress criterion. Originally, the characteristic distance corresponded to the distance at which the local stress reached the critical value in cleavage fracture initiation [29], but its physical meaning is not clear. Although the employed characteristic distance (0.15 mm) originated from the experimental results in Chapter 3, and a half of that of the conventional model [5]. However this value is in the range of the characteristic distances employed by previous literatures [27,30]. In fact, Prabel et al. did not provide the characteristic distance meanings of fracture mechanics [27] as same as the conventional model. Berdin determined the characteristic distance based on element division of the finite element model [30]. Although, originally, the characteristic distance is a size of the process zone where the fracture occurs, such it is difficult to identify the process zone size in brittle crack propagation behaviors [1,31]. The characteristic distance and other similar spatial idea in cleavage fracture initiation have been related to microstructural characteristics, such as the size distribution and volume fraction of carbide [32,33]. These characteristic distances in cleavage fracture initiation is related to the weakest linkage idea (for

example, Weibull stress is one of such ideas [34]), which is not valid in cleavage crack propagation behaviors. Furthermore, although the local maximum stress point can be often found near the initial notch tip to investigate cleavage crack initiation [35,36], the local stress was monotonically increasing as the evaluation point approached to the crack tip in rapid crack propagation as long as analyses of this study.

As above discussion indicated, it is hard to deal the characteristic distance in cleavage crack propagation as same idea in cleavage fracture initiation. Furthermore, the present experiments and numerical analyses are not enough to conclude the physical meaning of the characteristic distances in cleavage crack propagation. However, based on fracture mechanical view, the local fracture stress criterion may be understood as the two parameter fracture mechanics. Namely, the combination of the local fracture stress and the characteristic distance express the amplitude of the resistance against cleavage crack propagation. Similarly, the combination of the local tensile stress and the characteristic distance corresponds to the amplitude of crack driving force. This idea is supported by that change the characteristic distance from 0.1 to 0.2 mm did not influence the overall trend in Chapter 3. On the other hand, the characteristic distance may be related to the microstructure, especially grain size. Although the employed steels' grain sizes in Chapter 3 were similar, such relationship between the grain size and the characteristic distance can be examined using the steels with extremely different grain sizes, which is, for example, 200 μm.

7.6.2. $K_{ca} - T$ relationship

As shown in Fig. 7-14, the $K_{ca} - T$ relationship called as Arrhenius plot was successfully reproduced by the developed simulation model based on the local fracture stress criterion. Here, the local fracture stress in the model was a unique parameter independent on any other parameter such as strain rate and temperatures. Arrhenius plot is usually evaluated in the range of $-30 \sim 10$ ℃ because the design temperature of container ships is usually -10 ℃. Such temperature range is higher than the temperature for the local fracture stress evaluation in Chapter 3. As noted in Section 7.5.3, the identified local fracture stress in above simulations was almost same as the experimentally evaluated value. This consistency indicated that the local fracture stress which experimentally evaluated under lower temperature condition is available for the higher temperatures which are used for temperature gradient crack arrest tests. This trend consists with the independency of the evaluated local fracture stress in Chapter 3 on the temperature. Accordingly, it can be said that such independency of the local fracture stress on

temperature can be applicable to the higher temperature. This finding is important to develop easier and simpler method to evaluate the local fracture stress because it is usually difficult to cope with both cleavage crack initiation and arrest under high temperatures.

It is widely known that $K_{ca} - T$ relationship can be approximated by Eq. (7-14). Because this approximation is similar to so called Arrhenius equation, $K_{ca} - T$ plot is called as Arrhenius plot. By transforming Eq. (7-14), the $K_{ca} - T$ relationship can be approximated by the temperature T,

$$K_{ca} = K_0 \exp(-\frac{C_1}{T}) \tag{7-17}$$

where K_0 and C_1 are fitting parameters. The value of C corresponds to $-E_A/R$, where E_A is the activation energy and R is the gas constant [37]. Here, E_A is calculated as $E_A = C_1 R$ and thus $E_A \fallingdotseq 2.77 \times 10^4$ J/mol for steel N. This is 0.287 eV.

However, it is hard to relate brittle crack arrest toughness to activation energy and related idea, which is based on chemical kinetics. Akita and Ikeda mentioned such Arrhenius type relationship was found in the relation of plastic dissipation surface energy and the temperature for the first time [38]. Koshiga et al. pointed out brittle crack arrest toughness had Arrhenius type relationship with the temperature for the first time [39]. However, these studies did not pointed out the physical meaning of Arrhenius type relationship in brittle crack arrest and only mentioned about convenience of using Arrhenius type expression of brittle crack arrest toughness. Therefore, it is reasonable to consider the applicability of Arrhenius type expression to $K_{ca} - T$ relationship does not provide any thermodynamics meaning, and it is just a technique to interpret the experimental result statistically. On the other hand, if the role of Arrhenius plot in brittle crack arrest is discussed daringly, it can be pointed out the yield stress contributes to the local tensile stress, shear lip thickness, and closure stress. Because strain rate effect can be integrated with the temperature effect against yield stress [40], the activation energy of above $K_{ca} - T$ relationship may be able to be related to the sensitivity of the yield stress on the temperature.

7.6.3. Fracture surface simulation

In order to focus on the simulation of fracture surfaces, two experiments were picked up as the representatives. To choose the examples, the experiments where the crack re-initiation was found were excluded because crack re-initiation made the crack arrest point obscure and fracture surface until the first crack arrest cannot be identified. In addition, because shear lip is influenced by SIF, the representative examples at which SIFs at crack arrests were the maximum and minimum values were chosen. Although the maximum SIF at the crack arrest was the maximum in Mark 11, the gap between the simulation and experiment was relatively larger. Thus, instead of Mark 11, Mark 9 was chosen because the SIF at crack arrest in SIF was maximum except Mark 11. The minimum SIF at the crack arrest was Mark 10. These experimental fracture surfaces are shown in Fig. 7-16. As clearly shown in the difference between Figs. 7-16(a) and (b), the shear lip thickness was thicker in Mark 9, which experienced higher SIF.

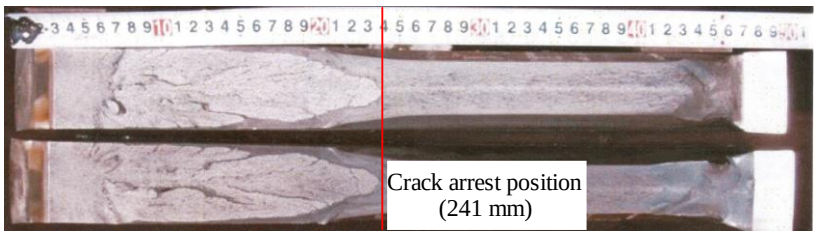

(a) Fracture surface of Mark 9

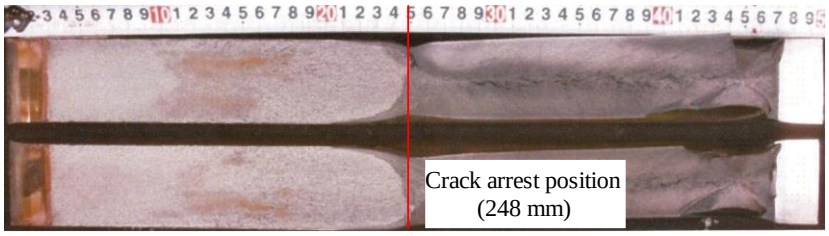

(b) Fracture surface of Mark 10

Fig. 7-16 Experimental fracture surfaces of Mark 9 and 10

This trend is successfully simulated in Fig. 7-17, which shows the simulated fracture surfaces of Mark 9 and 10. Especially, the shear lip is merely found in the experimental fracture surface of

Mark 10 except just before the crack arrest. This is also shown in the simulated fracture surface shown in Fig. 7-17(b). On the other hand, because the shear lip formation is influenced the SIF, the impact effect transition is needed to accurately simulate shear lip formation history. However, because the impact coefficient is uniformly set to a constant, the simulated shear lip formation histories are not perfect in this chapter.

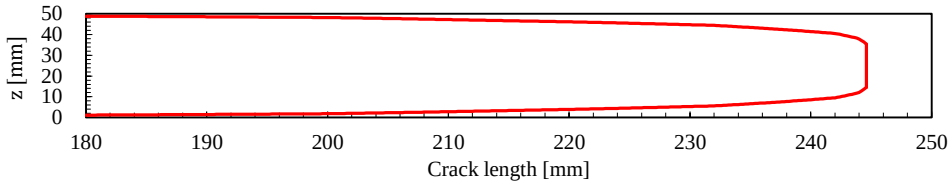

(a) Simulated fracture surface of Mark 9

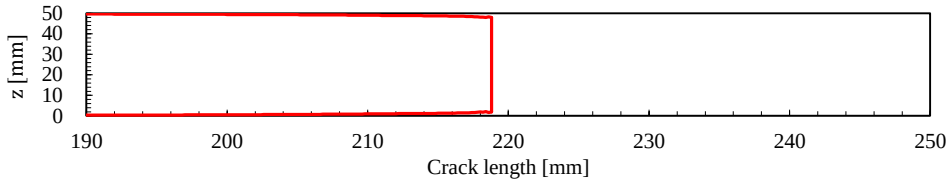

(b) Simulated fracture surface of Mark 10

Fig. 7-17 Simulated fracture surfaces of Mark 9 and 10

In addition, Fig. 7-18 shows the unbroken shear lip lengths of Mark 9 and Mark 10. The unbroken shear lip lengths gradually increased, but the fracture of the unbroken shear lip occurred in the calculations according to Fig. 7-18. This increasing unbroken shear lip length can be attributed to strain reduction due to thicker shear lip thickness because the strain is defined as Eq. (7-5). Fig. 7-19 shows SIF transitions calculated by the tangent formula shown in Eq. (7-13) with impact and the model simulation against crack length. Although the simulated effective SIF of Mark 10 was almost same as the SIF calculated by tangent formula, which is shown in Eq. (7-13), the simulated SIF of Mark 9 deviated from the tangent formula and led to be arrested due to the closure effects of unbroken shear lip. Thus, the experimental crack arrest of Mark 9 cannot be explained without the closure effect of the unbroken shear lips.

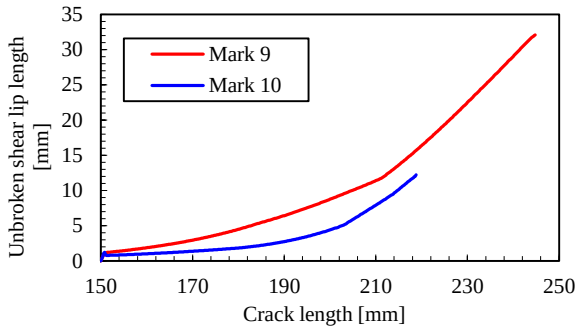

Fig. 7-18 Unbroken shear lip length

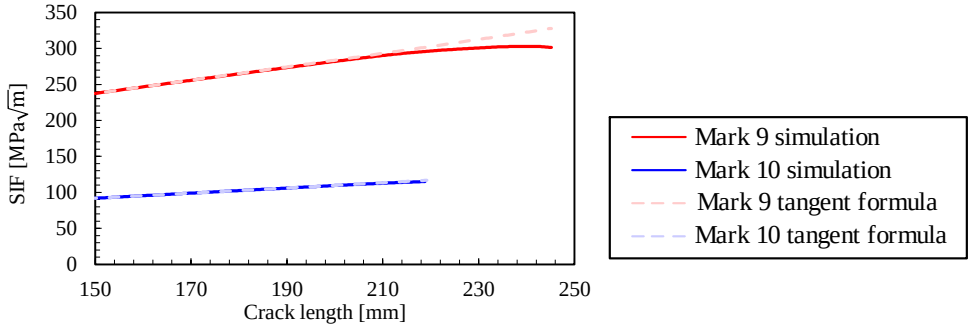

Fig. 7-19 SIF transition

7.7. Conclusion

This chapter developed a new simulation model to explain brittle crack propagation and arrest behaviors in steel, based on the results and findings obtained from Chapter 3 to Chapter 6. The developed simulation model was based on the local fracture stress criterion and incorporated closure effects of the unbroken shear lips. The thickness of shear lips was determined by the formula experimentally proposed in Section 6.3. The closure stress was also determined from a series of analyses in Section 6.2. The local stress near the crack tip was evaluated using the response surfaces which related the crack velocity, applied stress, crack length, and temperature to the local tensile stress. The model considered the impact effect based on previous studies, and the simulated results agreed well with the experimental $K_{ca} - T$ relationship. In addition, the simulated crack arrest lengths also consisted with the experimental crack arrest lengths. It is worth noting that the local fracture stress identified in the simulations almost consisted with the experimentally evaluated local fracture stress. This consistency could not be reproduced by the conventional model and strongly supported the validity of the local fracture stress evaluated in Chapter 3.

According to the above results, the proposed simulation model was validated quantitatively. It means that the proposed model could make the fundamental mechanism of brittle crack propagation and arrest behaviors clear through the comparison of the simulations and experiments including the value of the local fracture stress. This consistency has not been achieved by the conventional studies, and therefore the proposed simulation model is regarded to reproduce actual fracture phenomena appropriately.

It is worth noting that some issues remains to be solved in brittle crack propagation and arrest behaviors in steel. Microstructural factors are one of the most important issues. Chapter 8 will investigate the microstructural effect to the local fracture stress using a simplified evaluation method. And, to provide microscopic meanings to the local fracture stress is hard, but should be solved. Previous literature considered the microscopic energy absorption as resistance against cleavage crack propagation in microscopic view [41,42]. Thus, it is needed to interpret the local fracture stress by relating it to the energy dissipation near the crack tip. And one of the other important issues is to develop the generic simulation of brittle crack propagation and arrest behaviors in steel. Because the proposed model in this chapter aimed to develop a theory to explain brittle crack propagation and arrest behaviors, its applicable range is limited. For example, it can be only applied to plate specimens. Therefore, the complicated configuration specimen cannot be dealt with by the simulation model and it is needed to use other numerical method such as finite element method which can be applied to broader range. As the steel N was uniform, the local fracture stress can be evaluated only at the thickness center. However, in order to analyze brittle crack propagation and arrest behaviors in the steels which have complicated microstructure distribution, the developed model has to be modified because the local fracture stress is not uniform in thickness direction in such steels [6]. Because such case is difficult to analyze in the present simulation, the numerical method is also required. Thus, new numerical method which can deal with complicated geometry has to be developed to carry out crack propagation and arrest simulation based on the local fracture stress criterion in the range of realistic numerical costs.

Reference

[1] S. Machida, H. Yoshinari, M. Yasuda, S. Aihara, H. Mabuchi, Fracture mechanicsl modeling of brittle fracture propagation and arrest of steel (1) A fundamental model, J. Soc. Nav. Archit. Japan. 177 (1995) 243–258.

[2] S. Aihara, S. Machida, H. Yoshinari, H. Mabuchi, Fracture mechanical model of brittle fracture propagation and arrest of steel (2) Application to Temperature-gradient Type Test, J. Soc. Nav. Archit. Japan. 178 (1995) 545–554.

[3] S. Aihara, S. Machida, H. Yoshinari, Y. Tsuchida, Fracture mechanical modeling of brittle fracture propagation and arrest of steel (3) Application to Duplex Type Test, J. Soc. Nav. Archit. Japan. 179 (1996).
[4] K. Shibanuma, F. Yanagimoto, T. Namegawa, K. Suzuki, S. Aihara, Brittle crack propagation/arrest behavior in steel plate - Part II: Experiments and model validation, Eng. Fract. Mech. (2016). doi:10.1016/j.engfracmech.2016.02.053.
[5] K. Shibanuma, F. Yanagimoto, T. Namegawa, K. Suzuki, S. Aihara, Brittle crack propagation/arrest behavior in steel plate - Part I: Model formulation, Eng. Fract. Mech. 162 (2016) 324–340. doi:10.1016/j.engfracmech.2016.02.054.
[6] T. Handa, S. Igi, K. Nishimura, H. Tajika, T. Tagawa, S. Tsuyama, Effect of Toughness Distribution in the Thickness Direction on Long Brittle Crack Propagation/Arrest Behavior of Heavy Gage Shipbuilding Steel, Q. J. Japan Weld. Soc. 34 (2016) 211–217.
[7] K. Sugimoto, I. Kawata, S. Aihara, H. Shirahata, Analysis of Cleavage Crack Propagation in Steels Having Anisotropy by Means of Three-Dimensional Polycrystalline Cleavage Fracture Simulation Model, Tetsu-to-Hagane. 100 (2014) 1274–1280.
[8] K. Hase, K. Ichinomiya, K. Ueda, T. Handa, T. Eto, M. Aoki, Development of YP460 N/mm2 Class Heavy Thick Plate with Excellent Brittle Crack Arrestability for Mega Container Carriers, in: 27th Int. Ocean Polar Eng. Conf., 2017.
[9] SIMULIA, Abaqus Analysis User's Guide Version 6.14, Dassault Systemes, 2014.
[10] G.T. Embley, G.C. Sih, Plastic flow around an expanding crack, Eng. Fract. Mech. 4 (1972) 431–442. doi:10.1016/0013-7944(72)90055-0.
[11] W.R. Tyson, J.C. Newman, S. Xu, Characterization of stable ductile crack propagation by CTOA: Review of theory and applications, Fatigue Fract. Eng. Mater. Struct. (2018) 1–17. doi:10.1111/ffe.12916.
[12] A. Slimane, B. Bouchouicha, M. Benguediab, S.A. Slimane, Parametric study of the ductile damage by the Gurson-Tvergaard-Needleman model of structures in carbon steel A48-AP, J. Mater. Res. Technol. 4 (2015) 217–223. doi:10.1016/j.jmrt.2014.12.011.
[13] A.A. Benzerga, J.B. Leblond, A. Needleman, V. Tvergaard, Ductile failure modeling, 2016. doi:10.1007/s10704-016-0142-6.
[14] H. Mimura, Method to estimate Kca from K1a, J. High Press. Inst. Japan. 31 (1993) 58–64.
[15] T. Ono, A. Sato, T. Yokokawa, N. Aikawa, The Criterion for Ductile Crack Iniaition in Structural Steels, J. Struct. Constr. Eng. (Transactions AIJ). 68 (2003) 127–134.
[16] The Japan Wedling Engineering Society, WES2815: Test method for brittle crack arrest toughness, Kca Explanation, 2014.
[17] The Japan Wedling Engineering Society, WES2815 Test method for brittle crack arrest toughness, (2014). http://www-it.jwes.or.jp/wes_ki/wesippan.jsp?arg=2815e-1.
[18] ClassNK, Development on standarization of evaluation methods of brittle crack arrest toughness, (2013). http://report.classnkrx.com/researchresult.nsf/0/C1604873ECD6C4A749257F78003ABB31/$File/10-31_1.pdf?OpenElement.
[19] Y. Shimada, T. Inoue, T. Kawabata, S. Aihara, Effect of specimen size, applied stress and temperature gradient on brittle crack arrest toughness test, Int. J. Fract. 204 (2017). doi:10.1007/s10704-016-0179-6.
[20] M. Yoshiki, T. Kanazawa, S. Machida, A Consideration on Brittle Fracture Test of Steel Plates -with special reference to flat-temperature & gradient-temperature type Double Tension Test-, J. Zosen Kiokai. 113 (1963) 125–135.
[21] T. Kanazawa, S. Machida, H. Yajima, M. Aoki, Effects of Specimen Size and Loading Condition on the Brittle Fracture Propagation Arrest Characteristics, J. Soc. Nav. Archit. Japan. 130 (1971) 345–351.

[22] R.C. Rice, D.E. Tritsch, Effects of Product Quality and Design Criteria on Structural Integrity, ASTM International, 1998.
[23] M. Kaneko, T. Kawabata, S. Aihara, Effect of Impact Energy in ESSO Test ((Part 2: Proposal of Validity Criteria of Impact Condition in ESSO Test by FEM Crack Propagation Analysis), J. Test. Eval. 47 (2019) 20170151. doi:10.1520/JTE20170150.
[24] T. Kawabata, M. Kaneko, S. Aihara, Effect of Impact Energy in the Esso Test (Part 1 : Basic Experiments and Validation of FEM Analysis), J. Test. Eval. 46 (2018). doi:10.1520/JTE20170045.
[25] M. Kaneko, T. Kawabata, S. Aihara, Effect of Impact Energy in ESSO Test (Part 3: Experimental Validation for New Validity Criteria of Impact Condition Giving Constant Evaluation in ESSO Test), J. Test. Eval. 47 (2019) 20170150. doi:10.1520/JTE20170150.
[26] Y.C. Jang, Y. Lee, G.B. An, J.S. Park, J.B. Lee, S. Il Kim, Temperature Dependent Fracture Model and Its Application To Ultra Heavy Thick Steel Plate Used for Shipbuilding, Int. J. Mod. Phys. B. 22 (2008) 5483–5488. doi:10.1142/S0217979208050693.
[27] B. Prabel, S. Marie, A. Combescure, Using the X-FEM method to model the dynamic propagation and arrest of cleavage cracks in ferritic steel, Eng. Fract. Mech. 75 (2008) 2984–3009. doi:10.1016/j.engfracmech.2008.01.008.
[28] X. Yang, S. Marie, C. Jacquemoud, P. Bompard, Prediction of cleavage crack propagation path in a nuclear pressure vessel steel, Eng. Fract. Mech. 191 (2018) 486–503. doi:10.1016/j.engfracmech.2018.01.015.
[29] R.O. Ritchie, J.F. Knott, J.R. Rice, On the relationship between critical tensile stress and fracture toughness in mild steel, J. Mech. Phys. Solids. 21 (1973) 395–410. doi:10.1016/0022-5096(73)90008-2.
[30] C. Berdin, 3D modeling of cleavage crack arrest with a stress criterion, Eng. Fract. Mech. 90 (2012) 161–171. doi:10.1016/j.engfracmech.2012.05.002.
[31] M. Enoki, S. Fujiwara, T. Kishi, Quantitative Evaluation of Toughning Mechanisms of TiAl with Lamellar Structure, J. Japan Inst. Met. Mater. 58 (1994) 418–423.
[32] A.G. Evans, Statistical aspects of cleavage fracture in steel, Metall. Trans. A. 14 (1983) 1349–1355. doi:10.1007/BF02664818.
[33] T. Lin, A.G. Evans, R.O. Ritchie, A statistical model of brittle fracture by transgranular cleavage, J. Mech. Phys. Solids. 34 (1986) 477–497. doi:10.1016/0022-5096(86)90013-X.
[34] F.M. Beremin, A Local Criterion for Cleavage Fracture of a Nuclear Pressure Vessel Steel, Metall. Trans. A. 14 (1983) 2277–2287.
[35] K. Ishihara, T. Hamada, T. Meshii, The scaling method for stress distribution scaling under small-scale yielding and its application to the prediction of fracture toughness temperature dependence, Trans. JSME. 90 (2017) 182–192. doi:10.1016/j.tafmec.2017.04.008.
[36] S. Wu, H. Jin, Y. Sun, L. Cao, Critical cleavage fracture stress characterization of A508 nuclear pressure vessel steels, Int. J. Press. Vessel. Pip. 123 (2014) 92–98. doi:10.1016/j.ijpvp.2014.08.003.
[37] H. Kimizuka, H. Mori, H. Ushida, S. Ogata, Evaluation of Hydrogen Diffusivity and Its Temperature Dependence in BCC Metals: A Path Integral Centroid Molecular Dynamics Study, J. Japan Inst. Met. Mater. 73 (2009) 571–576.
[38] Y. Akita, K. Ikeda, On the Brittle Crack Propagation and Arrest with Special Reference to ESSO Test with Temperature Gradient, J. Zosen Kiokai. 112 (1962) 153–162.
[39] F. Koshiga, O. Imazawa, S. Takehana, Arrest-Transition of Brittle Crack in Steel Plate, J. Zosen Kiokai. 114 (1963) 200–209.
[40] P.E. Bennett, G.M. Sinclair, Parameter Representation of Low-Temperature Yield

Behavior of Body-Centered Cubic Transition Metals, J. Basic Eng. 88 (1966) 518–524.
[41] K. Shibanuma, Y. Yamamoto, F. Yanagimoto, K. Suzuki, S. Aihara, H. Shirahata, Multiscale model synthesis to clarify the relationship between microstructures of steel and macroscopic brittle crack arrest behavior - Part I: Model presentation, ISIJ Int. 56 (2016). doi:10.2355/isijinternational.ISIJINT-2015-449.
[42] Y. Yamamoto, K. Shibanuma, F. Yanagimoto, K. Suzuki, S. Aihara, Multiscale Model Synthesis to Clarify the Relationship between Microstructures of Steel and Macroscopic Brittle Crack Arrest Behavior - Part II : Application to Crack Arrest Test, ISIJ Int. 56 (2016) 350–358. doi:10.2355/isijinternational.ISIJINT-2015-450.

Chapter 8 Experimental investigation of grain size effect to cleavage crack propagation resistance in ferrite-pearlite steel

8.1. Introduction

Controlling the steel microstructure is an effective methodology to develop steel plates with higher brittle crack arrest toughness. To use additional elements, such as nickel, is also an effective way [1], but it makes the steel cost higher [2]. Thus, to control microstructure of steel is a hopeful method and practically employed to develop higher crack arrest steel in relatively lower cost [3]. One of most fundamental factors of steel microstructures is grain size, which is known to strongly influence the strength and brittle crack initiation toughness [4,5]. Therefore, grain size is also expected to contribute to brittle crack arrest toughness.

Some previous studies took care of grain size effect against cleavage crack propagation and arrest behaviors in steel. In Bullock and Smith [6], although they noted that increasing grain size made the crack propagation easier and more difficult to arrest the crack from Charpy impact test, they could not evaluate the crack arrest toughness because they focused on just the crack arrest lengths in spite of differences of crack initiation load. Furukimi et al. carried out a series of temperature gradient crack arrest experiments using some steels whose grain sizes were different [7]. However, because the chemical compositions of them were not same and the steels were made by thermo mechanical control process (TMCP), which generated texture in steel microstructures, their evaluation included some factors other than the grain size and did not appropriately consider the grain size effect on brittle crack arrest toughness. Ohmori et al. evaluated brittle crack arrest

toughness of various grain size steels using Double Cantilever Beam (DCB) specimen [8]. However, the chemical compositions of their steels were different, so the grain size effect could not be appropriately extracted from their data.

The simulations in Chapter 7 show brittle crack propagation and arrest behavior in steel is a complicated phenomenon composed of cleavage crack propagation and plastic deformation and ductile fracture of unbroken shear lips. Thus, K_{ca} and other indicators of brittle crack arrest toughness include both cleavage crack arrest and unbroken shear lip behaviors without distinction. Thus, the previous studies explained above could not separate the resistance against cleavage crack propagation from brittle crack arrest toughness to evaluate grain size effect. Thus, their results included the contribution of the closure effect due to the unbroken shear lips.

Now then, the microstructural effect against the local fracture stress is important issue from engineering perspective because it is a critical factor to determine brittle crack arrest toughness of steels as shown in Chapter 3. Because the local fracture stress is an indicator to express cleavage crack propagation resistance, to use this indicator is appropriate to evaluate grain size contribution to only cleavage crack propagation resistance. Accordingly, this chapter will explain grain size contribution to cleavage crack propagation resistance by experimentally evaluating the local fracture stress of some levels of grain size steels.

8.2. Materials

In order to appropriately evaluate the grain size effect against the local fracture stress of steels, the chemical compositions should be uniform in employed steels. In addition, ferrite-pearlite steels were desirable because they are relatively simpler than other types of microstructures such as bainite and martensite. The employed steels were prepared based on these considerations.

Table 8-1 shows the chemical compositions. The chemical compositions were almost constant. The mechanical properties of these steels are shown in Table 8-2. The original plate thickness of all the employed steels were 30 mm. The steels were named as S1, S2 and S3 in the order of their average grain size. The average grain sizes were measured by EBSD. Fig. 8-1 shows grain size distributions of the employed steels. Fig. 8-2 shows the optical observations of microstructures of the steels. They were observed after they were polished and etched with 2 % nital. Grain orientations were obtained by EBSD to examine the existence of the textures in the steels, which shown as polar figures in Fig. 8-3. These polar figures show the employed steels did not have the texture and can be regarded as isotropic.

Table 8-1 Chemical compositions of employed steels

	C	Si	Mn	P	S	Al	N
S1	0.1	0.2	1.51	0.01	0.003	0.027	0.0031
S2	0.1	0.19	1.5	0.01	0.003	0.028	0.0029
S3	0.1	0.2	1.5	0.01	0.003	0.028	0.003

Table 8-2 Mechanical properties of S1, S2, and S3

	Yield stress at room temperature [MPa]	Tensile strength at room temperature [MPa]	FATT[℃]	Average grain size[μm]
S1	325	458	-72.7	17.7
S2	319	459	-48.1	24.9
S3	279	439	-48.2	41.9

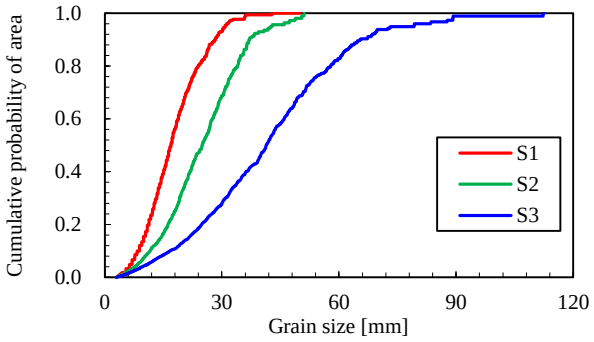

Fig. 8-1 Grain size distributions

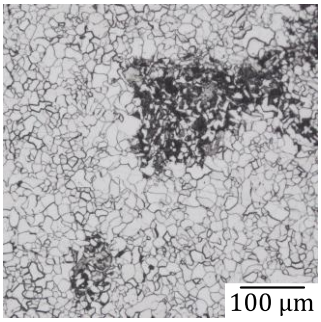

S1

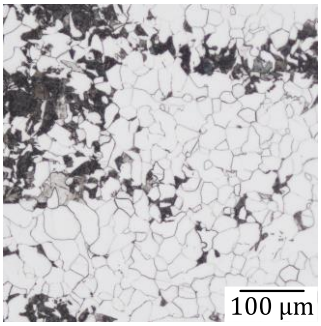

S2

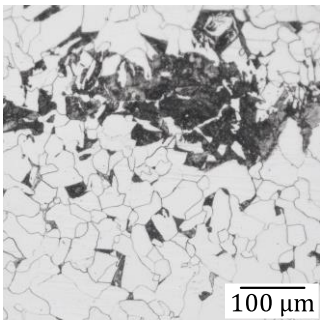

S3

Fig. 8-2 Microstructure of employed steels

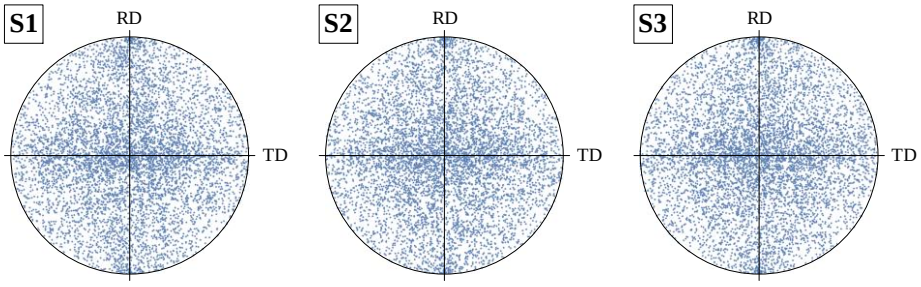

Fig. 8-3 Polar figure

8.3. Local fracture stress estimation

8.3.1. Estimation procedure

Because accurate evaluation of the local fracture stress explained in Chapter 3 is time consuming and requires a lot of cost, it was hard to apply such evaluation to the three steels. Therefore, a simplified method was carried out, focusing on the characteristics of the local fracture stress that the local fracture stress is a material constant and independent on temperature, SIF, and crack velocity. Fig. 8-4 shows the schematic illustration of the simplified method to evaluate the local fracture stress criterion. Namely, in the crack arrest experiments under bending, the crack arrest event occurs after decreasing of SIF even though the peak of SIF can be found [9,10]. And, the crack velocity just before crack arrest should be equal to the maximum stress crack velocity, which was explained in Chapter 4. Therefore, because the local tensile stress is not practically influenced by the crack acceleration as shown in Section 4.4, the local tensile stress at the crack arrest length when the crack velocity is the maximum stress crack velocity can be regarded to consist with the local fracture stress as schematically illustrated in Fig. 8-4.

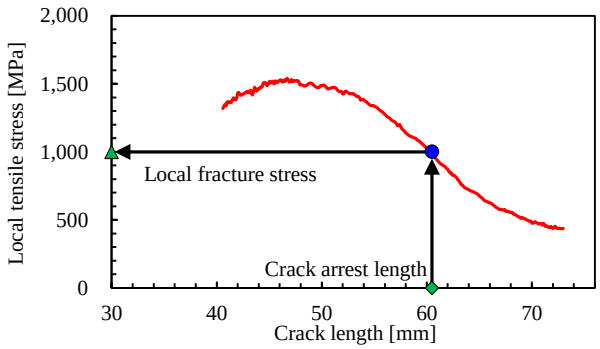

Fig. 8-4 Schematic illustration of a simplified method to evaluate the local fracture stress

To employ the above simplified method, it was desirable to conduct experiments under low temperature and low SIF. This was because the shear lip formation and remarkable crack front tunneling should be prevented as long as possible. Both of the crack initiation and crack arrest had to be compatible under these conditions. Therefore, although there were some widely used methods such as compact crack arrest (CCA) test [11] and three point bending (3PB) tests [12], DCB tests were employed to conduct the above method. Under CCA and 3PB tests, the SIFs usually become larger and approach to SIFs found in temperature gradient crack arrest test. In addition, these method were

difficult for the crack initiation and arrest to be compatible. On the other hand, the crack was relatively easier to be arrested even under low temperature in DCB tests.

8.3.2. Specimen and experimental procedure

The employed specimen configuration is shown in Fig. 8-5. The specimen thickness was 8 mm, and the width was set to 76 mm. The crack propagation direction was perpendicular to the rolling direction. A chevron notch was also processed on the specimen in order to make cleavage fracture initiation easier and help the initiated crack path become straight because the crack is generally likely to deviate from straight crack path in DCB specimens [12,13]. An initial notch was processed by electrical discharge machining and the notch tip root was 0.25 mm.

The crack arrest experiment is schematically illustrated in Fig. 8-6. By pushing the wedge from above, the pins moved in the direction to open the initial notch. The load and displacement of the wedge were measured. In addition, the clip gauge was used to record crack opening displacement at the top of the specimen for validate finite element analyses. Because the duration from the crack initiation to arrest was extremely short, the specimen could be regarded to be fixed-displacement condition during crack propagation.

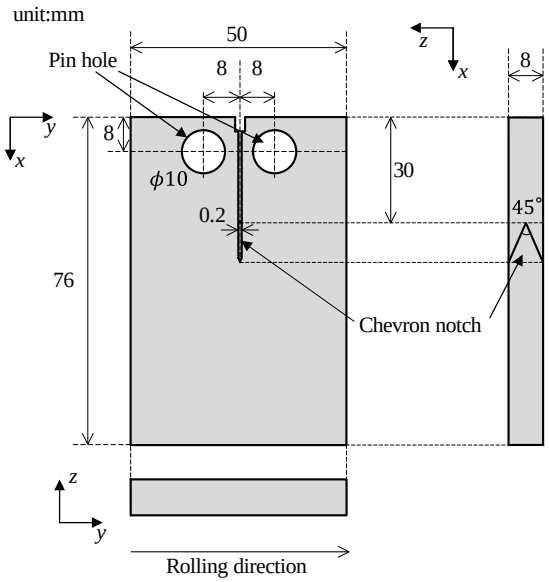

Fig. 8-5 Specimen configuration

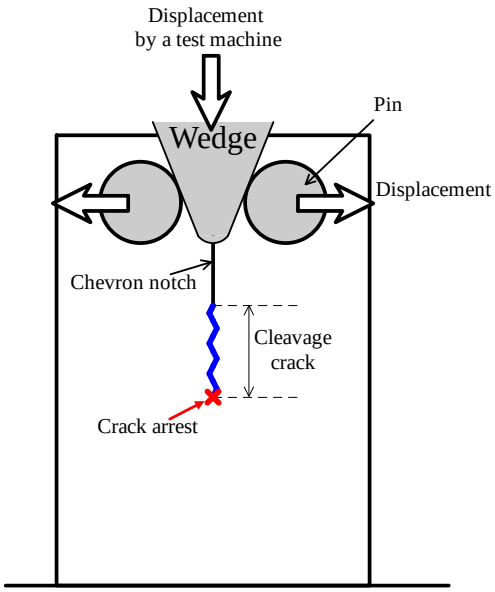

Fig. 8-6 Schematic illustration of the experiment

The crack arrest experiments were carried out under $-50 \sim -90$ ℃ in order to prevent the remarkable shear lip from forming as noted above. The temperatures, which was measured by a thermocouple glued on the specimen surface, were controlled by using dry ice and ethanol, in addition to liquid nitrogen. After the temperature reached the aimed temperature, that temperature was kept for 5 minutes to make the whole of the specimen isothermal.

In some cases, the cleavage crack was not initiated or propagated through the specimen width. Such experiments were invalid. In the tests where the crack was arrested, the crack lengths were measured from the fracture surfaces after the ligament was broken under -196 ℃. Here, just before loading under -196 ℃, the load was applied to some extent under room temperature to make a ductile crack advance from the cleavage arrest crack front to help identification of the crack arrest point. However, because such pre ductile crack extension was not enough to make the finding of the crack arrest point easy, heat tint method was employed to pigment the cleavage fracture surface obtained in above experiment [14]. Heat tint method is a technique to pigment surfaces after the end of the experiment by oxidizing in an electric furnace as shown in Fig. 8-7(a). The temperature in the furnace was kept 330 ℃ for 20 minutes to make the fracture surface browned [15]. The fracture surface after heat tint and ligament fracture is shown in Fig.8-7(b). The browned region corresponded to the fracture surface obtained in the experiment. The crack arrest length was obtained by finding the most advance point of the fracture surface.

(a) Specimens in an electronic furnace

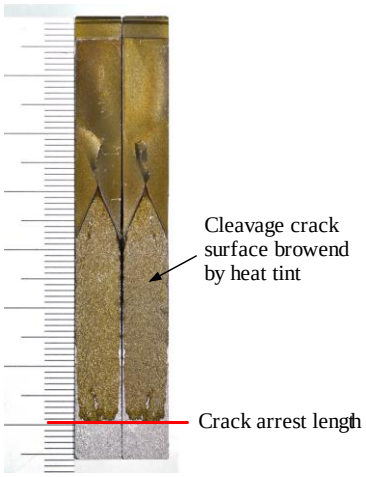

(b) Fracture surface after heat tint

Fig. 8-7 Heat tint technique

8.3.3. Experimental results

The experimental results are shown in Table 8-3. In some cases, the crack was not arrested or the crack was not initiated. In addition, the experiments where the crack deviated from the straight crack path was also regarded to be invalid. These invalid cases were excluded from Table 8-3. As the overall trend, the crack was arrested in the shorter length in the steel with coarser grains. The obtain crack arrest length of each experiment was applied finite element analyses explained below.

Table 8-3 Experimental results

Steel	Mark	Temp [deg.]	Crack arrest length [mm]	Maximum load [kN]
S1	S1-1	-70	70	22.1
	S1-2	-75	74	19.2
S2	S2-1	-70	67	16.3
	S2-3	-80	75	17.8
S3	S3-1	-50	42	18.6
	S3-2	-60	40	18.0
	S3-3	-70	53	18.1

8.3.4. Estimation of the local fracture stress

The procedure to estimate the local fracture stress was explained in Section 8.3.1. The obtained crack arrest length and the recorded displacement were input to finite element analyses using Abaqus 6.14 [16]. Fig. 8-8 shows the finite element model employed in this study. The model was divided by hexahedral elements which was full-integration solid except the tip of a chevron notch tip. The chevron notch tip was difficult to divide by hexahedral elements and thus partly divided by tetrahedron elements. The model was a quarter model considering symmetry. The pin was modelled by rigid body to help convergence. The mesh size along crack path was set to 0.1 mm except in the chevron notch.

Although, in the actual experiments, the pins were moved by the wedge, the contact between the pin and the wedge was hard to consider in finite element analyses from the perspective of convergence. Thus, referring some literatures [17,18], the wedge was not modelled and the forced displacement was directly applied to the pin. The contact between the pin and the specimen was considered. The provided displacements to the pins were calculated from the recorded displacement of the wedge.

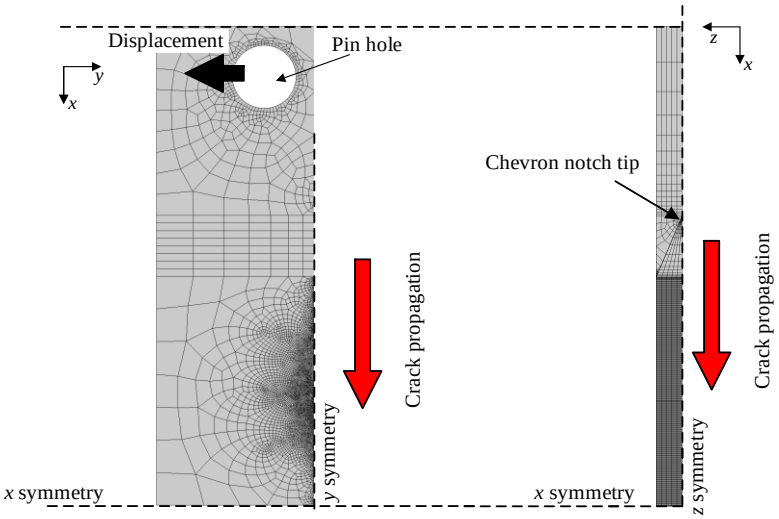

(a) xy view of specimen (b) xz view of specimen

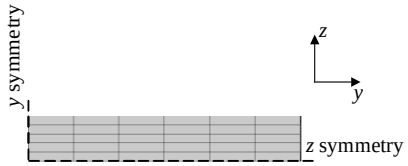

(c) yz view of specimen

Fig. 8-8 Finite element model

At the first step of the analyses, the forced displacement of the pin was statically applied. After the displacement reached the aimed value, the crack propagation analyses were carried out dynamically. Dynamic crack propagation was expressed by so-called nodal force release technique in generation phase analyses by implicit HHT method. Examples of the analyses are shown in Fig. 8-9. As explained in Chapter 3, the accurate evaluation of the local fracture stress needs to use the experimentally measured crack velocity as input information. However, the supposed maximum stress crack velocity was input in this simplified method. According to the parametric analyses carried out in Chapter 4, the maximum stress crack velocity depended on the conditions such as temperature and SIF. In lower temperature and lower SIFs, the maximum stress crack velocity becomes lower. Because the experimental conditions were low temperature and

low SIF as shown in Table 8-3, the maximum crack velocities were supposed to be 100~300 m/s. The crack velocity which could provide the maximum local tensile stress was regarded to be the maximum stress crack velocity. The characteristic distance was set to 0.15 mm according to Chapter 3. The mean of the local tensile stresses at 0.15 mm from the crack front was regarded to be the local fracture stress.

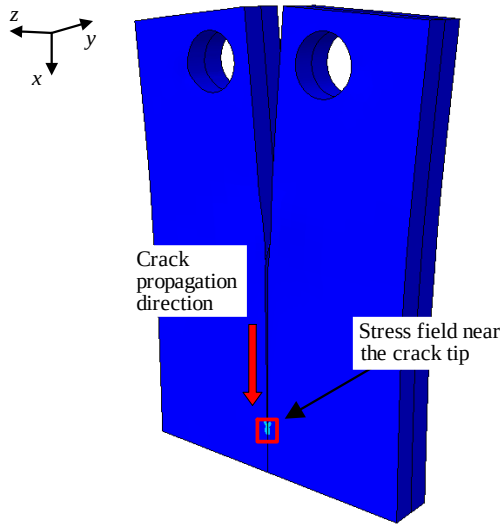

(a) Whole of model during crack propagation

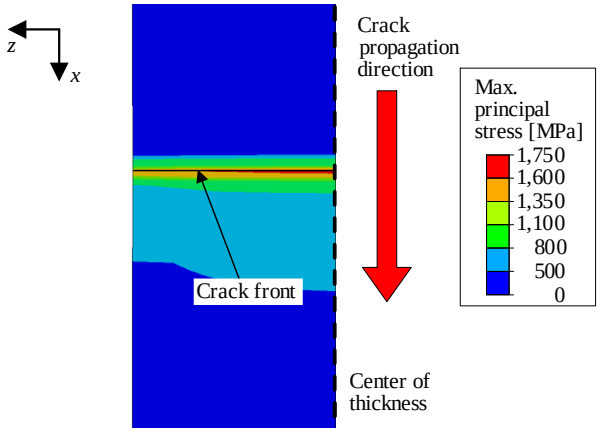

(b) Stress distribution near the crack front

Fig. 8-9 Finite element analysis examples

The local fracture stresses estimated from above procedure are shown in Fig. 8-10. Although the estimated local fracture stresses for each steel have a scatter, the estimated values for each steel are almost constant considering even the accurate evaluation in Chapter 3 had scatters to some extent.

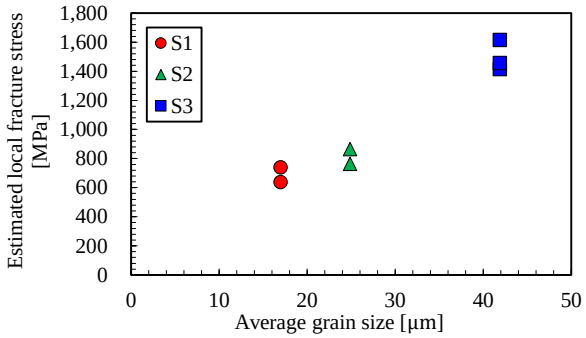

Fig. 8-10 Estimated local fracture stress

8.4. Discussion

As shown in Section 8.3.4, the estimated local fracture stresses, which corresponded to cleavage crack propagation resistance, were larger in coarser grain steels than in finer grain steels. Because the chemical compositions of all the employed steels were almost same and they did not have remarkable texture as noted in Section 8.2, this trend of cleavage crack propagation resistance basically reflected the grain size effect.

Above trend does not consist with grain size effect to cleavage fracture initiation toughness. In ferrite-pearlite steels, the cleavage fracture initiation process is generally composed of three steps: (a) microcrack formation at pearlite colony, (b) propagation into ferrite matrix, and (c) propagation across ferrite grain boundary [19,20]. During these steps, grain boundary works to prevent the initiated microcrack from propagating to neighbor grain. Therefore, the smaller grain size steel has higher resistance against cleavage crack initiation because the crack encounters the grain boundary in shorter crack length in fine grain microstructures [21].

On the other hand, the absorbed energy due to cleavage fracture surface formation is relatively small compared to the total energy absorbed during cleavage crack propagation. The tear ridge (Fig. 8-11), which is a ligament broken in ductile manner between the cleavage facets, plays a dominant role to absorb energy [22–25]. Namely, the plastic deformation and ductile fracture of

the ligaments between cleavage faces are main mechanism to absorb energy during cleavage crack propagation in ferrite-pearlite steels. The energy absorbed by tear ridge formation was reported to be larger in coarser grain steel due to contribution of thickness of tear ridge (ch in Fig. 8-11(b)) [26].

Above findings were observed also in this study. Fig. 8-12(a) shows the cross section of the cleavage fracture surface of S2 under −196 ℃. The red lines are cleavage planes, which were distinguished by Euler angle obtained by EBSD data and the regions surrounded by white circle are tear ridges. Karnel Average Misorientation (KAM) map of same cross section as Fig. 8-12(a) is shown in Fig. 8-12(b). It is widely known that KAM value is correlated to plastic strain [27,28], and thus Fig. 8-12(b) shows tear ridge experienced more strain than cleavage planes, which means that the plastic work in the tear ridge was larger than that in cleavage planes.

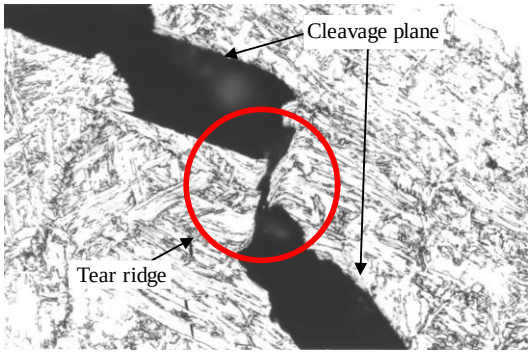

(a) SEM image of a tear ridge

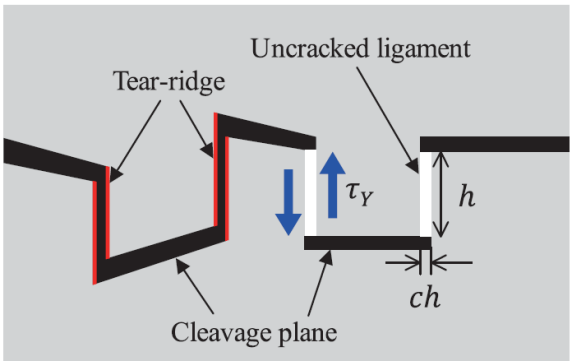

(b) Schematic illustration of tear ridge

Fig. 8-11 Tear ridge formation between cleavage planes [29]

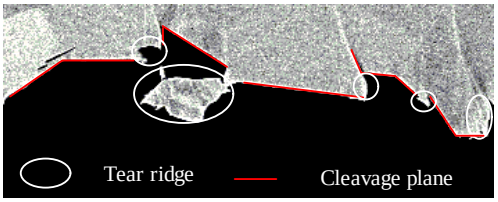

(a) Cross section of cleavage fracture surface

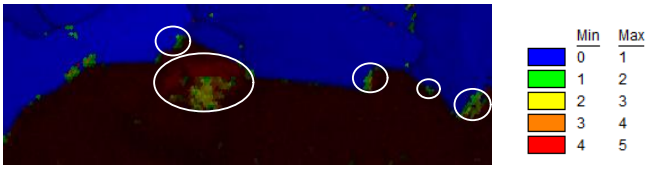

(b) KAM map of cross section

Fig. 8-12 Cross section observation of cleavage fracture surface

Effective surface energy during cleavage crack propagation in bcc steels was calculated by incorporating above tear ridge formation [26]. The effective surface energy corresponds to the cleavage crack propagation resistance in microscopic view. This calculation was conducted by evaluating tear ridge formation on the cleavage fracture surface, which was simulated by a numerical model focusing on steel microstructures [30]. This calculation was conducted for three levels of average grain size. The calculation result is shown in Fig. 8-13, where the effective surface energy was larger in coarser grain steel although the data have some scatters due to grain and grain size distribution in the calculation zone. This trend was attributed to that plastic work until tear ridge fracture was governed by the gap between cleavage planes [26].

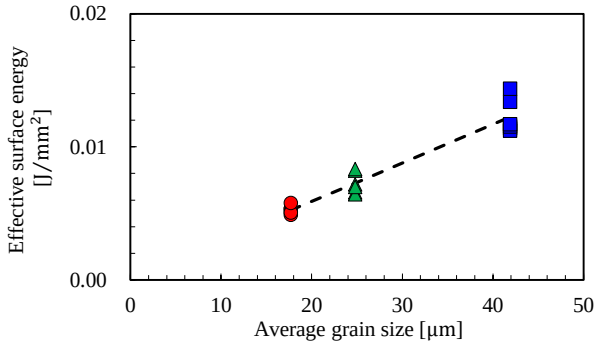

Fig. 8-13 Effective surface energy for each average grain size [26]

In fact, some previous studies discussed grain size effect to crack propagation across neighbor grains. Stec and Faleskog showed the cleavage crack is hard to go through the grain boundary when it attempted to propagate to the neighbor grains in fine grain microstructures [31]. In addition, Qiao and his coworkers carried out a series of studies to calculate resistance against cleavage crack propagation across the grain boundaries [32,33]. However, these study did not consider tear ridge formation, and thus they could not appropriately deal with cleavage crack propagation behaviors associated to macroscopic brittle crack arrest event.

Although the above study showed that the local fracture stress was estimated to become higher in coarser grain steels, it is needed to pay attention to the differences between brittle crack arrest toughness and the local fracture stress. The local fracture stress corresponds to only the cleavage crack propagation resistance, but the brittle crack arrest toughness is composed of not only the cleavage crack propagation resistance, but also other phenomena, such as shear lip closure effects. In particular, the closure stress is expected to be higher in fine grain steels because the yield stress, which strongly influences closure stress, is usually higher in finer grain steels [34]. Therefore, the brittle crack arrest toughness may show other dependency on the grain size, and then, it is expected to be a subsequent study.

8.5. Conclusion

In order to investigate the grain size contribution to the cleavage crack propagation resistance in ferrite-pearlite steels, a series of experiments and finite element analyses were carried out. By focusing on that the local fracture stress expresses only the cleavage crack propagation resistance, the stress was employed as an indicator of experimentally measured cleavage crack propagation resistance. Three steels with different grain size and same chemical compositions were prepared, and they did not have remarkable texture in their microstructures.

Because the accurate evaluation of the stress requires a lot of cost and time, a simplified method was adopted to estimate the local fracture stress. This simplified method was an approach which input the experimentally obtained crack arrest length in the DCB crack arrest tests to the finite element analyses assuming the maximum stress crack velocity. Although this method was much simplified and rough, the estimated local fracture stresses under different temperatures were almost constant for each steel, which consisted with the trend shown by Chapter 3. The estimation showed that the local fracture stress was larger in coarser grain steels than in finer grain steels. This trend was also found in the numerical approach which simulated tear ridge formation and its

energy absorption [26]. The calculated absorbed energy was larger in coarser grain steels than finer grain steels.

The above trend did not consist with that of cleavage crack initiation toughness. This was explained by focusing on the differences in the resistance mechanism. In cleavage crack propagation, tear ridge is a dominant factor of energy absorption. This absorbed energy due to tear ridge can be expressed by the function of the gap between the cleavage planes.

This chapter showed the relationship between the grain size and the local fracture stress although the simplified estimation of the local fracture stress was carried out. This is the first trial to examine grain size contribution to the local fracture stress. It is worth noting that the other characteristics of steel microstructures, such as texture, should be investigated from the perspective of contribution to the local fracture stress in the subsequent works. In particular, this study does not consider the influence of grains themselves and grain boundaries. Considering that characteristics of grain boundary is reported to influence brittle crack arrest toughness [35], more detailed investigation on microstructures is expected as the future research.

Reference

[1] N. Kubo, M. Takata, M. Yamashita, D. Knowles, H. Hirose, N. Sakato, S. Muramoto, S. Hirai, M. Mitsumoto, K. Arimochi, T. Kawabata, T. Kamo, Development of 7%Ni-TMCP Steel Plato for LGN Sotrage tanks, Q. J. JAPAN Weld. Soc. 28 (2010) 130–140.

[2] J. Jang, B. Lee, J. Ju, D. Kwon, W. Kim, Crack-initiation toughness and crack-arrest toughness in advanced 9 pct Ni steel welds containing local brittle zones, Metall. Mater. Trans. A. 33 (2002) 2615–2622. doi:10.1007/s11661-002-0383-z.

[3] T. Handa, S. Igi, S. Tsuyama, T. Tagawa, F. Minami, Mechanism of Brittle Crack Arrest Toughness Improvement Due to Texture, Tetsu-to-Hagane. 98 (2012) 548–557.

[4] S. Kim, S. Lee, B.S. Lee, Effects of grain size on fracture toughness in transition temperature region of Mn-Mo-Ni low-alloy steels, Mater. Sci. Eng. A. 359 (2003) 198–209. doi:10.1016/S0921-5093(03)00344-7.

[5] D. Bhattacharjee, J.F. Knott, C.L. Davis, Charpy-impact-toughness prediction using an “effective” grain size for thermomechanically controlled rolled microalloyed steels, Metall. Mater. Trans. A. 35 (2004) 121–130. doi:10.1007/s11661-004-0115-7.

[6] G. Bullock, E. Smith, Effects of Grain Size and Temperature on Flat Fracture Propagation and Arrest in mild steel, in: Fast Fract. Crack Arrest, ASTM International, 1977.

[7] O. Furukimi, A. Narumoto, Y. Nakano, C. Shiga, T. Tanaka, Toughness of Welded Joint and Crack Arrestability of Base in Ultra Low C-2 . 5 % Ni Steel Produced by Thermo-mechanical Control Process, Trans. ISIJ. 27 (1987) 460–466.

[8] Y. Ohmori, H. Iwanaga, Y. Kawaguchi, F. Terasaki, Brittle Fracture Initiation and Propagation-Arrest Characteristics in Ferritic-Pearlitic Steels, Tetsu-to-Hagane. 62 (1976) 67–74.

[9] T. Kawabata, Y. Nishizono, S. Aihara, Brittle crack propagation behavior in a member subjected to bending load, Theor. Appl. Fract. Mech. 92 (2017) 266–275.

doi:10.1016/j.tafmec.2017.09.005.
[10] P.B. Crosley, E.J. Ripling, Compact Specimen for Plane Strain Crack Arrest Toughness Testing., J. Test. Eval. 8 (1980) 25–31. doi:10.1080/21513732.2014.983549.
[11] J.A. Joyce, R.E. Link, C. Roe, J.C. Sobotka, Dynamic and static characterization of compact crack arrest tests of navy and nuclear steels, Eng. Fract. Mech. 77 (2010) 337–347. doi:10.1016/j.engfracmech.2009.04.006.
[12] I. Soya, M. Sato, Y. Nakamura, N. Taniguchi, On a Modified Three Point Bending Test for Determining Brittle Fracture Arresting Properties, J. Japan Soc. Nav. Archit. 139 (1976) 274–283.
[13] M.R. Ayatollahi, M. Rashidi Moghaddam, S.M.J. Razavi, F. Berto, Geometry effects on fracture trajectory of PMMA samples under pure mode-I loading, Eng. Fract. Mech. 163 (2016) 449–461.
[14] E. Bouyne, P. Joly, B. Houssin, C.S. Wiesner, A. Pineau, Mechanical and microstructural investigations into the crack arrest behaviour of a modern 2 1/4 Cr-1 Mo pressure vessel steel, Fatigue Fract. Eng. Mater. Struct. 24 (2001) 105–116. doi:10.1046/j.1460-2695.2001.00363.x.
[15] T. Matsuno, A. Seto, M. Suehiro, Y. Yoshida, Effect of Punch Wear on Fatigue Strength of Pierced High-Strength Steel Sheets, J. Japan Soc. Technol. Plast. 55 (2014) 228–232.
[16] Dassault Systems, SIMULA Abaqus Analysis User's Manual, (2014).
[17] A.R. Shahani, M.R. Amini Fasakhodi, Finite element analysis of dynamic crack propagation using remeshing technique, Mater. Des. 30 (2009) 1032–1041.
[18] S.J. Hudak, R.J. Dexter, J.H. Fitzgerald, M.F. Kanninen, The influence of specimen boundary conditions on the fracture toughness of running cracks, Eng. Fract. Mech. 23 (1986) 201–213.
[19] G. Qian, W.S. Lei, M. Niffenegger, V.F. González-Albuixech, On the temperature independence of statistical model parameters for cleavage fracture in ferritic steels, Philos. Mag. 98 (2018) 959–1004. doi:10.1080/14786435.2018.1425011.
[20] K. Shibanuma, Y. Nemoto, T. Hiraide, K. Suzuki, S. Sadamatsu, Y. Adachi, S. Aihara, A strategy to predict the fracture toughness of steels with a banded ferrite–pearlite structure based on the micromechanics of brittle fracture initiation, Acta Mater. 144 (2018) 386–399. doi:10.1016/j.actamat.2017.10.046.
[21] B. Hwang, Y.G. Kim, S. Lee, Y.M. Kim, N.J. Kim, J.Y. Yoo, Effective grain size and charpy impact properties of high-toughness X70 pipeline steels, Metall. Mater. Trans. A. 36 (2005) 2107–2114. doi:10.1007/s11661-005-0331-9.
[22] H. Jaeckels, T. Iung, A. Pineau, Dynamic Crack Propagation and Crack Arrest Behaviour in Relation To Brittle Intergranular and Cleavage Fracture, Fatigue Fract. Eng. Mater. Struct. 17 (1994) 1281–1293. doi:10.1111/j.1460-2695.1994.tb00216.x.
[23] T. Iung, A. Pineau, Dynamic Crack Propagation and Crack Arrest Investigated With a New Specimen Geometry : Part II : Experimental Study on a Low-Alloy Ferritic Steel, Fatigue Fract. Eng. Mater. Struct. 19 (1996) 1369–1381.
[24] P. Haušild, I. Nedbal, C. Berdin, C. Prioul, The influence of ductile tearing on fracture energy in the ductile-to-brittle transition temperature range, Mater. Sci. Eng. A. 335 (2002) 164–174. doi:10.1016/S0921-5093(01)01913-X.
[25] X. Yang, S. Marie, C. Jacquemoud, P. Bompard, Prediction of cleavage crack propagation path in a nuclear pressure vessel steel, Eng. Fract. Mech. 191 (2018) 486–503. doi:10.1016/j.engfracmech.2018.01.015.
[26] F. Yanagimoto, Y. Suzuki, T. Hemmi, Y. Takashima, T. Kawabata, K. Shibanuma, Contribution of grain size to resistance against cleavage crack propagation in ferritic steel, Acta Mater. Submitted (n.d.).
[27] K. Nomura, K. Keiji, Y. Sakakibara, S. Takahashi, H. Yoshizawa, Effect of Grain Size on Plastic Strain Analysis by EBSD for Austenitic Stainless Steels with Tensile Strain at

650°C, J. Soc. Mater. Sci. Japan. 61 (2012) 371–376. doi:10.2472/jsms.61.371.
[28] N. Allain-Bonasso, F. Wagner, S. Berbenni, D.P. Field, A study of the heterogeneity of plastic deformation in IF steel by EBSD, Mater. Sci. Eng. A. 548 (2012) 56–63. doi:10.1016/j.msea.2012.03.068.
[29] K. Shibanuma, Y. Yamamoto, F. Yanagimoto, K. Suzuki, S. Aihara, H. Shirahata, Multiscale model synthesis to clarify the relationship between microstructures of steel and macroscopic brittle crack arrest behavior - Part I: Model presentation, ISIJ Int. 56 (2016). doi:10.2355/isijinternational.ISIJINT-2015-449.
[30] K. Shibanuma, Y. Suzuki, K. Kiriyama, S. Katsuyuki, H. Shirahata, A model of cleavage crack propagation in a BCC polycrystalline solid based on the extended finite element method, Acta Mater. (n.d.) submitted.
[31] M. Stec, J. Faleskog, Influence of grain size on arrest of a dynamically propagating cleavage crack in ferritic steels - Micromechanics, Int. J. Fract. 158 (2009) 51–71. doi:10.1007/s10704-009-9374-z.
[32] W. Lu, J. Chen, S.S. Chakravarthula, Y. Qiao, Resistance to cleavage cracking and subsequent shearing of high-angle grain boundary, Eng. Fract. Mech. 77 (2010) 768–775. doi:10.1016/j.engfracmech.2009.12.009.
[33] Y. Qiao, A.S. Argon, Cleavage crack-growth-resistance of grain boundaries in polycrystalline Fe – 2 % Si alloy : experiments and modeling, Mech. Mater. 35 (2003) 129–154.
[34] J.F. Lancaster, Metallurgy of Welding, Springer, 1980.
[35] M. Kaneko, JP2011184754A:Steel having excellent brittle crack arrest property, and method of producing the same, 2010.

Chapter 9 High speed observation of rapidly propagating cracks in 3D structures

9.1. Introduction

Structural crack arrest design is an important technique to achieve required brittle crack arrest performance as same as material crack arrest design [1]. Originally, large structures with double integrity was designed to arrest the brittle crack running in weld by appropriately deploying base metals working as crack arrestor which have higher brittle crack arrest toughness [2,3]. On the other hand, a technique to use structural factor to arrest the running brittle crack has been focused on in order to reduce use of high performance steels which essentially needs higher cost [4]. This technique has been called as structural crack arrest design and practically applied to the ships.

According to literatures on structural crack arrest design, the crack behaviors in the structural crack arrest design can be categorized to four types. The first one is crack propagation through the structure. Namely, the crack is not arrested in this case. The second one is the crack arrest in the weld bead in fillet welding joint. This case can be found when the employed welding metal has better performance, but it can be also attributed to the relaxation of the plastic constraint. In the weld bead in fillet welding [5], the thickness becomes thinner than the base metal plate. Thus, the plain strain region becomes small and the unbroken shear lip rapidly grows to arrest the crack. The third one is the crack arrest just after the crack entered the flange. This case was observed in the experiments using the higher grade steel for flange [6,7]. Thus, this case is attributed to the higher local fracture stress of the flange steel although the compressive residual stress also works to arrest the crack. The last one is the crack arrest after the crack propagates in the flange to some extent. The crack front shape contributes to the crack arrest in the last case. It was reported that the crack was arrested by the crack front shape effect even when the employed steel did not have higher crack arrestability [6,8]. Thus, the crack front shape effect is valuable to investigate

because to effectively use the crack front shape effect can reduce cost of steels.

Although a series of analyses have been carried out to clarify the performance of structural crack arrest design [9–11], the detail mechanism to arrest brittle cracks are still unclear due to some reasons. One reason is difficulty to measure brittle crack behaviors in 3D structure such as T-joint and cross joint. Strain gauges and crack gauges, which are usually used to measure the crack behaviors, can only deal with cracks in 2D. The other reason is about simulation. Although the local fracture stress criterion has been incorporated by some simulation models including that proposed in Chapter 7, such simulations have supposed only plate specimen and not considered 3D structure. This is because the crack front effect and interaction between the crack and structures are much complicated to deal with in the above simplified simulation. As pointed out in the end of Chapter 7, it is needed to implement the local fracture stress criterion in application phase finite element analyses to accurately deal with 3D structures.

According to the reason mentioned above, the mechanism of crack arrest in the structural crack arrest design has been still unclear. On the other hand, the crack front shape in the 3D structure was focused on [12,13]. Handa et al. pointed out the crack front shape becomes semi-elliptical after the crack entered the flange and thus SIF at the crack front becomes smaller [12,13]. They carried out finite element analyses assuming crack front shape from the fracture surface after crack arrest and showed the SIF decreased by the crack front shape change. Although such suggestion is noteworthy, the actual crack front shape during crack propagation could not be observed in steels. Thus, it is needed to directly observe the crack front shape in 3D structure to validate above suggestion. Accordingly, this study employed PMMA, which is transparent elastic brittle material, instead of steel to observe the crack front because the steels are not transparent. PMMA has been widely employed for rapid crack propagation studies and findings from them have provided valuable knowledge to study brittle crack propagation and arrest behaviors in steel [14–16]. Although, of course, PMMA's deformation behavior is different from steels, the fundamental behaviors of rapid crack propagation are useful to understand brittle crack propagation in steels which has been often approximated as linear elastic fracture mechanics due to the higher strain rate near the crack tip [17,18].

In fact, 3D effect related to crack front shape has been examined in the context of fracture mechanics [19,20]. In particular, the crack front shape during crack propagation was observed by Nishioka et al. [21,22]. They employed PMMA plate specimen for the observation of crack front shape and singularity of the plate surface although the 3D structure like cross joints were not dealt with in the literatures. Thus, referring to above works, specimens simulating cross-joint structural

arrest design were made from PMMA. The crack fronts running in the specimens were observed by high speed camera.

9.2. Experiments

9.2.1. Materials and specimens

PMMA, which is polymethyl methacrylate, was employed in this chapter as noted above. Fig. 9-1 shows the chemical structural formula of PMMA. PMMA is almost linear elastic and brittle at room temperature, although it shows a little nonlinearity just before it is broken in stress-strain curve [23–25]. The crack tip field in this material has been regarded to be elastic during rapid crack propagation [26,27]. The representative example of the mechanical properties of PMMA is shown in Table 9-1.

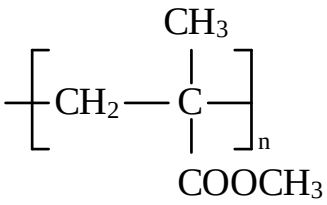

Fig. 9-1 Chemical structural formula of PMMA

Table 9-1 Mechanical property of PMMA

Tensile strength[MPa]	Charpy absorbed energy [kJ/m^2]	Young's modulus [MPa]	density [kg/m^3]	Rayleigh wave velocity [m/s]
74	17	3200	1170	954

The specimen configuration is shown Fig. 9-2. A specimen is composed of three parts; upper and lower web, and flange. The webs and the flange were joined by solvent bonding in some specimens, but some specimens were hewn from one thick PMMA plate, whose thickness was 50 mm. Two types of the specimen were employed in this study. One is a specimen simulating full-penetration welding between the webs and a flange in Fig. 9-2(a). The other one is simulating the fillet welding in Fig. 9-2(b). As noted above, welding technique was not employed in this study,

and thus the residual stress and microstructural change due to welding were not considered in this study [28]. Both types of welding are actually applied to shipbuilding [13], but it is known that fillet welding with un-welded section has the higher crack arrestability than the full penetration welding [12,29]. The rectangular hole of the specimen shown in Fig. 9-2(b) corresponded to the un-welded section of the actual cross-joint structure with fillet welding joint. Therefore, the specimens shown in Fig. 9-2(b) corresponded to scenario 1 in the structural crack arrest design [10]. The specimen shown in Fig. 9-2(b) was also used for the experiments simulating full-penetration welding.

As shown in Fig. 9-2, the specimens were designed for DCB type crack arrest test. Although it was desirable to employ tensile type crack arrest test because the actual structural crack arrest test employs tensile type specimens, jigs for tensile tests prevented the high speed camera from observing crack fronts. Therefore, DCB type specimens were prepared to secure the field of view of the high speed camera. Fig. 9-3 shows a schematic illustration of the experiment using the specimen shown in Fig. 9-3. The green surface in Fig. 9-4 is especially etched to be transparent for high speed camera observation although other surfaces were also etched. Jigs and pins were designed not to prevent the camera from watching the crack propagation. The specimen surfaces were etched to make them clearer for the high speed camera to observe the crack fronts easily. Fig. 9-4 shows one example of the specimen photo, which is the type of specimen shown in Fig. 9-2(b).

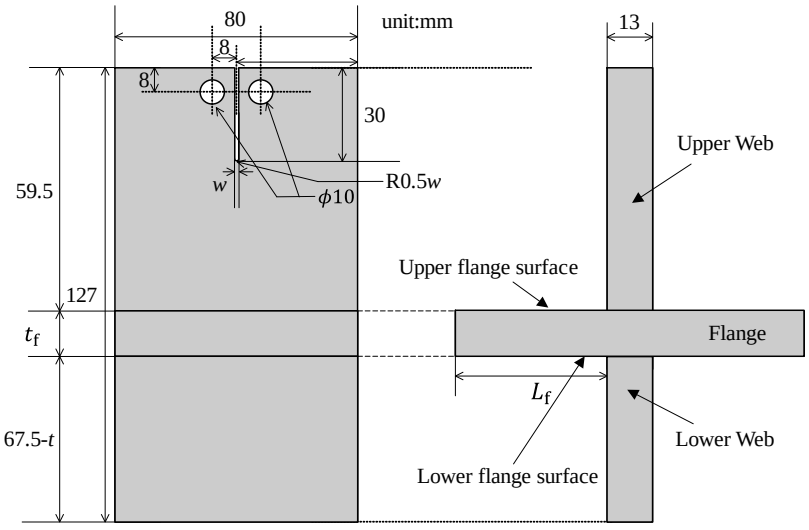

(a) Specimen simulating full-penetration joint

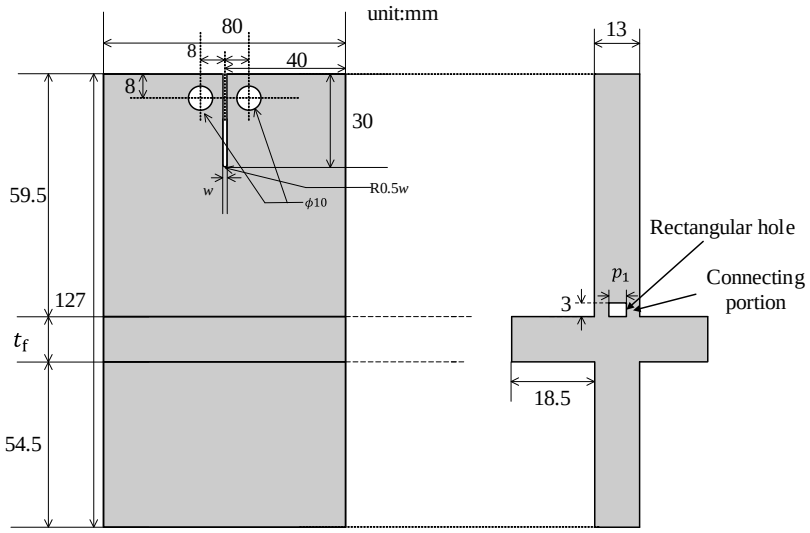

(b) Specimen simulating fillet welding joint

Fig. 9-2 Specimen configurations

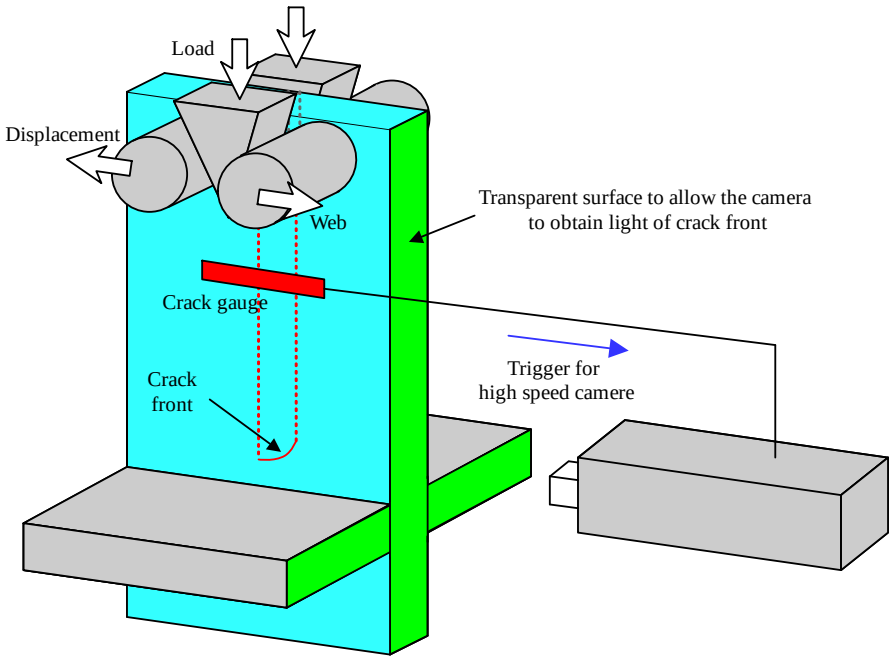

Fig. 9-3 Schematic illustration of experiments

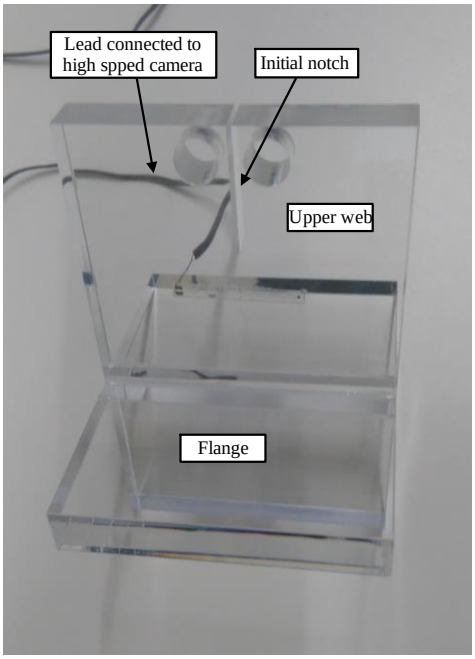

Fig. 9-4 Specimen photo

9.2.2. Experimental procedure

Figure 9-5 shows a photo of the experimental set up. The wedge was used to move the pins to open the initial notch until the fracture was initiated. These jigs and the experimental procedure were same as those in Chapter 8. The high speed camera, SHIMADZU HPV-2, was located as shown in Fig. 9-4. Four lights were used to light up the specimen. Fig. 9-6 shows the specimen under lighting.

Although the maximum frame speed of SHIMADZU HPV-2 is $10^6\ s^1$, this camera can record only 100 frames. Considering that the crack velocity in PMMA is expected to be slower than that in steels, the frame speed was set to $2.5 \times 10^5\ s^{-1}$. Thus, the record duration was $400\ \mu s$. The camera observation was initiated by external signal from the crack gauge glued on the expected crack path. Namely, the record was initiated just after the crack gauge was broken by crack propagation. This trigger system was same as that employed for crack velocity measurement in Chapter 3, 5, and 6. However, the record duration of the camera was much shorter than that of oscilloscope employed in Chapter 3, 5, and 6. All experiments were carried out under static loading and room temperature condition. The load-displacement relationship of the wedge was measured.

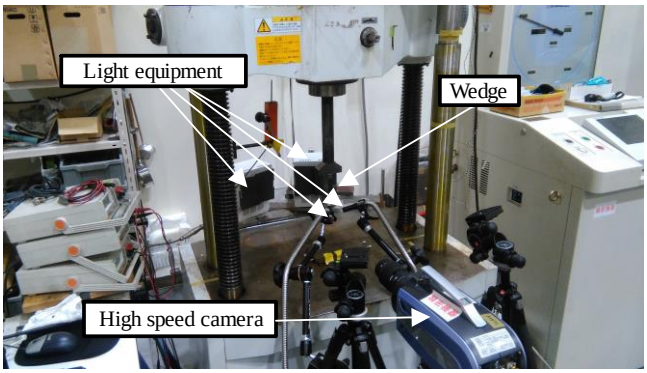

Fig. 9-5 Experimental set up

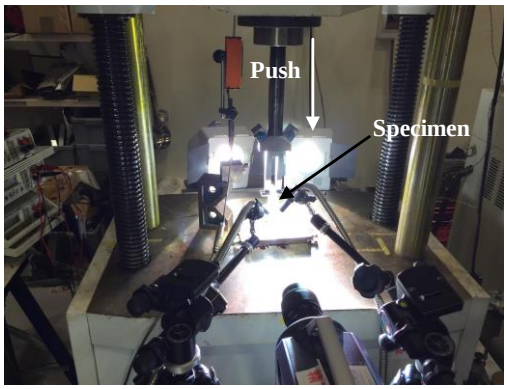

Fig. 9-6 Specimen set up under lighting

9.2.3. Experimental result

The experimental results are shown in Table 9-2. The specimens are categorized to two types in terms of bond types, solvent bonding or cut-off from one plate. The specimens are also categorized to two types in terms of joint types, full-penetration and fillet. The load-displacement relationship were linear until the fracture was caused, so all the specimens were broken in linear elastic manner. The crack arrest positions are also written in Table 9-2. The crack arrest positions can be categorized to three types. One is the crack arrest in the fillet. This crack arrest position was observed in the fillet-welding specimen. The second one is the crack arrest in the stiffener. The example of the specimen after crack arrest shown in Fig. 9-7 is categorized to this type. The last type is the crack arrest in the lower web. This type means that the crack cannot be arrested by the joint. In fact, the re-initiation of the arrested crack was observed in some experiments. According to the high speed camera images, the crack was arrested in the flange in B3, but the specimen after the experiment was completely broken in such cases. This was because the crack

was reinitiated after the end of high speed camera observation due to the residual movement of the jig. And, even though the crack arrest position was in the lower web in A2, the crack arrest was relatively early in A2 compared to A3. The crack arrest positions were in the flange when the flange thickness was 13 mm. On the other hand, the crack arrest positions were in the lower web when the flange thickness was 5 mm although the fracture loads were different.

Table 9-2 Experimental results

No.	Bond type	Joint type	t_f[mm]	Notch root [mm]	p_1 [mm]	Fracture load [kN]	Arrest position
A1	Solvent bonding	Full-penetration	13	0.6		2.9	Flange
A2	Solvent bonding	Full-penetration	10	1		3.45	Lower web
A3	Solvent bonding	Full-penetration	5	1		3.64	Lower web
A4	Solvent bonding	Full-penetration	13	0.8		2.9	Flange
B1	cut-out	Full-penetration	13	0.9		2.4	Flange
B2	cut-out	Full-penetration	5	0.9		3.2	Lower web
B3	cut-out	Full-penetration	13	1.0		3.38	Flange
B4	cut-out	Full-penetration	13	0.9		3.08	Flange
C1	cut-out	Fillet	13	0.9	3	2.97	Flange
C2	cut-out	Fillet	13	0.9	3	2.19	Flange
C3	cut-out	Fillet	13	0.9	6.5	3.2	Fillet
C4	cut-out	Fillet	13	0.9	8	2.42	Fillet
C5	cut-out	Fillet	13	0.9	4	2.82	Flange
C6	cut-out	Fillet	13	0.9	6	2.46	Fillet

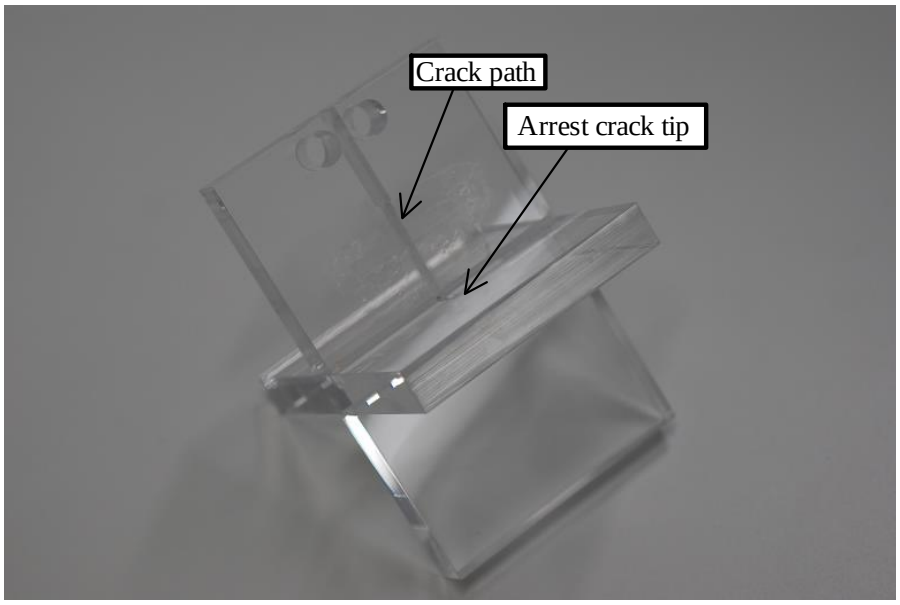

Fig. 9-7 Specimen after crack arrest (A1)

The fracture surface became foggy except just before the crack arrest. This characteristic fracture surface is typically observed in the fracture of polymers [30]. This foggy fracture surface is caused by the surface roughness, and determined by crack velocity and stress intensity factor [31–33]. When the crack velocity and stress intensity factor are low, the fracture surface approaches to transparent. Namely, because the transparent fracture surface is hard to distinguish in the high speed camera images, the observation may not be able to accurately capture the crack arrest event.

In order to clarify the crack propagation and arrest behaviors in 3D structures, high speed camera images were investigated in detail. B2 and B3 were chosen as the representative cases because their fracture loads were similar but the crack arrest positions were different.

Figure 9-8 shows the images of crack propagation in B2. Time zero second corresponded to the initiation of the high speed camera observation. At $76\ \mu s$ from the observation beginning, the crack tip entered the flange from the upper web. The most advancing point of the crack front reached the lower web at $100\ \mu s$. Because the crack front became tunneling after it entered the flange, the crack propagated in the x direction in the flange only a little until it reached the lower flange. The crack front reached the surface of the lower web at about $108\ \mu s$. Thus, after $108\ \mu s$, the crack front became through crack in the flange and lower web. This crack continued to propagate after it entered the lower web and it almost propagated through the web. On the other hand, Fig. 9-9 shows the crack propagation images of B3. The images shown in Fig. 9-9 are in

the range from the crack arrival at the flange to the crack arrest in y direction. The crack was arrested in the flange, so the crack front shape remained a half of rugby ball shape even after it was arrested. After the crack was arrested in the y direction, the crack continued to propagate in the flange in x direction. By using image processing software, ImageJ [34], the crack fronts until it entered the lower web were analyzed. The center point of the boundary between the upper web and the flange was set to (0, 0) and the coordinates of some points along the crack front were captured by ImageJ and plotted in Figs. 9-10 and 9-11 for B2 and B3, respectively. Due to the reflection and deflection of light at the surface, the crack front shape near plate surfaces were ambiguous and difficult to identify [21]. Thus, because the plots were obtained by looking for the crack front points which could be distinguished easily, the intervals between the plots are not constant. However, because this chapter aims to evaluate the difference between the crack front shapes due to the structural design, these discrete plot did not hinder the analyses below. In addition to discrete plots obtained by ImageJ, the plots were well approximated by quadratic functions, which are expressed by dashed curve in Figs. 9-10 and 9-11. In both cases, the crack front shapes were nearly flat just after the crack fronts entered the flange, and gradually became the shapes of downward convex. In the case of B3 shown in Fig. 9-11, the crack was arrested to keep the quadratic shape although the crack front shape became through crack after the crack entered the lower web in the case of B2. Because this difference of the crack front shape characteristic is considered to cause the difference of crack propagation/arrest behaviors, this will be analyzed and discussed in detail in Section 9.3.1. It is worth noting that the similar crack front shapes mentioned above were observed in the other experiments.

On the other hand, the crack front shape in the specimen simulating fillet welding joint showed the branch of the crack front at the simulated un-welded part. Fig. 9-12 shows the crack propagation images of C5. The crack front was divided to two separated crack front by the rectangular hole at 80 μs. They kept separated fronts until 112 μs and they joined together after they entered the flange at 120 μs. According to the images of Fig. 9-12, the separated crack fronts were kept from 104 to 120 μs even after they entered the flange. Such duration while the crack propagates under separated crack front condition is expected to be longer when p_1, which is the length of the rectangular hole, is longer. According to finite element analyses by Handa et al. [29], the separated crack front shape showed the lower stress intensity factor compared to the one crack front shape. Although the cracks were not arrested while they kept the separated crack front in this study, this study clearly showed that the crack front branch which can reduce the stress intensity factors occurred in the structural crack arrest design for the first time.

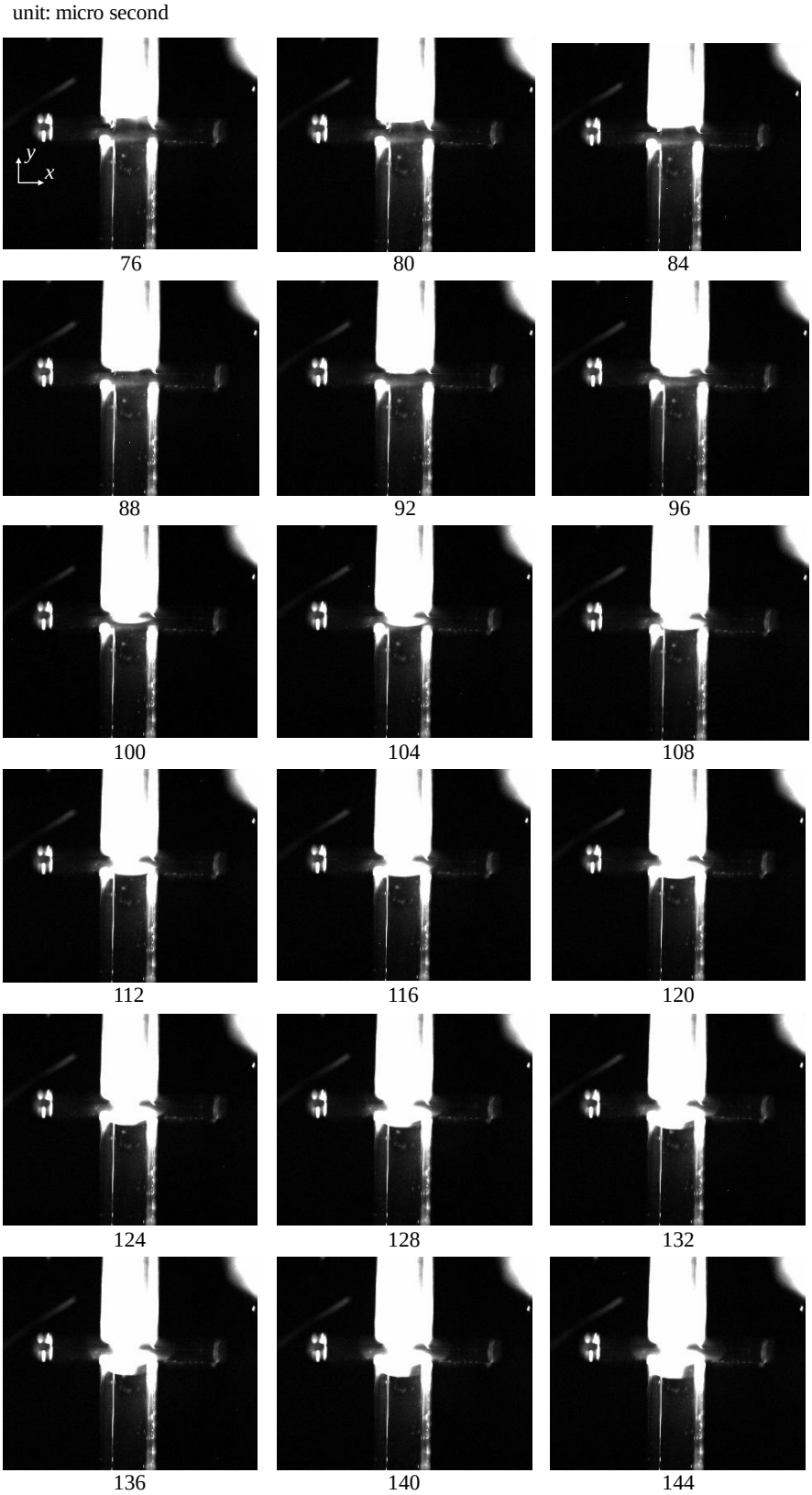

Fig. 9-8 Crack propagation images of B2

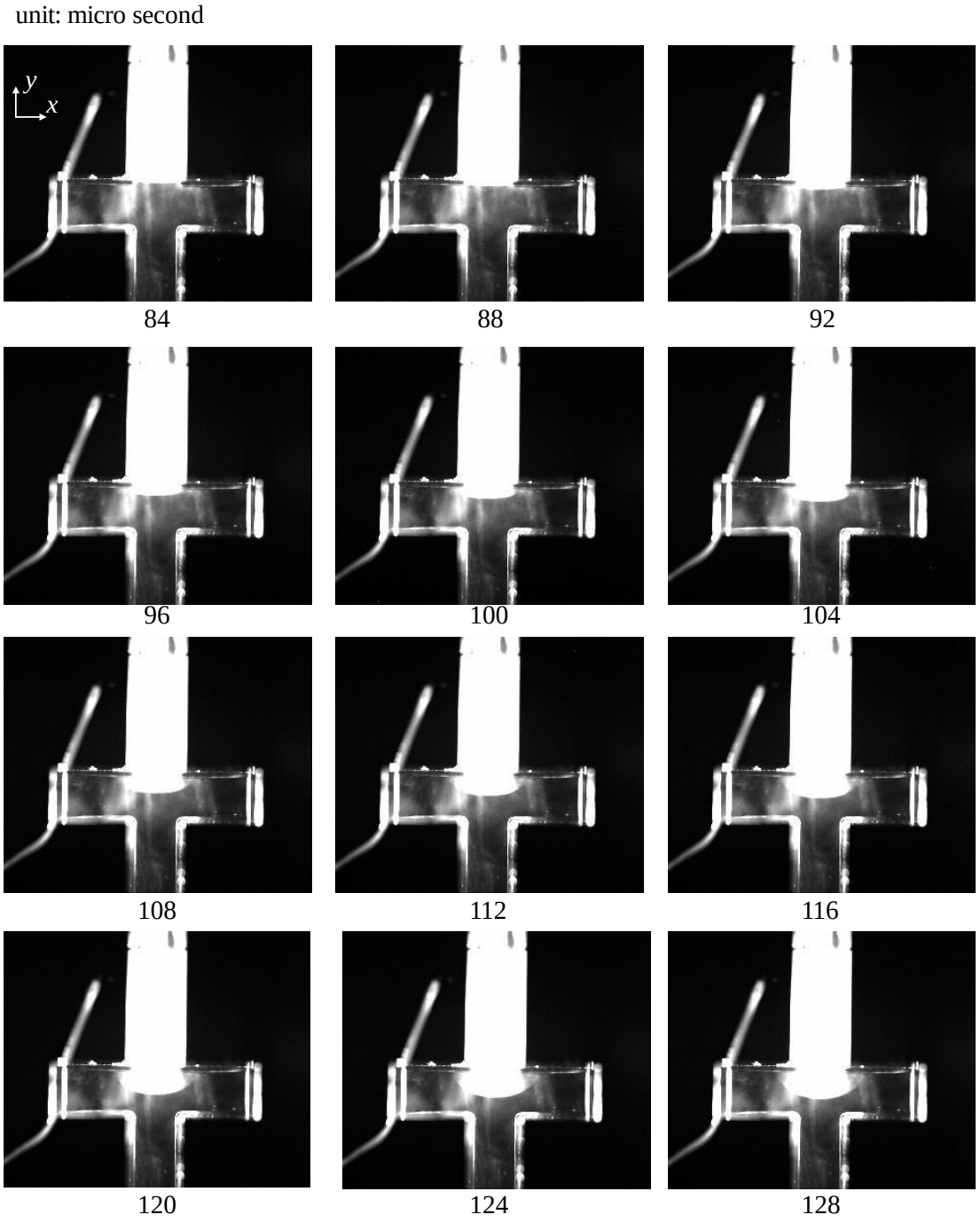

Fig. 9-9 Crack propagation images in B3

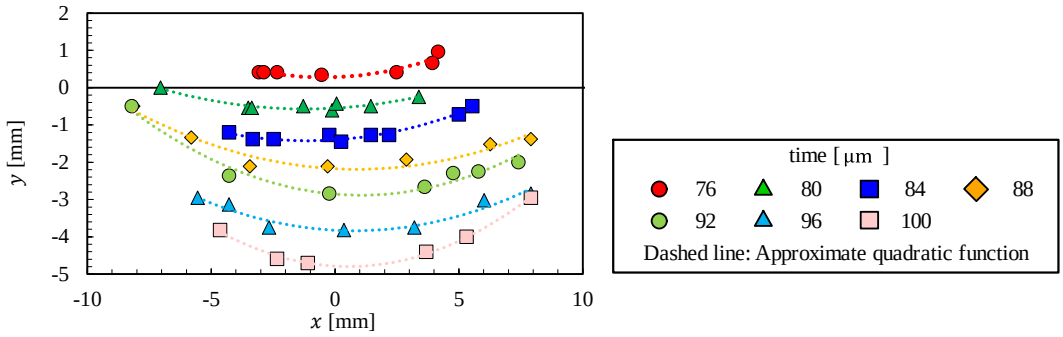

Fig. 9-10 Crack front points in B2 from high speed images

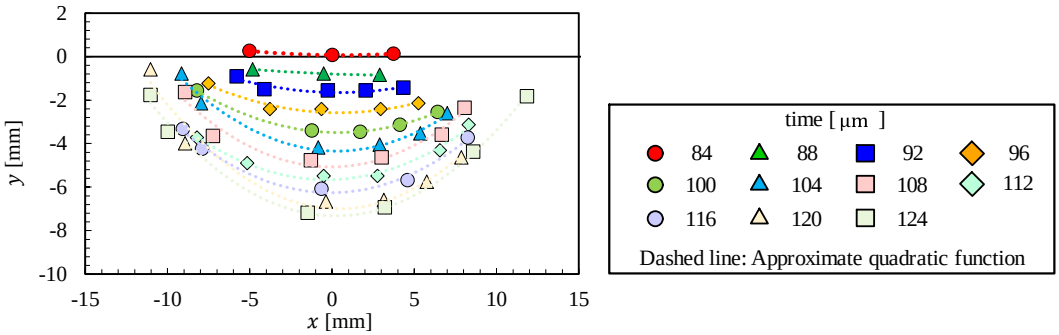

Fig. 9-11 Crack front points in B3 from high speed images

In C3, C4, and C6 of the experiments using the specimen simulating fillet welding joint, the cracks were arrested in the fillet before they entered the lower web. According to the high speed camera observations, the cracks which were arrested in the fillet were reinitiated to propagate along the boundary between the flange and upper web. Namely, the crack direction was changed from the prior crack propagation. This is partly because the boundary between the flange and upper web had smaller area, which is easy for the crack to propagate. The fillets were thinner in these cases than in the cases where the cracks were arrested in the flange. On the other hand, the cracks were arrested in the flange after they went through the fillet welding parts in other experiments simulating fillet welding joint (C1, C2, and C5). The fillet thickness of these experiments were relatively thicker in the C series experiments.

unit: micro second

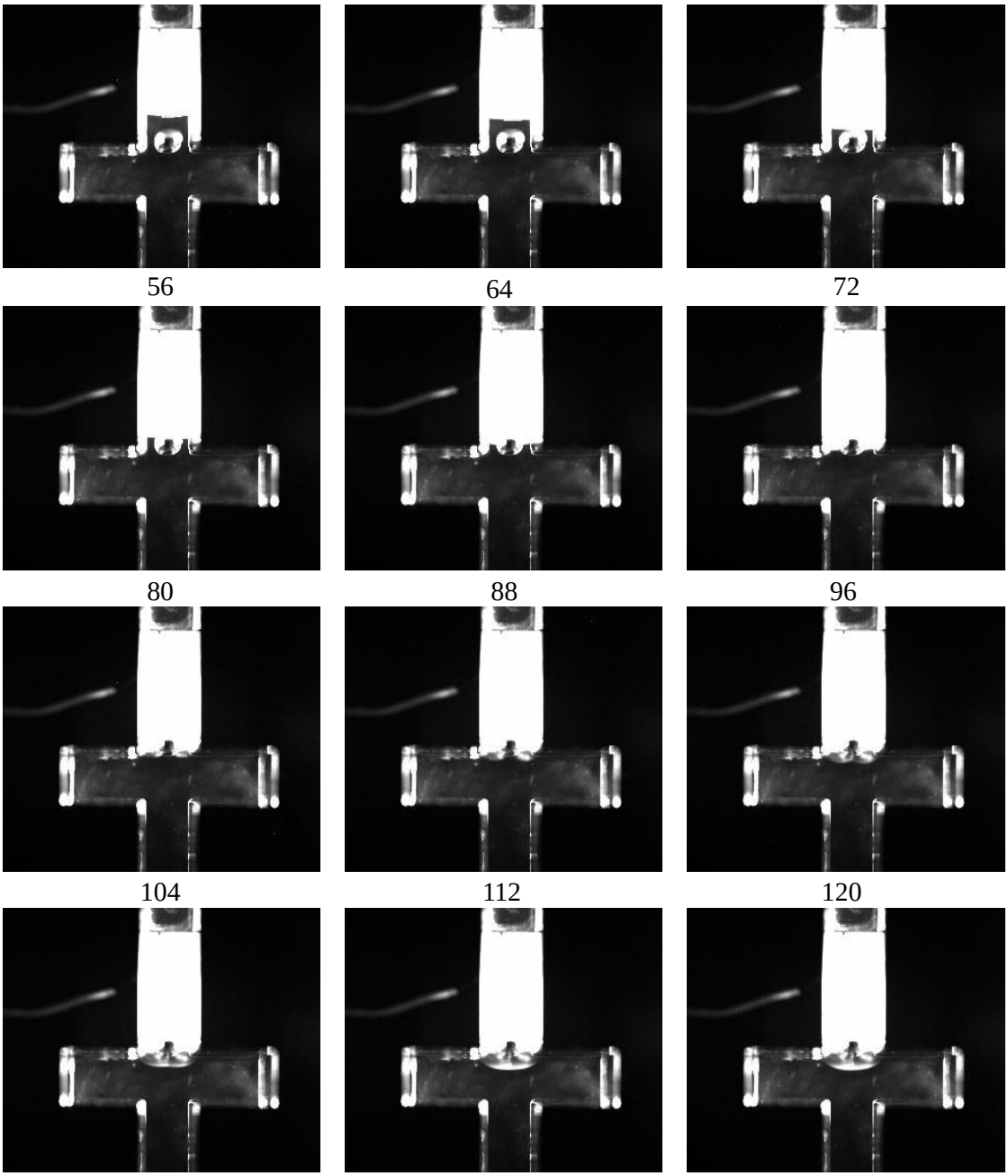

Fig. 9-12 Crack propagation images in C5

9.3. Discussion

9.3.1. Crack front shape effect

It is worth investigating in detail about the crack arrest mechanism in the flange as noted in Section 9.2.3. To focus on the crack front shape in the flange, finite element analyses were conducted to investigate the effect of crack front shapes to SIF. Referring the previous studies [13,29], the analyses were under elastic and static conditions because the analyses aimed to compare the SIF behaviors in different crack front shapes.

As shown in Figs. 9-10 and 9-11, the crack front shapes in the flange can be basically approximated by quadratic functions. Therefore, the crack front shape in finite element models were expressed by quadratic functions. The employed finite element model is shown in Fig. 9-13. The thickness of flange was set to 13 mm. The thickness of the lower and upper webs were 13 mm. Thus, this finite element model was a designed to simulate the specimen shown in Fig. 9-2(a). Although the detail specimen configuration may influence the quantitative results, this finite element model was employed because this analysis aimed to focus on the crack front shape.

The calculation area of Fig. 9-13(a), which is enlarged in Fig. 9-14, was divided by finest meshes, whose size were $0.13\ \text{mm} \times 0.13\ \text{mm}$ in $x-y$ view. In this calculation area, the crack front shape was expressed to analyze the crack front shape contribution to the SIF. The finite element model was quarter model considering the boundary conditions. The initial notch was also modelled in Fig. 9-13. The force displacement applied to the rigid pin was set to 1 mm. The calculations were carried out using Abaqus 6.14.

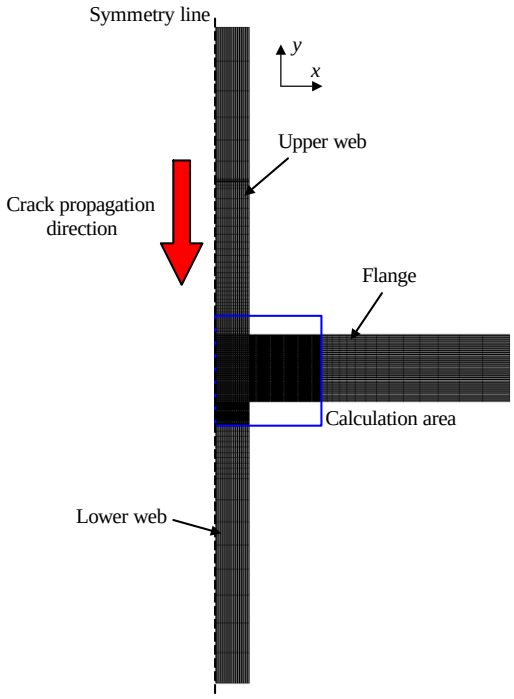

(a) $x-y$ view

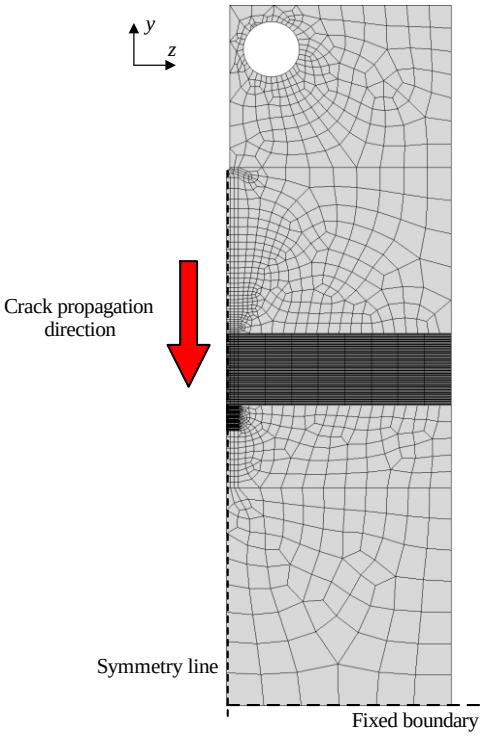

(b) $y-z$ view

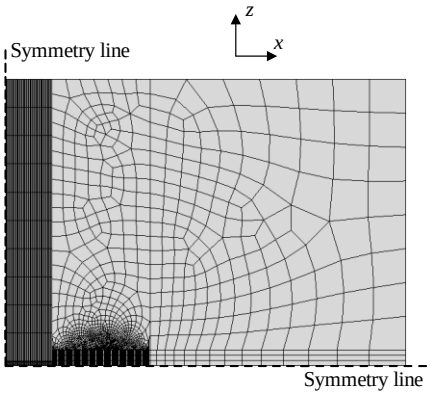

(c) $x-z$ view

Fig. 9-13 Finite element model

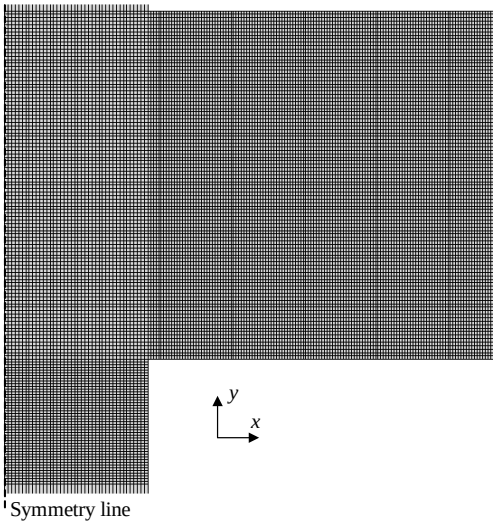

Fig. 9-14 Enlarged view of the calculation area (Blue area of Fig. 9-12(a))

Figure 9-15 shows the schematic illustration of the crack front shape in finite element models. For simplicity, the cross section of meshes were square in the flange, and the fracture surface was approximated by the aggregation of these square meshes like voxel method [35]. The center of the boundary line between the upper web and the flange was set to the origin of the coordinate axis. The distance between the deepest point of the crack front and the origin was expressed by Y_{d}. The intersection point of the flange surface and the crack front was $(X, 0)$. Namely, the quadratic function to express the crack front shape can be expressed as

$$x = \frac{X}{Y_{\mathrm{d}}^2} \mathrm{y}^2 + X \tag{9-1}$$

The calculation was divided to two steps. At first, the forced displacement was applied to the rigid pin to open the notch. All the nodes along the z symmetry line were fixed in this step. Then, the crack surface was simulated in the analysis. In this step, the nodes along the z symmetry line in the upper web and in the crack surface area, which corresponded to the nodes included in the blue zone in Fig. 9-15, were released. The other nodes in the flange and lower web were not released. Non linearity of deformation was considered. The SIF of the deepest position of the crack front was evaluated because the crack propagation in y direction is the most important to prevent the crack from entering the lower web. The SIF was calculated by fitting $1/\sqrt{r}$ singularity to the stress field in front of the crack front referring to previous studies [5,13]. It was confirmed that the stress field was governed by the singularity. The x coordinate of the intersection point between the crack front and the flange surface and the y coordinate of the deepest point of the crack front (expressed as Y_{d} in Fig. 9-15 were variables to define the crack front shape. To compare the numerical results, the analyses that the crack front shapes were rectangular were also carried out. In these cases, the lengths of the sides in x and y direction were set to $2X$ and Y_{d}, respectively. Thus, the length and depth of the rectangular crack were same as the quadratic function crack. In addition, the green dashed line in Fig. 9-15 shows a rectangular crack surface whose lengths of the sides in x and y direction were set to $2X$ and Y_{d}. Fig. 9-16 shows the differences of node constraints in finite element analyses between the quadratic function crack surface and the rectangular crack surface. The crack front shapes were well expressed even though the voxel-like method was employed.

Figure 9-17(a) shows the SIFs calculated by the above finite element method when X was fixed to 6.5 mm. In addition to the analysis results of quadratic function crack surface, SIFs for the rectangular crack surface represented by green dashed line in Fig. 9-15 are also shown for comparison. According to the high speed observations shown in Figs. 9-8 and 9-9, the crack front propagated in flange direction only a little just after the crack front entered the flange. The results of Fig. 9-17(a) reflected this finding. Because the DCB type specimen is K-decreasing specimen along crack propagation, it is natural that the SIFs becomes smaller when Y_{d} becomes larger. However, the decreasing ratio of the SIF is higher in the quadratic function case than in the rectangular case. Although Fig. 9-17(a) shows the case when the crack front tip did not propagate in $x-$direction, the case when the crack propagated about 4 mm in $x-$direction is shown in Fig. 9-17(b). Even when the crack propagated in the flange direction, the SIF in the quadratic function

cases was lower than in the rectangular cases. Accordingly, it can be said that the quadratic crack front shape made the crack tend to be arrested. As shown in Fig. 9-17, the effect to decrease the SIFs of the quadratic function crack front becomes remarkable when the crack front reached deeper position in the joint. Therefore, because in the thinner flange experiments, the crack front shape became the rectangular (corresponded to through crack) just after it entered the flange, the SIF reduction effect did not work enough. Thus, the structural crack arrest design contributed to promote the crack arrest by reducing the SIFs in the specimen simulating full-penetration joint.

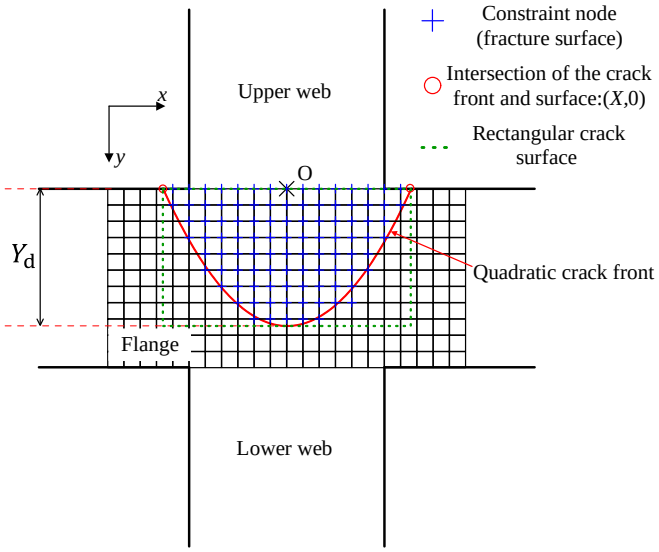

Fig. 9-15 Schematic illustration of fracture surface expression in finite element models

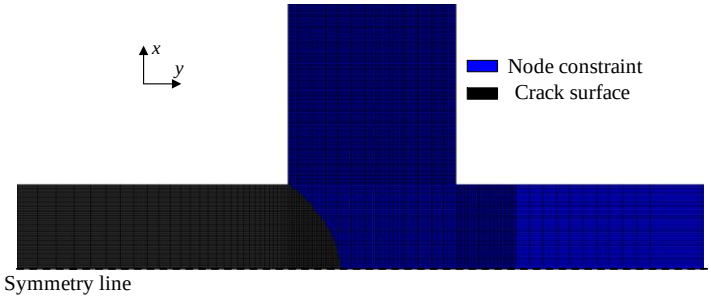

(a) Quadratic function crack surface

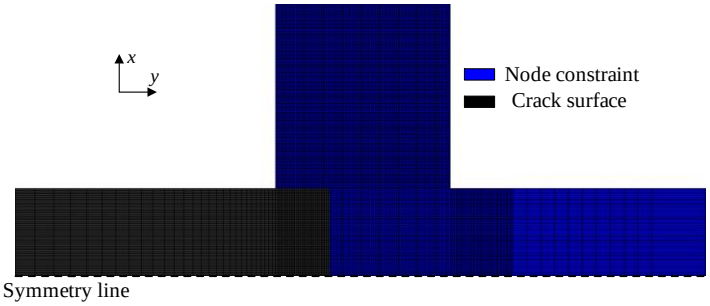

(a) Rectangular crack surface

Fig. 9-16 Mapping of the constraint nodes ($X = 6.5$ mm, $Y_d = 3.9$ mm)

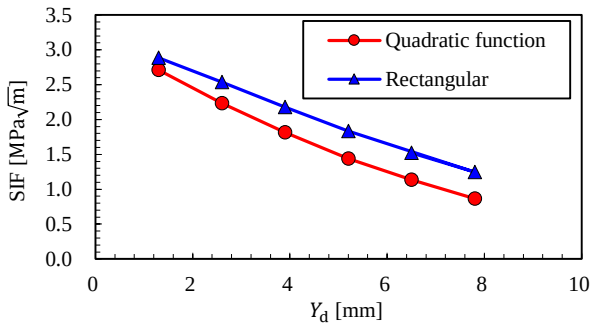

(a) $X = 6.5$ mm (A crack did not propagate in the flange direction)

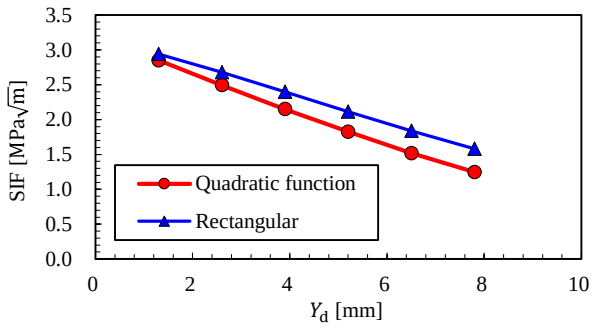

(b) $X = 10.4$ mm (A crack propagated for 3.9 mm in the flange direction)

Fig. 9-17 SIF transition against Y_d

9.3.2. Fillet welding effect

Even in the elastic solids, the crack front shape is not straight because the intersection point of the plate surface and straight crack front has weaker singularity [36]. Thus, the crack front becomes curve to make the singularity of the intersection point consist with $1/\sqrt{r}$. This was experimentally supported by Nishioka et al. for rapid crack propagation cases [21]. The thickness influenced the crack front shape even in PMMA according to high speed camera observations by Nishioka and Stan [22]. The PMMA plates with some types of thickness were used to observe the crack front shape, and it was pointed out that the crack front at the thickness center went in advance more in the thicker specimen than in thinner specimen. In addition, the stress triaxiality at the thickness center was higher in thicker specimens [22]. Nishioka et al. also reported that the dynamic SIFs were almost constant along the curved crack front during crack propagation in PMMA [37]. In other words, the crack front shape was determined so as to make the dynamic SIF along the crack front uniform in PMMA [37]. The conclusion by Nishioka and Stan indicated that stress state of the thickness center was similar to that of the plate surface in the thinner specimen [22]. Therefore, because the apparent crack fracture toughness of thinner specimen of PMMA has higher value, the crack is likely to be arrested in thinner plates. This phenomenon corresponds to literatures that mentioned the apparent fracture toughness of PMMA was larger in thinner plates than in thicker plates [38,39]. Consequently, the crack arrest events in fillet were explained by that the crack which entered the fillet was likely to be arrested because the apparent fracture toughness of thinner fillet was higher than the full thickness plates.

In fact, the crack arrest in the fillets were observed in the some experiments of structural crack arrest design using steels to evaluate brittle crack arrest capability of the structures. For example, the experiments with the widest un-welded section in showed the crack arrest in the fillet welding shown in Fig. 9-18 [29]. Kiji et al. also reported the crack arrest event in the fillet welding when the un-welded section became wider [40]. Because the 3D effect is expected to work more remarlably in elasto-plastic solids than elastic solids because of shear lip formation, the crack arrest in fillet welding before it entered the flange is expected to be likely to cause in steels due to the loss of the plastic constraint in thinner fillet.

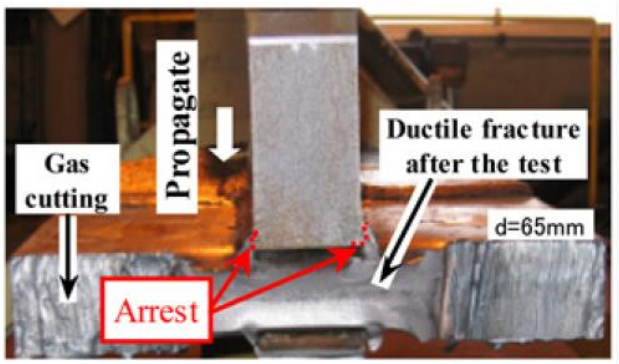

Fig. 9-18 Crack arrest in weld metal [29]

9.3.3. Transferability to steel

It should be noted about the transferability of the obtained findings to steels because the objective of this study is to aim to have findings beneficial to clarify the crack arrest mechanism in the steel structural crack arrest design although PMMA was employed as a material for the experiments.

The crack front shape is expected to be similar to the shape observed in this chapter in the actual steel structural crack arrest design. Therefore, overall principal that the crack front shape contributes to reduce SIFs in the flange is also expected to work in steels. On the other hand, the shear lip formation, which is not basically observed usually in PMMA, contributes to reduce the SIF also in the steel structural crack arrest design [13].

In addition, it is indispensable that the welding factors contribute to the crack arrest [41]. Although the welding effect is hard to quantitatively evaluate, the residual stress works to the brittle crack propagation and arrest behaviors [42,43]. Kihara et al. pointed out that the compressive residual stress worked to arrest the brittle cracks [42]. The toughness of weld metal is known to contribute to brittle crack arrest [5]. The change of the microstructure due to welding may influence the brittle crack arrest [44]. In addition to welding effect, the anisotropic microstructure may work to improve brittle crack arrest. Hiramatsu et al. already showed that brittle crack arrest toughness in thickness direction was higher than that in C direction [45]. These features are hard to simulate by using PMMA specimens, so it is needed to carry out brittle crack arrest experiments simulating the structural crack arrest design using steels.

9.4. Conclusion

This chapter carried out a series of crack arrest experiments simulating the structural crack arrest design using a transparent elastic material, PMMA. High speed camera was employed to observe the crack behaviors in the specimens, especially the crack behaviors after it entered the flange. These experiments showed a clear trend that the thicker flange made the crack likely to be arrested even when the load applied to the specimen was higher. According to the observations, the thicker flange contributed to keeping the crack front the shape similar to the shape approximated by the quadratic function. According to static elastic finite element analyses, this quadratic function shape reduced the SIF at the crack tip compared to the rectangular crack front shape, which corresponded to a through crack. Thus, although the crack front shape becomes a rectangular just after it enters the flange when the flange is thinner, the crack front can keep a quadratic function shape for long time enough to make the SIF lower than crack arrest toughness in thicker flange specimens. These observations and analyses supported the hypothesis on the crack arrest mechanism proposed by previous literatures [13].

In addition, the same experiments and observations were carried out for the specimen simulating fillet welding joint in order to study the un-welded part effect in the structural crack arrest design. The crack arrest events were found in the fillet section in some experiments. This can be attributed to the apparent higher toughness of plain stress conditions. On the other hand, the crack front branch was observed in the some fillet-welding like experiments where the crack was arrested in the flange. This crack front branch is expected to make the SIF smaller. Thus, in the fillet welding joint, the crack arrest is prompted by two factors in addition to same factor observed in the full-penetration welding. One is the stress state effect in the fillet welding, and the other is the crack front branch.

According to the above study, the role of structural factor working the structural crack arrest design was found experimentally for the first time. The transferability of the obtained results for PMMA specimen was also discussed, and it can be said that the crack front effect may be greater in steels than in PMMA due to plastic constraint. Although the other factors due to welding also influence the crack propagation and arrest behaviors, this study showed how the structural factor contributes to the brittle crack arrest in structural crack arrest design.

Reference

[1] R.A. Ibrahim, Overview of Structural Life Assessment and Reliability, Part VI: Crack Arresters, J. Sh. Prod. Des. 32 (2016) 71–98.

[2] Y. Sumi, Fracture morphology and its evolution a review on crack path stability and brittle fracture along butt-weld, Frat. Ed Integrita Strutt. 9 (2015) 42–58. doi:10.3221/IGF-ESIS.34.04.

[3] T. Fukui, H. Kitada, Arrestability Requirement for Crack Arrestor in Hull Structure, J. High Press. Inst. Japan. 41 (2003) 303–315.

[4] M. Toyoda, T. Handa, Structural Brittle Crack Arrest Design for Ultra Large Container Ship, J. Japan Weld. Soc. 81 (2012) 485–488.

[5] T. Handa, N. Kiji, M. Toyoda, R. Ikeda, Effect of Fillet Weld Metal Toughness and Leg Length on Long Brittle Crack Arrest Behavior in Tee Joint, in: Conf. Proc. Japan Soc. Nav. Archit. Ocean Eng., 2018: pp. 291–294.

[6] T. Kanazawa, S. Machida, M. Ohyagi, Some Basic Considerations on Crack Arresters (The 5th Report) -with special reference to “Ditch-type” & “Stiffener-type arresters”-, J. Zosen Kiokai. 122 (1967) 200–214.

[7] E. Tamura, T. Nakagawa, N. Furukawa, M. Toyoda, N. Kiji, Investigation on Brittle Crack Arrest Behavior of Weld Joint Structure using Thick Plate, in: Conf. Proc. Japan Soc. Nav. Archit. Ocean Eng., 2007: pp. 455–458.

[8] T. Kanazawa, S. Machida, H. Doi, Some Basic Consideration on Crack Arresters (The 6th Report) -with special reference of “Stiffeners Plate-type Arrester”-, J. Zosen Kiokai. 124 (1968) 321–330.

[9] T. Handa, S. Igi, H. Tajika, T. Tagawa, K. Hase, T. Fukui, S. Aihara, Experimental Proof of Brittle Crack Arrestability by Large Scale Structural Model Test Simulating Ultra Large Container Ship, Proc. 27th Int. Offshore Polar Eng. Conf. (2017) 14–23.

[10] K. Matsumoto, T. Fukui, S. Nanno, S. Aihar, T. Kawabata, K. Shibanuma, T. Inoue, T. Okawa, T. Tagawa, H. Tajika, H. Imamura, Brittle Crack Arrest Toughness for Extremely Thick Steel Plates -Required Kca Value of Steel Plates with Thickness of 100 mm Used in Ultra-Large Container Ships-, in: Proc. 28th Int. Ocean Polar Eng. Conf., 2018: pp. 91–97.

[11] A. Kubo, H. Yajima, S. Aihara, H. Yoshinari, K. Hirota, M. Toyoda, T. Kiyosue, T. Inoue, T. Handa, T. Kawabata, T. Tani, Y. Yamaguchi, Experimental study on brittle crack propagation behavior with large scale structural component model tests - Brittle crack arrest design for large container ships -5 -, in: Proc. Twenty-Second Int. Offshore Polar Eng. Conf., 2012: pp. 36–43.

[12] T. Handa, S. Igi, K. Oi, T. Tagawa, F. Minami, Brittle crack propagation / arrest behavior in T-joint structure of heavy gauge steel plate, Weld. World. 59 (2015) 823–838. doi:10.1007/s40194-015-0242-3.

[13] T. Handa, S. Igi, K. Oi, K. Nishimura, T. Tagawa, F. Minami, Brittle Crack Propagation/Arrest Behavior in Full Penetration T-joint, J. Japan Soc. Nav. Archit. Ocean Eng. 19 (2014) 179–185.

[14] K. Arakawa, T. Mada, Unsteady dynamic crack propagation in a brittle polymer, Exp. Mech. 47 (2007) 609–615. doi:10.1007/s11340-006-9020-x.

[15] T. Kanazawa, S. Machida, Y. Nimura, T. Teramoto, Study on Fast Fracture and Crack Arrest 2nd Report, J. Soc. Nav. Archit. Japan. 142 (1977) 156–163.

[16] M.R. Ayatollahi, M. Rashidi Moghaddam, S.M.J. Razavi, F. Berto, Geometry effects on fracture trajectory of PMMA samples under pure mode-I loading, Eng. Fract. Mech. 163 (2016) 449–461.

[17] D.J. Naus, B.R. Bass, J. Keeney-Walker, R.J. Fields, R. deWit, S.R. Low III, HSST Wide-plate Test Results and Analysis, Nucl. Eng. Des. 118 (1990) 283–295.

[18] T. Teramoto, S. Machida, T. Kanazawa, Study on Fast Fracture and Crack Arrest -The

4th Report-, J. Soc. Nav. Archit. Jappan. 146 (1979) 465–473.
[19] M. Heyder, G. Kuhn, 3D fatigue crack propagation: Experimental studies, Int. J. Fatigue. 28 (2006) 627–634. doi:10.1016/j.ijfatigue.2005.06.052.
[20] C. Ruggieri, E. Hippert, Delamination effects on fracture behavior of a pipeline steel: Anumerical investigation of 3-D crack front fields and constraint, Int. J. Press. Vessel. Pip. 128 (2015) 18–35. doi:10.1016/j.ijpvp.2015.01.004.
[21] T. Nishioka, M. Nishi, T. Fujimoto, K. Sakakura, A study on the Front Shapes and Surface Singularity of Dynamically Propagating Cracks, Trans. Japan Soc. Mech. Eng. A. 33 (1985) 1660–1668. doi:10.1248/cpb.37.3229.
[22] T. Nishioka, F. Stan, A Hybrid Experimental-Numerical Study on the Mechanism of Three-Dimensional Dynamic Fracture, Comput. Model. Eng. Sci. 4 (2003) 119–139.
[23] T. Teramoto, M. Saito, A Study on Fracture Behaviour of PMMA using AE Technique, J. High Press. Inst. Japan. 20 (1982) 92–97.
[24] G. Gonalves, P.A.A.P. Marques, A. Barros-Timmons, I. Bdkin, M.K. Singh, N. Emami, J. Grácio, Graphene oxide modified with PMMA via ATRP as a reinforcement filler, J. Mater. Chem. 20 (2010) 9927–9934. doi:10.1039/c0jm01674h.
[25] A.A. Abdel-Wahab, S. Ataya, V. V. Silberschmidt, Temperature-dependent mechanical behaviour of PMMA: Experimental analysis and modelling, Polym. Test. 58 (2017) 86–95. doi:10.1016/j.polymertesting.2016.12.016.
[26] T. Nishioka, S.N. Atluri, Numerical analysis of dynamic crack propagation: Generation and prediction studies, Eng. Fract. Mech. 16 (1982) 303–332. doi:10.1016/0013-7944(82)90111-4.
[27] K. Arakawa, T. Mada, K. Takahashi, On the Correlations among Dynamic Stress Intensity Factor, Crack Velocity and Acceleration in Fast Fracture., Trans. Japan Soc. Mech. Eng. Ser. A. 66 (2000) 883–887. doi:10.1299/kikaia.66.883.
[28] M. Ohata, Strength of Welded Joint, J. Japan Weld. Soc. 77 (2008) 678–684.
[29] T. Handa, S. Suzuki, N. Kiji, M. Toyoda, T. Miyata, Effect of Un-welded Length on Behavior of Brittle Crack Arrest in tee joint structure, Q. J. Japan Weld. Soc. 26 (2008) 124–130.
[30] P.A. Klein, J.W. Foulk, E.P. Chen, S.A. Wimmer, H.J. Gao, Physics-based modeling of brittle fracture: Cohesive formulations and the application of meshfree methods, 2001. doi:10.1016/S0167-8442(01)00091-X.
[31] F. Zhou, J.F. Molinari, T. Shioya, A rate-dependent cohesive model for simulating dynamic crack propagation in brittle materials, Eng. Fract. Mech. 72 (2005) 1383–1410. doi:10.1016/j.engfracmech.2004.10.011.
[32] D. Rittel, H. Maigre, An investigation of dynamic crack initiation in PMMA, Mech. Mater. 23 (1996) 229–239.
[33] D. Hull, Influence of stress intensity and crack speed on fracture surface topography: Mirror to mist to macroscopic bifurcation, J. Mater. Sci. 31 (1996) 4483–4492. doi:10.1007/BF00366344.
[34] C.A. Schneider, W.S. Rasband, K.W. Eliceiri, NIH Image to ImageJ: 25 years of image analysis, Nat. Methods. 9 (2012) 671–675. doi:10.1038/nmeth.2089.
[35] M. Hasegawa, T. Adachi, T. Takano-Yamamoto, Computer simulation of orthodontic tooth movement using CT image-based voxel finite element models with the level set method, Comput. Methods Biomech. Biomed. Engin. 19 (2016) 474–483. doi:10.1080/10255842.2015.1042463.
[36] J.P. Benthem, State of stress at the vertex of a quarter-infinite crack in a half-space, Int. J. Solids Struct. 13 (1977) 479–492. doi:10.1016/j.cej.2018.01.049.
[37] T. Nishioka, F. Stan, T. Fujimoto, Dynamic J Integral and Dynamic Stress Intensity Factor Distributions along Naturally and Dynamically Propagating Three-Dimensional Fracture Fronts, JSME Int. J. Ser. A. 45 (2002) 523–537.

[38] H. Wada, M. Seika, T.C. Kennedy, C.A. Calder, K. Murase, Investigation of loading rate and plate thickness effects on dynamic fracture toughness of PMMA, Eng. Fract. Mech. 54 (1996) 805–811.
[39] H. Wada, M. Seika, K. Murase, Investigation of Specimen Thickness Effect on Dynamic Fracture Toughness of PMMA, Trans. JSME. 60 (1994) 1183–1187. doi:10.1061/ASCE1090-0241 2003 129:1 12.
[40] N. Kiji, Y. Nakanishi, M. Toyoda, T. Yokura, E. Tamura, T. Nakagawa, N. Furukawa, Investigation on Brittle Crack Arrest Behavior in Practical Weld Joint of Thick Plates, in: Prepr. Natl. Meet. JWS, 2007.
[41] G.B. An, W. Woo, J.U. Park, V. Em, Comparison of crack-arrest fracture toughness between low and high heat-input thick weld specimens, Int. J. Fract. 194 (2015) 197–203. doi:10.1007/s10704-015-0041-2.
[42] H. Kihara, T. Kanazawa, K. Ikeda, H. Maenaka, M. Kinoshita, R. Nagamoto, H. Yajima, Effectiveness of Crack Arrester (First Report), J. Zosen Kiokai. 122 (1967) 191–199.
[43] H. Nakai, H. Yoshinari, T. Inoue, S. Aihar, Development of Three-Dimensional Crack Path Prediction Model for Brittle Fracture in Welded Joint with Residual Stress, Toughness Distribution and Various Types of Welding Groove, J. Japan Soc. Nav. Archit. Ocean Eng. 19 (2014) 123–137.
[44] J. il Jang, B.W. Lee, J.B. Ju, D. Kwon, W.S. Kim, Experimental analysis of the practical LBZ effects on the brittle fracture performance of cryogenic steel HAZs with respect to crack arrest toughness near fusion line, Eng. Fract. Mech. 70 (2003) 1245–1257. doi:10.1016/S0013-7944(02)00111-X.
[45] H. Hiramatsu, H. Matsuda, K. Michiba, G. Nishiyama, T. Kiyose, M. Matsuura, K. Okamoto, T. Kabawata, T. Maeda, A. Inami, S. Kubo, Investigation on the brittle crack propagation behaviour of heavy thick shipbuilding steel plate (Report 1: The crack arrestability of brittle crack propagation in the thickness direction in steel plates), Conf. Proc. Japan Soc. Nav. Archit. Ocean Eng. 5E (2007) 131–134.

Chapter 10 Conclusion

10.1. Conclusions and implications

This dissertation aims to theoretically explain brittle crack propagation and arrest behaviors in steels by focusing on the local fracture stress criterion. To achieve this objective, each element factors which constitute brittle crack propagation and arrest behaviors were investigated in detail by both experimental and numerical approaches to be appropriately understood. A series of these experimental and numerical studies were integrated to develop a new numerical physics-based model to simulate brittle crack propagation and arrest behaviors. After a comprehensive literature review of latest studies on brittle crack arrest in Chapter 1, each chapter provided below results;

Chapter 2

The verification of the local stress evaluation was carried out and it was pointed out that the accurate local stress evaluation was hindered by the vibration of the nodes. To retain such vibrations, the artificial damping method was employed based on systematic investigation on nodal force release technique. This method remarkably improved the accuracy of the local stress evaluation, especially in the application-phase method.

Chapter 3

The local fracture stress in the vicinity of the propagating cleavage crack tip was evaluated using the side-grooved specimens because it was needed to eliminate 3D effects. The generation-phase finite element analyses of the experiments showed that the local tensile stresses at the characteristic distance from the crack tip were almost constant regardless of the temperature, crack velocity, and stress intensity factor. This result strongly supported the validity of the local fracture stress criterion.

Chapter 4

A series of finite element analyses of the local tensile stress were carried out to clarify what governed the local tensile stress in the vicinity of the rapidly propagating crack tip in steels. Both of steady-state and unsteady-state crack propagations were analyzed using generation-phase nodal force release technique. According to these analyses, this chapter reported that the local tensile stress was governed by the applied stress, crack length, temperature, and crack velocity. Unsteady effect was practically negligible in elastic-viscoplastic solids including steels.

Chapter 5

To investigate brittle crack propagation and arrest behaviors in steel under extremely higher stress intensity factor conditions, two crack arrest experiments were carried out under isothermal and extremely high stress intensity factor conditions. Based on the experimental results, the conventional model based on the local fracture stress criterion was modified to consider that the effective stress intensity factor governed the shear lip thickness. This modification enabled the model simulation to predict the crack propagation or arrest under extremely high stress intensity factor conditions.

Chapter 6

This chapter focused on the contribution of the shear lip to brittle crack propagation and arrest behaviors in steels from two perspectives. One was the closure stress of unbroken shear lips. The closure stress was quantitatively evaluated by 3D elastic-viscoplastic finite element analyses assuming virtual unbroken shear lips. These analyses showed that the closure stress was well described by the plastic strain. The other was the thickness of shear lips. Shear lip thickness was measured in brittle crack propagation experiments under some temperature and applied stress conditions. It showed that the shear lip thickness could be modelled using the small scale plastic zone size and crack velocity.

Chapter 7

This chapter integrated the obtained results described above to develop a physics-based simulation model of brittle crack propagation and arrest behaviors in steels based on the local

fracture stress criterion by incorporating the contribution of shear lips. The proposed model simulation showed the results which agreed well with the experimentally evaluated $K_{ca} - T$ relationship and the crack arrest length of each crack arrest experiment. And, the identified local fracture stress in the model simulation was almost equal to the value experimentally evaluated in Chapter 3. These agreement strongly validated the proposed model simulation, including the local fracture stress criterion.

In addition to above studies, this dissertation conducted fundamental studies for crack arrest design. Studies on material design and structural design were noted in Chapter 8 and 9, respectively.

Chapter 8

The contributions of grain size, which is a fundamental feature of steel microstructures, was evaluated experimentally in the context of cleavage crack propagation resistance. The local fracture stresses were estimated using a simplified method for three ferrite-pearlite steels with same chemical compositions and different grain sizes. A series of experiments and analyses showed the local fracture stress was larger in coarser grain steel than finer grain steel. This could be related to the microstructural mechanics to absorb the energy during cleavage crack propagation.

Chapter 9

In order to investigate mechanisms to arrest a dynamically running brittle crack in the structural crack arrest design, a series of crack arrest experiments using PMMA specimens simulating the design were carried out. High speed camera was used to observe the cross section of the crack running in the specimens to clarify the crack front shape effect in the structures. As a result, the brittle cracks were likely to be arrested in the specimens with thicker flanges. The high speed observation showed that the crack fronts had the shapes which could be approximated by a quadratic function after they entered the flanges. Because such crack front shape can reduce SIF according to static finite element analyses, the cracks were arrested in the specimens with the thicker flange where the crack front could keep the quadratic function shape until it was arrested. In addition, the crack arrest tests simulating fillet welding were carried out and it was shown that

the longer un-welded section promoted the brittle crack arrest.

10.2. Limitations of this study

Although this dissertation dealt with the wide topics related to brittle crack propagation and arrest behaviors, it has several limitations. These limitations can provide some directions for future studies

Firstly, the shear lip thickness was modelled based on the experimental measurement results in Chapter 6. However, the shear lip is originally a region where the local fracture stress cannot be satisfied, therefore such thickness can be predicted using the 3D application-phase analyses based on the local fracture stress criterion. And, the closure stress calculation is naturally enabled in such 3D application phase analyses although this study developed the approximated formulation. Although this study did not employ such application phase analyses because it presently required impractically enormous numerical costs, future developments of computing and numerical methods will enable such calculation in realistic numerical time. Because the proposed simulation model in Chapter 7 depended only simplified evaluation of the shear lip thickness based on the experiment, the accuracy of shear lip thickness is still concerned. However, the appropriate 3D application phase analyses will enable the accurate prediction of the shear lip thickness.

The study on the structural crack arrest design also involves same problems. Although Chapter 9 firstly showed the crack front shape during crack propagation in PMMA, reducing numerical costs will enables such crack front shape prediction in the application phase analyses based on the local fracture stress criterion. The experimentally obtained results in this study will be available to validate the prediction by the application phase analyses in the future.

In addition, the microstructural effect to the cleavage crack propagation resistance has to be studied more. Although tear ridge formation is a critical factor to cleavage crack propagation, it is needed to quantitatively evaluate tear ridge formation under various conditions, especially in case when the microstructure has the texture. The model simulation of tear ridge formation noted in Chapter 8 may be available to optimize the microstructure to maximize the energy absorption. Actually, the simplified estimation method of the local fracture stress should be also refined. And, this study employed only the ferrite-pearlite steels. Therefore, the applicability of the findings to other microstructures, such as bainite microstructure, is expected to be clarified as the future work.

Associated Achievements

Peer-reviewed papers

(1) Fuminori Yanagimoto, Kazuki Shibanuma, Katsuyuki Suzuki, Toshiyuki Matsumoto, Shuji Aihara: Local stress in the vicinity of the propagating cleavage crack tip in ferritic steel, Materials & Design, Vol. 144. pp. 361-373, 2018

(2) Fuminori Yanagimoto, Kazuki Shibanuma, Yo Nishioka, Yuya Shirai, Toshiyuki Matsumoto, Katsuyuki Suzuki: Local stress evaluation of rapid crack propagation in finite element analyses, International Journal of Solids and Structures, Vol. 144-145, 66-77, 2018

(3) Kazuki Shibanuma, Fuminori Yanagimoto, Tetsuya Namegawa, Katsuyuki Suzuki, Shuji Aihara: Brittle crack propagation/arrest behavior in steel plate-Part III: Discussion on arrest design, Engineering Fracture Mechanics, Vol. 190, pp.104-109, 2017

(4) Yuki Yamamoto, Kazuki Shibanuma, Fuminori Yanagimoto, Katsuyuki Suzuki, Shuji Aihara, Hiroyuki Shirahata: Multiscale Model Synthesis to Clarify the Relationship between Microstructures of Steel and Macroscopic Brittle Crack Arrest Behavior – Part II: Application to Crack Arrest Test, ISIJ International, Vol.56, No.2, pp.350-358, 2016

(5) Kazuki Shibanuma, Yuki Yamamoto, Fuminori Yanagimoto, Katsuyuki Suzuki, Shuji Aihara, Hiroyuki Shirahata: Multiscale Model Synthesis to Clarify the Relationship between Microstructures of Steel and Macroscopic Brittle Crack Arrest Behavior - Part I: Model Presentation, ISIJ International, Vol.56, No.2, pp.341-349, 2016

(6) Kazuki Shibanuma, Fuminori Yanagimoto, Tetsuya Namegawa, Katsuyuki Suzuki, Shuji Aihara: Brittle crack propagation/arrest behavior in steel plate-Part II: Experiments and model validation, Engineering Fracture Mechanics, Vol.162, pp.341-360, 2016

(7) Kazuki Shibanuma, Fuminori Yanagimoto, Tetsuya Namegawa, Katsuyuki Suzuki, Shuji Aihara: Brittle crack propagation/arrest behavior in steel plate-Part I: Model formulation, Engineering Fracture Mechanics, Vol.162, pp.324-340, 2016

(8) Fuminori Yanagimoto, Kazuki Shibanuma, Katsuyuki Suzuki：Fundamental Study on the

Simulation of Fast Crack Propagation by Finite Element Method, Journal of Japan Society of Civil Engineers, Ser. A2 (Applied Mechanics (AM)), Vol.71, No.2, I_29-I_38, 2016 (in Japanese)

(9) Fuminori Yanagimoto, Kazuki Shibanuma, Katsuyuki Suzuki, Toshiyuki Matsumoto: Governing factors of the local tensile stress in the vicinity of a rapidly propagating crack tip in elastic-viscoplastic solids, Engineering Fracture Mechanics, submitted

(10) Fuminori Yanagimoto, Kazuki Shibanuma, Katsuyuki Suzuki, Toshiyuki Matsumoto: A physics based model to simulate brittle crack arrest in steel plates without adjustable parameters, Engineering Fracture Mechanics, submitted

(11) Fuminori Yanagimoto, Yuta Suzuki, Takuhiro Hemmi, Yasuhito Takashima, Tomoya Kawabata, Kazuki Shibanuma: Contribution of grain size to resistance against cleavage crack propagation in ferritic steel, Acta Materialia, submitted

Peer-reviewed presentation in international conferences

(1) ○ Taiko Aikawa, Shuji Aihara, Fuminori Yanagimoto, Tomoya Kawabata, Kazuki Shibanuma: Computer simulation of cleavage fracture surface morphology in steel plates, 22nd European Conference on Fracture, August, Belglade, 2018

(2)○ Fuminori Yanagimoto, Kazuki Shibanuma, Teppei Okawa, Katsuyuki Suzuki, Shuji Aihara: Investigation on brittle crack propagation and arrest behaviors under high crack driving force in steel, 22nd European Conference on Fracture, August, Belglade, 2018

(3) ○ Yasuyuki Furuta, Shuji Aihara, Yuki Nishizono, Fuminori Yanagimoto, Tomoya Kawabata, Kazuki Shibanuma, Carlos Augusto Oliveira, Armando Shinohara: Simulated running ductile fracture experiment using rubber tube, 22nd European Conference on Fracture, August, Belgrade, 2018

(4)○Kota Kishi, Kasuki Shibanuma, Fuminori Yanagimoto, Katsuyuki Suzuki: Development of dynamic s-version FEM for local tensile stress evaluation, 22nd European Conference on Fracture, August, Belglade, 2018

(5)○Fuminori Yanagimoto, Kazuki Shibanuma, Katsuyuki Suzuki: High Speed Observation of Fast Crack propagation and Arrest behaviors in 3D Transparent Structures, 22nd European Conference on Fracture, Belglade, August, 2018

(6)○ Yuta Suzuki, Takuhiro Hemmi, Fuminori Yanagimoto, Hiroyuki Shirahata, Kazuki Shibanuma; The influence of grain size on cleavage crack propagation resistance in ferritic steels, 22nd European Conference on Fracture, Belglade, 2018

(7) Shuji Aihara, ○Fuminori Yanagimoto, Kazuki Shibanuma, T. Namegawa, H. Nakai, T. Kawabata, H. Yoshinari: Numerical simulation of brittle crack propagation incorporating toughness and residual stress distribution in weld, 10th International Conference on Trends in Welding Research, Tokyo, October, 2016

(8) ○Fuminori Yanagimoto, Kazuki Shibanuma, Katsuyuki Suzuki, Shuji Aihara: A New Model to Simulate Crack Arrest Behavior in Steel Plates Used for Naval Structures, Techno-Ocean 2016, Kobe, October, 2016

(9) ○Fuminori Yanagimoto, Kazuki Shibanuma, Tomoya Kawabata, Katsuyuki Suzuki, Shuji Aihara: Measurement of local brittle fracture stress for dynamic crack propagation in steel, 21st European Conference on Fracture, Catania, June, 2016

(10) ○Yo Nishioka, Kazuki Shibanuma, Katsuyuki Suzuki, Fuminori Yanagimoto: Finite element model to simulate crack propagation based on local fracture stress criterion, 21st European Conference on Fracture, Catania, 2016

Non-peer-reviewed presentation in international conferences

(1) ○ Fuminori Yanagimoto, Kazuki Shibanuma, Katsuyuki Suzuki, Shuji Aihara: Measurement of Local Fracture Stress during Cleavage Crack Propagation in Steels, 14th International Conference on Fracture, Rhodes, Greece, June, 2017

(2) ○Fuminori Yanagimoto, Takuhiro Henmi, Kazuki Shibanuma, Katsuyuki Suzuki, Shuji Aihara, Hiroyuki Shirahata: Experimental Evaluation of Grain Size Effects on Crack Arrestability in ferrite-pearlite steels, International Society of Offshore and Polar Engineering 2018, Sapporo, June, 2018

Presentation in domestic conferences (in Japanese)

(1) ○ Fuminori Yanagimoto, Kazuki Shibauma, Katsuyuki Suzuki: The Fundamental Analyses of dynamic crack propagation by Finite Element Method, 18th Applied Mechanics Symposium, 100089, Kanazawa, 2015

(2) ○Fuminori Yanagimoto, Kazuki Shibauma, Katsuyuki Suzuki, Suji Aihara: The Study on Controlling Brittle Crack Propagation and Arrest in Heavy-Section Steel Plates by the Model Calculation, JASNAOE (The Japan Society of Naval Architects and Ocean Engineering) Annual Autumn Meeting 2015, 2015A-GS8-4, Tokyo, 2015

(3) ○Fuminori Yanagimoto, Kazuki Shibauma, Katsuyuki Suzuki, Shuji Aihara: Evaluation of local fracture stress during brittle crack propagation in steel, 172th ISIJ (The Iron and Steel Institute of Japan) Meeting, PS-60, Osaka, 2016

(4) ○Fuminori Yanagimoto, Kazuki Shibanuma, Yo Nishioka, Yuya Shirai, Katsuyuki Suzuki：Evaluation of the local stress near the tip of a fast crack in finite element analyses, JASNAOE Annual Autumn Meeting 2017, 2017A-GS2-5, Hiroshima, 2017

(5) ○ Fuminori Yanagimoto, Kazuki Shibauma, Katsuyuki Suzuki, Shuji Aihara : Experimental Evaluation of Local Fracture Stress of Cleavage Crack Propagation in Ferrite-Pearlite Steels, 175th ISIJ Meeting, 247, Narashino, 2018

(6) ○Fuminori Yanagimoto, Kazuki Shibauma, Katsuyuki Suzuki: Parametric Study on Factors Governing Crack Tip Stress Fields of a Rapidly Propagating Crack, JASNAOE Annual Spring Meeting 2018, 2018S-GS5-4, Osaka, 2018

(7) ○Fuminori Yanagimoto, Kota Kishi, Kazuki Shibauma: Recent Study on Brittle Crack Propagation and Arrest Behavior Based on the Local Fracture Stress Criterion, JASNAOE Annual Autumn Meeting 2018, 2018S-OS4-7, Kashiwa, 2018

(8) ○Fuminori Yanagimoto, Kazuki Shibanuma, Katsuyuki Suzuki: Observation of 3D Fast Crack Propagation in Joint Structures of Transparent Solids, The Japan Society of Mechanical Engineers M&M 2018 Conference, GS0703, Fukui, 2018

Award

(1) Dean’s Award (Research) in Graduate School of Engineering, the University of Tokyo, March, 2016

(2) Award for Outstanding Presentation of Young Researcher in JASNAOE Annual Spring Meeting 2018, June, 2018